# STUDY OF ARCHITECTURED MATERIALS WITH A CORRUGATED GEOMETRY

# THE STUDY OF ARCHITECTURED MATERIALS WITH A CORRUGATED GEOMETRY

By MARK FRASER, B. ENG. MGT.

A Thesis Submitted to the School of Graduate Studies in Partial Fulfilment of the Requirements for the Degree Doctor of Philosophy

DOCTOR OF PHILOSOPHY (2017)

Materials Science and Engineering

McMaster University, Hamilton, Ontario

TITLE: The Study of Architectured Materials with a Corrugated Geometry

AUTHOR: Mark Fraser, B.Eng. Mgt. (McMaster University)

SUPERVISOR: Professor Hatem Zurob

NUMBER OF PAGES: xxvii, 330

# LAY ABSTRACT

It is uncommon to find a material that possesses both high strength as well as the ability to elongate a lot without failing. One way to achieve this combination of properties is to use a wavy or corrugated structure that provides increased elongation when loaded due to the straightening of the corrugation. The purpose of this thesis was to study how materials which possess a wavy or corrugated geometry behave when they are subjected to a stretching load. This research utilized computer simulations and simple experimental testing to evaluate both isolated corrugations and corrugations embedded in another material. It was found that the amount of improvement in elongation is dependent on the initial amount of waviness. Also, whether a material shows improved elongation depends on whether the corrugation is able to unbend, which in turn depends on the corrugation geometry and the relative mechanical properties of the two materials.

# ABSTRACT

Compared to materials with a straight geometry, materials with a corrugated architecture have shown potential to improve ductility without sacrificing strength due to the unbending of the corrugation during loading. The purpose of this research was to study the effect of geometric and material parameters on the stress-strain response of materials with a corrugated geometry and understand what controls the unbending process and under what conditions improved ductility was achievable. This involved studying isolated corrugations and corrugation reinforced composites under tensile and transverse compressive loading by performing parametric studies using Finite Element Modeling (FEM) simulations. These simulations showed that improvements in ductility are directly related to the degree of corrugation present and can be attributed to an initial bending dominated process. The unbending of the corrugation leads to an evolving geometry which causes the material to strengthen and ultimately delays necking. For corrugated composites, it was found that there is significant interplay between the properties of the components and the geometry of the corrugation. To obtain a benefit in ductility through corrugation, the matrix must have sufficiently high work hardening to accommodate the unbending corrugation without itself necking, but also have sufficiently low flow stress relative to the reinforcement yield strength to prevent the corrugation from stretching instead of unbending. Also, if the boost in work hardening from unbending occurs too early, no gain in ductility is achieved. In addition to these findings, tools for predicting the strength and ductility of these materials were developed, including an analytical model for the isolated corrugations and a series of benefit maps and surfaces for the corrugated composites. These tools proved to be fairly effective. Finally, the FEM findings were compared to experimental stress-strain curves and strain maps for validation and showed relatively good qualitative agreement.

# ACKNOWLEDGEMENTS

I would like to acknowledge a number of people without whom this thesis would not be possible.

First off, I would like to express my sincere thanks to my supervisor Dr. Hatem Zurob for his guidance and encouragement throughout my time at McMaster. His support and constant enthusiasm were extremely helpful in getting through the tough stages of this degree. I would also like to thank him for our many interesting discussions over the years.

I would also like to thank my supervisory committee members Dr. David Embury and Dr. Peidong Wu for their advice and guidance. Our discussions were always illuminating and very helpful towards solidifying my understanding of the research topics.

I would like to extend my gratitude towards Dr. Yves Brechet and Dr. Olivier Bouaziz for many exciting discussions, both in France and Canada, about architectured materials. Your enthusiasm and knowledge in these meetings kept me engaged and motivated to study in this field.

I would also like to say many thanks to Jim Garrett, Doug Culley, Dr. Xiaogang Li and Dr. Mike Bruhis for their many hours of assistance in helping me design experiments and teaching me how to perform many different tasks in the labs. I am also grateful to all the members of the MSE department at McMaster for the years of fun both professionally and socially. I will look back fondly at my time spent at McMaster with this great group of people.

I would like to say a special thanks to my family and close friends for their constant support. I am forever grateful. Finally, I would like to thank my wonderful girlfriend Danielle for her endless encouragement and support, without which I would not have been able to complete this work.

# Table of Contents

# Table of Figures

# Table of Tables

# DECLARATION OF ACADEMIC ACHIEVEMENT

This dissertation contains original research that I, Mark Fraser, conducted on my own. I performed the literature review, designed the parametric studies, ran the computer simulations, designed the experiments, fabricated and tested the samples. I also performed the analysis of the results of the simulations and experimental testing. I performed all these tasks with the guidance of my supervisor, Dr. Hatem Zurob, and my supervisory committee members, Dr. David Embury and Dr. Peidong Wu. The manuscript for this thesis was written by me with editorial input from Dr. Hatem Zurob.

# 1 Introduction

As a starting point in the development of new materials it is beneficial to examine the range of materials that are currently available. Every material is defined by the set of properties which it possesses, whether they are physical properties, mechanical properties or functional properties. These materials populate an n dimensional space, where n is the number of properties being considered. Obviously, it is not easy to visualize this n dimensional space; however it is possible and often enlightening to obtain two-dimensional slices of this material property space. In these two dimensional slices, two specific properties can be examined and a plot can be populated with all the materials available. One example of a material properties plot can be seen in Figure 1-1 below, displaying the Young's Modulus versus density of a number of materials. One feature that is common in these material property charts is the presence of gaps or holes in property space. These holes frequently represent highly desirable combinations of properties, for example, high Young's Modulus and low density. A material possessing this combination is extremely desirable as it represents stiff lightweight materials. It is often the aim in materials design to try and fabricate materials that have properties such that they fill these holes. Unfortunately, these holes typically exist for a reason; it is very difficult to design homogenous materials with these properties, often due to limitations at the bonding level as is the case with achieving high Young's Modulus and low density. Therefore, it may be advantageous to try a different approach to materials design. One approach that has proven effective in filling these holes is the design of hybrid or composite materials.

The combination of two or more materials can yield a new material with a unique set of properties. There are a number of possible outcomes that are the result of combining two

materials, the extreme cases illustrated in Figure 1-2. The worst case scenario, case D, occurs when the resulting material exhibits the undesirable property of material 1 and the undesirable property of material 2. The best case scenario, case A, is when the composite material acquires the desirable property of each of the constituent materials. More likely than these extreme cases are cases B, C or anything between cases A and D. Case B, can be considered a rule of mixtures whereby the properties of the composite material are a linear combination of the two materials weighted by volume fraction. This is typically the case for longitudinal Young's Modulus vs. density plots for composites which contain the reinforcing phase arrayed in a continuous, linear fashion, for example a fibre reinforced composite. Case C, is similar to case B except there is synergistic losses in the combination. The combination is not limited to these cases and can result in material properties that follow any path that is between the two extreme cases.

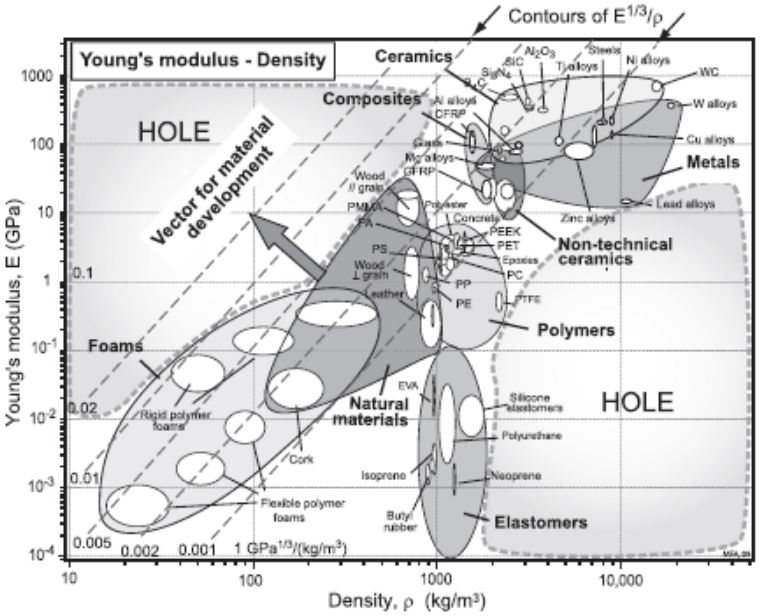


**Figure 1-1: Property map of Young's Modulus vs. density taken from Ashby.**[1]

Which path a given composite material will follow depends on a number of factors. The same composite material may show different paths depending on the two specific properties being

examined (i.e. it may follow a rule of mixtures for Young's Modulus vs. density and a worst case scenario for electrical conductivity vs. yield strength). Additionally, the combination of the same two materials and the same two properties may follow different paths if the geometry of the constituent components is different. For example, for heat conductivity vs. density, a rule of mixtures will exist for a composite with a continuous aligned straight reinforcement whereas, a composite reinforced by particles will demonstrate a non-linear relationship. This is due to the fact that heat conduction is highly dependent on path. This importance of geometry has led to a modified approach to material design that is known as architectured material design.

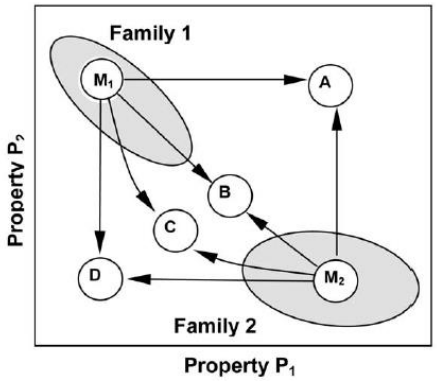


**Figure 1-2: Hypothetical property chart showing possibilities obtainable by combining materials (Ashby and Brechet).**[2]

Typically, when trying to design or improve a material, the approach of the materials scientist involves altering the microstructure of the material. This can be accomplished using a multitude of methods including heat treatments, alloying elements and mechanical processing. Conversely, a mechanical engineer would approach this problem from a different angle and try and improve the properties of a material by optimizing the geometry of the overall part, i.e. altering the macrostructure. A third approach, one which until recently was not well defined, is termed architectured materials design, and it attempts to combine the other two approaches in order to

obtain the benefits from each approach. This concept of architectured materials essentially involves consciously designing materials on multiple length scales.

Recently, materials scientists have begun to employ this methodology of architectured materials and have begun to design materials with an outlook that includes design on the meso and macro scales. One such example is a composite material with curvilinear reinforcement geometry. This curvilinear geometry can come in the form of a corrugation or a helix as illustrated in Figure 1-3, or some other more complicated curvilinear geometry. The reason that this architecture is of interest is that it facilitates increasing work hardening behaviour as a result of the unbending process of the reinforcement. This type of material can be referred to as a geometrically induced strain hardening material. The increasing work hardening behaviour results in higher work hardening rates at larger values of strain, which ultimately leads to an increase in the necking strain of the material. Additionally, unlike conventional techniques that improve necking strain, the use of this geometry does not come with a significant sacrifice in strength. The aim of these materials with geometrically induced strain hardening behaviour is it to populate the region of material property space containing the combination of high strength and high uniform elongation. The modeling, fabrication and evaluation of these corrugation reinforced composites is the focus of this thesis.

Previous work on corrugation based composites has mainly focused on the deformation behaviour of isolated corrugations or sandwich panels and much of the work that has looked into corrugations embedded in a matrix material has been either mainly a proof of concept or looked at general geometric trends. The purpose of this present research is to not only build on the current knowledge with regards to the effect of the geometry of the corrugated composite, but to also investigate the contribution of the component materials on the behaviour of these

composites and to understand the interplay between materials and geometry in dictating the overall response of the composite. Additionally, this work aims to provide a framework and some tools for determining the composite systems for which it is possible to take advantage of a corrugated architecture. Finally, this work aims to use the information pertaining to local stress and strain patterns to understand the resultant global stress-strain response of these composites.

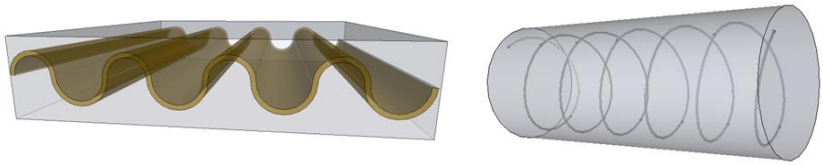

**Figure 1-3: Composites with curvilinear reinforcements (corrugation, left, and helix, right).**

The approach that was taken to study these corrugation based architectured materials focused on performing parametric studies to determine the contributions of important geometric and materials parameters on the stress-strain behaviour of the composite material. These parametric studies were performed using the numerical modeling technique of Finite Element Modeling (FEM). The FEM simulations were performed for both isolated corrugations and corrugation reinforced composites. The work on the isolated corrugations was performed to gain an understanding of how the corrugation behaves without the constraint of the surrounding matrix, which could then be compared to the behaviour of an embedded corrugation. Through the use of these parametric studies, it was possible to determine what to expect from these corrugation reinforced composites and to develop tools for predicting under what conditions they are beneficial. This FEM work was then supplemented with simple experiments whose aim was to validate some of the observations made through the modeling efforts. The experimental work involved the creation of corrugated strips for reinforcement and casting a matrix material around these corrugations to form a composite. These composites were then tested in a variety of

loading geometries and when possible local strain maps were acquired using Digital Image Correlation (DIC).

This thesis has been structured in the following fashion. Chapter 2 provides a review of some of the relevant literature pertaining to this topic. Although not an exhaustive review, it does provide a good picture of the work that has been done in related topics. The thesis is then divided into a section that focuses on the modeling work and a section on the experimental work. Starting with the modeling work, Chapter 3 presents details on the modeling method that was used, details the parametric studies that were performed and presents the results of these modeling studies. Chapter 4 presents a discussion of the modeling results and includes some additional modeling work that was inspired by the analysis of the results. The section on the experimental work is next, with Chapter 5 detailing the experimental approach that was employed and the results of this approach. Also included in this chapter is some analysis of the experimental results including comparisons to the modeling work. The thesis is completed with Chapter 6, which summarizes the findings of the thesis and makes suggestions for future work.

# 2 Literature Review

The review of the literature pertaining to this research topic has been divided into a number of different sections. The first section is a review of some of the classical methods available for obtaining high strength, high uniform elongation materials. This is followed by a section which explores the architectured materials design methodology. The next section examines some of the key foundational work with regards to composite systems in general. Finally, the last section surveys the work that has been performed with respect to the geometry of interest for this research; the corrugation.

## 2.1 Methods for Achieving High Strength and High Uniform Elongation

As mentioned before, one of the attractive aspects of composite or hybrid materials is their ability to fill holes in materials space that are characterized by seemingly contradictory combinations of properties. One of the most desirable, yet extremely difficult to achieve, combinations of properties is high strength and high uniform elongation. For the purposes of this thesis the terms uniform elongation, necking strain and ductility will be used interchangeably. The ability to achieve this combination of properties is desirable for energy absorption purposes. Additionally, there are a number of materials that currently exhibit high strength, such as nano-crystalline materials, but have very minimal ductility, leaving them with very poor formability. The ability to boost this ductility, even to a small degree, without losing out on strength would be highly desirable. Achieving this combination of high strength and high uniform elongation is the impetus for this research project and the reason that the corrugated architecture is being explored. That being said, this is not the only approach possible for achieving this property combination, as other, more classical materials have been developed that are capable of

achieving high strength and high uniform elongation. Each of the following subsections presents a class of materials that is capable of achieving this combination of properties. These subsections will consider nano-scale twins, twinning induced plasticity (TWIP), transformation induced plasticity (TRIP), and waiting elements.

### 2.1.1 Nano-scale Twins

The first method revolves around the inclusion of coherent internal boundaries on a nano-scale. The two papers Lu et al.[3] and Lu et al.[4] provide an example of this class of material and examine the use of these boundaries in copper in order to strengthen the material without sacrificing ductility. Similar to nano-grain refinement, coherent nano-scale internal boundaries, for example nano-scale twins, offer significant strengthening through the impedance of dislocations. However, nano-scale twins can also result in high ductility due to an increase in work-hardening with decreasing twin size. The twin boundaries act as barriers to dislocation motion, but also provide more local sites for the nucleation of dislocations thus allowing additional elongation. This is due to the interaction between twin boundaries and dislocations which differs from the interaction between grain boundaries and dislocations. The disordered structure of grain boundaries inhibit the ability of dislocations to slide, limiting the ability of the grain boundary to accommodate dislocations and ultimately leading to increased strength but decreased ductility. Twin boundaries on the other hand can accumulate dislocations much more easily due to their coherent nature. The presence of these nano-twins ultimately leads to a high strength-high ductility material.

### 2.1.2 Twinning Induced Plasticity (TWIP)

A second class of materials that circumvents the trade-off of strength for ductility are materials which employ twinning induced plasticity (TWIP).The most noteworthy example of a material

employing this behaviour are TWIP steels. As discussed in review paper of De Cooman et al.[5], TWIP steels offer both high strength and through a high strain hardening rate, a large degree of ductility. This high work hardening is achieved through a dynamic process whereby upon straining the steel, mechanical twins are continuously formed, further refining the microstructure and maintaining a high work hardening rate. These twins act as obstacles to dislocation glide increasing the flow stress in the material, which when coupled with the high work hardening rate lead to a high strength material capable of large uniform elongation. This introduction of a new source of work hardening is common to a number of these classes of material that are capable of achieving high strength and high uniform elongation.

### 2.1.3 Transformation Induced Plasticity (TRIP) Steels

A third example of a high strength, high uniform elongation material is a transformation induced plasticity (TRIP) steel. As described in the paper written by Jacques et al.[6], the TRIP effect is a result of the transformation from retained austenite to martensite when the material is subject to a sufficiently large stress. TRIP steels initially contain a fraction of retained austenite and as the stress in the material is increased parts of this retained austenite will transform into martensite until all of the retained austenite becomes martensite. Martensite is stronger than austenite and therefore this transformation results in an increase in the work hardening of the material. This increase in work hardening delays the strain at which the Considere criterion is met and thus increases both the strength and the uniform elongation of the steel.

### 2.1.4 Waiting Elements

A final method involves the design of "waiting" elements, which postpone the failure of a material. The paper by Cherkaev and Slepyan[7] explores dynamic tensile loading leading to failure and introduces potential methods to postpone this failure. This paper discusses ways of

distributing large strains throughout the sample to postpone failure by altering the overall structure. One of the ways discussed involves the use of parallel waiting elements whose involvement is triggered once a certain strain level is reached. A waiting system will often sacrifice strength in an initial stage in order to obtain additional strength in the next stage when it is more needed, as it is in the latter stage where an instability would normally develop. This can be accomplished by looking at a system of parallel bars which are loaded in stages due to slightly different lengths and comparing their behaviour to a single bar of the same cross sectional area. The waiting system employing the parallel bars results in more energy absorbed before failure. Another way to delay necking proposed in this paper is to transform macro-strains into micro-strains that exist in a more stable state. One example of this is through the straightening of a helical reinforcement. This is also a waiting type structure that leads to high energy absorption as the component that has the highest resistance to failure is not activated until unbending has occurred. The design of these waiting element structures often involves designing the structure or architecture of the material on an intermediate scale, and therefore these materials can be considered architectured materials. The next section will explore this notion of architectured materials in more detail.

## 2.2 Architectured Materials

When performing a review of the relevant research pertaining to these geometrically induced strain hardening materials, it is important to consider the concept of architectured materials. It is difficult to differentiate between the terms architectured, hybrid and composite materials, as there is a great deal of overlap in their definitions. These terms are often used to describe the same materials, with the difference mainly being in the context in which they are examined. The terms composite and hybrid basically mean the same thing, a combination of two or more

materials (or lack of materials in the cases of foams and other lattice structures) to form a new heterogeneous material. Architectured materials are the same thing, however, this term is often used to describe a more conscious effort of designing the material structure on different scales. The following review of architectured materials is divided into two subsections. The first focuses on the concept of architectured materials. The second section examines some examples of architectured materials including instances found in nature.

### 2.2.1 Architectured Materials Concept

As described in Ashby and Brechet[2] and Ashby[8], the main goal of architectured or hybrid materials is to create a material with a desirable combination of properties to fill holes in material property space that cannot be filled using monolithic materials. One approach that can be applied in the design of these materials, is that proposed by Ashby[8], which can be summarized by the statement 'A + B + configuration + scale'. In this approach A and B represent the constituent components of the hybrid, configuration has to do with the geometric arrangement and relative amounts and scale relates to the size of the constituent components. The way in which the concept of architectured materials differs from that of hybrid and composite materials is in its focus on the importance of the configurations and scales of the material. Another paper written by Ashby[1] highlights the importance of component materials, volume fractions, configurations, connectivity and scale on the final material properties of architectured materials.

The combination of connectivity and configuration in an architectured material can have important influences on the stress-strain behaviour as discussed in Ashby[8] and Fleck et al.[9] For instance different arrangements of lattice structures with different nodal connectivities can yield very different stress-strain responses. Depending on the relative numbers of nodes and struts present in a foam or lattice structure either bending dominated or stretching dominated

deformation may occur. In cases when an insufficient number of struts are present relative to joints, such as the case with foams, the structure will be bending dominated and possess low structural efficiency. This will result in the bending and collapse of the struts in the foam which can lead to a large amount of deformation. When a sufficient number of struts are present relative to the number of joints, such as the case for micro-trusses, the material will be stretching dominated and will have a high structural efficiency. A comparison of the attainable strengths for stretching and bending dominated structures can be seen in the property map taken from Ashby[10] in Figure 2-1 below. The large degree and manner of deformation present in corrugated materials is similar to that seen in foams and suggests that bending dominated deformation is likely present.

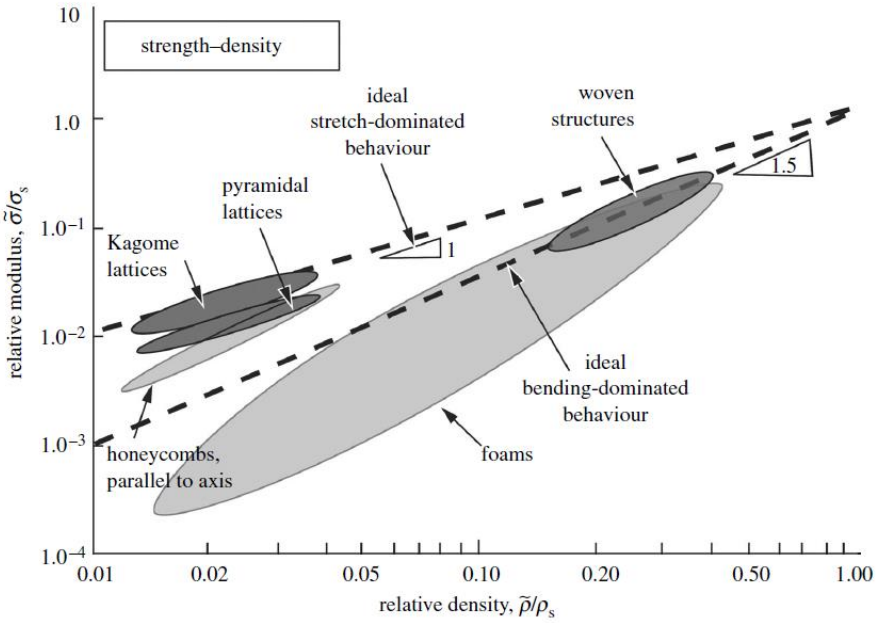


**Figure 2-1: Materials property chart of relative strength plotted against relative density for both stretch dominated and bending dominated cellular structures (Ashby).[10]**

Another manner of presenting the concept of architectured materials is introduced by Bouaziz et al.[11] and was briefly discussed in the introduction. The traditional approach for material design

by materials scientists is the improvement of properties through changes in the microstructure. This can be accomplished through heat treatments, alloying additions and mechanical processing. The mechanical engineer on the other hand traditionally improves the performance of a part by optimizing the macrostructure for a given application. The idea behind the architectured materials design approach is to combine these two approaches in order to obtain the benefits from both of the methods. The combination of these two approaches introduces a new design variable which can be thought of as the architecture. Architectured materials can be used to address seemingly contradictory design requirements, characterized by holes in material property space, by employing benefits given by geometrical design on an intermediate scale. For example, by spatially varying carbon composition in steels it is possible to get both high strength and high uniform elongation. This desirable combination of properties is achieved through the design of architecture on an intermediate length scale, that length scale being related to the diffusion of carbon in the steel. This topic of compositionally graded materials will be discussed in more detail later in the chapter.

Two considerations that are of great importance in the development of architectured materials are, one, the interfacial constitution, and two, fabrication routes, as highlighted in Bouaziz et al.[11] The interface plays a very important role in composite materials and its strength and gradation can have significant effects on mechanical behaviour. The strength of the interface can influence the strength and toughness of composites as if it has low strength it can result in ineffective stress transfer, resulting in a lower composite strength, but it can also act as a crack arrestor through decohesion and increase the toughness of the material as a whole. Additionally, the chemistry of the interface can limit the selection of component materials, as in certain instances undesirable intermetallics may form and degrade the strength and toughness of a material. The difference

between sharp and diffuse interfaces is also an important consideration in the design of architectured materials. Sharp interfaces provide potential weak points in a composite whereas graded interfaces remove this issue. However, as mentioned above, sharp interfaces can also act as crack arrestors if high toughness is desired. In addition to recognizing the importance of the interface when designing these architectured materials, it is important to realize that the creation of these materials will often require the development of new fabrication methods or the adaptation of current techniques. The addition of design on intermediate scales, often in the form of a hierarchical structure, will require additional levels of control in the fabrication processes as discussed in Brechet and Embury[12].

### 2.2.2 Examples of Architectured Materials

It may be instructional to include some examples of architectured materials to demonstrate the benefits of this design technique and show the range of materials that fall under this heading. This section will look at interlocking materials, microtrusses, compositionally graded materials, and will explore the idea of biomimetics.

#### *2.2.2.1 Interlocking Materials*

The first example is interlocking materials. These are considered an architectured material because of the subdivision of components that exists on an intermediate scale. The paper written by Dyskin et al.[13] explores the use of interlocking osteomorphic blocks for their improved flexibility and damage tolerance when compared to a homogenous material. The interlocking blocks consist of concave and convex surfaces that can be arranged to interlock with increased surface area and hence frictional force compared to a rectangular system of blocks. A system of these interlocking blocks was created out of a polyester resin, assembled, and was subject to a compressive load in the transverse direction. This was compared to a similar test performed on a

system of the same material and thickness but a solid block. It was observed that the solid block offered higher stiffness and larger failure stress, but the interlocking blocks demonstrated much larger deflections and higher bending flexibility. Additionally, damage in the interlocking system was constrained to the blocks in which it was initiated and cracks did not propagate through the entire system unlike in the solid material case as seen in Figure 2-2. This highlights the attractive damage tolerance properties of these interlocking systems and demonstrates how subdividing and designing a component on an intermediate scale can lead to an improved material for a specific application.

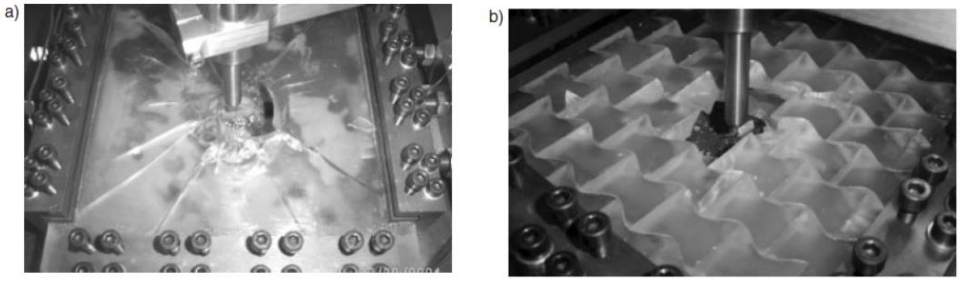


**Figure 2-2: Concentrated loading tests on a) solid sample and b) interlocking osteomorphic brick sample (Dyskin et al).**[13]

#### *2.2.2.2 Microtrusses*

A second example of an architectured material is a microtruss, as illustrated in Figure 2-3. Microtrusses are an architectured material combining the strut material and free space in a lattice structure, which provide a high degree of structural efficiency, due to the stretch dominated loading, and offer impressive specific strength. Microtruss structures are a form of architectured materials that transform external loads into axial loads acting along the members of the lattice system. Further design of these microtrusses can be done to improve the properties as seen in the paper completed by Bouwhuis et al[14]. This paper investigates the use of twinning induced plasticity (TWIP) steels in microtruss structures. In this study, TWIP steels are used to improve

the work hardening behaviour of the struts as the presence of nano-twins inhibits dislocation glide. TWIP steel based microtrusses were constructed and during the forming process the ultrafine mechanical twins were formed. These microtrusses were then tested in compression and compared to compression tests of microtrusses which had undergone a further annealing process to remove the twinning structure. It was found that the unannealed samples provided double the improvement in terms of compressive strength over the annealed samples demonstrating the huge benefit of the nano-twin based microstructure. Additionally, the effect of the truss angle was demonstrated for these TWIP based systems. The results of these tests were plotted on a property map of strength vs. density, as shown in Figure 2-4, which highlighted the attractive vector for development achievable using these TWIP microtrusses. This is an excellent example of an architectured material which employs a hierarchical design including not only the microtruss structure but also on a smaller scale, a twinned microstructure in the struts.

#### *2.2.2.3 Compositionally Graded Materials*

A third example of architectured materials is the class of materials called compositionally graded materials. A compositionally graded material is a material in which the concentration of an element or component is spatially varied within a material. This can be considered an architectured material as it involves designing the structure of the material on the scale of the spatial variations. These spatial variations are often achieved through diffusion related processes. As described in the paper written by Chehab et al.[15] compositionally graded steels can be designed to try and overcome conflicting design requirements, such as high strength and fracture resistance. This paper proposes the use of carburization/decarburization treatments in order to create compositionally graded steels and explores the range of microstructures that can be achieved using these techniques. A sample of some of the potential architectures is shown in

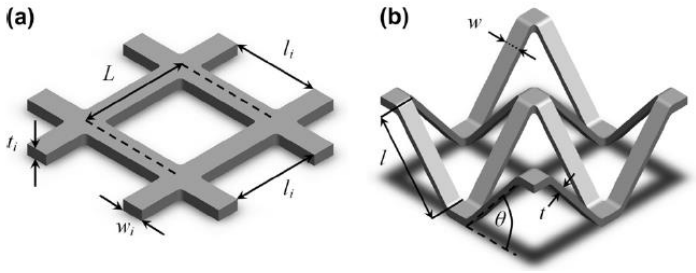


**Figure 2-3: Illustration showing a) grid precursor and b) stretch formed microtruss (Abu Samk et al).**[16]

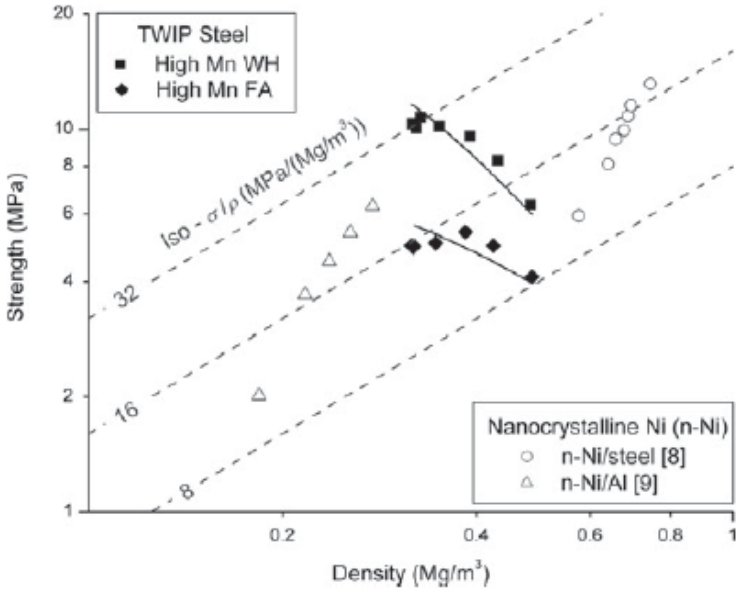


**Figure 2-4: Strength vs. density property map highlighting vector for development for TWIP steel based microtrusses (solid squares), taken from Bouwhuis et al.**[14]

Figure 2-5, many of which require the application of diffusion masks to achieve the desired pattern.

A diffusion mask is applied to selectively prevent diffusion from occurring in certain locations of a sample. When performing a diffusion masking operation there are two options to choose from; extrinsic masking (ex. application of copper coating on the surface, which inhibits carbon diffusion) and intrinsic masking (ex. successive machining and thermochemical treatment steps). In addition to the use of diffusion masks, there are a number of design variables that can be

controlled in order to achieve a desired compositionally graded structure as highlighted in the article by Chehab et al.[15], including surface concentration or activity, diffusion depth, resultant phases and interfacial sharpness.

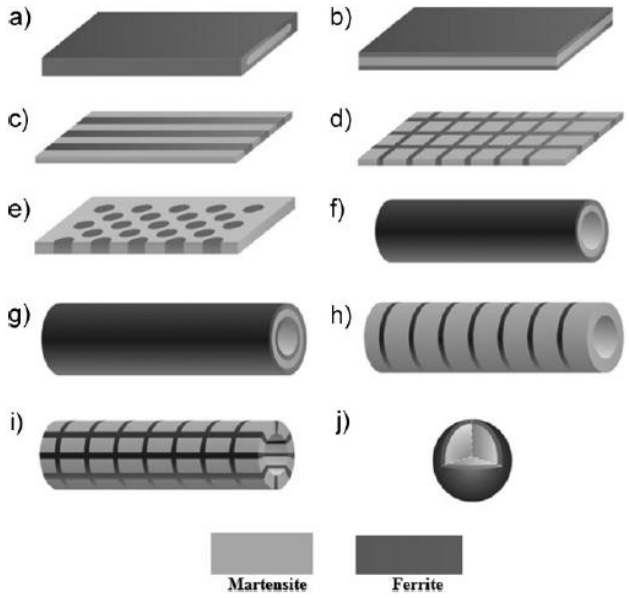


**Figure 2-5: Sampling of potential architectures obtainable through diffusion masking combined with carburization/decarburization (Chehab et al).**[15]

The idea of employing diffusion as a means to fabricate architectured materials was further explored by Cicoria et al.[17] This paper focuses on carbon diffusion in steel through carburization and decarburization treatments in order to create compositionally graded materials and presents experimental results as a proof of concept with the creation of simple martensitic wires reinforcing ferritic steel. The images in Figure 2-6 show a summary of this experiment, with the microstructure and hardness map showing the success of this technique at acquiring the target architecture. The goal of this technique is to create an architecture on an intermediate scale, that being the scale of the diffusion in the material. In order to control the diffusion profile one can control the activity of carbon at the surface through the gas ratio, change the temperature or

treatment time or apply diffusion masks. However, one issue that needs to be considered when using this technique is lateral diffusion as it will to reduce the sharpness of a given pattern. Another variable that is explored in this work is the use of different phase transformations in order to achieve specific mechanical properties. By altering the treatment conditions it is possible to achieve a range of microstructural phases. These phase transformations can also be utilized to adjust the interfaces in the structure and can be used to create both sharp and diffuse interfaces.

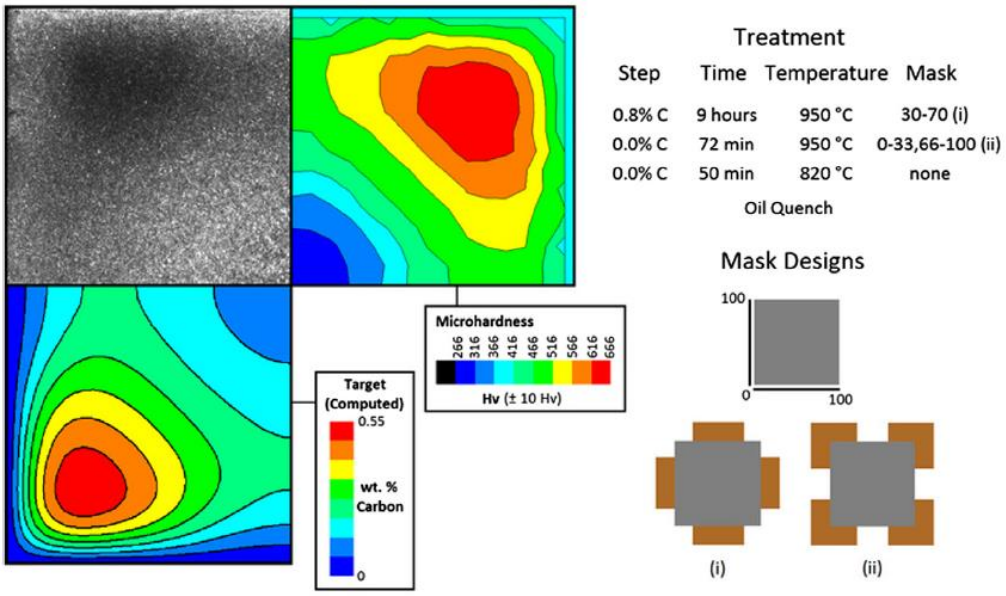


**Figure 2-6: Explanation and results of masking and carburization/decarburization experiment (Cicoria et al).**[17]

### *2.2.2.4 Biomimetics*

The above sections have demonstrated some examples of materials which employ this architectured materials design concept. This review was not exhaustive and there are other examples of architectured materials found in the engineering world. That being said, this idea of architectured materials design is in its infancy and the number of current engineering materials employing this design methodology are limited. The natural world, on the other hand, has been designing architectured materials for millions of years. One of the inspirations behind the

adoption of this architectured materials design concept is the methodology of material design found in nature. By observing the techniques employed in nature, which have been perfected over years of evolution, it is possible to obtain ideas for the improvement of materials design. This act of observing and understanding the structure and design of natural materials and using this information as a guide for material design is called biomimetics. One common theme found in the structure of natural materials is a hierarchical design, that is, nested levels of architecture on different scales. In the paper written by Srinivasan et al.[18] some examples of these hierarchical biological materials are discussed. One such biological structure that employs this hierarchical nature is the tendon. The tendon employs a triple helix structure of tropocollagen on a microscale, which forms microfibrils which are organized in a tetragonal lattice. These tetragonal lattices comprise the components of a larger fibrous structure. This hierarchical structure has evolved to produce an optimal structure for its function, producing a material with flexibility and high toughness. The utilization of the helical architecture is something that is commonly found in natural materials and is observed in the architecture of bone and wood in order to improve the toughness of these materials. It is clear that nature has opted to use curvilinear architectures, such as helices and corrugations, for their ability to improve ductility and toughness, which can be used as inspiration in the design of engineering materials.

It should also be noted, as highlighted in the work of by Dunlop and Brechet[19], that despite limitations with regards to available elements, mostly those of low atomic number, and low temperature processing, nature has been able to develop highly effective, adaptable and often multifunctional materials. The means with which nature accomplishes these feats is often through the use of hierarchical, architectured materials. Therefore, by employing biomimetics, engineers can seek inspiration from natural materials and with the added benefit of accessibility

to a larger range of elements and a larger temperature range for processing routes, should be capable of designing highly effective architectured materials to meet increasingly more demanding specifications.

## 2.3 Composite Materials

Before discussing the geometry of interest for this research topic, that is the corrugation, it is instructive to take a step back and provide a brief review of some of the key work performed on the mechanics of composites in general, as this provides some important context for viewing the present work. In particular the focus will be on metal matrix composites.

Composite materials are generally considered to be a combination of two or more materials, or a material and empty space, with the purpose of forming a new hybrid material possessing different properties than its constituent materials. Some common forms of composite materials can be seen illustrated in Figure 2-7, as taken from Ashby,[8] and include, fiber reinforced composites, particle reinforced composites, sandwich panels, foams, lattices and laminates. The properties of these composite materials are dependent on the properties of the constituents, their relative amounts and geometries, and how they are arranged in space.

One of the first studies that looked at metal matrix composites was performed by Kelly and Tyson[20] which utilized tungsten and molybdenum reinforcing wires in copper matrices, aligned with the tensile loading direction. The work done on these test systems led to the development of some of the fundamental theories of composite science. The effect of volume fraction on tensile strength was plotted, showing a highly linear relationship described by a rule of mixtures. This led to the proposal of the iso-strain model, or the slab model, which is used in composite science to estimate the stiffness and strength, along with a number of other properties, of long fibre

reinforced composites. For example, the iso-strain equation seen for composite stiffness, $E_c$, is as follows:

$$E_c = (1 - f)E_m + fE_f \quad (2\text{-}1)$$

where f is the volume fraction, $E_m$ is the matrix stiffness and $E_f$ is the reinforcement stiffness. This model is also applied for sandwich panel type composites. Kelly and Tyson also performed tensile tests of discontinuous fibres with different aspect ratios and demonstrated a reduction in strength and elongation that result from having smaller aspect ratios. Additionally, formulations for stress transfer through shear forces at the interface were examined. The models generated in this paper have been used as the basis for other composite systems.

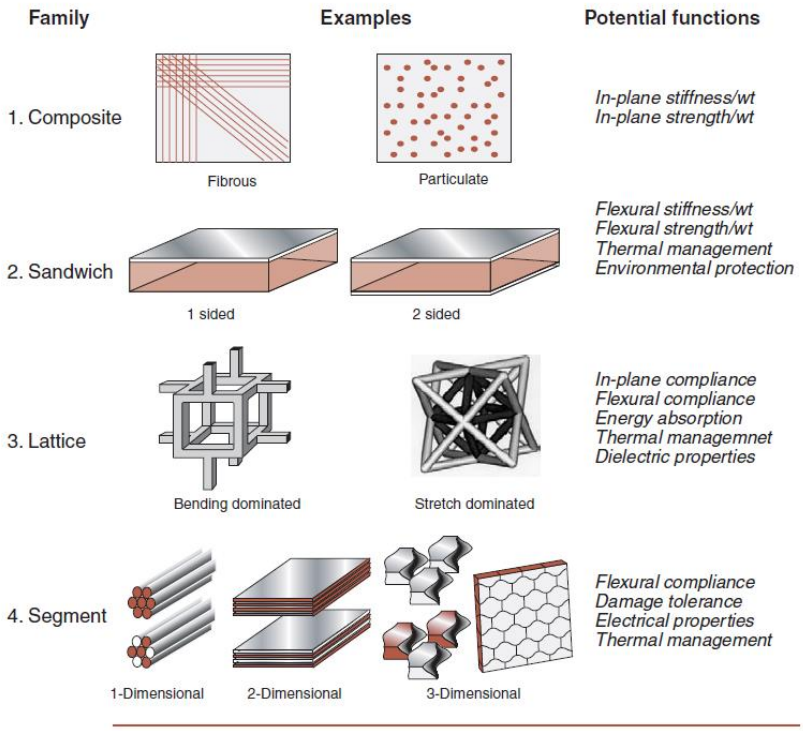


**Figure 2-7: Categories of composite materials and their desirable properties, as taken from Ashby.**[8]

Other work that has been done using the copper-tungsten system as a model includes that performed by Brown and Clarke[21] and Mortensen et al.[22] who both examined the work hardening

in fibre reinforced composites. Ozturk et al.[23]examined the behaviour of copper tungsten laminates in compression and Poole[24] looked at tungsten wire reinforced copper in plane strain compression, examining the strain distribution, texture evolution and damage formation and propagation during loading for different geometric configurations of the wires. In particular, Poole showed how the arrangement of the reinforcement phase can significantly affect and constrain the strain patterns in the matrix phase, and ultimately the stress-strain response of the material. All of these studies utilized the tungsten-copper system as a model system to examine the behaviour of a composite system with a certain configuration or geometry under specific loading conditions.

When considering a more complicated reinforcement than a continuous fibre or sandwich panel, it becomes more difficult to predict the mechanical properties of the composite. With that being said, much work has been done to develop methods for modeling this behaviour, especially for the elastic behaviour of short fibre and particulate reinforced composites. The two most common approaches for modeling the tensile loading of these systems are the shear lag approach and the Eshelby approach. The shear lag approach was first proposed by Cox[25] and is based on the idea of the stress being transferred from the matrix to the short fibers through interfacial shear stresses. This approach is capable of calculating the stresses present along the fiber and can be used to predict the stress-strain response of these composites. It has been used to show that there is a build-up in stress from the ends of the fibers towards a peak in the middle and that this peak stress increases with fiber length until such a length is reached that the stress plateaus at a value equivalent to that seen for a long fiber composite. The Eshelby approach, on the other hand, was first proposed by Eshelby,[26] and is based on the concept of using ellipsoid shaped reinforcements. This approach uses a thought experiment involving cutting the reinforcement

from the matrix, applying a shape change related to the applied stresses, applying forces to the cut out reinforcement to return it to its original shape and then placing it back into the hole in the matrix and allowing it to deform. This approach has been proven to be quite effective at estimating the stress-strain response of these composite materials. These tools have been used extensively for estimating composite stiffness and stress under elastic and plastic loading conditions. More commonly now, these composite systems are modeled using numerical techniques such as Finite Element Modeling (FEM), however, these older analytical models still prove quite effective for certain simpler systems and do not require major computational resources.

In addition to having knowledge concerning the elastic response and plastic deformation of these composite materials, it is also desirable to know at what point they will stop deforming uniformly and begin to neck. A pair of papers by Semiatin and Piehler[27,28] examine the deformation and formability of sandwich sheet materials under different loading conditions including uniaxial tension, plane strain compression and rolling. These papers examine the deformation of both steel clad aluminum sandwich sheets and aluminum clad steel sandwich sheets. The paper on uniaxial tension shows that although the stress-strain curve of the composite can be predicted accurately using a rule-of-mixtures technique, the necking strain cannot be calculated as a weighted average of the component's necking strains. This paper shows that for sandwich sheet materials, just like for continuous fibre reinforced composites, that the necking strain can be estimated using the maximum load condition and the rule-of-mixtures definition of the stress for the material. This leads to a force weighted average of the necking strains of the components in order to calculate the sandwich sheet necking strain, $\varepsilon_{neck,sand}$,

$$\varepsilon_{neck,sand} = \frac{F_m \varepsilon_{neck,m} + F_c \varepsilon_{neck,c}}{F_T} \quad (2\text{-}2)$$

where $F_m$ is the force on the middle layer, $F_c$ is the force on the cladding layers, $F_T$ is the total force, $\varepsilon_{neck,m}$ is the necking strain of the middle material on its own and $\varepsilon_{neck,c}$ is the necking strain of the cladding material on its own. The values of $F_m$ and $F_c$ are not known, but can be approximated by the values for each component at its ultimate tensile strength. The second paper that focuses on compression and rolling showed that the pressure required for plane strain compression could be calculated as a rule-of-mixtures model of the component plane strain flow stresses. It also showed that the plane strain compression will result in overall iso-strain behaviour in the longitudinal direction with positive longitudinal forces in the stronger material and negative longitudinal forces in the weaker material and a net zero force in this direction. Although no global instability can form in this longitudinal direction due to the net force being zero, it is possible for an instability to form as a result of a force maximum in the stronger component which is being subject to tensile loading. A simple model based on the maximum load condition was proposed for determining the strain at which this necking was occurred and was validated with the experimental results. For the steel clad aluminum, multiple periodic necks formed as a result of the instability condition being met but for aluminum clad steel, only a single neck formed. This periodic necking occurs due to the fact that the average thickness strain of the two components must be equal to ensure iso-strain conditions, and thus a neck in the top cladding is matched by no neck in the bottom cladding. This is not possible with the single steel core in the other system and thus a single neck forms and thins. In addition to the necking behaviour modeling, calculations and testing were also performed with regards to residual stresses in the components.

## 2.4 Corrugated Geometry

As mentioned earlier, the geometry of interest for this research topic is the corrugation. Conventional materials exhibit decreasing work hardening behaviour with increasing strain often as a result of dynamic recovery. However, in order to increase the necking strain it is advantageous to have a material with increasing work hardening behaviour. One way to achieve this is to implement a corrugated geometry. The unbending of the corrugation during loading facilitates an increase in work hardening and ultimately leads to an increase in necking strain. This can be considered a geometry which employs a waiting element as the unbending process delays the point at which the strength of the material is used. The following reviews some of the past research that has been performed with regards to the corrugated geometry. This overview is by no means complete and there are many more papers in this area, particularly on corrugated panels and sheets. Additionally, the focus of this review is mainly on tensile and compressive loading, and as such does not contain mention of a lot of the research pertaining to bending, vibration, fatigue and impact. This section starts with the work that has been performed on the behaviour of isolated corrugations. This will be followed by a review of some of the applications of the corrugation geometry. Next, will be an examination of the work related to composites containing this corrugated structure, followed by a look at some of the fabrication routes that have been proposed for creating these composites. Finally, this section will conclude with some research on the related helical geometry

### 2.4.1 Isolated Corrugations

When an isolated corrugated structure is used without being embedded in a matrix material it is possible to improve the failure strain when compared to the straight case. This isolated corrugated geometry has been studied by Dayyani et al.[29] for trapezoidal corrugations made of

fibreglass sandwich structures, by Thill et al.[30] for aramid/epoxy laminate trapezoidal corrugations and by Bouaziz[31], experimental, and Boke[32], FEM, for sinusoidal corrugations of interstitial free (IF) steel, all for tensile loading. Dayyani et al.[29] also investigated behaviour of the corrugated strip subjected to three point bending. All of the tensile studies demonstrate similar stress strain behaviour as a result of the unbending process of the corrugation. The characteristic shape of the stress strain curve can be seen in Figure 2-8, as taken from the work of Dayyani et al.[29], which shows the results from both FEM simulations and experiments. In this work, the curve is dissected into three phases. The first phase is linear and characterized by small deformations in the horizontal and inclined members. The second phase is an unbending phase characterized by rotation of the members around the joints. The third phase begins when the structure is flattened and behaves like a straight strip. The unbending phase demonstrates increasing work hardening behaviour which is caused by the straightening action and ultimately leads to a delay in the failure of the part when compared to the straight case. Thill et al.[30] refers to the unbending process as a pseudo-plastic hinge effect and likens the response to that observed for cellular solids in the bending and collapse of their struts.

The term geometrically induced strain hardening materials is introduced by Bouaziz[31]. This concept is initially illustrated in this paper by creating isolated corrugated strips of IF steel and pulling them in tension, the results of which are pictured in Figure 2-9, showing this increasing work hardening behaviour. This figure also demonstrates that the necking strain increases as the number of corrugations, or more accurately, the percentage corrugated, is increased. Additionally, a simple geometric model is presented to estimate the critical or unbending strain, which is the point at which the corrugation is unbent and the behaviour of a flat material takes over.

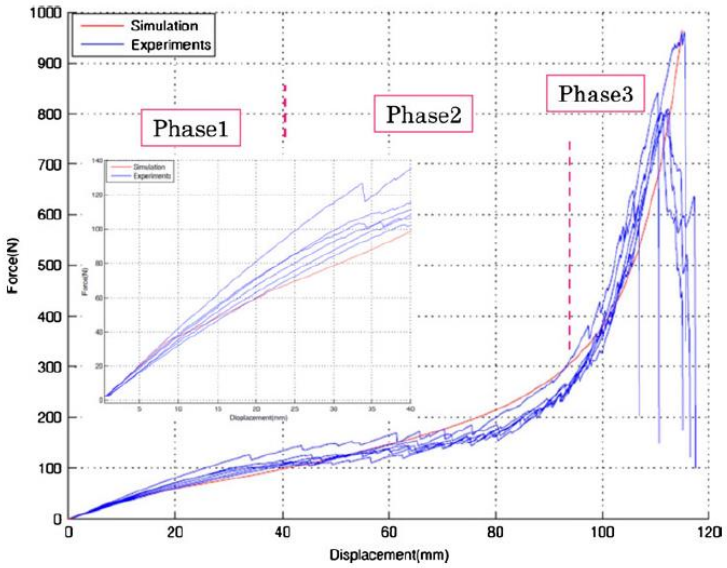


**Figure 2-8: Comparison of FEM and experimental tensile tests on trapezoidal corrugated fibreglass (Dayyani et al).**[29]

It is not enough to just know that a corrugated geometry will create improvements in necking strain, but it is also necessary to know how the shape and scale of the corrugation will affect the stress-strain behaviour. FEM simulations were performed by Boke[32] on an isolated corrugated strip of a material possessing power law work hardening attributes and was used to examine the effect of the different geometric parameters, including, period, height and radius of curvature on the stress strain behaviour, an example of which is shown in Figure 2-10 for the case of variable period. In general, it was found that decreasing the period and increasing the height led to an increase in the necking strain of the material and changing the radius of curvature of the corrugation had minimal effect. Additionally, different corrugation shapes were examined including arced, triangular and a mix of the two, with the conclusion that the shape of the corrugation affected the shape of the stress strain curve but had minimal effect on the failure stress or strain. An optimization of the number of corrugations in a given total length was also undertaken, with the conclusion that 14 corrugations was the optimal number for a length of 16mm and a height to period ratio of 0.375.

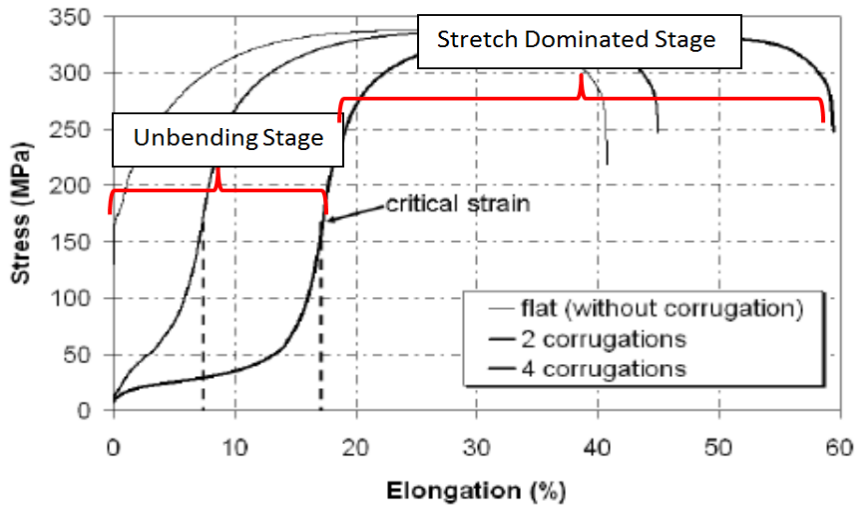


**Figure 2-9: Experimental tensile stress-strain curves of corrugated IF steel, taken from Bouaziz.**[31]

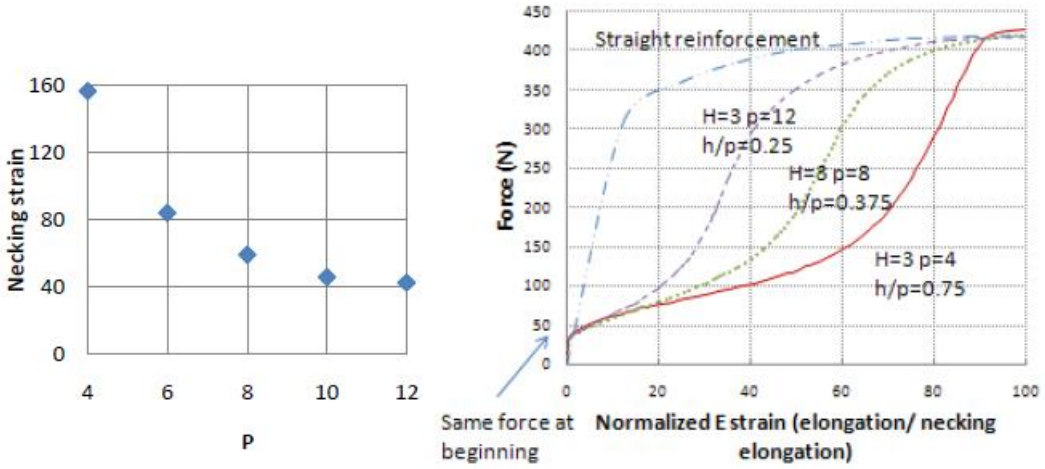


**Figure 2-10: Effect of period, P, of corrugation on necking and work hardening behaviour of corrugated strips simulated using FEM (Boke).**[32]

In order to predict the behaviour of these corrugated materials several attempts have been made to model the behaviour. Dayyani et al.[29] developed an analytical model to describe the behaviour of a trapezoidal corrugated strip in tension. The strain of the sample is calculated through a derivation of the elastic strain energy in each of the members, which is divided into a tensile and a bending component. Castigliano`s theorem is then applied to get the strain. A similar approach is utilized by Thill et al.[30] also using strain energy principles and Castigliano's theorem. Both of

these attempts at modeling the behaviour were compared to FEM and experimental results and showed reasonable success with regards to predicting effective elastic properties. It should be mentioned at this point that these models have only approached this process from an elastic viewpoint and do not consider any plastic behaviour. Additionally, they are limited to the trapezoidal corrugation shape.

### 2.4.2 Applications of Isolated Corrugated Geometry

The corrugated architecture has been used in a number of different industries due to its ability to provide high stiffness in the transverse direction and high energy absorption and flexibility in the longitudinal direction. As summarized in the review by Dayyani et al.[33], the high transverse stiffness to weight ratio makes it an ideal candidate in the construction industry in the form of corrugated roofing, corrugated walls and corrugated piping and in the aerospace industry to be used for wings. The high energy absorption, coupled with the transverse stiffness has led to application in packaging, with corrugated board becoming a standard packaging material. A couple of these applications will now be discussed in more detail.

One modern application of this corrugated geometry that has recently received attention is for the skin of morphing wings in airplanes. This idea of using the corrugated architecture for the skin of morphing wings was explored by Ge et al.[34] due to the potential for increased elongation in the corrugation/loading direction and the high stiffness in the transverse direction. The research included both FEM and experiments on isolated corrugated samples, looking at a composite material of E-glass reinforced resin. It was found that the elongation was larger for thinner samples, that the peaks and troughs of the corrugation experienced the highest local stresses, that the larger the number of corrugations, the higher the elongation and that the number of corrugations had no effect on the failure stress. However, the stress strain curves obtained from

these simulations and experiments showed linear behaviour and did not demonstrate the increasing work hardening behaviour characteristic of corrugated geometries as discussed above for the other studies. Another paper by Park et al.[35], develops an analytical model for calculating the stiffness of corrugated panels for morphing wings in different directions and for different corrugation geometries. They found general trends of decreasing longitudinal stiffness and increasing lateral and shear stiffness with increased corrugation.

Another common application of the corrugated geometry is in corrugated board. In this case a corrugated strip is bounded by flat plates on top and bottom which are attached to the corrugation at peaks and troughs as shown in Figure 2-11. The materials are often used in packaging due to their high specific stiffnesses and strengths.

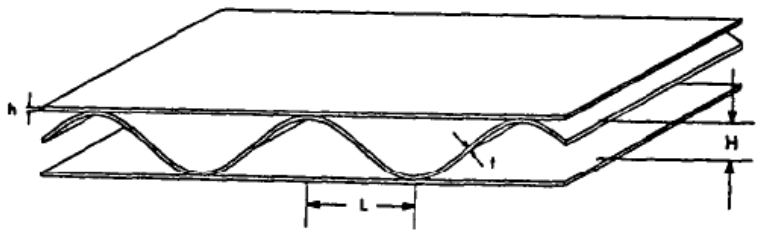


**Figure 2-11: Schematic of corrugated board taken from Luo et al.**[36]

Analytical analysis on the bending stiffness of corrugated board has been performed by Luo et al.[36] using the equivalent plate method whereby a simple plate is assumed with the same properties as that of the sandwich structure. In order to calculate the elastic constants to determine the bending stiffness, the area moment of inertia of the corrugated core was calculated for a number of different corrugated geometries including sinusoidal, semi-elliptical and arc and tangent. The high moment of inertia coupled with a minimal increase in weight due to the corrugation leads to high stiffness properties. Other work on the mechanical behaviour of corrugated board includes that done by Gilchrist et al.[37] who conducted non-linear FEM to

simulate the behaviour of corrugated paper board under four point bending, edge crush test and anticlastic bending for twisting stiffness. These simulations were then compared to experiments for validation purposes.

The corrugated geometry can also be used in the walls of boxes. The work done by Zangani et al.[38] explores the use of foam-filled corrugated sandwich walls in hollow tubes. It is shown through FEM and experimental testing that the corrugated core results in progressive failure and high energy absorption when subject to compressive loads. In addition to the traditional loading directions, corrugations have been studied for use in compression in the in-plane direction. The paper written by Hanagud et al.[39] examines the behaviour of sine wave webs in compression in the direction perpendicular to both the amplitude and the wavelength as illustrated in Figure 2-12. The wavelength and offset of the sine waves appear to have minimal influence in these loading conditions, suggesting that the corrugation will have neither negative nor positive effects on compressive properties in the in-plane direction.

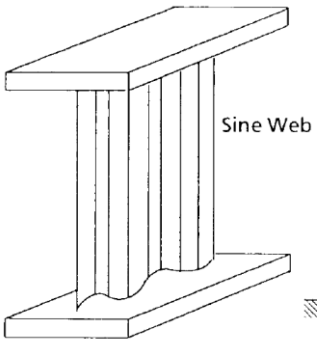


**Figure 2-12: Schematic of sine wave web for use in compression, taken from Hanagud et al.**[39]

### 2.4.3 Composites with Corrugated Reinforcement

All of this previous work has been limited to isolated or bounded corrugation architectures. However, ultimately, it is the behaviour of a composite reinforced with a corrugated geometry

that is of interest in this thesis. Initial research on this topic was conducted to investigate the effect of unintentional ply or fibre waviness in composites. The investigation performed by Bogetti et al.[40] was motivated by the claim that the defect of ply waviness observed in thick section composites can result in significant decreases in stiffness and strength. An analytical model was created for a 90/0/90 composite with a wavy 0 layer using laminate theory with an alteration to take into consideration the sinusoidal geometry of the middle ply in order to determine the stiffness of the composite. It was found that increasing ply waviness results in a decrease of stiffness in the longitudinal direction. (Note: this is as expected and says nothing about the stress strain behaviour only that initial stiffness is reduced). It should be noted that this study placed emphasis on behaviour of these composites under longitudinal compression. A reduction in compressive strength with ply waviness was demonstrated with a parametric analysis and attributed to interlaminar shear failure. This is an important finding as it suggests a sacrifice in strength in order to improve the uniform elongation of the composite. Additionally, it was found that ply waviness had very little effect on transverse mechanical properties. A similar model describing the sinusoidal variation in stiffness properties resulting from the wavy nature of the fibres using elasticity equations was derived by McIntyre et al.[41] but was applied to determine its effect on resonance in the material.

Experimental testing has also been conducted on sandwich structures with a corrugated core structure. This was done by Williams et al.[42] who compared a flat core geometry to a corrugated core geometry. It should be noted that the corrugated sandwich structure possessed not only a corrugated core but corrugated outer layers as well. It was shown that the corrugated composite would have a higher strength, bending stiffness and local buckling resistance when compared to the flat composite due to a larger area moment of inertia and lower average shear stresses due to

a larger interfacial area. This idea of an improved strength through corrugation has not been replicated elsewhere; in fact usually there is a loss of strength reported when a corrugation is used.

Other modeling attempts have been pursued for corrugated reinforcement geometries for systems with elastic matrices, Chiskis and Parnes[43] and Chou and Takahashi[44], and have demonstrated the benefits in terms of increased ductility as a result of the increasing work hardening behaviour of the reinforcement. This can be seen in Figure 2-13 for the Kevlar/PBT composite modeled by Chou and Takahashi[44]. In Chou and Takahashi[44] it is suggested that an elastomeric matrix material would serve as an effective component for this specific architecture. The elastomer can support large deformations upon loading. However, these large deformations cannot be realized when it is combined with a straight fibre composite due to the minimal ductility of the fibres. But, if the fibres undergo an unbending process while the matrix deforms then both high ductility and improved strength can be achieved. Additionally, the unbending process results in low composite stiffness at low values of strain and increasing stiffness at higher values of strain, which can be a desirable attribute. This idea of a matrix material which can undergo the deformation necessary to accommodate the reinforcement unbending is an important consideration when selecting potential material systems for these architectured materials.

In addition to knowledge of the global stress strain behaviour, it can be advantageous to understand the local stresses within a material during loading. In the work done by Abdelrahman and Nayfeh[45], an analytical model of the elastic behaviour of a corrugated fiber embedded in a cylindrical matrix is created, with an image of the unit cell shown in Figure 2-14. This model is able to predict the stress distribution within the fiber and the interfacial shear stress of the fiber during loading. It was found that the effect of the corrugation on local stresses was largest at the

areas for which the angle of the corrugation deviated the most from the horizontal alignment and was most similar to the straight case for the areas in which the angle was zero. This micromechanical model was developed by applying interfacial and boundary conditions to field equations describing the stresses in a system with a straight fibre reinforcement and applying a change of reference system based on the changing angle of the corrugation. Although, this model provides valuable information on the stress state of the fibers it does not predict the global stress strain behaviour and is limited to the elastic regime.

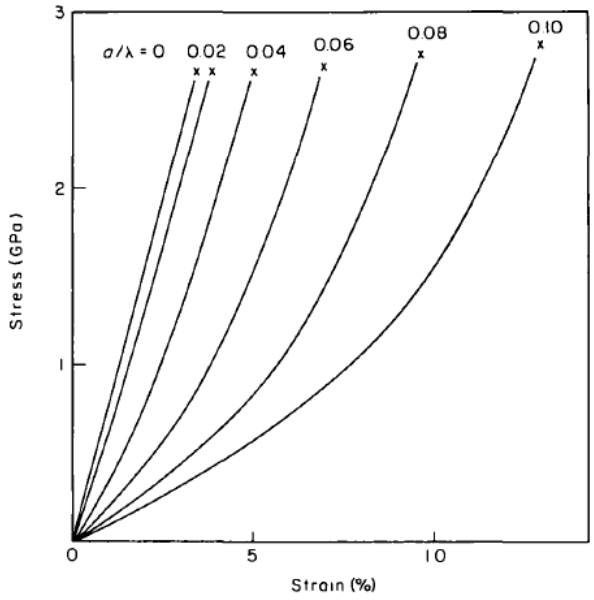


**Figure 2-13: Model predicted stress-strain curves for a composite with corrugated Kevlar wires in an elastomeric PBT matrix with different height/wavelength (a/λ) ratios (Chou and Takahashi).**[44]

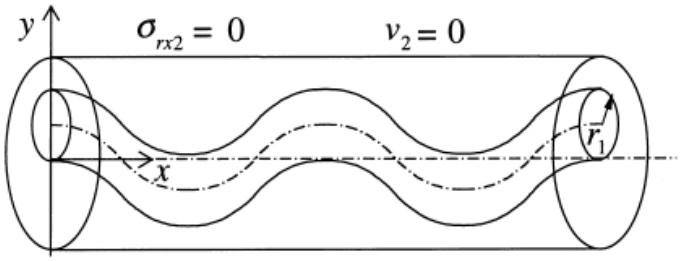


**Figure 2-14: Illustration of unit cell of corrugated fiber used in a micromechanical model by Abdelrahman and Nayfeh.**[45]

Taking inspiration from the brick and mortar structure of the natural material nacre, Katz et al. [46] modeled the effect of waviness of the discontinuous reinforcing phase on ductility and strength using finite volume direct averaged micromechanics (FVDAM) simulations. An example of the structure they modeled can be seen in Figure 2-15 below, with a linear hardening aluminum matrix and elastic silicon carbide plates. They performed simulations of horizontal tension and vertical compression and found that increasing the height/period ratio of the wave decreased the stiffness of the sample, reduced the stress carried by the composite and increased the ductility. They attributed these trends to localized bending in the peaks and troughs, and high shear stresses in the regions between peaks and troughs. They also found that a small offsetting of the bricks through shifting of the layers resulted in more compliance and lower stresses in the structure, the effect of which reduced with further offsetting. This offsetting effect was more pronounced for the straight structure and became less significant as the waviness was increased. The reason for this offset effect is due to the fact that with no offset, the regions between the ends of adjacent plates in the same row have high hydrostatic stresses due to the constraint of surrounding plates and thus carry high stresses and efficiently transfer stress horizontally between plates. When the offset occurs, this hydrostatic stress is reduced and the load transfer becomes less effective, lowering the stress in the plates, requiring larger deformation in the matrix regions between plates and causing higher amounts of shear stress in the matrix which reduces the transfer of stress to the plates.

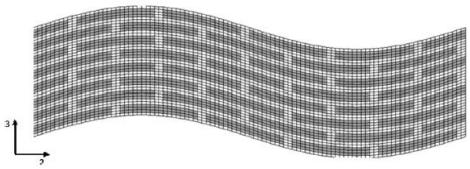

**Figure 2-15: Nacre-like wavy brick and mortar composite structure with offset bricks (Katz et al).**[46]

In a series of papers, Khatam and Pindera, inspired by wavy reinforcing structures found in nature, performed a number of simulations using FVDAM to model the behaviour of wavy multilayers consisting of alternating soft and stiff elastically deforming layers. One of the papers[47] looks at the elastic moduli, thermal expansion coefficients and internal stress fields of these composites, for both a corrugated matrix shape and rectangular matrix shape, subjected to tensile loading. In both matrix geometries the moduli and stress fields are found to be similar, with the stress being localized in the peaks and troughs of the stiff reinforcing phase, as seen in Figure 2-16 for the corrugated matrix shape. In addition, when the ratio of height/period was increased the stress levels were magnified in these regions, and the elastic modulus of the composite reduced.

Another of the papers[48], performs similar simulations, but includes plasticity in the matrix in the form of an elastic perfectly plastic material. In this case when the wavy multilayer is loaded in tension, the stress carried by the composite is less than if a straight multilayer geometry was used, especially once the matrix layers have yielded, as shown in Figure 2-17 with curves representing different volume fractions. Note that the simulations only go to a total strain of 1%.

Another of their studies[49] looks at the effect of the thickness of the stiff layers while maintaining volume fraction, on the stress-strain response, again performing FVDAM simulations with elastic perfectly plastic soft phases. In this study it was found that as the thickness was decreased the reduction in stress during plastic deformation was increased. Additionally, the larger the volume fraction of the stiff layer, the more pronounced this effect. Also, when the ratio of height/period is increased, the modulus and stresses during plastic response decrease, but so does the sensitivity of the composite to the layer thickness. Some additional simulations were also performed under shear loading as well, which tended to show opposite effects to tensile loading.

The effect of the layer thickness on the stress carried by this material is attributed to the resultant differences in stress distribution in the soft phase causing differences in local strains in the soft phase and thus differences in stress transfer across the interface.

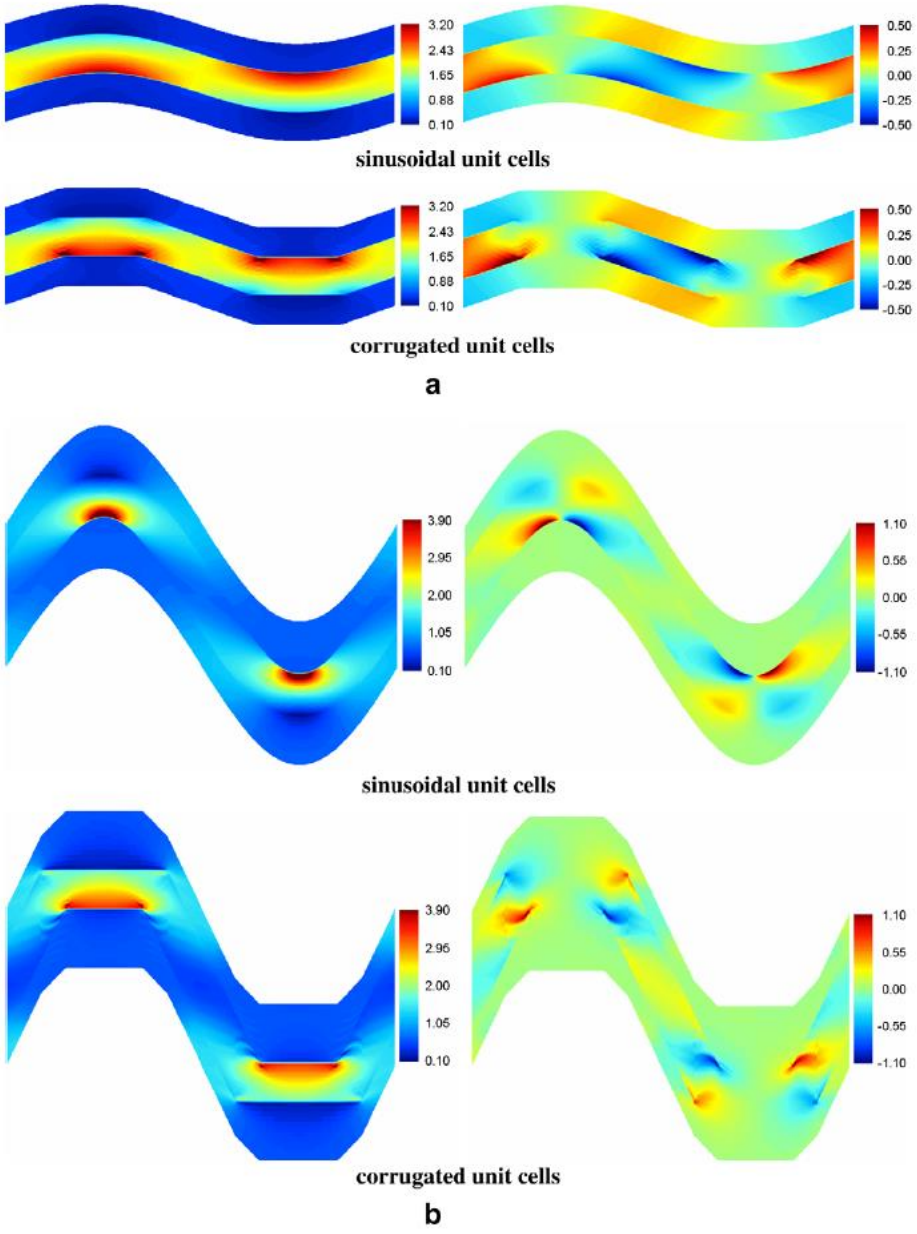


**Figure 2-16: FVDAM stress maps taken from Khatam and Pindera[47] of wavy multilayers with stiff reinforcement and soft matrix. Horizontal stress maps (left) and shear stress maps (right) for A) small height/period ratio of 0.05 and B) larger height/period ratio of 0.25.**

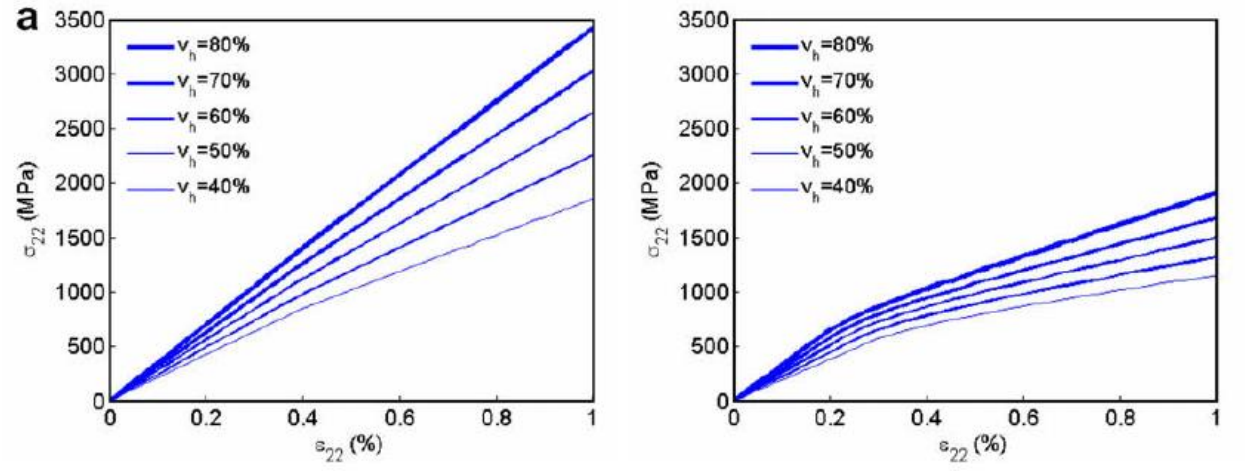


**Figure 2-17: Longitudinal stress as a function of strain for different volume fractions of hard phase from FVDAM simulations (Khatam and Pindera)[48]. Stress is for straight multilayers (left) and wavy multilayers (right).**

Cavalcante et al.[50] also used FVDAM and FEM to examine the effect on overall hardening of changing the thickness of the hard layer while maintaining the volume fraction. They performed these simulations for elastic corrugated reinforcements and linear hardening matrix materials. Similar to Khatam and Pindera, in this study both the reinforcement and the matrix have a corrugated structure. They found that increasing the number of reinforcements and hence reducing the thickness, led to a reduction in overall hardening due to plastic strain localization at the interface between the peaks, and thus less stress transfer to the reinforcement. This effect is reduced as the linear hardening of the matrix is increased. This study did not look at changes in the corrugation geometry or proceed past a strain of 1%.

A final study by Khatam and Pindera,[51] looks at the effect of the height/period ratio, the relative stiffness of the components, the volume fraction, and the layer thickness of these wavy multilayered materials on the stress-strain response and local stress patterns. Using FVDAM for elastic materials it was found that the rate of unbending was higher when the stiffness of the soft material was lower, the volume fraction of the hard material was higher or when the thickness of

the hard layers was smaller. When the height/period ratio is larger the amount of unbending that occurs is greater and takes longer and the initial reduction in strength is larger and subsequent hardening more drastic. This paper also aimed to simulate the unbending response seen in chordae tendineae, which is biological tissue found in heart valves of mammals that has a wavy architecture. This tissue shows significant strengthening due to an unbending of its wavy structure. They were able to get a relatively good match with experimental data by adjusting the matrix stiffness, height/period ratio and the thickness of the hard layers, as seen in Figure 2-18. These curves are able to capture the characteristic increasing strength behaviour that is indicative of an unbending corrugation. All of these studies by Khatam and Pindera and Cavalcante et al. on wavy multilayers provide some valuable insight into the contributions of geometry, volume fraction and materials. That being said, these studies focused on mostly elastic or elastic perfectly plastic materials and looked at the initial softening effects of a corrugated structure and did not look at the behaviour as unbending progressed further to the point of necking.

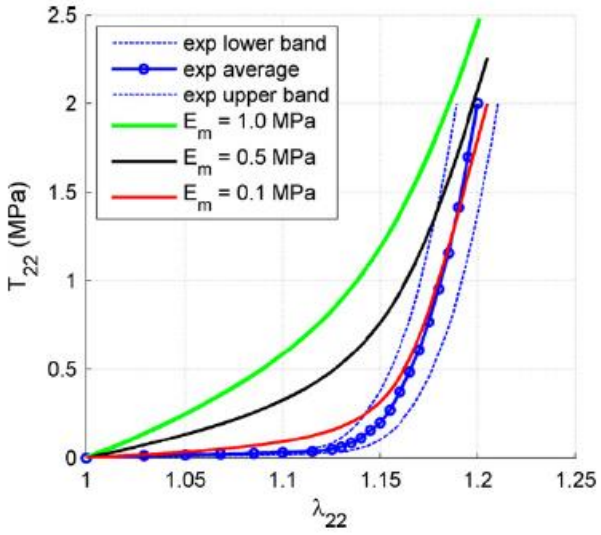


**Figure 2-18: Stress-strain curves for wavy multilayers under tensile loading generated by FVDAM simulations for various matrix stiffness and compared to experimental curves for chordae tendineae, (Khatam and Pindera).**[51]

All of this previous work has mostly been limited to elastic, polymeric matrix materials. However, if this concept is expanded to metallic composites, work hardening behaviour will become important. Shifting to systems with a non-corrugated surrounding matrix geometry and plastic material behaviour, it was shown in Bouaziz[31] using FEM that for an elastic perfectly plastic matrix material, increasing work hardening behaviour as a result of unbending is still present, only to a lesser degree to what it was for the isolated corrugations. A case that is more common for many metal systems is the case characterized by power-law work hardening behaviour. This was explored by Boke[32] for a composite consisting of two theoretical steels for the matrix and reinforcement, both with power law behaviour. Boke also observed the improvements with regards to necking strain with minimal sacrifice in strength. Bouaziz[31] and Boke[32] both also investigated the effect of the geometric parameters defining the corrugation on the stress-strain and work hardening behaviour. The effect of the degree of corrugation or the height to period ratio can be seen in Figure 2-19 as taken from Bouaziz[31] which shows the results for both the stress-strain curves and the work hardening. As is clear, increasing the degree of corrugation leads to a prolonged stage of increased work hardening and ultimately will lead to a higher necking strain. Boke[32] observed similar effects of the degree of corrugation. Similar to the case for the isolated corrugation, Boke[32] attempted to find the optimal geometry for the composite case and concluded that the optimal number of corrugations in the composite differed from that found for the independent corrugation. This suggests that the constraint of the matrix material in these composites plays an important role that should be investigated further.

In a paper written by Shi et al.[52], FEM simulations are used to study the effect of strain-rate sensitivity and geometry on the stress-strain response of corrugation reinforced composites with elastic viscoplastic reinforcements under plane strain tension. Similar to Boke, Shi et al. used

ABAQUS software and first-order, quadrilateral, plane strain, CPE4 elements in their FEM simulations of these corrugated composites. One of the interesting findings was that there is an improvement in necking strain (both diffuse and local) for corrugated composites with intermediate periods compared to straight reinforced composites, but if the degree of corrugation is increased too much and the period is too small, the corrugated composite has a lower necking strain than the straight composite. Additionally, as the strain rate sensitivity is increased the local necking strain increases for all geometries, and the improvement achievable through corrugation is diminished. Also, when the strain rate sensitivity is high, as the degree of corrugation increases, there is an initial drop in local necking strain, followed by an increase to a maximum value, higher than that for the straight geometry. Subsequent increases in the degree of corrugation reduce the necking strain, due to incomplete unbending occurring. These trends suggest that there is significant interplay between the materials and the geometry and that further study of this relationship would be beneficial.

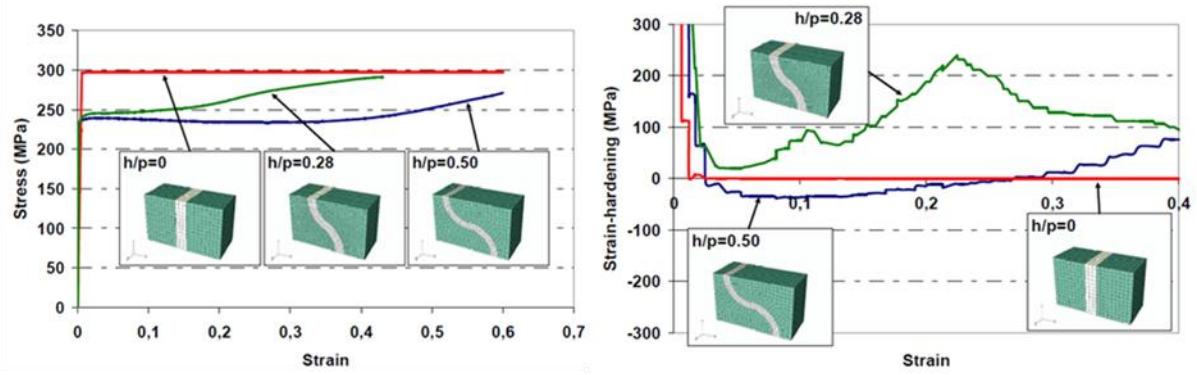


**Figure 2-19: Stress-strain (left) and work hardening (right) curves from FEM simulation of corrugation reinforced composites with different height to period ratios, h/p (Bouaziz).**[31]

Another interesting variation of the corrugated reinforcement was proposed by Boke[32] which involves extending the corrugated pattern in a second direction to create a three dimensional reinforcement structure as pictured in Figure 2-20. Some work using a similar geometry for a

sandwich panel core created by sheet stamping has been investigated by Besse and Mohr[53] in which they modeled and experimentally tested the shear stiffness of the sandwich panel. They found that the highest shear stiffness is accomplished when the cups have a large height to width ratio, but that the shear stiffness is outperformed by hexagonal honeycombs of similar density. Additional FEM simulations were conducted[54] that looked at uniaxial out of plane compression, and in plane uniaxial and biaxial tension. These simulations showed behaviour closer to that of the plate material than that of a cellular sandwich structure. Other groups, Seong et al.[55] and Hu et al.[56], have also expanded the corrugated geometry into the third dimension, creating sandwich panels with bi-directional corrugated cores. Seong et al. fabricated and tested a sandwich panel with the bi-directional core, with a goal of achieving more isotropic behaviour with regards to the bending response of these materials. Hu et al. on the other hand employed a bidirectional design with offsetting orthogonal peaks and troughs, as seen in Figure 2-21, and tested carbon-fiber reinforced composite (CFRC) sandwich structures in compression to observe their failure behaviour and found improvements in compressive strength compared to other lattice truss composites. These multi-directional corrugated architectures show an area for potential development in the future, particularly once a better understanding of the single directional corrugation is obtained.

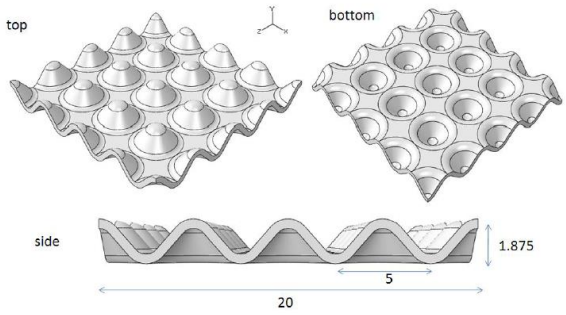


**Figure 2-20: Illustration of two-dimensional corrugation geometry explored by Boke.**[32]

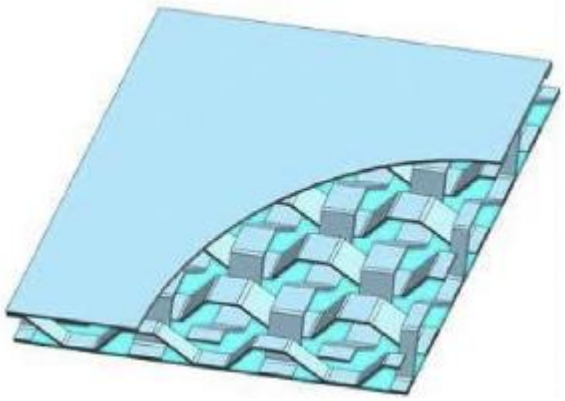

**Figure 2-21: Bi-directional offsetting orthogonal corrugation design proposed by Hu et al.**[56]

### 2.4.4 Fabrication of Corrugation Reinforced Composites

As mentioned earlier one of the greatest obstacles to the advancement and implementation of these architectured materials is the ability to develop feasible fabrication techniques. One potential technique for the fabrication of corrugated cores for these composites is rapid prototyping. Williams et al.[42] explored the use of three different rapid prototyping techniques for core fabrication in carbon-epoxy composites; stereolithography, fused deposition modeling, and three dimensional printing. It was found that due to superior strength of the cores and adhesion to the outer carbon-epoxy skins that stereolithography was the best option of these three rapid prototyping techniques for this application. With regards to metallic systems Bouaziz[31] has introduced two potential fabrication routes, one a simple casting method used for copper reinforced tin, and the other a selective laser hardening of a dual phase steel. In the second method, a laser is rastered across a dual phase steel sample in a sinusoidal pattern, subjecting the corrugated area to a heat treatment in the austenitic region, which upon rapid cooling results in a martensitic corrugation in a dual phase matrix with a graded transition between the components.

Despite the promise of these techniques for fabricating these corrugation reinforced composites, additional techniques will need to be considered as restricting oneself to a limited number of

fabrication techniques will severely limit the potential material systems that can be tested with this architecture.

### 2.4.5 Helical Geometry

Although this thesis focuses on the behaviour of corrugation based materials, it is of interest to note the work that has been done for helical based systems due to the fact that they exhibit similar geometrically induced work hardening behaviour. This final section of the literature review investigates the work performed pertaining to the helical architecture. This section is divided into three subsections which will explore the isolated helical structure, the helixes role in natural materials and finally helically reinforced materials.

#### *2.4.5.1 Isolated Helix*

Similar to the corrugated case, it is useful to first consider the behaviour of an isolated helical material. When a helical material is subjected to a tensile load, a shifting of the stress strain curves to higher failure strains with decreasing helical angle, i.e. increasing degree of helicality, is observed as a result of the unbending process. This is seen in the stress-strain curves generated from the tensile tests conducted on isolated helical tungsten wires by Kagawa et al.[57], seen in Figure 2-22. In a later study by Kagawa et al.[58], analogous to the corrugated case, the three stages of deformation, elastic, unbending and plastic, were identified for the independent helical wires subject to tensile loading. It is clear that both the corrugation and the helix behave in a similar manner and demonstrate geometrically induced, increasing work hardening behaviour.

#### *2.4.5.2 Helix in Nature*

The helix can be found in numerous applications spanning both the natural and engineering world. The helical geometry is commonly found in nature due to its ability to impart flexibility

and ductility into a structure. For example, as discussed in Baley[59], one of the hierarchical layers present in flax fibres takes the form of helically wound cellulose fibres in a matrix of hemicellulose and lignin, as seen in Figure 2-23. Another incidence of the helix in nature is found in wood as examined in Reiterer et al.[60], which on one level of its hierarchy consists of partially crystalline helically oriented cellulose fibrils in an amorphous matrix of hemicellulose and lignin. In both of these materials the angle of the helix ultimately affects the mechanical behaviour of the material. In the case of flax fibres, Baley[59] uses a simplified model to capture the increase in tensile stiffness during loading assuming a linear change in helical angle towards

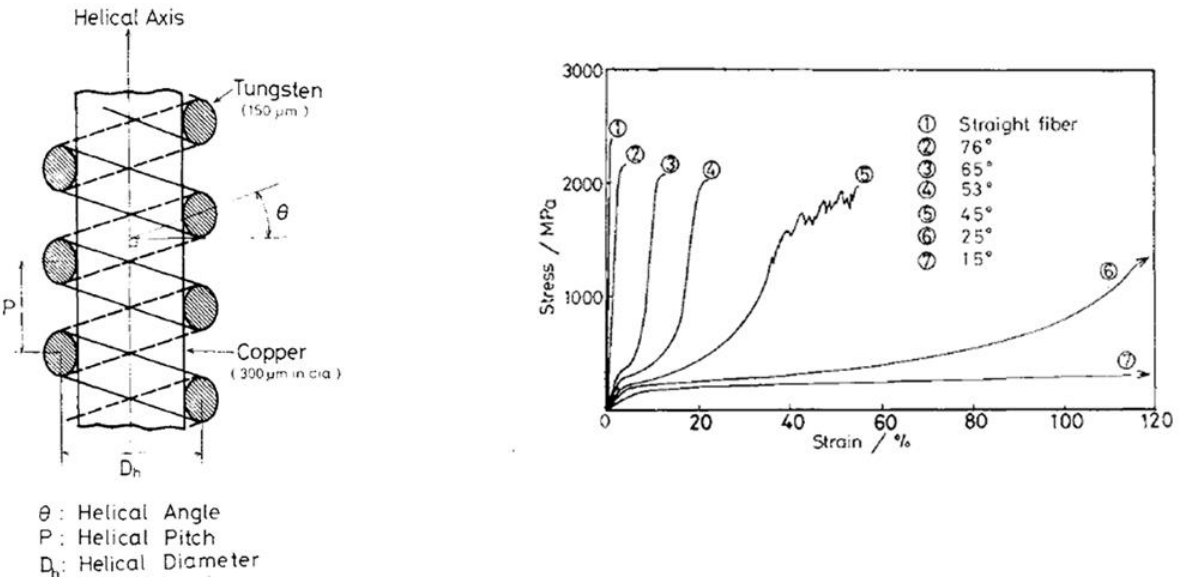


**Figure 2-22: Experimental stress-strain curves of helical tungsten wires with varying pitch angles (Kagawa et al).**[57]

a straight fibre with strain. The tensile elasticity is calculated using the Halpin-Tsai semi-empirical model involving micromechanical equations of elastic properties and involves the use of a change of coordinate axes based on the helix angle. In the case of wood, Reiterer et al.[60] found through tensile tests of wood samples that the elastic modulus decreases with increasing helical angle in a non-linear manner, that is, as the helical shape travels further from a straight

case. Small angle X-ray scattering was employed in order to determine the helical angle of the cellulose fibrils. Conversely it was found that extensibility increased non-linearly with increasing helical angle. However, upon looking at the stress strain curves it appears that the increase in extensibility comes at the cost of a decrease in ultimate tensile strength.

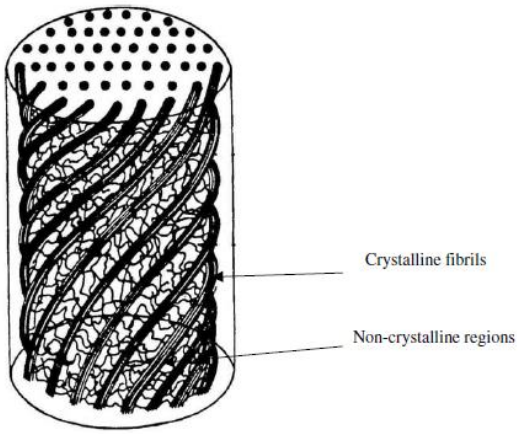


**Figure 2-23: Illustration of helical arrangement of cellulose fibrils in flax fibers (Baley).**[59]

### *2.4.5.3 Helically Reinforced Composite Materials*

Moving into the realm of engineering materials, attempts have been conducted at trying to model the behaviour of helically reinforced materials. Similar, to ply waviness, it is not uncommon for wire reinforcements to stray from their straight geometry and exhibit helical architectures. For this reason Ghahfarokhi et al.[61] focused on the effect of helical angle in fibre composites of polymeric matrices reinforced with carbon nanotubes. Using expressions based on Hooke's law to determine material constants for straight reinforced and helical reinforced composites, it was calculated that the increase of the helical angle will have a significant deleterious effect on the axial modulus of elasticity of the composite reducing the effectiveness of the carbon nanotube at reinforcing the matrix. This was supported by FEM simulations which also show that stress is not uniformly distributed throughout the nanotube in the helical case unlike the straight case.

However, this study did not examine any effects of the helix on the work hardening or failure strains of the material.

Similar to the corrugation reinforced composites, the presence of non-linear hardening was observed in the modeling of helically reinforced composites performed by Slepyan et al.[62] In this work it was found that by increasing the pitch angle the elastic modulus of the composite is decreased and there is an increase in the non-linear hardening. This was observed as a product of modeling efforts capturing the global stiffness of a material with a helical inclusion and modeling of the interaction between the helix and the matrix. Other benefits of curvilinear reinforcements discussed in this work, include their potential for increased extension and flexibility when compared to straight reinforcements.

The helical reinforcement is not limited to internal reinforcement cases and has also been used as an externally wrapped reinforcement. The use of external helical reinforcements in tubular structures provides flexibility in bending but can be very stiff in tension and torsion as investigated by Huang and You[63]. As described in the aforementioned paper, the geometric nonlinearity in tension for these structures, characterized by increasing work hardening behaviour, is caused by the evolution of the helical pitch angle with strain. These conclusions were drawn as a consequence of modeling the effect of the helical angle on the stress-strain behaviour. This was accomplished by isolating the helical reinforcement and the core pipe and individually modeling their stress strain responses. This analysis also included determining geometric conditions for which the radius of the helix contracts more quickly than the radius of the pipe and hence the helix contacts the pipe providing additional stiffening.

Once again, similar to the corrugated case, most of the work has been limited to elastic polymeric materials. However, some experimental work has been performed on metal matrix helically reinforced composites. The paper written by Kagawa et al.[57] and the related succeeding paper, Kagawa et al.[58], investigate the tensile behaviour of tungsten helix reinforced copper composites. With regards to internal helical reinforcements it was found in the second study, that for the same volume fraction of reinforcement, the composites with helical reinforcement offered significant improvement in terms of ultimate strains and only a minor decrease in ultimate stress compared to a straight wire reinforced composite, as illustrated in Figure 2-24.

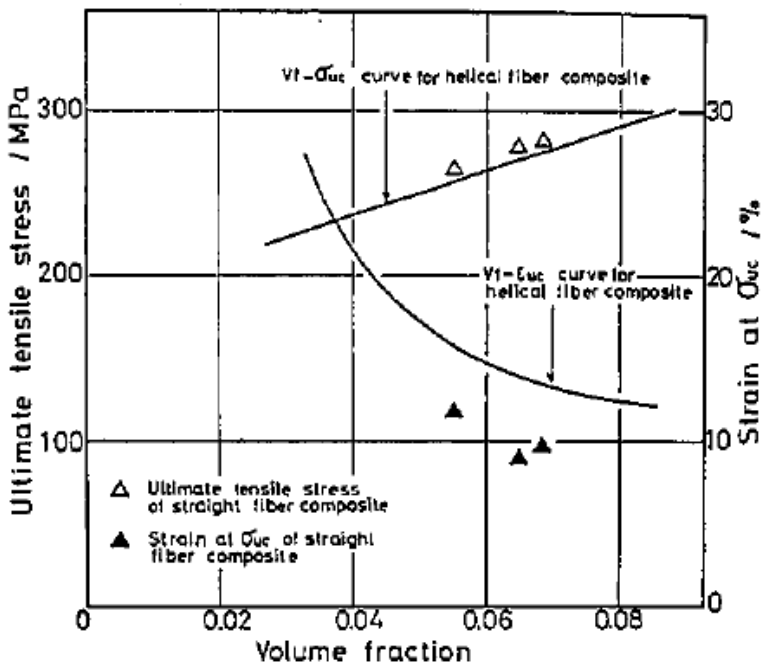


**Figure 2-24: Comparison of ultimate tensile stresses and strains for helical and straight reinforced composites with copper matrix and tungsten reinforcements (Kagawa et al).**[58]

It was also observed that the helical reinforced composites exhibited a larger degree of fibre pull out and demonstrated multiple necking and thus requires a larger work of fracture compared to the straight reinforced composites. These results would suggest that using highly helical tungsten

fibres, i.e. have a small helical angle, should provide the best results. However, it was shown in the first study that the samples with helical angles greater than 53 degrees, showed higher ultimate tensile stresses and strains and typically failed due to fibre fracture, demonstrating plastic deformation in the fibre. The samples with helical angles less than 45 degrees on the other hand showed lower ultimate tensile stresses and strains, failed due to fracture in the matrix and showed elastic deformation only in the fibres. This would suggest that the matrices inability to work harden and accommodate the large amount of unbending is likely the cause of failure for samples that possessed high variation from the straight case, i.e. low helical angle. Therefore, it is important to select a helical pitch or analogously a degree of corrugation whose unbending can be accommodated by the deformation of the matrix material.

## 2.5 Summary

Based on the work that has been done to date, described above, some of the general findings can be summarized as follows:

- A corrugated structure leads to a reduction in stiffness in the longitudinal direction and an improved stiffness in the transverse direction.
- A corrugated structure will have lower levels of stress for equivalent amounts of strain.
- As deformation proceeds the corrugated structure will unbend leading to increasing work hardening.
- The stress-strain response of an isolated corrugation can be divided into regions of unbending and stretching.
- Improvements in necking strain and energy absorption can be achieved through the use of corrugated architectures.

- During the unbending of the corrugation, the stress is concentrated in the peaks and troughs and there are high shear stresses present in the matrix in the regions between peaks and troughs.
- The degree of corrugation, volume fraction and arrangement of the reinforcing phase are important in dictating the resultant stress-strain response.
- The material properties of the components affect the resultant stress-strain response of corrugated structures. In particular, although not studied in depth the plasticity of the matrix material seems to have a large effect.
- Corrugated and helical structures are found in nature and seem to provide improved ductility and strengthening mechanisms for these materials
- Both helical and corrugated structures exhibit similar behaviour due to their curvilinear architecture.

It is clear that although the work performed thus far has provided a good base with regards to understanding the behaviour of corrugation reinforced composites, that further investigation is required. Much of the work done so far has concentrated on the initial response of these corrugated materials, but not the entire stress-strain response up to the point of necking. More study needs to be completed both with regards to simulations and experiments that spans a larger range of deformation behaviour in order gain a more complete understanding of the applicability of this architecture across material systems and to ultimately be able to predict the entire behaviour of a given corrugated composite system. In particular more work needs to be done exploring the effect of the component material properties and how they interact with the geometry of the system, particularly for more complex systems exhibiting plasticity and strain rate sensitivity. Also, it will be helpful to establish the differences in behaviour between isolated

corrugations and embedded corrugations in order to get a better idea of how the previous findings for isolated corrugations or corrugated sandwich cores can be adapted to give predictions for when corrugations are embedded in another material. Finally, it would be of great interest to see how and under what circumstances these corrugated materials fill desirable holes in material property space, particularly with regards to strength and ductility.

# 3 Modeling Procedure and Results

## 3.1 Introduction

This section describes the numerical modeling technique that was used to explore the mechanical behaviour of corrugation reinforced composites. The numerical modeling was completed using the Finite Element Modeling (FEM) technique. This section will explain the general approach used in FEM and then provide more details into particular studies that were performed using this tool and will present the results of these studies. These results will typically include the stress-strain curves that can be extracted from the simulation output data along with some stress or strain maps when this is deemed appropriate for the analysis and discussion presented later in this document.

## 3.2 Geometry Definitions

Before moving on to a description of the FEM procedure it is important to first define some key geometric parameters. A two dimensional representation of a corrugation reinforced composite can be seen below in Figure 3-1, with some key parameters labeled. This composite consists of a corrugated reinforcing phase and a surrounding matrix phase. The corrugation can be thought of as a wave and can thus be defined in a similar fashion to a wave. The vertical distance from the midline of a peak to the midline of a trough will be called the corrugation height, A or sometimes h, and is essentially twice the amplitude of the wave. The horizontal distance between one peak and an adjacent peak will be called the corrugation period, P, and is essentially the size of a single wave unit. Another important parameter is the thickness of the reinforcement, which is defined as the thickness of the corrugation at a peak. The volume fraction of reinforcement is an

additional key parameter which is related to the thickness and arc-length of the corrugation relative to the overall height of the composite.

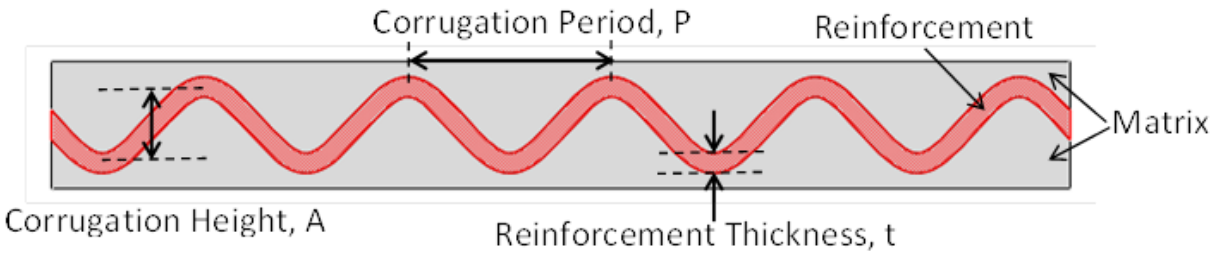


**Figure 3-1: Diagram defining key geometric parameters of a corrugation reinforced composite.**

## 3.3 Finite Element Modeling General Procedure

The FEM simulations were performed using the ABAQUS software package. The ability to investigate a number of different scenarios with regards to sample geometry, component materials and loading state, using this technique made it ideal for exploring the effect of the corrugated architecture. These scenarios include investigating the mechanical behaviour of both isolated corrugations and corrugation reinforced composites in plane strain tension and plane strain compression. In addition, simulations of the corrugation reinforced composites subjected to uniaxial tension and uniaxial compression were also performed. In each of these scenarios both the corrugation geometry and the material properties of the components were subjected to parametric studies. Due to the fact that a large number of simulations were performed, the procedure used for each simulation will not be explained, but instead the general procedure for setting up the FEM simulation in a couple of general categories will be explained and when needed any important changes to this procedure will be noted for individual simulations or for sets of similar simulations. It should be noted that the majority of the simulation work was performed for systems loaded in plane strain tension. The simulations that used plane strain compression, uniaxial tension and uniaxial compression loading conditions were mainly used to

validate and guide the direction of the experimental work that was performed. Therefore, although the procedure used to run these simulations will be described below, the results and discussion of these particular simulations will be included in the experimental section of the thesis.

### 3.3.1 Creation of the model geometry

The first step is to create a part that contains the geometry of interest. A brief explanation of this step for some broad categories of simulations is outlined below.

#### *3.3.1.1 Category I: Isolated Corrugation in Plane Strain Tension*

Due to the fact that plane strain conditions are being assumed in this scenario, the geometry of interest can be simplified to a 2D geometry. In the case of an isolated corrugation this geometry was just a thin wavy strip as seen in Figure 3-2. These corrugations were created in the ABAQUS software using the spline construct tool with points provided at each peak, trough and the midway point between peak and trough. The period of the corrugation can be altered by changing the horizontal distance between the points that define the corrugation. Also, by varying the vertical location of the peaks and troughs the height of these corrugations can be changed. The corrugated line was then thickened to the needed thickness using the offset method, by offsetting by half the thickness on both sides of the corrugated line. This method of thickening ensures a constant thickness. The other potential method was to copy the initial corrugated line and then translate its copy by the thickness, but this leads to variable thickness as seen in Figure 3-3, and thus was not used. In addition to isolated corrugations, isolated straight strips were considered for comparison purposes. The geometry of these straight strips consisted of a simple rectangle and if loaded in tension, with the top surface containing a very low amplitude and

small period wave, as seen in Figure 3-4. This essentially introduces surface roughness and imperfection such that there are locations where necking can be initiated during tensile loading.

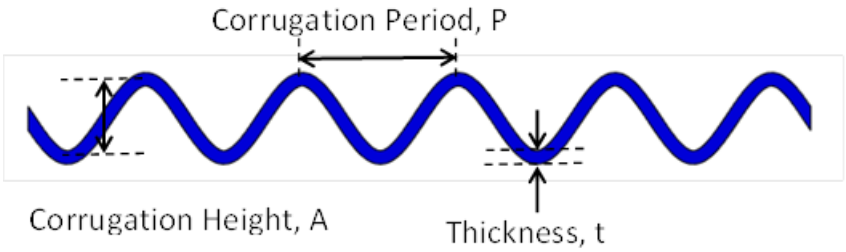


**Figure 3-2: Representation of an isolated corrugated strip, as used for FEM simulations.**

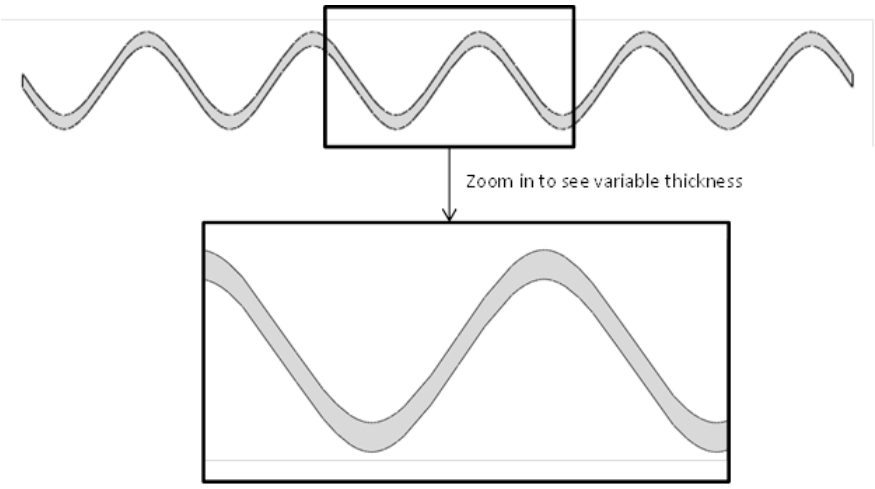


**Figure 3-3: Alternative thickening technique for the corrugations that used a vertical translation of a corrugated line.**

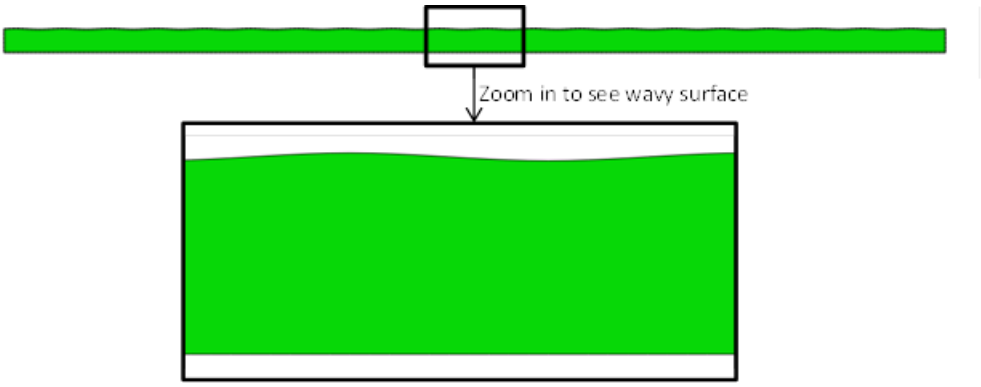


**Figure 3-4: Isolated straight strip with a zoomed in image of the top surface showing the wave that is present to ensure necking is triggered.**

#### *3.3.1.2 Category II: Corrugation Reinforced Composite in Plane Strain Tension or Compression*

Similar to the isolated corrugation subject to plane strain tension described above, the plane strain nature of the loading for this scenario allows the simplification to a 2D geometry. In this case the geometry consists of a rectangle that contains a wavy strip (or strips) in its interior that traverse its entire length, as depicted earlier in Figure 3-1. This is accomplished by creating a part that is a rectangle and then partitioning the face by drawing the corrugation. The corrugation geometry itself is drawn using the same method as for the isolated corrugation.

In order to understand the effect of reinforcement corrugation it is necessary to have a base-line for comparative purposes. Therefore, a number a simulations were conducted that consisted of a composite with a straight reinforcement geometry. When these simulations modeled plane strain tensile loading it was necessary to introduce a small flaw in order to trigger necking at the appropriate moment. This flaw was introduced in the form of a small amplitude (0.02mm), moderate period (2mm) wave along the top surface of the sample, similar to that used for isolated straight strips, as shown in Figure 3-4. Without this flaw necking may have been artificially delayed in these cases.

#### *3.3.1.3 Category III: Corrugation Reinforced Composite in Uniaxial Tension or Compression*

Due to the fact that these parts are being subject to uniaxial loading instead of plane strain, they are no longer constrained in the depth direction and will experience strain in this direction. Therefore, it is no longer an acceptable simplification to use a 2D geometry. In these situations a 3D geometry is employed. The overall 3D structure consists of a rectangular prism that is created by drawing a rectangle and extruding it by the appropriate depth. The front face is then

partitioned to include the corrugation similar to the case above for the corrugation reinforced composite in plane strain. This partitioned face is then extruded through the entire depth to create a rectangular prism that contains a corrugated strip travelling through its interior. An example of a part created for uniaxial tension loading is seen in Figure 3-5. Again, when simulating tensile loading for cases with a straight reinforcement, a wavy top surface was included.

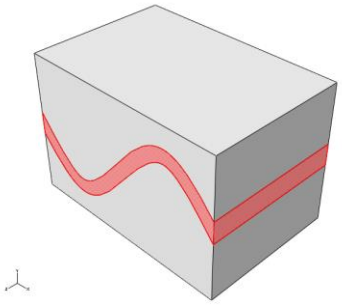

**Figure 3-5: Corrugation reinforced composite to be modeled under uniaxial tension or compression.**

### 3.3.2 Assignment of material properties

The second step involves both inputting the properties of the material of interest and then assigning it to the appropriate region of the part geometry. Similar to the geometric properties of the corrugation, the material properties of the components is a variable that is extensively explored in this thesis. In general, the materials that are used in these simulations are described based on simple elastic and plastic properties. The elastic properties are assumed to be isotropic and consist of the Young's Modulus and Poisson's ratio. The plastic properties are also isotropic and involve the definition of an initial yield stress and then a table of values listing subsequent yield stresses and their corresponding level of plastic strain. These values of stress and strain are inputted as true stress and true plastic strain. The plastic behaviour of the materials explored in this study are typically either described by a power law ($\sigma = K\varepsilon^n$) or are elastic, linearly plastic ($\sigma = K\varepsilon + \sigma_{YS}$). In general, power law hardening models tend to more accurately capture the

behaviour of metals compared to the linear hardening materials. With that being said, linear hardening materials are used extensively in this work as their formulation allows one to clearly separate the effects of yield strength and hardening rate. It should be noted that in both cases the material models extrapolate the behaviour at high strain values to follow the same material models and do not capture the stress saturation that is often observed in real materials. This was deemed an acceptable assumption as it allowed for a detailed exploration of the effect of the material parameters. Once the material has been defined with regards to its properties it is assigned to the appropriate region of the model. If the model is the isolated corrugation, then a single material is created and assigned to the entirety of the corrugated strip. In the case of a corrugation reinforced composite, two materials are defined and the matrix material is assigned to the regions surrounding the corrugated strip and the reinforcement material is assigned to the corrugated strip itself.

### 3.3.3 Defining the Parameters of the Simulation Step

The purpose of this step is to define what type of simulation you are performing and to set some constraints on the calculations that will be performed. Due to the fact that the interest in these simulations is the effect of essentially static loading, the step is defined as a general, static step. Since these simulations contain no time-dependent properties, the total time step of the simulation is irrelevant. For simplicity it is assumed to be a total time step of 1 second. In addition, due to the plasticity of the component materials, the complicated geometry and the large strains involved in these simulations, the non-linear geometry calculations setting is selected. This will allow the calculations to effectively handle the sources of non-linearity. The plastic nature of the materials makes it important to ensure the FEM calculations are performed with small enough step sizes such that they will converge to a convincing solution. However, too

small of a step size will make the calculations very time consuming. To determine an appropriate compromise, studies were performed on representative systems for which the simulation was repeated using different step size constraints. In particular the initial and maximum step sizes were varied between trials and the effect on the resultant stress-strain curve was documented. This process was completed for a corrugation reinforced composite system with a copper matrix and steel reinforcement loaded in plane strain tension and the maximum interval size was varied from 5% of the total increment to 0.1% of the total increment. For each of those maximum interval sizes tested the corresponding initial interval size was 10% of the maximum. Regardless of the interval sizes the stress-strain curves were almost identical and it was concluded that for these simulations there is minimal effect of the step size on the overall response of these systems. However, the step size is still important as it dictates the number of data points that are extractable from a simulation. For the purposes of these studies, the maximum step size was selected as 1% of the total deformation with the other constraints shown in Table 3-1 below.

**Table 3-1: FEM constraints with regards to the step size used for the simulations.**

| Initial Step Size (s) | Minimum Step Size (s) | Maximum Step Size (s) |
|---|---|---|
| 0.001 | $1x10^{-10}$ | 0.01 |

### 3.3.4 Defining Interactions

It is sometimes necessary in FEM to define the behaviour when two parts come into contact. For instance, it is necessary to define the friction coefficient between two surfaces that come into contact. An interaction that for some composite material simulations could require defining is the interfacial strength. In this particular study an ideal interface, with perfect strength was assumed and failure through interfacial decohesion was ignored. Therefore, it was not necessary to define any interfacial properties.

### 3.3.5 Assembling the System

For these simulations this is a very simple step as the purpose is to combine all of the different parts into a single instance.

### 3.3.6 Defining Boundary Conditions

In this step the loading conditions are represented through the imposition of boundary conditions. For all of the different categories, displacement boundary conditions were employed.

#### *3.3.6.1 Category I: Isolated Corrugation in Plane Strain Tension*

For the isolated corrugation, plane strain tension was accomplished by fixing one end of the corrugated strip in the horizontal direction and displacing the other end of the strip by some amount horizontally. In order to fix the whole part vertically in space and avoid the part floating around in space during the simulation, the vertical midpoints at both ends of the strip were fixed to zero vertical displacement.

#### *3.3.6.2 Category II: Corrugation Reinforced Composite in Plane Strain Tension or Compression*

The boundary conditions for the corrugation reinforced composite in plane strain tension are very similar to that of the isolated corrugation in plane strain tension. The tensile load is simulated by fixing one side of the composite in the horizontal direction (both the matrix and reinforcement regions) and by applying a horizontal displacement of the other side of the composite (again both matrix and reinforcement). Additionally, the vertical midpoint of both sides is fixed in the vertical direction to prevent the part from floating in space.

For the cases when plane strain compression is applied to the corrugation reinforced composite, new boundary conditions need to be applied. The entire bottom surface (all matrix) is fixed

vertically and the entire top surface (again all matrix) is subject to a vertical displacement in order to simulate compression. The midpoints of both the top and bottom surfaces are fixed horizontally in space to once again avoid the floating phenomena.

#### *3.3.6.3 Category III: Corrugation Reinforced Composite in Uniaxial Tension or Compression*

The boundary conditions are a little bit different for the 3D cases of uniaxial tension and compression. For uniaxial tension, one end of the composite is fixed horizontally by applying a zero displacement boundary condition to the entire face (includes both matrix and reinforcement regions) while the face of the other end (again both matrix and reinforcement) of the composite is subject to a horizontal displacement of some finite amount. The horizontal midlines that traverse the depth of both end faces are fixed vertically to prevent vertical floating and the vertical midlines that traverse the height of both end faces are fixed in the depth direction to prevent out-of-plane floating.

In the case of uniaxial compression, the entire bottom face (all matrix) is fixed vertically and the entire top face (all matrix) is subject to a finite vertical displacement. The midlines that traverse the depth of the sample on both the top and bottom surfaces are fixed horizontally to prevent the horizontal floating of the part and the midlines that traverse the length of both the top and bottom faces are fixed in the depth direction to prevent out-of-plane floating of the part.

### 3.3.7 Defining the Mesh

This step is very important as it determines a number of the assumptions used with regards to the calculations performed, including the number of nodes, the degrees of freedom, the formulation

and the integration method. Due to the nature of the samples being simulated, continuum solid elements were selected.

First the mesh size needs to be selected such that there is sufficient detail in the calculations to give a realistic result. This mesh size should be optimized through a mesh refinement process that involves using progressively finer meshes until there is minimal benefit with regards to improved accuracy that accompanies the increased cost of additional elements. The results of such a mesh refinement study can be seen in Figure 3-6, which shows the stress-strain curves for the same corrugation reinforced system under plane strain tension using different mesh sizes. Looking at this figure it seems that the mesh size does not have a significant effect in the range considered, with decreasing mesh size resulting in very slight reductions in necking strain and ultimate tensile strength and a slight change in the shape of the curve. This is further highlighted in a plot of necking strain and ultimate tensile strength versus mesh size, seen in Figure 3-7. Based on these finding it was found that a mesh size of 0.1 mm was sufficiently refined for 2D simulations. In the case of an isolated corrugation, this usually led to between 4000 and 5000 elements, and for the corrugation reinforced composites, this usually corresponded to between 20,000 and 25,000 elements, with an example of the mesh used shown in Figure 3-8. For the 3D simulations, the computing requirements are much greater and therefore, for most simulations a mesh size of 0.5 was deemed sufficient after a mesh refinement study. This corresponded to between 10,000 and 20,000 elements, with an example shown in Figure 3-9.

The number of nodes and the degrees of freedom in a given simulation depends not only on the mesh size, but also the element geometry and the order of interpolation. For the 2D simulations the quadrilateral element geometry was selected. For these simulations the quadrilateral shape was capable of filling the parts with only minimal initial mesh distortion. In general,

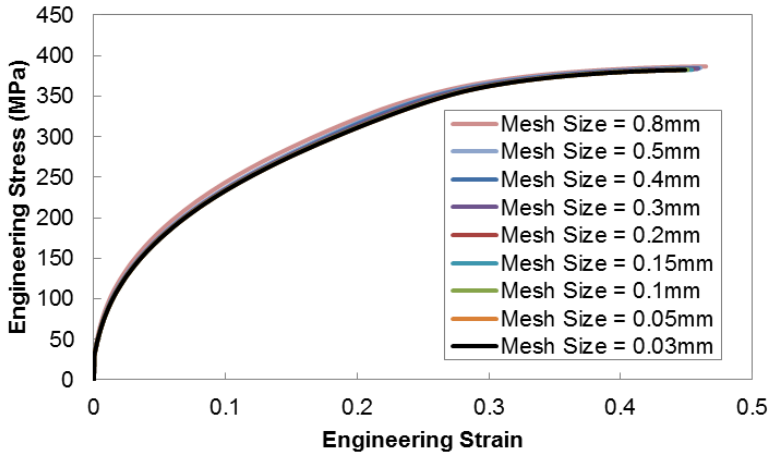


**Figure 3-6: Mesh refinement study showing stress-strain curves from FEM simulations of corrugation reinforced composites under plane strain tension with variable mesh size.**

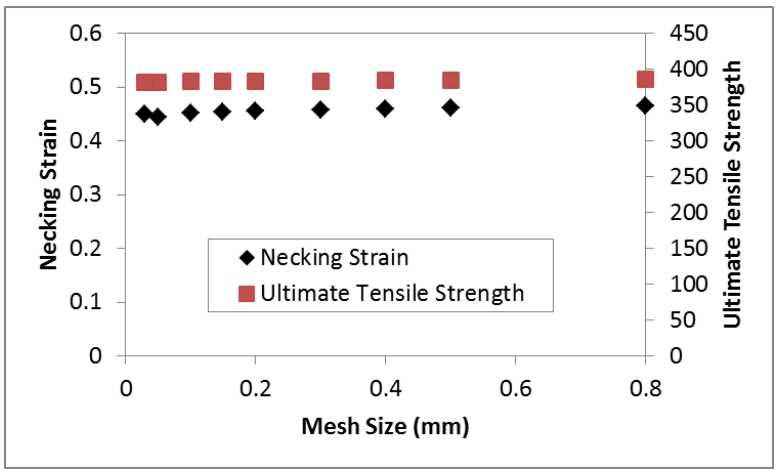


**Figure 3-7: Mesh refinement study showing the necking strain and ultimate tensile strength data taken from Figure 3-6 from FEM simulations of corrugation reinforced composites under plane strain tension as a function of mesh size.**

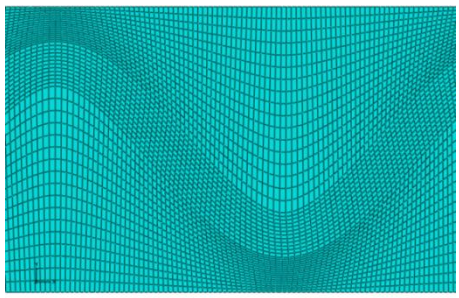

**Figure 3-8: Typical FEM mesh used for 2D simulations of corrugation reinforced composites with a mesh size of 0.1mm.**

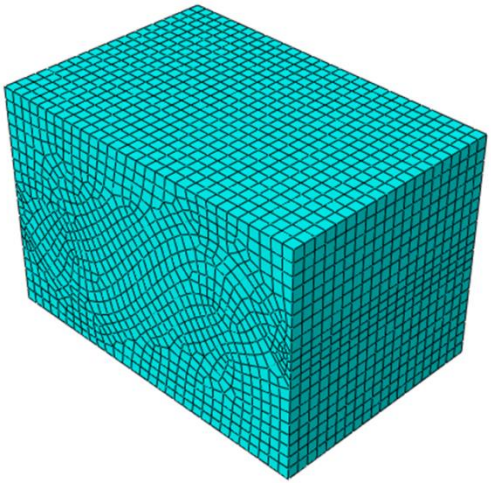

**Figure 3-9: Typical FEM mesh used for 3D simulations of corrugation reinforced composites with a mesh size of 0.5mm.**

quadrilateral elements should be selected instead of triangular elements as triangular elements have poor convergence rates and are more likely to suffer from volumetric locking and are only really preferable if it is difficult to fill the space with quadrilaterals. Due to the high strains, large mesh distortion and complicated model geometry first order interpolation with full integration was selected for the 2D simulations. Second order interpolation is computationally more expensive and would likely have performed poorly due to the large strains and mesh distortion. For the 3D simulations, first order hexahedral elements were selected with reduced integration. The reduced integration was selected to reduce the computational cost of the simulations, as the jump to 3D increases the computation time significantly.

Considering all that has just been discussed, CPE4 elements were used for the 2D plane strain simulations and C3D8R elements were used for the 3D uniaxial tension and compression simulations. When the geometry of the part permitted, structured meshing was selected and if necessary free meshing was employed.

### 3.3.8 Job Creation & Analysis

After all of the previously outlined steps are taken, a job is created and the calculations are performed. Once the simulation is completed the results can be viewed and analyzed.

## 3.4 Finite Element Modeling Studies

Throughout this research a number of FEM studies were performed that investigated various aspects of corrugation reinforced composites. In this section a number of studies that focused on plane strain tensile loading will be introduced below along with the values of the key variables that define each system, including geometric, material and simulation parameters. This chapter will also present the results of these studies, mainly in the form of stress-strain curves. The subsequent discussion of these results is presented later in the thesis. The focus of this work is on plane strain tension because the tensile loading allows one to evaluate the uniform deformation and necking behaviour of these materials, which are key in evaluating the metrics of interest, mainly the ductility and strength of these materials. Plane-strain loading has been focused on due to the fact that it allows for computationally cheaper, 2D modeling, and because it is likely that these materials would be manufactured in sheet form and thus plane-strain conditions would be present. The simulations that explored isolated corrugations will be presented first followed by those that explore the corrugation reinforced composites. Before testing the behaviour of the corrugation reinforced composite material, it was important to first understand how an isolated corrugation will behave. Once this behaviour is understood, it can be compared to that of a corrugation that is embedded within a matrix in order to identify the impact that the matrix material is having on the corrugation's behaviour.

### 3.4.1 Isolated Corrugation in Plane Strain Tension

The details of the FEM simulations and their corresponding results for isolated corrugations subject to plane strain tension will be presented in this section. They will be organized into one subsection that looks at the effect on geometry and one subsection that looks at the effect of material. Due to the fact that the stress-strain response of these materials is a focus of this research, a stress-strain curve was calculated for each simulation from the data available. The values for the engineering strain of the sample, $e_x$, are calculated by dividing the horizontal distance the displaced end of a corrugation has moved, $\Delta L_x$, by the initial length of the corrugation, $L_0$.

$$\boldsymbol{e_x = \frac{\Delta L_x}{L_0}} \tag{3-1}$$

The engineering stress, $S_x$, on the other hand, is calculated by summing the horizontal reactionary forces that are present at all of the nodes of the fixed end of the corrugation, $\Sigma F_{x,\text{ end nodes}}$, and dividing this by the thickness of the corrugation, t. This division of force by the thickness is acceptable as the plane-strain simulations assume a width, w, of the sample of 1 unit distance.

$$\boldsymbol{S = \frac{\sum F_{x,end\ node}}{wt} = \frac{\sum F_{x,end\ nodes}}{(1)t}} \tag{3-2}$$

The force was divided by the overall sample thickness and not the vertical thickness observed at the end of the sample. Due to the fact that the end of the sample is halfway between a peak and a trough the thickness at the end is actually greater than the overall sample thickness. A data point for a value of stress and strain was calculated at each time increment of the simulation.

In addition to the overall stress-strain response it can be beneficial to observe snapshots of local stress and strain maps of these samples as they undergo deformation. In the cases of these

isolated corrugation materials the stress and strain maps tend to be fairly similar from one corrugation geometry to another. Due to this similarity between samples, a series of stress and strain maps for a single representative simulation will first be highlighted below. The representative simulation selected for illustration is an isolated corrugation with a period of 8mm, height of 3mm, thickness of 0.78mm, total length of 40mm and a copper material model. First off, a zoomed out progression of the entire strip at different stages of deformation is shown in Figure 3-10. Figure 3-11 shows a progression of the von Mises stress map at different levels of overall strain, zooming in on the middle of the corrugated strip. Similar progressions highlighting x-direction stress, $\sigma_x$ and y-direction stress, $\sigma_y$, are shown in Figure 3-12 and Figure 3-13, respectively. In addition, strain maps for the same simulation are found in Figure 3-14 and Figure 3-15 for x-direction strain, $\varepsilon_x$, and y-direction strain, $\varepsilon_y$, respectively.

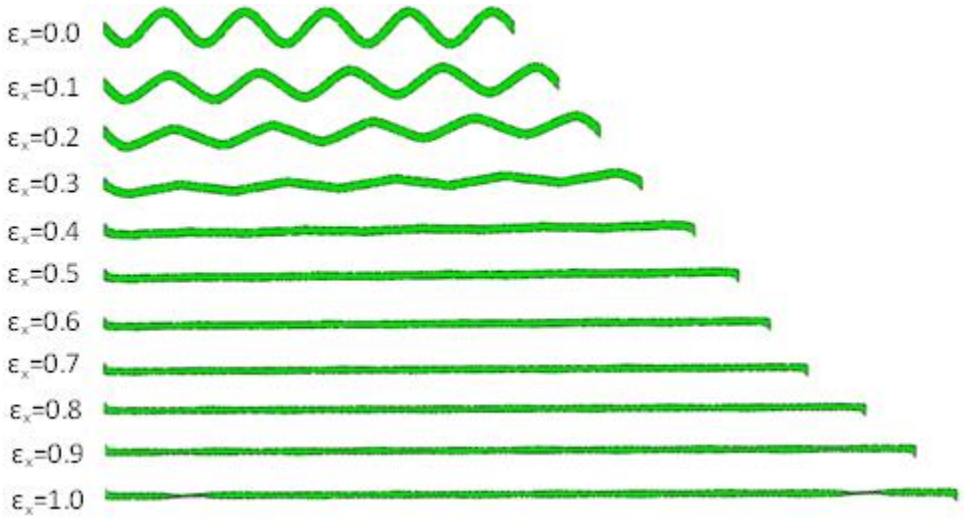


**Figure 3-10: Progression of isolated corrugation shape from FEM simulation of copper at different values of total horizontal strain, $\varepsilon_x$.**

### *3.4.1.1 Effect of Geometry*

The geometry of a corrugation can be defined by a few key parameters; height, period, thickness and percentage corrugated. The effect of these key geometric parameters on the stress strain

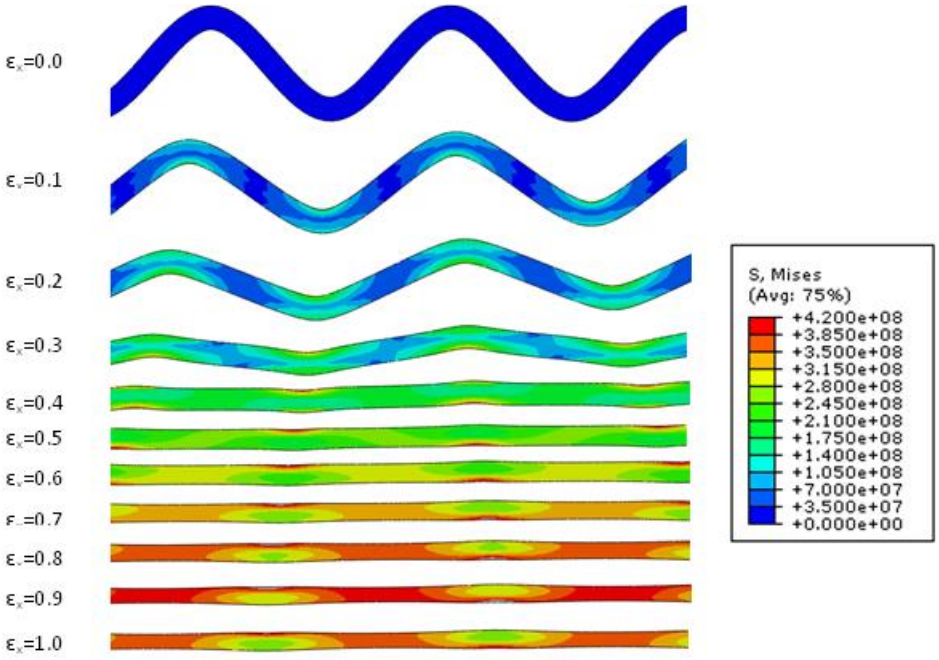


**Figure 3-11: Progression of von Mises stress map from FEM simulation of isolated copper corrugation at different values of total horizontal strain, $\varepsilon_x$.**

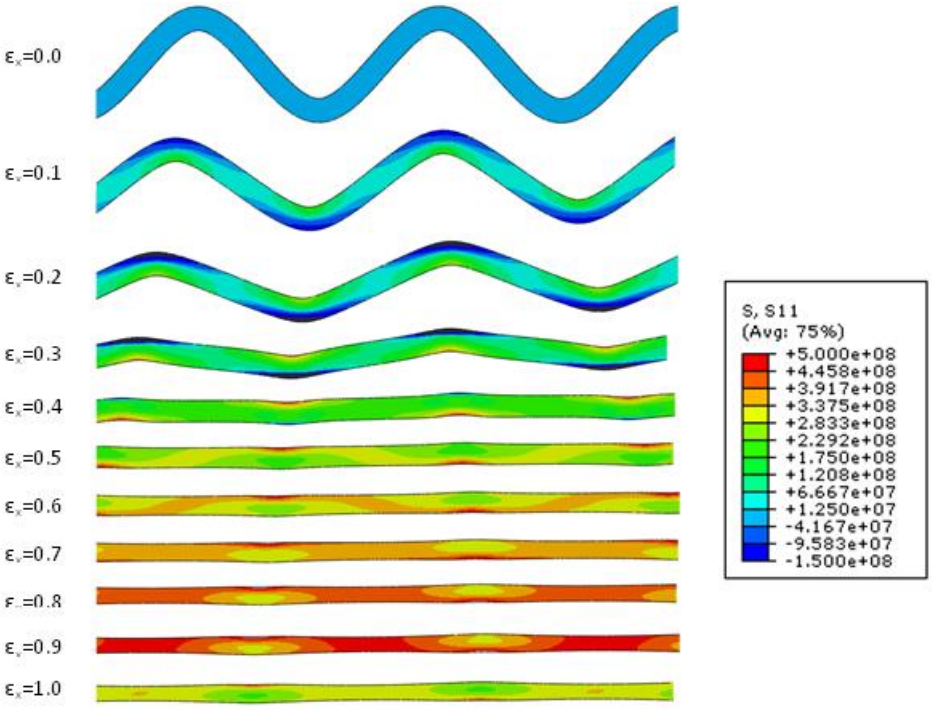


**Figure 3-12: Progression of longitudinal stress map from FEM simulation of isolated copper corrugation at different values of total longitudinal strain, $\varepsilon_x$.**

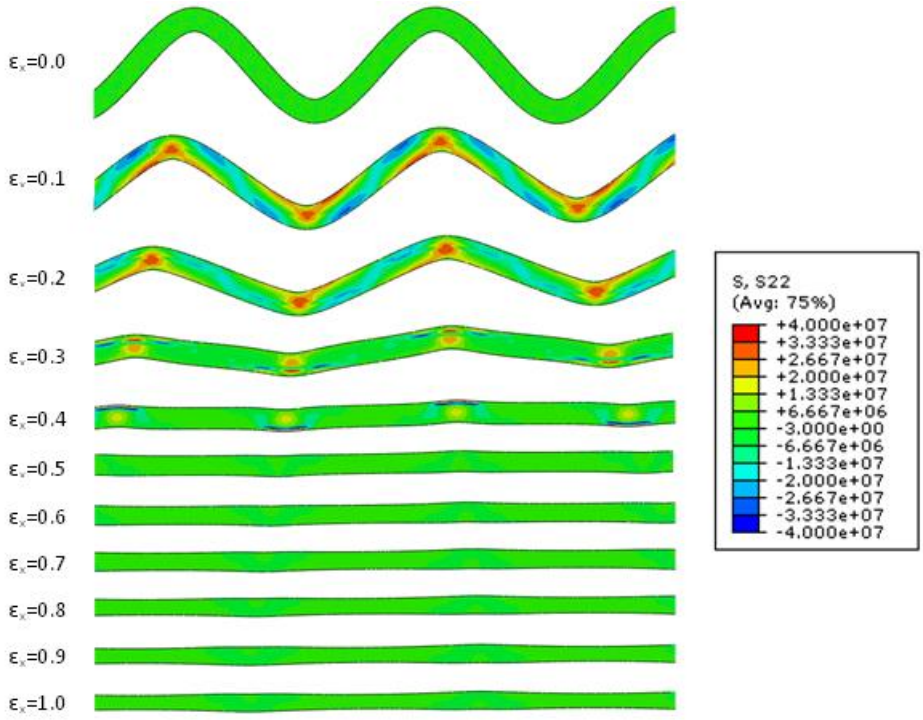


**Figure 3-13: Progression of transverse stress map from FEM simulation of isolated copper corrugation at different values of total longitudinal strain, $\varepsilon_x$.**

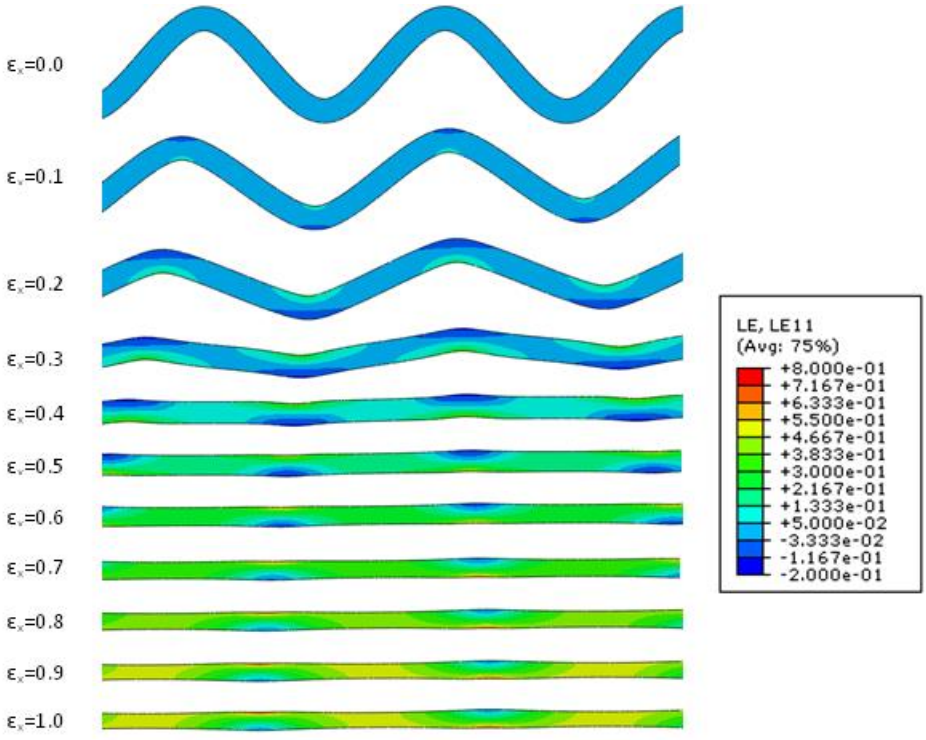


**Figure 3-14: Progression of longitudinal strain map from FEM simulation of isolated copper corrugation at different values of total longitudinal strain, $\varepsilon_x$.**

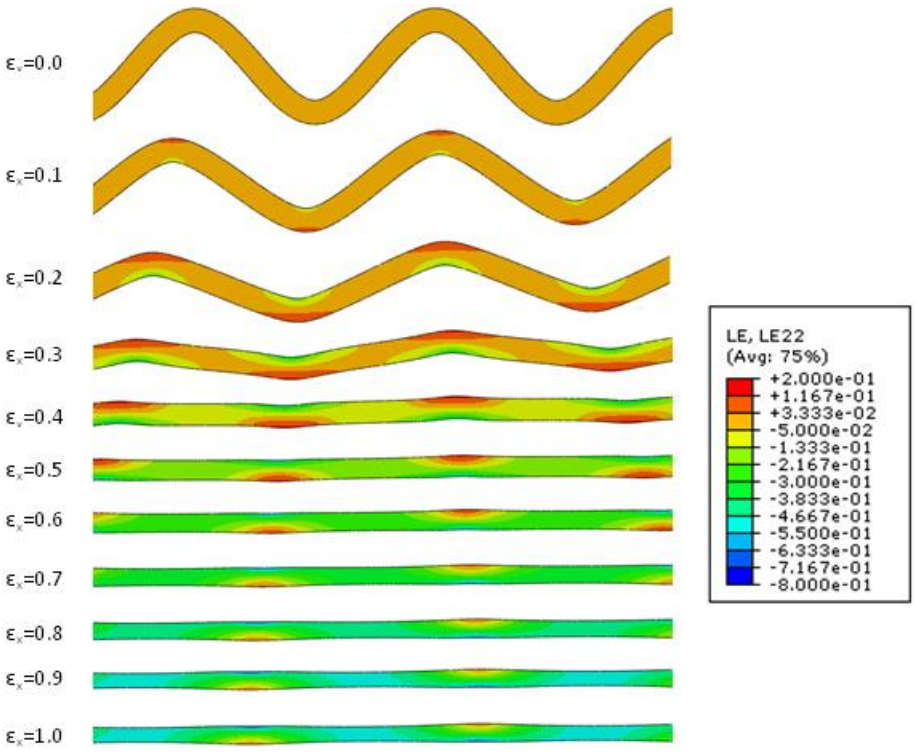


**Figure 3-15: Progression of transverse strain map from FEM simulation of isolated copper corrugation at different values of total longitudinal strain, $\varepsilon_x$.**

response was investigated using parametric studies. These parametric studies investigated a plane-strain loading state and were performed using a couple of different model materials to ensure that the geometric effects were observable regardless of the material of the corrugation.

The materials that were selected for these parametric studies were copper, 4130 steel and a theoretical material, referred to as LinMat1, which follows a linear hardening law. The copper and the 4130 steel were both modeled using a power-law hardening model ($\sigma=K\varepsilon^n$), and LinMat1 using a linear hardening model ($\sigma=\sigma_{YS}+K\varepsilon$). The parameters describing the plastic behaviour of the copper were taken from tensile test experiments that will be described later in Chapter 5. The parameters for the 4130 steel were approximated from the data provided in the lecture notes of Labossiere[64] which were fairly similar to the experimental tensile tests by Melonas and Kattus found in the Atlas of Stress-Strain Curves.[65] Finally, the parameters for LinMat1 were selected to

be reasonable for describing a generic, ferrous-like metal. The elastic and plastic parameters for copper, 4130 steel and LinMat1 can be found in Table 3-2.

**Table 3-2: Material parameters of copper, 4130 steel and LinMat1 used for FEM simulations.**

| Property | Copper | 4130 Steel | LinMat1 |
|---|---|---|---|
| Young's Modulus (GPa) | 115 | 207 | 207 |
| Poisson's Ratio | 0.33 | 0.3 | 0.3 |
| Yield Strength, $\sigma_{ys}$ (MPa) | 25 | 350 | 300 |
| Hardening Coefficient, K (MPa) | 540 | 1200 | NA |
| Hardening Exponent, n | 0.53 | 0.12 | NA |
| Linear Hardening Coefficient, K (MPa) | NA | NA | 500 |

For a parametric study, in order to isolate the effect of individual geometric parameters, all other factors must be kept constant. However, some geometric parameters are interconnected and changing one will affect the value of another. For instance, if the total length of a sample is 40mm and the period of the corrugation is changed from 10mm to 20mm, this will change the number of full cycles found in the sample from four to two. Additionally, to try and preserve the total volume of material from a sample with one corrugation geometry to a sample with a different corrugation geometry, the thickness of the corrugation needs to be adjusted accordingly. For example, a sample with a corrugation height of 4mm might require a thickness of 0.68mm to match the volume of a sample with a corrugation height of 2mm, which has a thickness of 0.88mm. For these isolated corrugations these thicknesses are not very important, however, when these corrugations become embedded in a matrix to form a composite, the thickness of the corrugation will help dictate the volume fraction of reinforcement. For all of the simulations performed in this section the initial horizontal length of each sample was set at 40mm.

#### 3.4.1.1.1 Effect of Corrugation Height

The first parametric study looks at the effect of the corrugation height on the stress strain response. The values of the geometric parameters for each simulation in this study are summarized in Table 3-3. In addition to all of the corrugated geometries, a straight strip geometry was also simulated, for comparative purposes. Notice that the thickness of the corrugations decreases as the height of the corrugation increases in order to maintain the volume of the sample.

**Table 3-3: Values of geometric parameters of corrugations to investigate the effect of corrugation height.**

| Simulation # | Period (mm) | Height (mm) | Thickness (mm) | # of Cycles | % Corrugated |
|---|---|---|---|---|---|
| 1 | 8 | **2** | 0.88 | 5 | 100% |
| 2 | 8 | **2.5** | 0.83 | 5 | 100% |
| 3 | 8 | **3** | 0.78 | 5 | 100% |
| 4 | 8 | **3.5** | 0.73 | 5 | 100% |
| 5 | 8 | **4** | 0.68 | 5 | 100% |
| 6 (straight) | NA | **NA** | 1 | NA | 0% |

The stress-strain curves generated from the output of simulations with variable corrugation height can be seen in Figure 3-16 for copper. The stress-strain curves for the 4130 steel and LinMat1 simulations were not included as they demonstrated very similar trends to those seen for copper. Each of the curves represents a corrugated strip with a different corrugation height. All of the stress-strain curves presented in this work are shown only up until the point where the maximum engineering stress is reached, i.e. the ultimate tensile strength. This ultimate tensile strength happens at the value of strain where necking begins.

The purpose of showing this portion of the stress-strain curves is to focus only on the portion of the deformation in which uniform elongation occurs such that the strength and ductility of the

samples can be considered, but not necessarily the damage and failure of the materials. Looking at the behaviour after necking is initiated could be an area for future work on this topic.

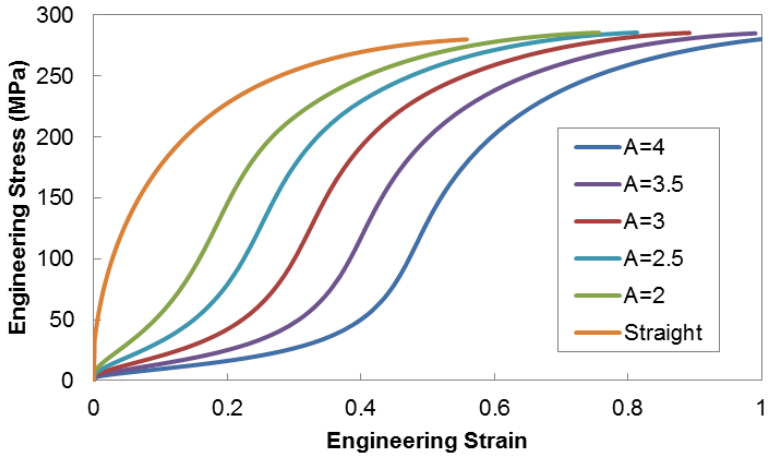


**Figure 3-16: FEM generated stress-strain curves of isolated copper corrugations with variable corrugation height, A, under plane strain tension.**

#### 3.4.1.1.2 Effect of Corrugation Period

The next parametric study looks at the effect of the period on the stress strain response. The values of the geometric parameters for each simulation in this study are summarized in Table 3-4. Once again, a straight strip geometry was also simulated. Also, similar to decreasing the height, increasing the period of the samples is accompanied by an increase in sample thickness.

**Table 3-4: Values of geometric parameters of corrugations to investigate the effect of corrugation period.**

| Simulation # | Period (mm) | Height (mm) | Thickness (mm) | # of Cycles | % Corrugated |
|---|---|---|---|---|---|
| 1 | **8** | 4 | 0.68 | 5 | 100% |
| 2 | **10** | 4 | 0.76 | 4 | 100% |
| 3 | **13.33** | 4 | 0.84 | 3 | 100% |
| 4 | **20** | 4 | 0.92 | 2 | 100% |
| 5 | **40** | 4 | 0.98 | 1 | 100% |
| 6 (straight) | **NA** | NA | 1 | NA | 0% |

Additionally, the number of cycles decreases with an increase in period as each cycle covers a larger portion of the 40mm long sample. The stress-strain curves showing the effect of the period of the corrugation are found below in Figure 3-17 for copper. Again, the stress-strain curves for 4130 steel and LinMat show similar trends to that of copper and thus were not included. Each of the curves in this graph represents the simulation results of a corrugated strip with a different period of corrugation.

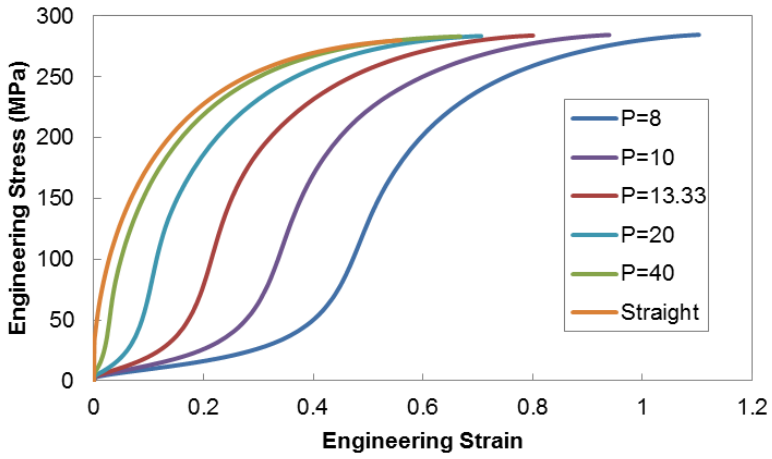


**Figure 3-17: FEM generated stress-strain curves of isolated copper corrugations with variable corrugation period, P, under plane strain tension.**

#### 3.4.1.1.3 Effect of Percentage Corrugated

The third parametric study investigates the effect of the percentage of corrugation of the sample on the stress strain response. In this study the same corrugation geometry is employed (period, height, thickness); however, for the cases when the sample is less than 100% corrugated, some fraction of the 40mm length is straight. In this study it was not possible to maintain the volume of the sample and keep the same basic unit of corrugation. Therefore, in this case the basic unit was maintained and the total volume increases as the corrugation percent increases. The values of the geometric parameters for each simulation in this study are summarized in Table 3-5.

**Table 3-5: Values of geometric parameters of corrugations to investigate the effect of corrugation percentage.**

| Simulation # | Period (mm) | Height (mm) | Thickness (mm) | # of Cycles | % Corrugated |
|---|---|---|---|---|---|
| 1 | 8 | 3 | 0.78 | **5** | **100%** |
| 2 | 8 | 3 | 0.78 | **4.5** | **90%** |
| 3 | 8 | 3 | 0.78 | **4** | **80%** |
| 4 | 8 | 3 | 0.78 | **3** | **60%** |
| 5 | 8 | 3 | 0.78 | **2** | **40%** |
| 6 (straight) | NA | NA | 1 | **NA** | **0%** |

Figure 3-18 shows the stress-strain curves with variable corrugation percentages for the copper system. Each individual curves represent the calculated stress-strain response of a single geometry representing a different relative combination of corrugated and straight geometries. The trends relating to the effect of corrugation percentage for the 4130 steel and LinMat1 systems are similar to those seen for copper and thus these plots were not included.

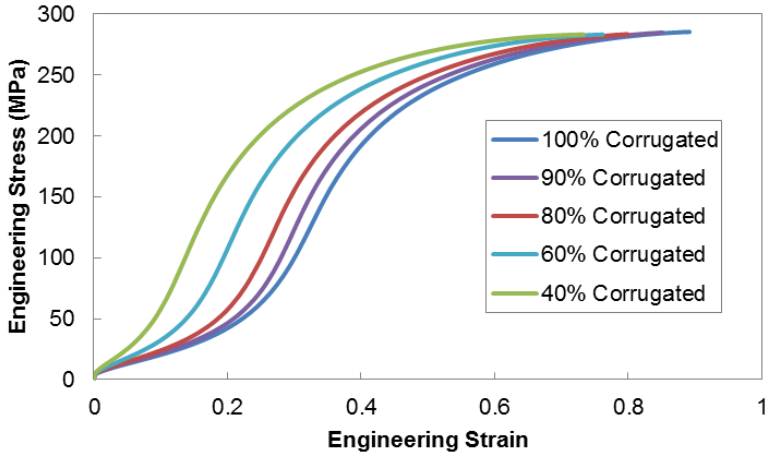


**Figure 3-18: FEM generated stress-strain curves of isolated copper corrugations with variable percentages of corrugation under plane strain tension.**

#### 3.4.1.1.4 Effect of Corrugation Thickness

The final geometric parametric study investigates the effect of the corrugation thickness on the stress strain response. The values of the geometric parameters for each simulation in this study

are summarized in Table 3-6. The stress-strain curves that show the effect of corrugation thickness are seen in Figure 3-19, Figure 3-20 and Figure 3-21, for copper, 4130 steel and LinMat1, respectively. Each individual curve in these plots represents the stress-strain response of a corrugated sample with a different thickness but the same core wave structure.

**Table 3-6: Values of geometric parameters of corrugations to investigate the effect of corrugation thickness.**

| Simulation # | Period (mm) | Height (mm) | Thickness (mm) | # of Cycles | % Corrugated |
|---|---|---|---|---|---|
| 1 | 8 | 3 | **0.39** | 5 | 100% |
| 2 | 8 | 3 | **0.78** | 5 | 100% |
| 3 | 8 | 3 | **1.17** | 5 | 100% |
| 4 | 8 | 3 | **1.56** | 5 | 100% |

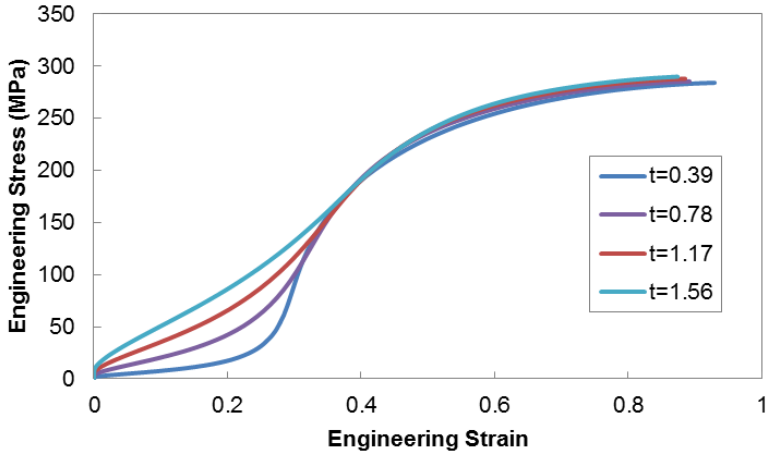


**Figure 3-19: FEM generated stress-strain curves of isolated copper corrugations with variable corrugation thickness, t, under plane strain tension.**

### *3.4.1.2 Effect of Material Parameters*

There are a number of parameters that can be used to model the mechanical response of a material. Depending on the application of interest and the loading conditions being examined, this model of material behaviour can be greatly simplified. For the purposes of these parametric

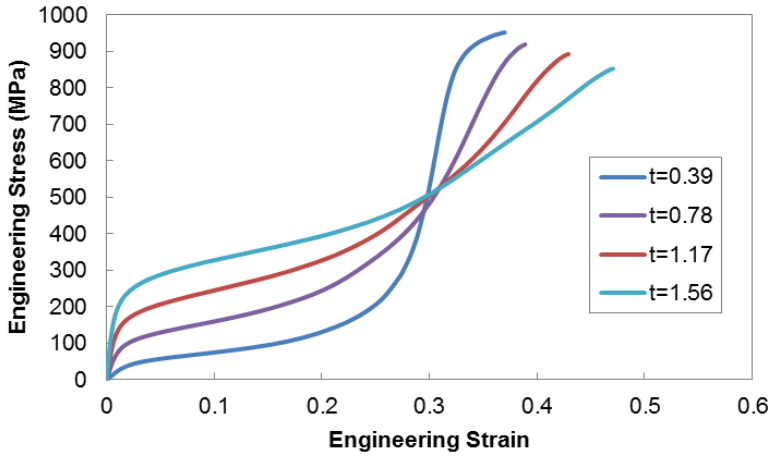


**Figure 3-20: FEM generated stress-strain curves of isolated 4130 steel corrugations with variable corrugation thickness, t, under plane strain tension.**

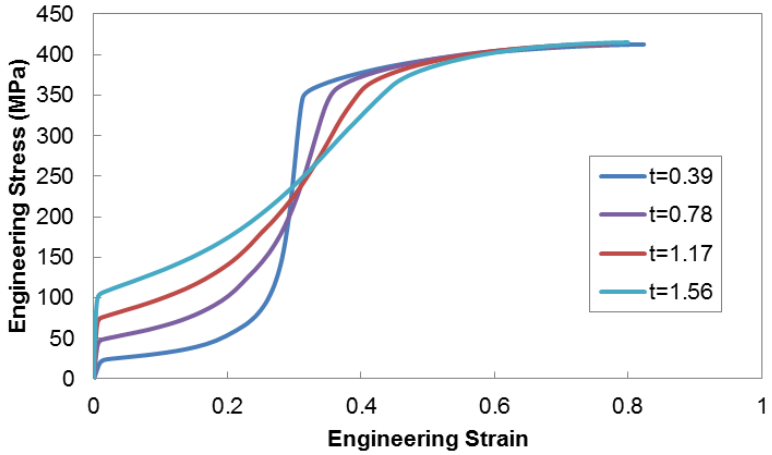


**Figure 3-21: FEM generated stress-strain curves of isolated LinMat1 corrugations with variable corrugation thickness, t, under plane strain tension.**

studies that investigate the behaviour of an isolated corrugation, two simple material models were employed. In both of these models the elastic response of the materials is assumed to be isotropic and can be simply described using an elastic modulus and the Poisson's ratio. The onset of plasticity is defined through the use of a yield strength. With regards to the plasticity of the materials, the first model uses a power-law hardening model whose stress strain relationship is described by the equation, $\sigma = K\varepsilon^n$, where K is a hardening coefficient and n is a hardening

exponent. The plasticity of the second model employs a linear hardening model following the equation, $\sigma = K\varepsilon + \sigma_{YS}$, where K is again a hardening coefficient and $\sigma_{YS}$ is the yield strength of the material. Parametric studies were performed for corrugated systems using each type of material model to investigate the effect of the key material parameters on the stress-strain response of an isolated corrugation. The parameters investigated were $\sigma_{YS}$, K and n for the power-law hardening materials, and $\sigma_{YS}$ and K for the linear hardening materials.

For all of the parametric studies that explore the effect of material properties, the geometry of the isolated corrugation is kept constant. The geometry consists of a corrugation with a period of 8mm, a corrugation height of 3mm, a thickness of 0.78mm, and a total length of 40mm. For each of the different materials simulated a straight sample was also modeled. By obtaining stress-strain curves for both corrugated and straight samples for each material, one can determine the effect of the material properties on the change in stress-strain response of using a corrugated geometry instead of a simple straight geometry. The straight geometry consisted of a sample with a length of 40mm and a thickness of 1mm which results in the same volume as the corrugated samples.

#### 3.4.1.2.1 Power-Law Hardening Material: Effect of Yield Strength

The first material parametric study investigates the effect of the yield strength on the stress strain response of an isolated corrugation. In order to isolate the effect of yield strength the other material parameters must be kept constant. For this parametric study the other parameters were selected to be similar to those for the 4130 steel. The summary of the material parameters for each simulation in this parametric study are found in Table 3-7. The yield strength had almost no effect on the behaviour of these materials and the stress-strain curves were essentially unaltered by changing this parameter for both the straight and corrugated geometries.

**Table 3-7: Values of material property parameters to investigate the effect of yield strength for power-law hardening material.**

| Simulation # | Elastic Modulus (GPa) | Poisson's Ratio | Yield Strength (MPa) | Hardening Coefficient, K (MPa) | Hardening Exponent, n |
|---|---|---|---|---|---|
| 1 | 207 | 0.3 | **100** | 1200 | 0.12 |
| 2 | 207 | 0.3 | **200** | 1200 | 0.12 |
| 3 | 207 | 0.3 | **300** | 1200 | 0.12 |
| 4 | 207 | 0.3 | **350** | 1200 | 0.12 |
| 5 | 207 | 0.3 | **400** | 1200 | 0.12 |
| 6 | 207 | 0.3 | **500** | 1200 | 0.12 |

#### 3.4.1.2.2 Power-Law Hardening Material: Effect of Hardening Coefficient, K

The next parametric study explores the effect of the hardening coefficient K, on the stress-strain behaviour of an isolated corrugation. In this parametric study the hardening coefficient is varied and all other material parameters are kept constant, similar to those for a copper material. A summary of the material parameters used in the simulations can be found in Table 3-8. The stress-strain curves that were extracted from these FEM simulations can be seen in Figure 3-22 for straight samples and in Figure 3-23 for isolated corrugations. Each curve represents the result of a simulation using a unique hardening coefficient, K, with all else being held constant.

**Table 3-8: Values of material property parameters to investigate the effect of hardening coefficient, K, for power-law hardening material.**

| Simulation # | Elastic Modulus (GPa) | Poisson's Ratio | Yield Strength (MPa) | Hardening Coefficient, K (MPa) | Hardening Exponent, n |
|---|---|---|---|---|---|
| 1 | 115 | 0.33 | 25 | **200** | 0.53 |
| 2 | 115 | 0.33 | 25 | **540** | 0.53 |
| 3 | 115 | 0.33 | 25 | **1000** | 0.53 |

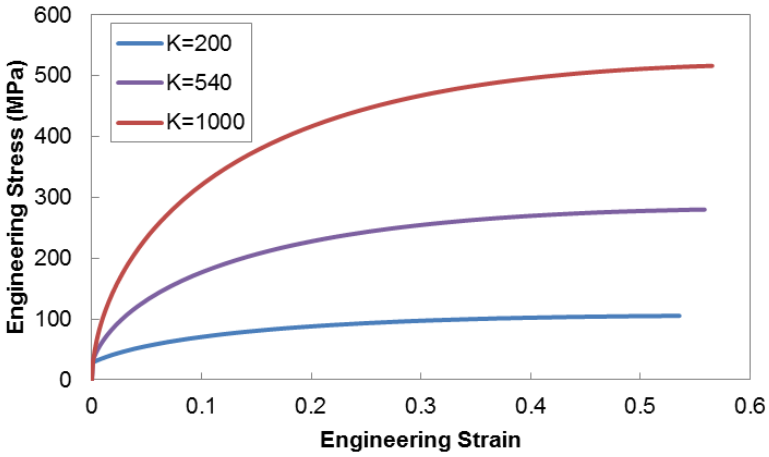


**Figure 3-22: FEM generated stress-strain curves of power-law hardening straight samples with variable hardening coefficient, K, under plane strain tension.**

#### 3.4.1.2.3 Power-Law Hardening Material: Effect of Hardening Exponent, n

This parametric study looked at the effect of the hardening exponent on the stress-strain response of an isolated corrugation. Similar to the previous case, all other material parameters were similar to those for copper, however in this case the hardening exponent was varied from one simulation to the next. The material parameters used in these simulations are summarized in Table 3-9. The stress-strain curves that were generated from these simulations are displayed in

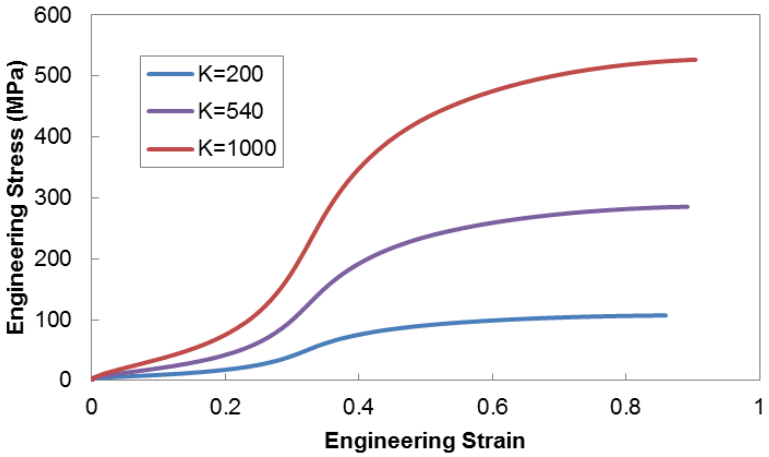


**Figure 3-23: FEM generated stress-strain curves of power-law hardening corrugated samples with variable hardening coefficient, K, under plane strain tension.**

Figure 3-24 and Figure 3-25 for straight samples and isolated corrugations, respectively. The individual curves in these plots each represent a single simulation that is identical to the others in terms of its inputs with the exception of the hardening exponent, n, of the material.

**Table 3-9: Values of material property parameters to investigate the effect of hardening exponent, n, for power-law hardening material.**

| Simulation # | Elastic Modulus (GPa) | Poisson's Ratio | Yield Strength (MPa) | Hardening Coefficient, K (MPa) | Hardening Exponent, n |
|---|---|---|---|---|---|
| 1 | 115 | 0.33 | 25 | 540 | **0.1** |
| 2 | 115 | 0.33 | 25 | 540 | **0.25** |
| 3 | 115 | 0.33 | 25 | 540 | **0.4** |
| 4 | 115 | 0.33 | 25 | 540 | **0.53** |
| 5 | 115 | 0.33 | 25 | 540 | **0.75** |

#### 3.4.1.2.4 Linear Hardening Material: Effect of Yield Strength

For this next parametric study, the general material model is now one of an elastic, linearly plastic material. The elastic properties are similar to those of 4130 steel and the hardening rate (coefficient) is held constant between simulations. The yield strength however is varied in order

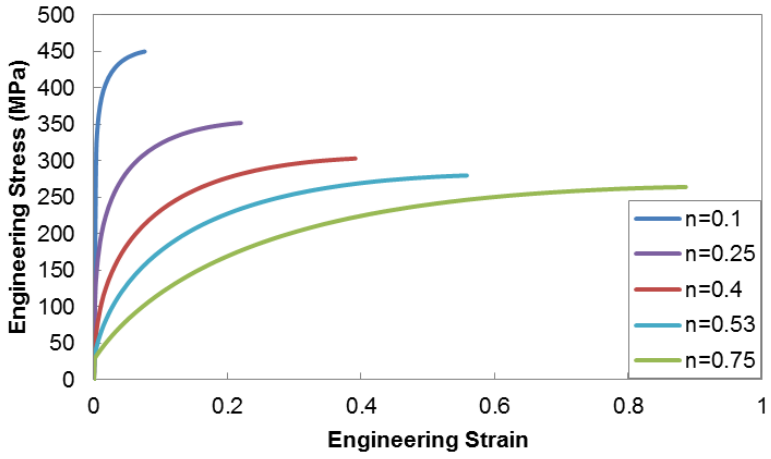


**Figure 3-24: FEM generated stress-strain curves of power-law hardening straight samples with variable hardening exponent, n, under plane strain tension.**

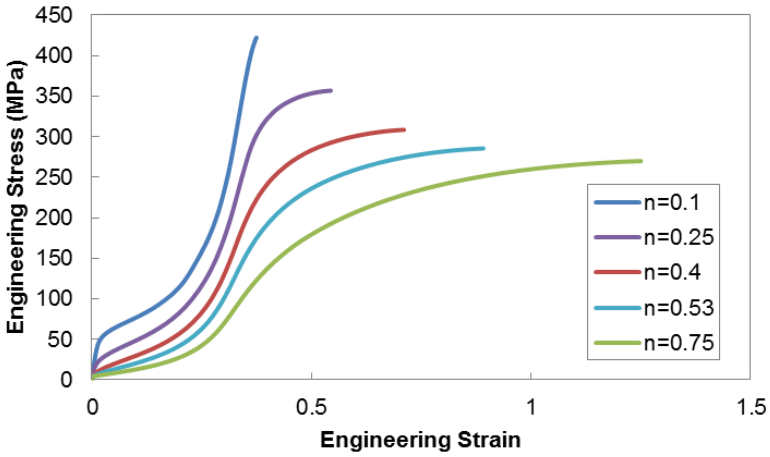


**Figure 3-25: FEM generated stress-strain curves of power-law hardening corrugated samples with variable hardening exponent, n, under plane strain tension.**

to determine its effect on overall stress-strain behaviour of an isolated corrugation. The summary of the material properties used in this parametric study is shown in Table 3-10. The stress-strain curves for this parametric study can be seen in Figure 3-26 for straight samples and in Figure 3-27 for isolated corrugations. Each of the curves represents a unique yield strength with all else kept constant between the curves.

**Table 3-10: Values of material property parameters to investigate the effect of yield strength for linear hardening material.**

| Simulation # | Elastic Modulus (GPa) | Poisson's Ratio | Yield Strength (MPa) | Hardening Coefficient, K (MPa) |
|---|---|---|---|---|
| 1 | 207 | 0.3 | **150** | 500 |
| 2 | 207 | 0.3 | **300** | 500 |
| 3 | 207 | 0.3 | **450** | 500 |
| 4 | 207 | 0.3 | **600** | 500 |
| 5 | 207 | 0.3 | **750** | 500 |
| 6 | 207 | 0.3 | **900** | 500 |

#### 3.4.1.2.5 Linear Hardening Material: Effect of Hardening Coefficient, K

In this final parametric study regarding the effect of material properties, the effect of the hardening coefficient on the stress-strain response of linear hardening materials is explored.

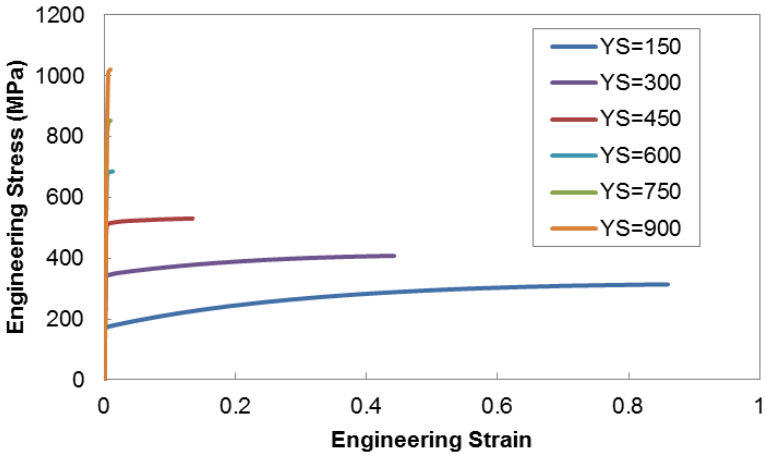


**Figure 3-26: FEM generated stress-strain curves of linear hardening straight samples with variable yield strength, YS, under plane strain tension.**

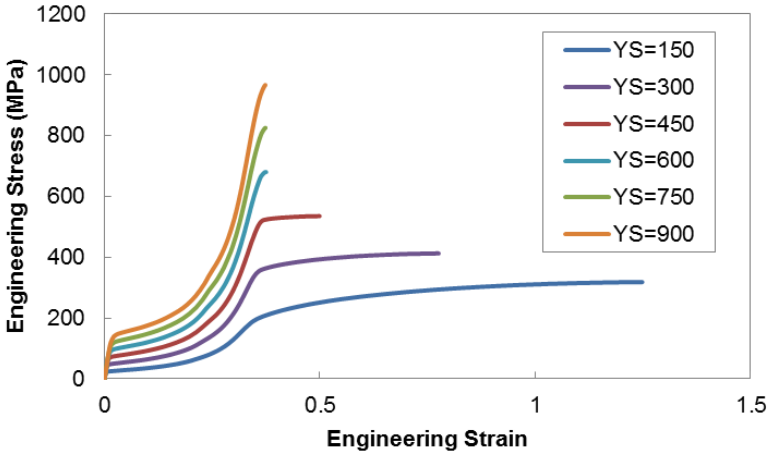


**Figure 3-27: FEM generated stress-strain curves of linear hardening corrugated samples with variable yield strength, YS, under plane strain tension.**

Once again, the material has the elastic properties of 4130 steel. However, in this study the yield strength is kept constant and the hardening coefficient is varied from one simulation to the next. The values of the material parameters used for this study are shown in Table 3-11. The stress-strain curves that were obtained from the FEM simulations are seen in Figure 3-28 for the straight sample geometry and in Figure 3-29 for the isolated corrugation geometry. Each

individual curve in these plots corresponds to the results of a single simulation that is identical to the other simulations represented in the plot, with the exception of the rate of hardening, K.

**Table 3-11: Values of material property parameters to investigate the effect of hardening coefficient, K, for linear hardening material.**

| Simulation # | Elastic Modulus (GPa) | Poisson's Ratio | Yield Strength (MPa) | Hardening Coefficient, K (MPa) |
|---|---|---|---|---|
| 1 | 207 | 0.3 | 300 | **500** |
| 2 | 207 | 0.3 | 300 | **750** |
| 3 | 207 | 0.3 | 300 | **1000** |
| 4 | 207 | 0.3 | 300 | **1250** |
| 5 | 207 | 0.3 | 300 | **1500** |

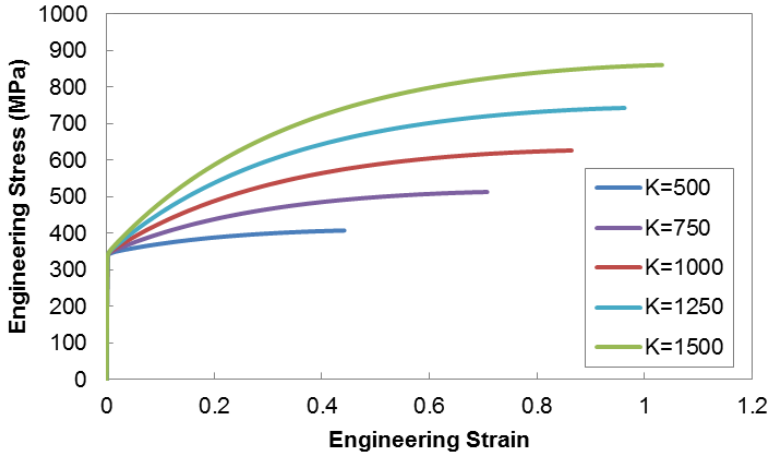


**Figure 3-28: FEM generated stress-strain curves of linear hardening straight samples with variable hardening coefficient, K, under plane strain tension.**

### 3.4.2 Corrugation Reinforced Composite in Plane Strain Tension

The main focus of this thesis is to examine the behaviour of corrugation reinforced composites. The purpose of the previous simulations was to determine the behaviour of an isolated corrugation. The simulations in this section aim to investigate how the behaviour of the corrugation differs when it is embedded in a matrix material and ultimately how this geometry alters the stress-strain response of a composite compared to a simple straight reinforced

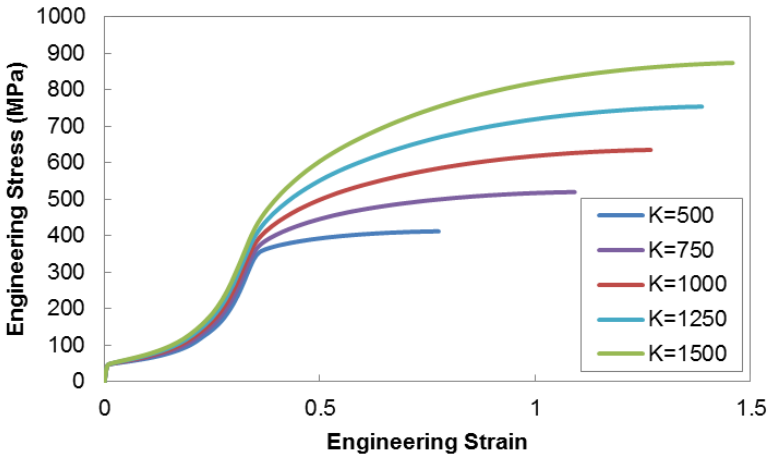


**Figure 3-29: FEM generated stress-strain curves of linear hardening corrugated samples with variable hardening coefficient, K, under plane strain tension.**

composite. In order to obtain a full understanding of how a corrugation affects the stress-strain response of a composite, a number of variables need to be explored. In this section a number of different groups of simulations will be presented, each of which aim to investigate a contributing aspect to the corrugation's effect. Similar to the isolated corrugation, these aspects can be divided into geometrical aspects and material aspects. However, in the case of the corrugation reinforced composites there is a lot more to consider in each of these areas, as we are now dealing with a two-component system and the relative properties of the two components will now need to be considered. Additional studies have been performed that look at the effect of the volume fraction and spatial arrangement of the reinforcement.

Although, there is a lot of data available to be extracted from simulations, the results presented in these sections will tend to focus on the overall stress-strain response of these composites. In the later chapters where the results are being discussed, some of this other data, including local stresses and strains, metrics of geometry evolution, and derivative properties such as work

hardening, will be explored in order to try and explain the phenomena and trends that are observed.

The stress-strain behaviour of the composite systems that are covered in this section will be presented in the form of calculated, engineering stress-strain curves. In the case of these composites being subject to plane strain tension, for each time increment of the simulation, the stress can be calculated by summing the horizontal reactionary forces along the fixed end of the composite and dividing that by the total height of the composite. This number should also be divided by the depth dimension, but for the plane strain loading geometry, a unit depth is assumed. The strain on the other hand can be calculated by dividing the horizontal displacement of the moving end of the composite at each time increment by the initial length of the composite. Together these two values provide a stress-strain curve. Each stress strain curve is terminated at the point where the ultimate tensile strength is reached and necking is initiated.

Before moving on to the parametric studies for the composite systems it is beneficial to first explore the general behaviour of composite materials with straight and corrugated reinforcements. To do this, four simulations were conducted of a sample system. All four simulations were of samples that were subject to plane strain tensile loading and had a length of 40mm and height of 5mm. One sample was pure copper, one sample was pure 4130 steel and the other two samples were composites of these materials with 20% volume fraction of 4130 steel reinforcements. The material parameters for copper and 4130 steel were given earlier in Table 3-2. The first composite had a straight reinforcement of 1mm thickness and the second a corrugated reinforcement with a height of 3mm, period of 8mm and thickness of 0.78mm.

First off, stress-strain curves from the simulations of the homogenous systems, 100% copper and 100% 4130 steel can be seen in Figure 3-30. In addition, this figure also shows the stress-strain curve of the straight reinforced composite. The two homogenous curves combined with the straight composite curve can be used as a simple example for understanding the effect of creating composite materials. The effect of the corrugated shape of the reinforcement can be seen by comparing the stress-strain curves from the simulations of the straight and corrugation reinforced composite, as seen in Figure 3-31. The purpose of this plot is to introduce the types of behaviour that can be achieved through the use of corrugation. Now that the general effect of a corrugated reinforcing architecture has been presented, it is of interest to explore the effect of the different geometric parameters.

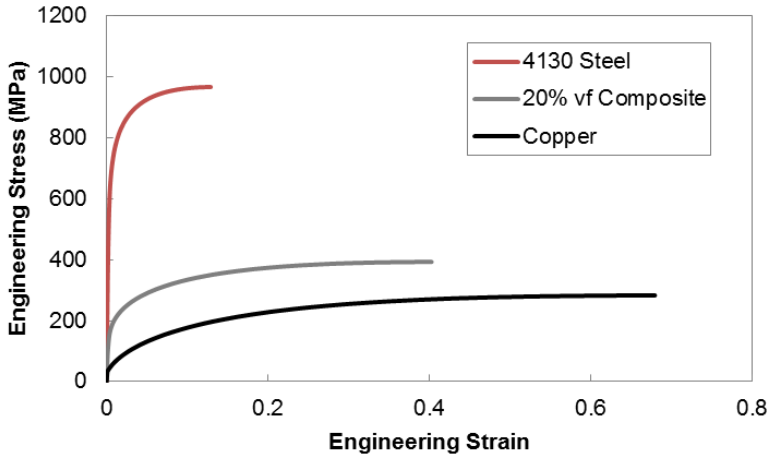


**Figure 3-30: FEM generated stress strain curves under plane strain tension loading of pure copper, pure 4130 steel and a copper-matrix, 20% volume fraction, straight reinforced composite.**

### *3.4.2.1 Effect of Geometry*

In this section, groups of simulations will be introduced that aim to look at the effect of different aspects of the reinforcement's geometry. These particular simulations all utilize the same combination of materials. The matrix material is copper and the reinforcement material is 4130

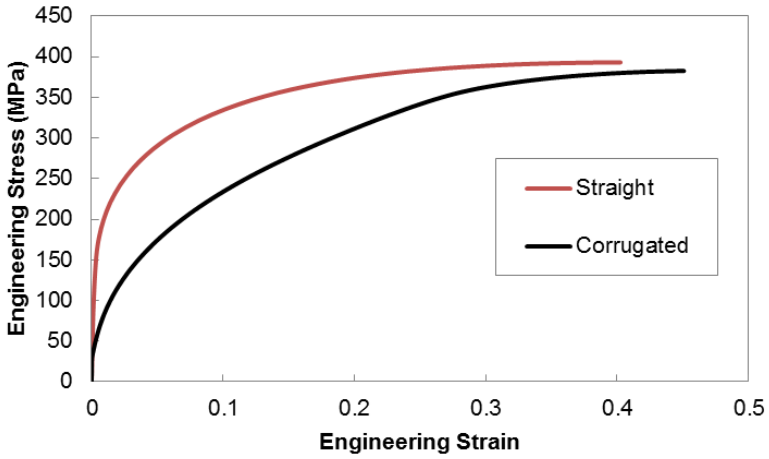


**Figure 3-31: FEM generated stress-strain curves of copper-matrix, 4130 steel reinforcement composites with `Straight` and `Corrugated` reinforcement geometries under plane strain tension.**

steel, both described by the same power-law hardening descriptions given above in Table 3-2 in the isolated corrugation section. These materials were selected as they were candidates that were explored in the experimental work on this project. In the following parametric studies the overall sample geometry was kept the same. Each sample was 40mm long, 5mm thick and had a unit thickness in the width direction (which was unimportant due to the plane strain nature of the simulation). Similar to the parametric studies performed for isolated corrugations, these studies will look at the effect of corrugation height, period, thickness and corrugation percentage on the stress-strain response of the composite materials.

#### 3.4.2.1.1 Effect of Corrugation Height

In this parametric study the values of the corrugation's height were varied between simulations, while the period and the volume fraction were kept constant. In order to maintain the same volume fraction between simulations, the thickness of the reinforcement was varied along with the corrugation height. The reinforcement thickness, $t_{rein}$, was determined by dividing the horizontal length of the corrugation, $L_{hor}$, by the arc length of the corrugation, $L_{arc}$, (i.e.

calculating the inverse of tortuosity) and multiplying this by the volume fraction of reinforcement, $v_f$, and by the total thickness of the composite, $t_{comp}$;

$$\boldsymbol{t_{rein} = \frac{L_{hor}}{L_{arc}}(v_f)(t_{comp})} \quad (3\text{-}3)$$

The arc length of the corrugation was calculated using Maple, assuming a sinusoidal corrugation, using the following standard arc-length equation;

$$\boldsymbol{L_{arc} = \int_0^{L_{hor}} \left( \sqrt{\left(\frac{\pi h}{P}\right)^2 \left(cos\left(\frac{2\pi}{P}x\right)\right)^2 + 1} \right) dx} \quad (3\text{-}4)$$

where h is the corrugation height and P is the corrugation period. The values of all of the geometric parameters used in this parametric study can be found in Table 3-12. In addition to the corrugated reinforcements, a simulation was also run that corresponded to a straight reinforcement of the same volume fraction. The stress-strain curves for this first parametric study can be found in Figure 3-32.

#### 3.4.2.1.2 Effect of Corrugation Period

In this parametric study the variable of interest was the period of the corrugation. From one simulation to the next the corrugation period was varied while keeping the corrugation height and volume fraction constant. Similar to the study on corrugation height, in order to maintain a constant reinforcement volume fraction, the thickness of the reinforcement was adjusted as the period was changed. Additionally, as the total length of the sample was fixed at 40mm the number of cycles changed as the period changed. A summary of the geometric parameters used in this study can be found in Table 3-13. Once again the results from these simulations are compared to those for a straight reinforced composite. The stress-strain curves corresponding to the simulations of interest can be found in Figure 3-33.

**Table 3-12: Values of geometric parameters of corrugations to investigate the effect of corrugation height in composites.**

| Simulation # | Period (mm) | Height (mm) | Reinforcement Thickness (mm) | Volume Fraction (%) | # of cycles | % Corrugated |
|---|---|---|---|---|---|---|
| 1 (straight) | NA | **NA** | 1 | 20 | 0 | 0 |
| 2 | 8 | **1** | 0.96 | 20 | 5 | 100 |
| 3 | 8 | **2** | 0.88 | 20 | 5 | 100 |
| 4 | 8 | **3** | 0.78 | 20 | 5 | 100 |
| 5 | 8 | **4** | 0.68 | 20 | 5 | 100 |

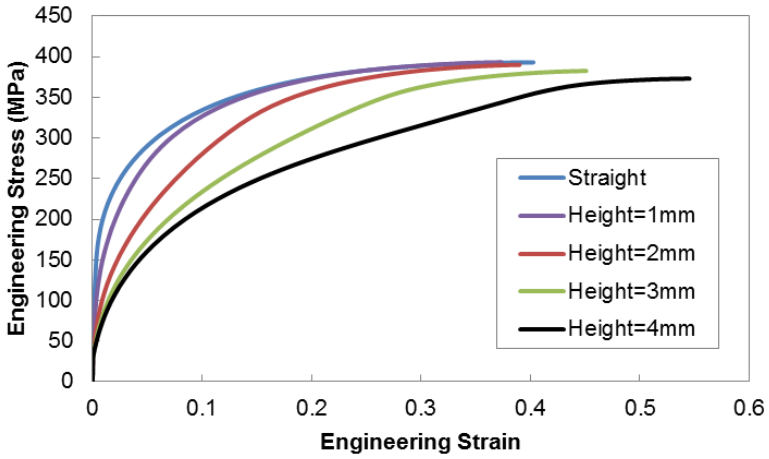


**Figure 3-32: FEM generated stress-strain curves of copper-matrix, 4130 steel reinforcement composites with variable corrugation height under plane strain tension.**

**Table 3-13: Values of geometric parameters of corrugations to investigate the effect of corrugation period in composites.**

| Simulation # | Period (mm) | Height (mm) | Reinforcement Thickness (mm) | Volume Fraction (%) | # of cycles | % Corrugated |
|---|---|---|---|---|---|---|
| 1 (straight) | **NA** | NA | 1 | 20 | 0 | 0 |
| 2 | **6.67** | 3 | 0.72 | 20 | 6 | 100 |
| 3 | **8** | 3 | 0.78 | 20 | 5 | 100 |
| 4 | **10** | 3 | 0.84 | 20 | 4 | 100 |
| 5 | **13.33** | 3 | 0.90 | 20 | 3 | 100 |
| 6 | **20** | 3 | 0.95 | 20 | 2 | 100 |
| 7 | **40** | 3 | 0.99 | 20 | 1 | 100 |

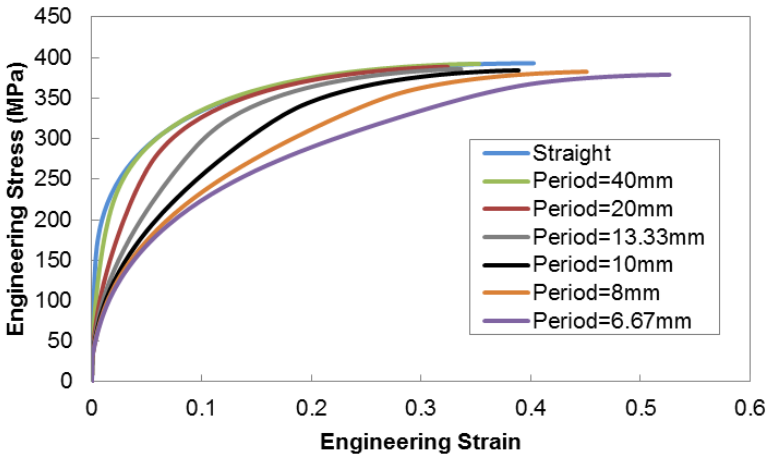


**Figure 3-33: FEM generated stress-strain curves of copper-matrix, 4130 steel reinforcement composites with variable corrugation period under plane strain tension.**

#### 3.4.2.1.3 Effect of Reinforcement Thickness

In this particular study the effect of the reinforcement thickness on the stress-strain response of the composite is studied. In these simulations the period and height of the corrugation are kept constant while the reinforcement thickness and subsequently the volume fraction are varied. In order to have a meaningful basis for comparison to the straight reinforcement geometry, additional simulations were run with thicknesses that corresponded to the appropriate volume fractions used in the corrugated composites. A summary of the geometric parameters used in this parametric study can be seen in Table 3-14. The stress-strain curves corresponding to the simulations of the straight reinforced composites are found in Figure 3-34 below. Also included in this plot is the case of pure copper in order to observe the trend in volume fraction.

Next, a series of stress-strain curves calculated from the results of simulations of the corrugation reinforced composites with variable reinforcement thicknesses can be seen in Figure 3-35. Again, the pure copper stress-strain curve is also included. Finally, for comparative purposes,

Figure 3-36 shows the stress-strain curves of the extreme cases of 10% and 40% volume fraction for both the straight and corrugated geometries.

**Table 3-14: Values of geometric parameters of corrugations to investigate the effect of corrugation thickness in composites.**

| Simulation # | Period (mm) | Height (mm) | Reinforcement Thickness (mm) | Volume Fraction (%) | # of cycles | % Corrugated |
|---|---|---|---|---|---|---|
| 1 (straight) | NA | NA | **0.5** | **10** | 0 | 0 |
| 2 (straight) | NA | NA | **1** | **20** | 0 | 0 |
| 3 (straight) | NA | NA | **1.5** | **30** | 0 | 0 |
| 4 (straight) | NA | NA | **2** | **40** | 0 | 0 |
| 5 | 8 | 3 | **0.39** | **10** | 5 | 100 |
| 6 | 8 | 3 | **0.78** | **20** | 5 | 100 |
| 7 | 8 | 3 | **1.17** | **30** | 5 | 100 |
| 8 | 8 | 3 | **1.56** | **40** | 5 | 100 |

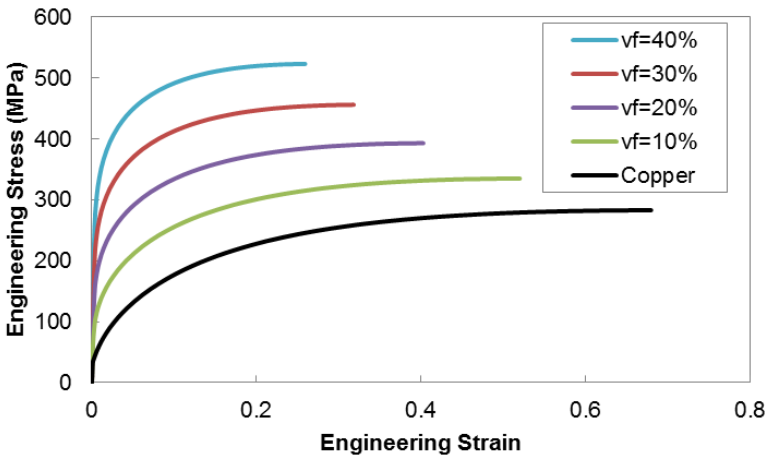


**Figure 3-34: FEM generated stress-strain curves of copper-matrix, straight 4130 steel reinforcement composites with variable reinforcement volume fraction, vf, and thickness under plane strain tension.**

### 3.4.2.1.4 Effect of Percentage Corrugated

This parametric study investigated the effect of the percentage of the reinforcement that is corrugated on the stress-strain response of the composite. In these simulations the corrugation

height, period and volume fraction are kept constant, while the percentage corrugated is varied. This variation in the percentage corrugated is accomplished by varying the number of cycles.

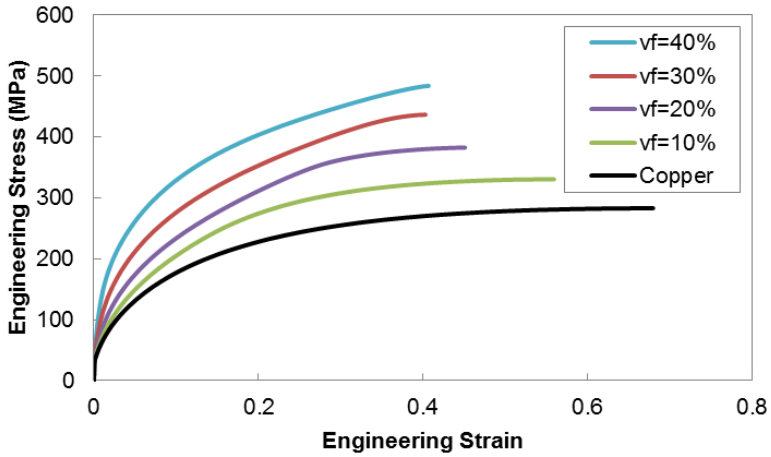


**Figure 3-35: FEM generated stress-strain curves of copper-matrix, corrugated 4130 steel reinforcement composites with variable reinforcement volume fraction, vf, and thickness (period=8mm, corrugation height=3mm) under plane strain tension.**

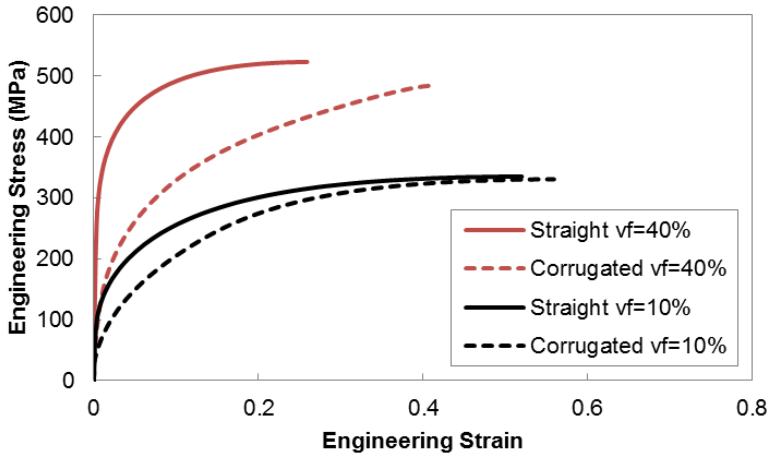


**Figure 3-36: FEM generated stress-strain curves of copper-matrix, 4130 steel reinforcement composites under plane strain tension. Both `Straight` and `Corrugated` composites are included at volume fractions, vf, of 10% and 40%.**

The percentage corrugated is reduced by having a larger portion of the corrugation possess a straight geometry. In order to maintain the volume fraction of the reinforcement, the thickness of the reinforcement is varied with the percentage corrugated. Similar to the above studies, a

comparison is made to a simulation of a straight reinforced composite. A summary of the geometric parameters for these simulations is found in Table 3-15. A series of stress-strain curves can be found in Figure 3-37 that correspond to the results of these simulations. Each of the curves models a composite that has a reinforcement that possesses a different ratio of corrugated reinforcement to straight reinforcement. The case that is labeled 0% corrugated is essentially just the straight reinforcement case with 20% volume fraction presented earlier.

**Table 3-15: Values of geometric parameters of corrugations to investigate the effect of corrugation percentage in composites.**

| Simulation # | Period (mm) | Height (mm) | Reinforcement Thickness (mm) | Volume Fraction (%) | # of cycles | % Corrugated |
|---|---|---|---|---|---|---|
| 1 (straight) | NA | NA | 1 | 20 | **0** | **0** |
| 2 | 8 | 3 | 0.96 | 20 | **1** | **20** |
| 3 | 8 | 3 | 0.91 | 20 | **2** | **40** |
| 4 | 8 | 3 | 0.87 | 20 | **3** | **60** |
| 5 | 8 | 3 | 0.82 | 20 | **4** | **80** |
| 6 | 8 | 3 | 0.78 | 20 | **5** | **100** |

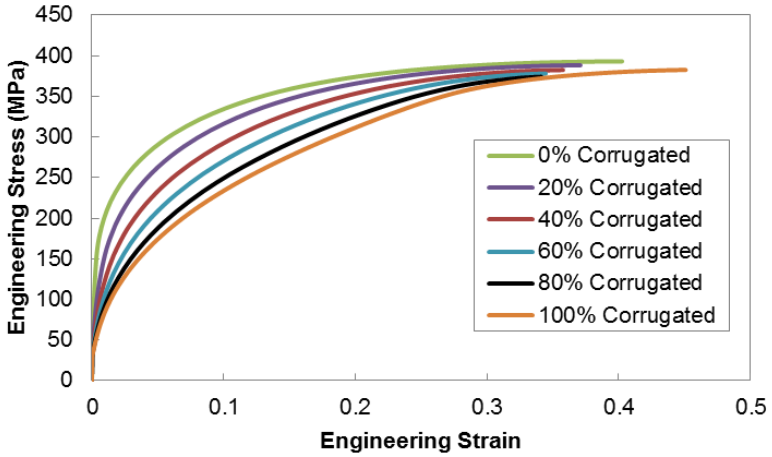


**Figure 3-37: FEM generated stress-strain curves of copper-matrix, corrugated 4130 steel reinforcement composites with variable corrugation percentage under plane strain tension.**

#### *3.4.2.2 Effect of Reinforcement Volume Fraction and Spacing*

The relative quantities of the components of a composite can play a large role in the ultimate mechanical response of the material. In the above section the geometry of a single reinforcement was changed in different ways and the effects of these changes on stress-strain behaviour was explored. This can be very informative; however, it can also be advantageous to examine the effect of the volume fraction of the reinforcement by changing the number of reinforcements that are present in a composite. In these cases, one can determine the effect of volume fraction of reinforcement by strictly changing the number of reinforcements used, while maintaining identical reinforcement geometries. In these situations it is not the geometry that is important but rather the relative amounts of the components and how they are arranged in space.

All of the simulations in this section have a constant overall sample geometry. Each sample has a length of 10mm, a total height of 5mm and unit depth. Due to the need for finer detail in the sample geometry the mesh size used in these simulations was reduced from 0.1mm to 0.05mm. The materials that are used in this study are also kept consistent from one simulation to the next. The matrix material is copper and the reinforcement material is 4130 steel, as described by the power-law hardening descriptions given in Table 3-2.

##### 3.4.2.2.1 Effect of Reinforcement Volume Fraction

The first round of simulations in this study uses a straight reinforcement geometry. Studying the behaviour of these straight reinforced composites provides a base-line for which the corrugated composites can be compared. In these simulations each individual reinforcement is 0.25mm thick and the total volume fraction of reinforcement is increased by increasing the number of reinforcements. Therefore, a single reinforcement corresponds to a volume fraction of 5%, two reinforcements correspond to a volume fraction of 10%, and so on. The simulations that contain

multiple reinforcements aim to try and space them evenly throughout the height of the sample. A summary of the geometries of the reinforcements used in these simulations can be found in Table 3-16.

**Table 3-16: Values of geometric parameters of reinforcements to investigate the effect of volume fraction on straight reinforced composites.**

| Simulation # | Reinforcement thickness (mm) | # of reinforcements | Reinforcement spacing (mm) | Reinforcement volume fraction |
|---|---|---|---|---|
| 1 (Copper) | NA | 0 | NA | 0% |
| 2 | 0.25 | 1 | NA | 5% |
| 3 | 0.25 | 2 | 1.67 | 10% |
| 4 | 0.25 | 3 | 1.25 | 15% |
| 5 | 0.25 | 4 | 1.25 | 20% |
| 6 | 0.25 | 5 | 1 | 25% |
| 7 | 0.25 | 6 | 0.8 | 30% |
| 8 | 0.25 | 7 | 0.7 | 35% |
| 9 | 0.25 | 8 | 0.5 | 40% |

The reinforcement spacing listed in this table is defined as the distance between the centerlines of adjacent reinforcements, not the thickness of matrix between the adjacent reinforcements. Additionally, a 100% copper simulation was also included in this study. The results of these simulations can be seen in the collection of stress-strain curves presented in Figure 3-38. Each curve corresponds to a single simulation with a different number of straight reinforcements.

In order to investigate the effect of volume fraction on the corrugation reinforced composites a number of compilations of simulations were completed, each focusing on one specific corrugation geometry. First off, a set of simulations that spans the range of volume fractions from 5% to 40% was conducted for each of the corrugation geometries outlined in Table 3-17. A study of these geometries will show how the effect of volume fraction on stress strain behaviour changes with variations in corrugation height. To be clear, for each geometry given in Table 3-17

eight simulations were performed, each with a different number of the same corrugated reinforcement. The details, with regards to the reinforcement spacing and number for each of these 8 simulations can be found in Table 3-18. The thickness of these corrugations was selected such that a single corrugation would correspond to a 5% volume fraction.The stress-strain curves from these simulations spanning the volume fractions from 0% to 40% for corrugation heights of 0.25mm (Figure 3-39), 0.5mm (Figure 3-40), 0.75mm (Figure 3-41), 1mm (Figure 3-42), and 1.25mm (Figure 3-43) can be seen below. By comparing these 5 plots it is possible to examine the effect of corrugation height on the trends related to reinforcement volume fraction.

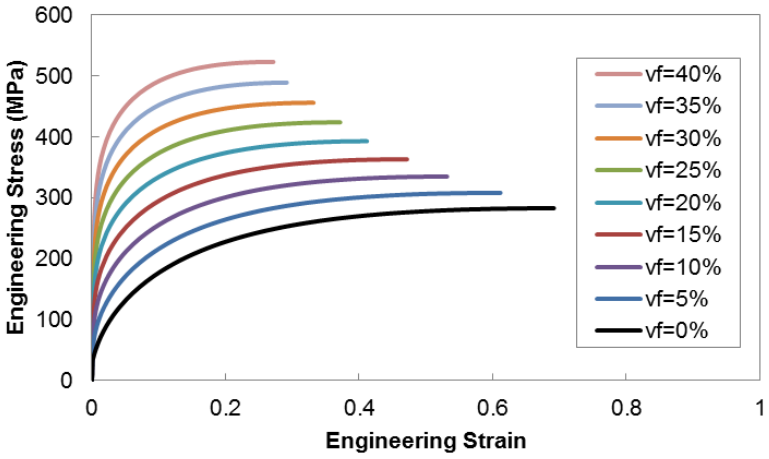


**Figure 3-38: FEM generated stress-strain curves of copper-matrix, straight 4130 steel reinforcement composites with variable numbers of reinforcements and hence volume fraction, vf, under plane strain tension.**

**Table 3-17: Geometric parameters of corrugations with variable height used in study of effect of reinforcement volume fraction.**

| Geometry # | Period (mm) | Height (mm) | Reinforcement thickness (mm) | # of cycles |
|---|---|---|---|---|
| 1 | 2 | **0.25** | 0.24 | 5 |
| 2 | 2 | **0.5** | 0.22 | 5 |
| 3 | 2 | **0.75** | 0.195 | 5 |
| 4 | 2 | **1** | 0.17 | 5 |
| 5 | 2 | **1.25** | 0.15 | 5 |

**Table 3-18: Values of reinforcement numbers and spacing used in simulations to investigate the effect of volume fraction on corrugation reinforced composites.**

| Simulation # | # of Reinforcements | Reinforcement spacing (mm) | Reinforcement volume fraction |
|---|---|---|---|
| 1 | 1 | NA | 5% |
| 2 | 2 | 1.67 | 10% |
| 3 | 3 | 1.25 | 15% |
| 4 | 4 | 1 | 20% |
| 5 | 5 | 0.8 | 25% |
| 6 | 6 | 0.7 | 30% |
| 7 | 7 | 0.6 | 35% |
| 8 | 8 | 0.5 | 40% |

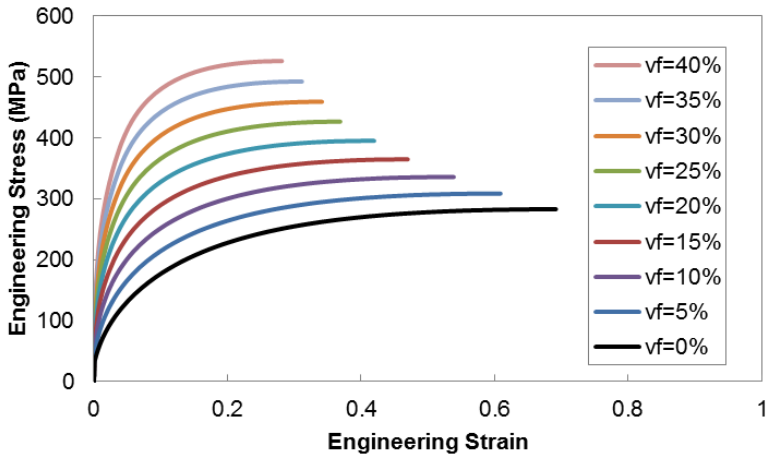


**Figure 3-39: FEM generated stress-strain curves of copper-matrix, corrugated 4130 steel reinforcement composites with variable numbers of reinforcements and hence volume fraction, vf, under plane strain tension. Corrugation height = 0.25mm.**

#### 3.4.2.2.2 Effect of Reinforcement Spacing

As mentioned above, it is not only important to know the effect of the relative quantities of components but also the effect of their location in space. To study this effect the same general geometry and material system that was used above to study the effect of volume fraction is used again. In this case the effect of reinforcement spacing is examined by selecting a given volume

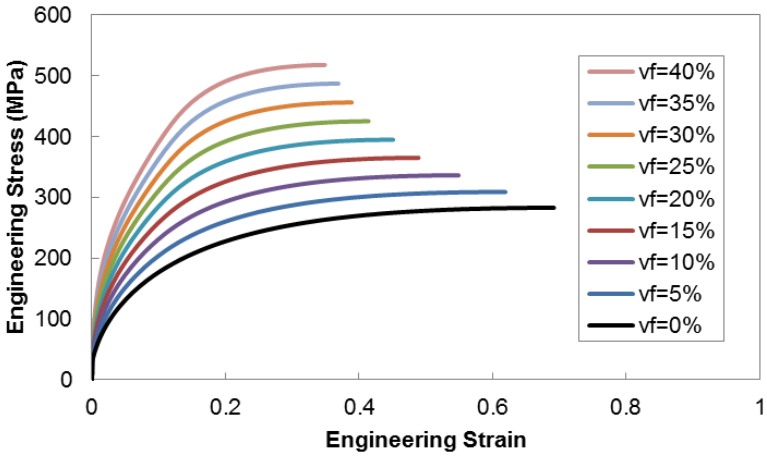


**Figure 3-40: FEM generated stress-strain curves of copper-matrix, corrugated 4130 steel reinforcement composites with variable numbers of reinforcements and hence volume fraction, vf, under plane strain tension. Corrugation height = 0.5mm.**

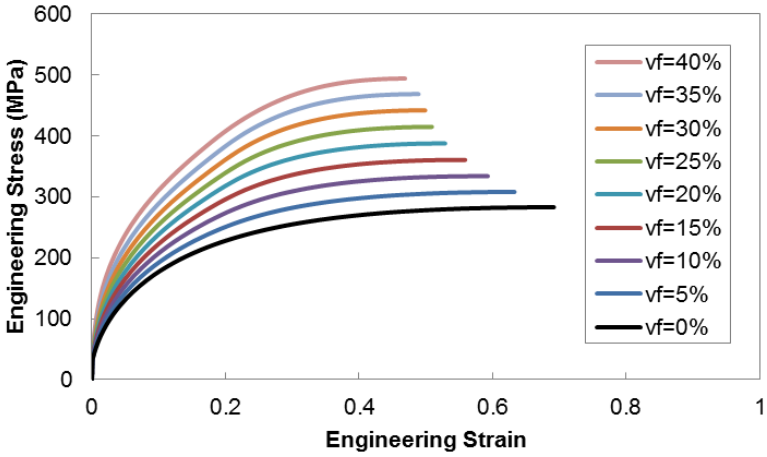


**Figure 3-41: FEM generated stress-strain curves of copper-matrix, corrugated 4130 steel reinforcement composites with variable numbers of reinforcements and hence volume fraction, vf, under plane strain tension. Corrugation height = 0.75mm.**

fraction, and hence number of reinforcements, and then varying the spacing between these reinforcements. A volume fraction of 25%, and therefore five individual reinforcements, was selected. The effect of the spacing of the reinforcements was investigated for a couple of representative geometries, including the straight reinforcement, and geometries # 3 and #5 from Table 3-17 above. For the straight reinforcements, four simulations were conducted with

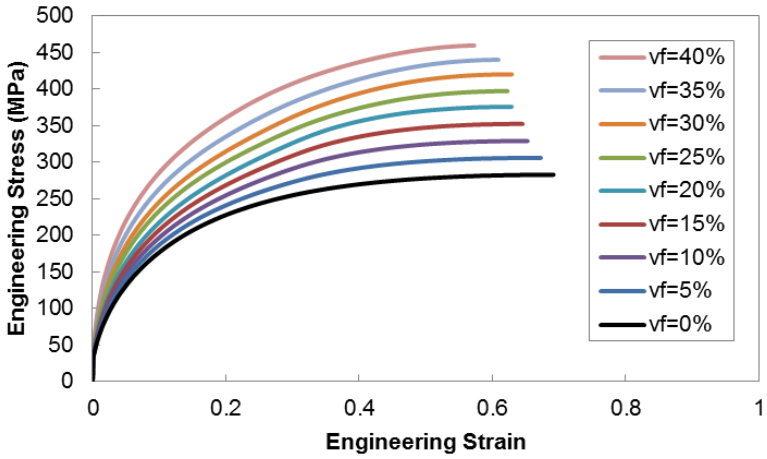


**Figure 3-42: FEM generated stress-strain curves of copper-matrix, corrugated 4130 steel reinforcement composites with variable numbers of reinforcements and hence volume fraction, vf, under plane strain tension. Corrugation height = 1mm.**

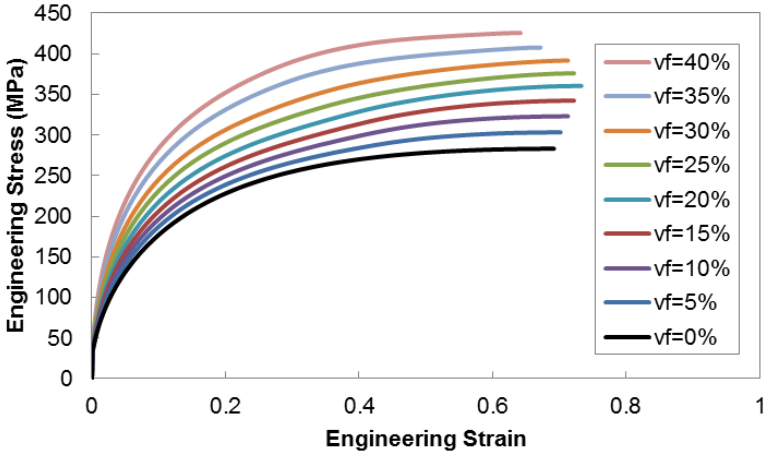


**Figure 3-43: FEM generated stress-strain curves of copper-matrix, corrugated 4130 steel reinforcement composites with variable numbers of reinforcements and hence volume fraction, vf, under plane strain tension. Corrugation height = 1.25mm.**

reinforcement spacing ranging from 0.4mm to 1.0mm. For reinforcements with geometry #3 (corrugation height of 0.75mm), five simulations were performed with reinforcement spacing that ranged between 0.5mm and 0.9mm. And finally, for the reinforcements with geometry #5 (corrugation height of 1.25mm), four simulations were conducted with reinforcement spacing varying from 0.5mm to 0.8mm. It should be noted that reinforcement spacing is defined as the

space between the centerline of one reinforcement and the centerline of an adjacent reinforcement. The range of spacing that was simulated for each geometry differs due to the fact that the more highly corrugated the geometry the larger the spacing needs to be between reinforcement centerlines to ensure no overlap between adjacent reinforcements.

The results showing this effect of reinforcement spacing were compiled for the three representative geometries. It was found that the spacing had no effect on the stress-strain response of the samples with the straight reinforcement or the corrugated reinforcement with the corrugation height of 0.75mm. Therefore, the stress-strain curves for these scenarios were not shown below. However, the spacing of the reinforcements did affect the stress-strain response of the corrugation reinforced composites with a corrugation height of 1.25mm as can be seen in the plot of stress-strain curves in Figure 3-44 below. Each of the stress-strain curves on this plot represents a different spacing between the reinforcements.

In addition to testing the effect of the spacing between reinforcements, the effect of the reinforcement alignment was also investigated. A study was performed in which the corrugations were shifted horizontally with respect to one another such that adjacent reinforcements were out of phase by a certain degree. The phase shifts that were tested were 0°, 45°, 90°, 135° and 180°. For each of these simulations four corrugated reinforcements were used, representing a volume fraction of 20%, with a vertical spacing between reinforcements of 1.25mm. Each of the reinforcements had a period of 2mm and a corrugation height of 0.75mm. The stress-strain curves calculated from these simulations were almost identical to one another suggesting a minimal effect of a phase shift.

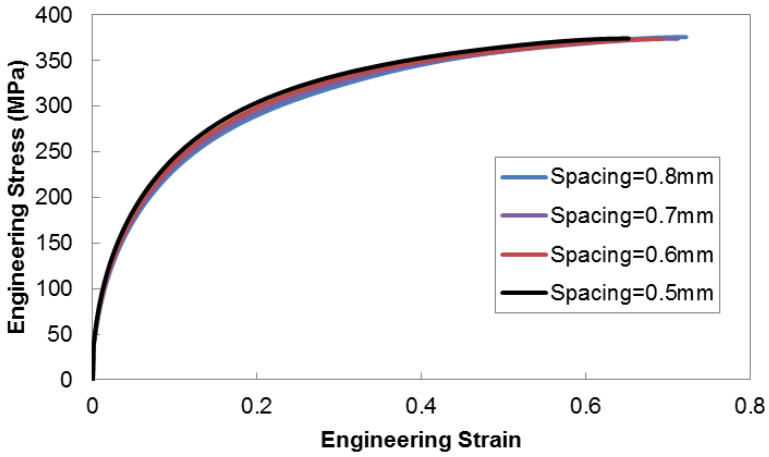


**Figure 3-44: FEM generated stress-strain curves of copper-matrix, corrugated 4130 steel reinforcement composites with variable spacing between reinforcements under plane strain tension. Corrugation height = 1.25mm.**

#### *3.4.2.3 Effect of Materials*

The purpose of this section is to introduce the details of the simulations that were conducted whose goal was to investigate the impact of using different matrix and reinforcement materials on the stress-strain response of the composite materials. Instead of just simulating random combinations of real materials, it was decided that a more systematic approach that varied parameters used to approximate the mechanical properties of these materials would be more informative. Both linear hardening and power law hardening approximations were used for these materials. With this approach in mind, a number parametric studies were performed in which for each study the effect of one of the parameters of these material models was determined by independently varying that material parameter. As one of the focuses of this research is comparing the mechanical behaviour of corrugated composite architectures to those of simpler straight composite architectures, each simulation of a corrugation reinforced composite is partnered with that of a straight reinforced composite that is comprised of the same component materials. Since these particular studies focus on the effect of the materials, the corrugated and straight geometries were kept identical from one simulation to another. To begin with, the

simpler linear hardening materials will be explored, followed by the more complex power-law hardening materials.

#### 3.4.2.3.1 Geometry of Interest

For the following studies that explore the effect of the material parameters, the samples will all have the following dimensions: 40mm length, 5mm thickness, unit thickness depth. The depth of the sample is unimportant due to the plane strain tensile nature of the loading. For each combination of materials that is explored both a corrugation reinforced composite and a straight reinforced composite are simulated. Both of these composites have a reinforcement volume fraction of 20%. The corrugated reinforcements possess a period of 8mm, a corrugation height of 3mm and a reinforcement thickness of 0.78mm. The straight reinforcements are 1mm thick.

#### 3.4.2.3.2 Linear Hardening Materials

In order to gain an understanding of the effect of the component materials, simple linear hardening materials are used first. The elastic behaviour of these materials is described by the Young's Modulus and Poisson's ratio. For all of these simulations the matrix has the elastic properties of copper with E=115GPa and ν=0.33 and the reinforcement has the elastic properties of steel with E=207GPa and ν=0.3. The plastic behaviour of these materials is described using a yield strength, $\sigma_{YS}$, and hardening rate, K, according to the following expression; $\sigma = \sigma_{YS} + K\varepsilon$. The effect of the yield strength and hardening rate on the stress-strain response of both matrix and reinforcement will be examined.

The first two parametric studies focus on the effect of the matrix material, starting with the matrix yield strength. The values of the properties of both the matrix and reinforcement for these simulations can be seen in Table 3-19. As is evident the matrix yield strength is varied from 50-

400MPa while all the other properties are kept constant. The stress-strain curves for the straight reinforcement geometry are found in Figure 3-45 and can be compared to those for the corrugation reinforced geometry, as seen in Figure 3-46.

**Table 3-19: Material parameters of linear hardening components with variable matrix yield strength.**

| Simulation # | Matrix Yield Strength (MPa) | Matrix Hardening Rate, K (MPa) | Reinforcement Yield Strength (MPa) | Reinforcement Hardening Rate, K (MPa) |
|---|---|---|---|---|
| 1 | **50** | 200 | 600 | 500 |
| 2 | **100** | 200 | 600 | 500 |
| 3 | **200** | 200 | 600 | 500 |
| 4 | **300** | 200 | 600 | 500 |
| 5 | **400** | 200 | 600 | 500 |

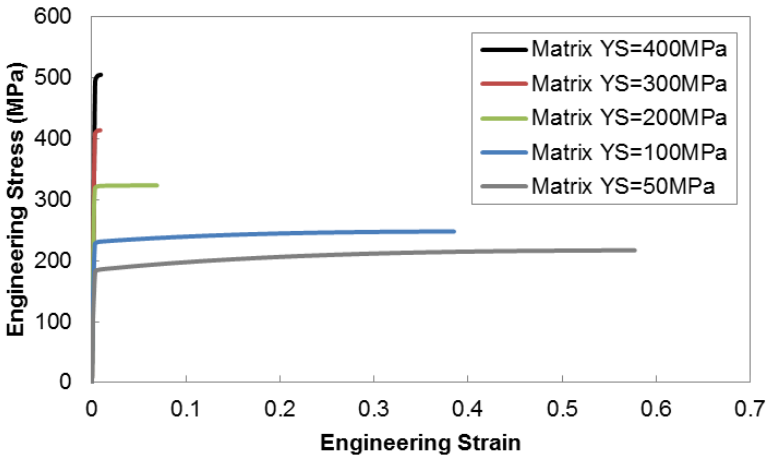


**Figure 3-45: FEM generated stress-strain curves of straight reinforced composites with linear hardening component materials under plane strain tension. Each curve corresponds to a different matrix yield strength (YS).**

The next set of simulations explored the effect of the matrix hardening rate on the stress-strain response of corrugated and straight composites. The values of the material properties used for both components in this study are shown below in Table 3-20. In this case the matrix hardening rate, K, is varied from 100-600MPa while all the other parameters are kept constant. The stress-

strain curves calculated from the simulation for the straight reinforcement geometry and the corrugated reinforcement geometry are found in Figure 3-47 and Figure 3-48, respectively.

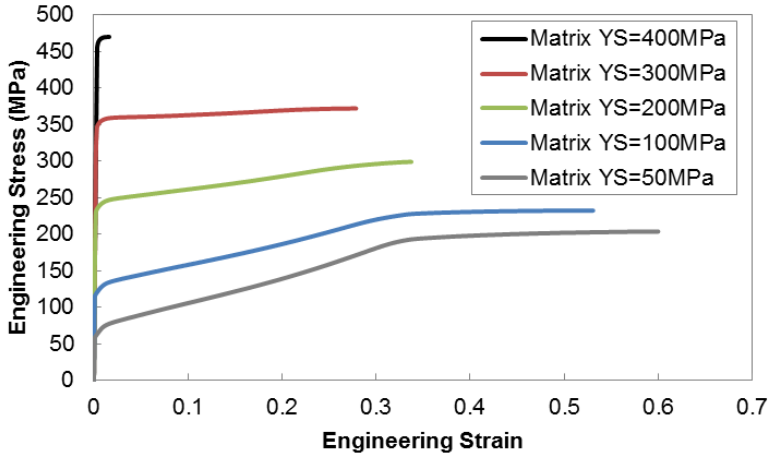


**Figure 3-46: FEM generated stress-strain curves of corrugation reinforced composites with linear hardening component materials under plane strain tension. Each curve corresponds to a different matrix yield strength (YS).**

**Table 3-20: Material parameters of linear hardening components with variable matrix hardening rate.**

| Simulation # | Matrix Yield Strength (MPa) | Matrix Hardening Rate, K (MPa) | Reinforcement Yield Strength (MPa) | Reinforcement Hardening Rate, K (MPa) |
|---|---|---|---|---|
| 1 | 300 | **100** | 600 | 500 |
| 2 | 300 | **200** | 600 | 500 |
| 3 | 300 | **300** | 600 | 500 |
| 4 | 300 | **400** | 600 | 500 |
| 4 | 300 | **600** | 600 | 500 |

The next set of parametric studies focus on the influence of the reinforcement material. The first of these studies investigates the effect of the yield strength of the reinforcement. The material parameter values for this set of simulations are found in Table 3-21 below. In this case the reinforcement yield strength ranges in value from 150-1800MPa while all other material parameters are kept constant. The stress-strain curves corresponding to this study are shown in

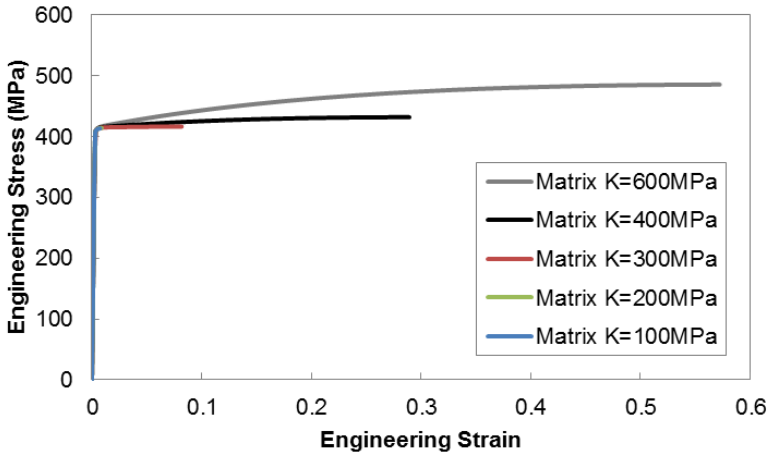


**Figure 3-47: FEM generated stress-strain curves of straight reinforced composites with linear hardening component materials under plane strain tension. Each curve corresponds to a different matrix hardening rate (K).**

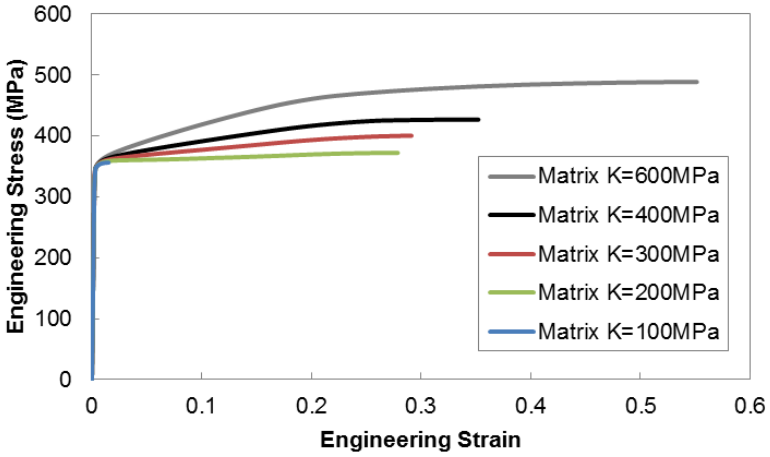


**Figure 3-48: FEM generated stress-strain curves of corrugation reinforced composites with linear hardening component materials under plane strain tension. Each curve corresponds to a different matrix hardening rate (K).**

Figure 3-49 for the straight composite geometry and in Figure 3-50 for the corrugated composite geometry.

This last parametric study focuses on the effect of the reinforcement hardening rate. The values of the material parameters used in this set of simulations can be found in Table 3-22 below in which the reinforcement hardening rate is varied from 500-5000MPa while all other material

**Table 3-21: Material parameters of linear hardening components with variable reinforcement yield strength.**

| Simulation # | Matrix Yield Strength (MPa) | Matrix Hardening Rate, K (MPa) | Reinforcement Yield Strength (MPa) | Reinforcement Hardening Rate, K (MPa) |
|---|---|---|---|---|
| 1 | 300 | 300 | **150** | 500 |
| 2 | 300 | 300 | **300** | 500 |
| 3 | 300 | 300 | **450** | 500 |
| 4 | 300 | 300 | **600** | 500 |
| 5 | 300 | 300 | **750** | 500 |
| 6 | 300 | 300 | **900** | 500 |
| 7 | 300 | 300 | **1200** | 500 |
| 8 | 300 | 300 | **1500** | 500 |
| 9 | 300 | 300 | **1800** | 500 |

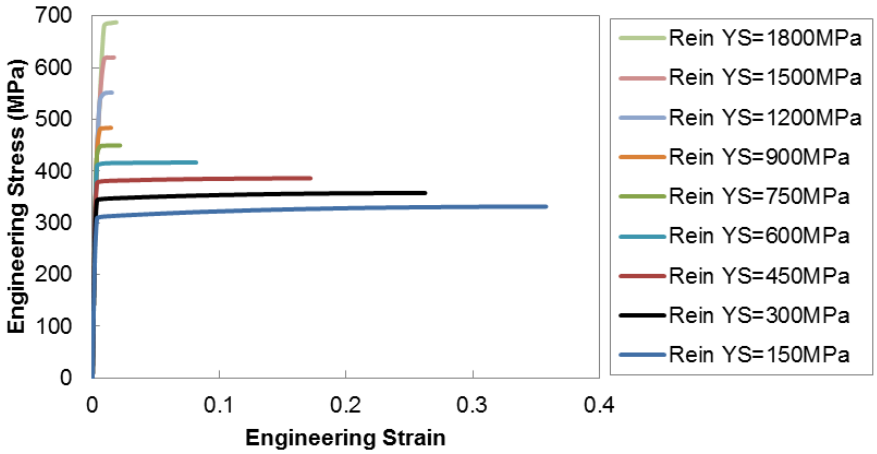


**Figure 3-49: FEM generated stress-strain curves of straight reinforced composites with linear hardening component materials under plane strain tension. Each curve corresponds to a different reinforcement yield strength (YS).**

parameters are kept constant. Figure 3-51 shows the stress-strain curves for the straight reinforced composites and Figure 3-52 shows those for the corrugated reinforced composites.

#### 3.4.2.3.3 Power-Law Hardening Materials

Due to the decreasing rate of hardening experienced by most metals, it is more realistic to model the component materials using a hardening model that captures this decreasing rate of hardening

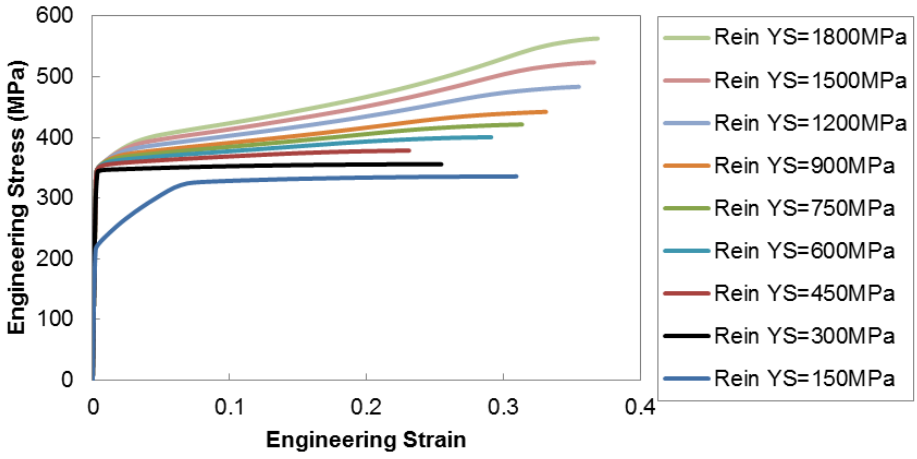


**Figure 3-50: FEM generated stress-strain curves of corrugation reinforced composites with linear hardening component materials under plane strain tension. Each curve corresponds to a different reinforcement yield strength (YS).**

**Table 3-22: Material parameters of linear hardening components with variable reinforcement hardening rate.**

| Simulation # | Matrix Yield Strength (MPa) | Matrix Hardening Rate, K (MPa) | Reinforcement Yield Strength (MPa) | Reinforcement Hardening Rate, K (MPa) |
|---|---|---|---|---|
| 1 | 300 | 100 | 600 | **500** |
| 2 | 300 | 100 | 600 | **1000** |
| 3 | 300 | 100 | 600 | **1500** |
| 4 | 300 | 100 | 600 | **2000** |
| 5 | 300 | 100 | 600 | **2500** |
| 6 | 300 | 100 | 600 | **3000** |
| 7 | 300 | 100 | 600 | **4000** |
| 8 | 300 | 100 | 600 | **5000** |

behaviour. For that reason a number of sets of simulations were conducted that instead used power law hardening materials. A material whose plastic behaviour is described by a power-law hardening model is defined by the expression, $\sigma=K\varepsilon^{n}$, where K is the hardening coefficient and n is the hardening rate. The onset of this plastic behaviour is determined by the yield strength ($\sigma_{YS}$) of the material, which must also be provided to ensure a complete model.

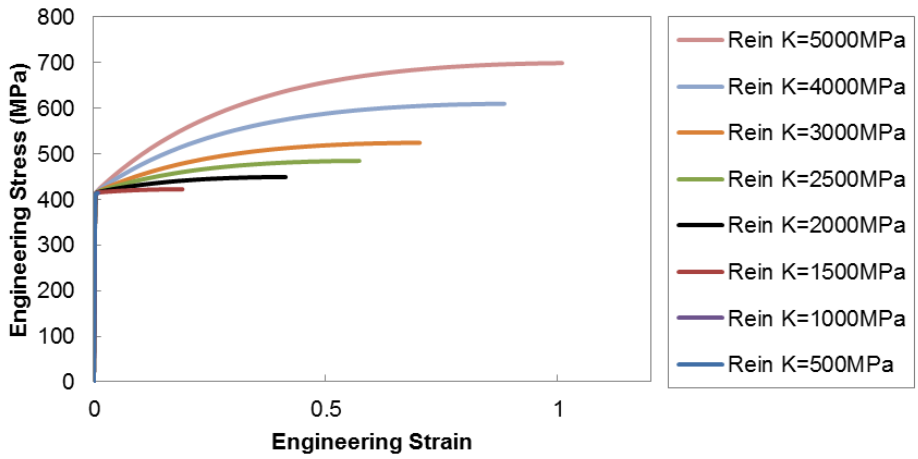


**Figure 3-51: FEM generated stress-strain curves of straight reinforced composites with linear hardening component materials under plane strain tension. Each curve corresponds to a different reinforcement hardening rate (K).**

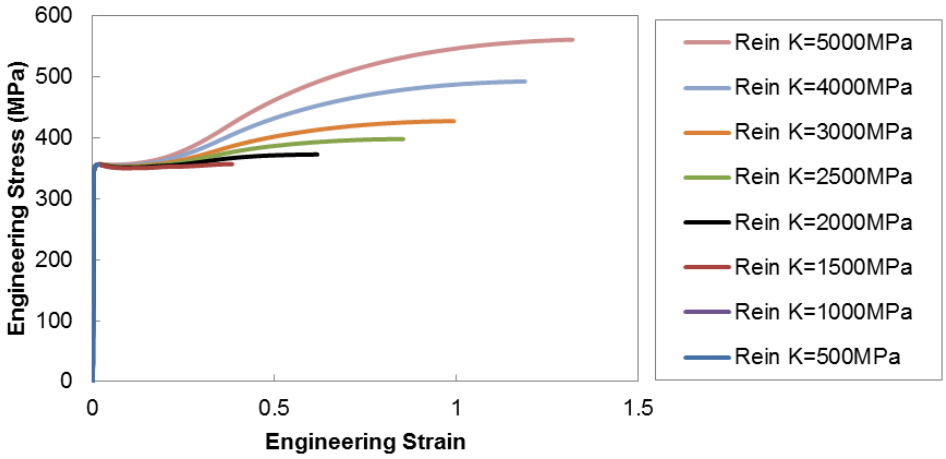


**Figure 3-52: FEM generated stress-strain curves of corrugation reinforced composites with linear hardening component materials under plane strain tension. Each curve corresponds to a different reinforcement hardening rate (K).**

There are six sets of simulations presented below. Each of these sets of simulations will focus on the effect of one parameter that is used in the modeling of the plastic behaviour of one of the components. The base case that has been selected for these simulations is a copper matrix ($\sigma_{YS}$=25MPa, K=540MPa, n=0.53) and a 4130 steel reinforcement ($\sigma_{YS}$=350MPa, K=1200MPa,

n=0.12). The elastic behaviour of the two components is also included in the material definitions with E=115GPa and ν=0.33 for copper and E=207GPa and ν=0.3 for 4130 steel.

The first three sets of simulations will focus on the effect of the matrix material on the stress-strain response of these composites. To begin with the effect of the matrix hardening coefficient, K, on both straight and corrugation reinforced composites is considered. The effect of the hardening coefficient of the matrix was explored using simulations that inputted the values of the material parameters as seen in Table 3-23 below. In this set of simulations the matrix hardening coefficient ranged in value from 250-1000MPa, while the rest of the material parameters of both the matrix and reinforcement were kept constant. The stress-strain curves corresponding to the simulations of the straight reinforcement geometry are shown first in Figure 3-53, followed by those for the corrugation reinforcement geometry in Figure 3-54. Each of the curves in these plots corresponds to a unique value of the matrix hardening coefficient, K.

**Table 3-23: Material parameters of power-law hardening components with variable matrix hardening coefficient, K.**

| | *Matrix* | | | *Reinforcement* | | |
|---|---|---|---|---|---|---|
| **Simulation #** | **Yield Strength (MPa)** | **Hardening Coefficient, K (MPa)** | **Hardening Exponent, n** | **Yield Strength (MPa)** | **Hardening Coefficient, K (MPa)** | **Hardening Exponent, n** |
| 1 | 25 | **250** | 0.53 | 350 | 1200 | 0.12 |
| 2 | 25 | **540** | 0.53 | 350 | 1200 | 0.12 |
| 3 | 25 | **750** | 0.53 | 350 | 1200 | 0.12 |
| 4 | 25 | **1000** | 0.53 | 350 | 1200 | 0.12 |

The next set of simulations focused on the effect of the matrix hardening exponent, n, on the stress-strain response of these composites. The values of the material parameters used in this parametric study are summarized below in Table 3-24 with a total of six simulations completed.

In this case the matrix hardening exponent was varied from 0.06-0.53 while the rest of the parameters were maintained constant between simulations. The stress-strain curves corresponding to the simulations investigating the matrix hardening exponent are seen in Figure 3-55 below for the straight geometry and in Figure 3-56 for the corrugated geometry.

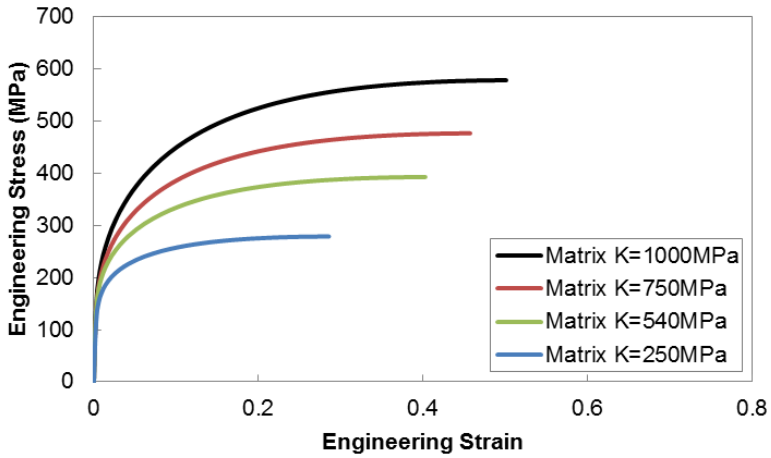


**Figure 3-53: FEM generated stress-strain curves of straight reinforced composites with power-law hardening component materials under plane strain tension. Each curve corresponds to a different matrix hardening coefficient (K).**

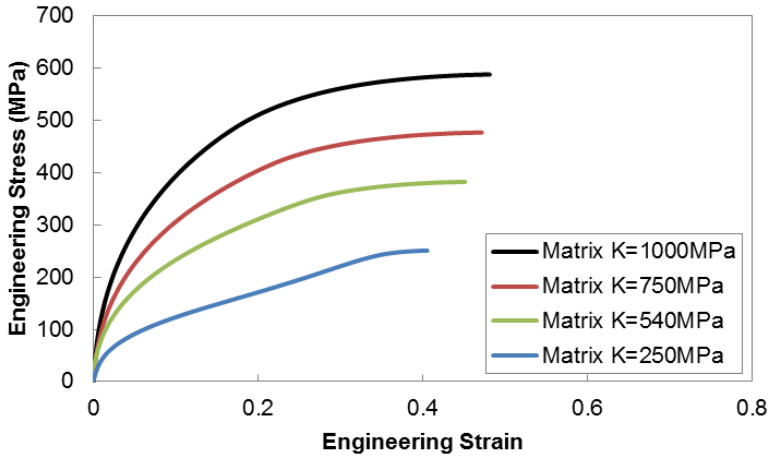


**Figure 3-54: FEM generated stress-strain curves of corrugation reinforced composites with power-law hardening component materials under plane strain tension. Each curve corresponds to a different matrix hardening coefficient (K).**

**Table 3-24: Material parameters of power-law hardening components with variable matrix hardening exponent, n.**

| | *Matrix* | | | *Reinforcement* | | |
|---|---|---|---|---|---|---|
| **Simulation #** | **Yield Strength (MPa)** | **Hardening Coefficient, K (MPa)** | **Hardening Exponent, n** | **Yield Strength (MPa)** | **Hardening Coefficient, K (MPa)** | **Hardening Exponent, n** |
| 1 | 25 | 540 | **0.06** | 350 | 1200 | 0.12 |
| 2 | 25 | 540 | **0.12** | 350 | 1200 | 0.12 |
| 3 | 25 | 540 | **0.25** | 350 | 1200 | 0.12 |
| 4 | 25 | 540 | **0.32** | 350 | 1200 | 0.12 |
| 5 | 25 | 540 | **0.40** | 350 | 1200 | 0.12 |
| 6 | 25 | 540 | **0.53** | 350 | 1200 | 0.12 |

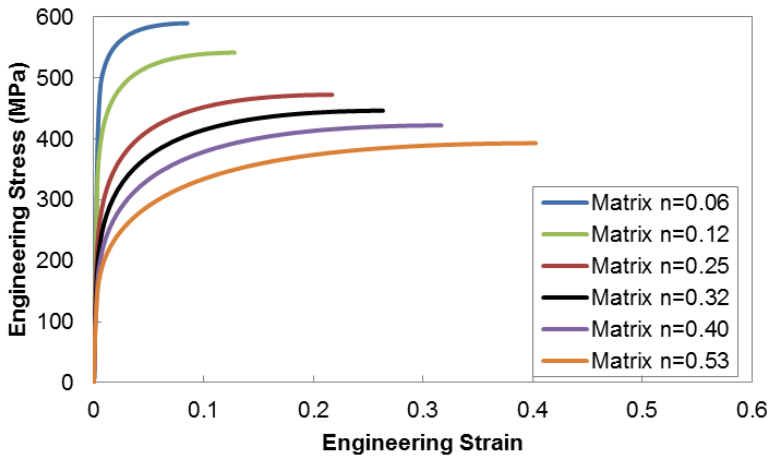


**Figure 3-55: FEM generated stress-strain curves of straight reinforced composites with power-law hardening component materials under plane strain tension. Each curve corresponds to a different matrix hardening exponent (n).**

The final parameter of the matrix material that was explored was the matrix yield strength. The values of the material parameters for both the matrix and reinforcement components that were used in this parametric study are shown in Table 3-25 with the matrix yield strength varying from 50-200MPa while all other parameters are kept constant. It should be noted in this case that the other parameters for the matrix material are not those seen for copper, but rather were selected to ensure both that the matrix was still softer than the reinforcement and that there was

not a drop in stress after the yield stress was reached when the plastic strain was incremented forward by a value of 0.001. In order for the FEM simulation to be successful, it is necessary that as the value of strain is increased in the material model, the stress must always increase as well. The stress-strain curves of both the straight and corrugation reinforced composites were found to be insensitive to the value of matrix yield strength and thus were not included below.

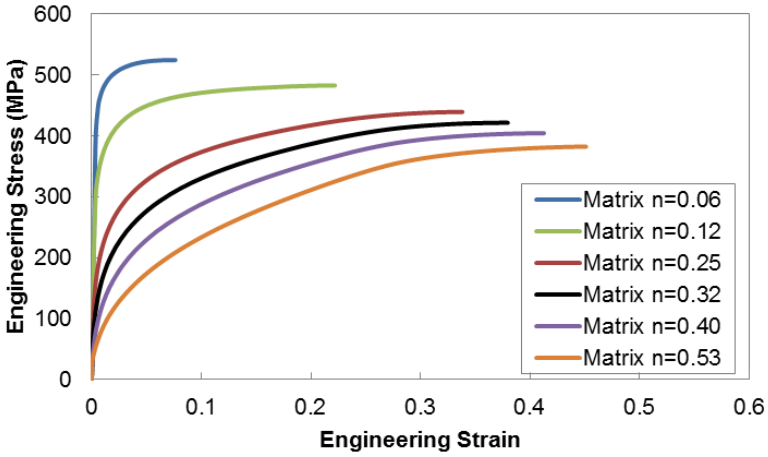


**Figure 3-56: FEM generated stress-strain curves of corrugation reinforced composites with power-law hardening component materials under plane strain tension. Each curve corresponds to a different matrix hardening exponent (n).**

**Table 3-25: Material parameters of power-law hardening components with variable matrix yield strength.**

| | *Matrix* | | | *Reinforcement* | | |
|---|---|---|---|---|---|---|
| **Simulation #** | **Yield Strength (MPa)** | **Hardening Coefficient, K (MPa)** | **Hardening Exponent, n** | **Yield Strength (MPa)** | **Hardening Coefficient, K (MPa)** | **Hardening Exponent, n** |
| 1 | **50** | 800 | 0.2 | 350 | 1200 | 0.12 |
| 2 | **100** | 800 | 0.2 | 350 | 1200 | 0.12 |
| 3 | **150** | 800 | 0.2 | 350 | 1200 | 0.12 |
| 4 | **200** | 800 | 0.2 | 350 | 1200 | 0.12 |

The next three sets of simulations moved the focus onto the reinforcement material to determine its effect on the stress-strain behaviour of the straight and corrugation reinforced composites.

Similar to those sets of simulations above for the matrix, these sets of simulations also looked at the effect of the yield strength, hardening coefficient and the hardening exponent. To begin with, a set of simulations were conducted that explored the effect of the reinforcement hardening coefficient, K. The values of the material parameters used in this set of simulations are found in Table 3-26 below. As is evident, the hardening coefficient of the matrix is varied in value from 900-1800MPa while the other reinforcement and matrix parameters are kept constant. The stress-strain curves that were generated for the straight and corrugated reinforcement geometries are shown below in Figure 3-57 and Figure 3-58, respectively.

**Table 3-26: Material parameters of power-law hardening materials with variable reinforcement hardening coefficient, K.**

| | *Matrix* | | | *Reinforcement* | | |
|---|---|---|---|---|---|---|
| **Simulation #** | **Yield Strength (MPa)** | **Hardening Coefficient, K (MPa)** | **Hardening Exponent, n** | **Yield Strength (MPa)** | **Hardening Coefficient, K (MPa)** | **Hardening Exponent, n** |
| 1 | 25 | 540 | 0.53 | 350 | **900** | 0.12 |
| 2 | 25 | 540 | 0.53 | 350 | **1200** | 0.12 |
| 3 | 25 | 540 | 0.53 | 350 | **1500** | 0.12 |
| 4 | 25 | 540 | 0.53 | 350 | **1800** | 0.12 |

The next set of simulations instead explores the effect of the reinforcement hardening exponent, n, on the stress-strain response of the composite materials. In this scenario the values of the hardening exponent of the reinforcement are varied from 0.05-0.35 while all else is kept constant, as summarized in Table 3-27. It should be noted that for similar reasons as for the changes made above for the study of matrix yield strength, the reinforcement yield strength in this study is dropped from that seen for 4130 steel at 350MPa to 100MPa, in order to avoid a drop in stress after yielding across the entire span of reinforcement hardening exponents being tested. The sets of stress-strain curves seen in Figure 3-59 and Figure 3-60 below for the straight

reinforcement and corrugated reinforcement composites, respectively, demonstrate the effect of the reinforcement's hardening exponent on the stress-strain response of these composites.

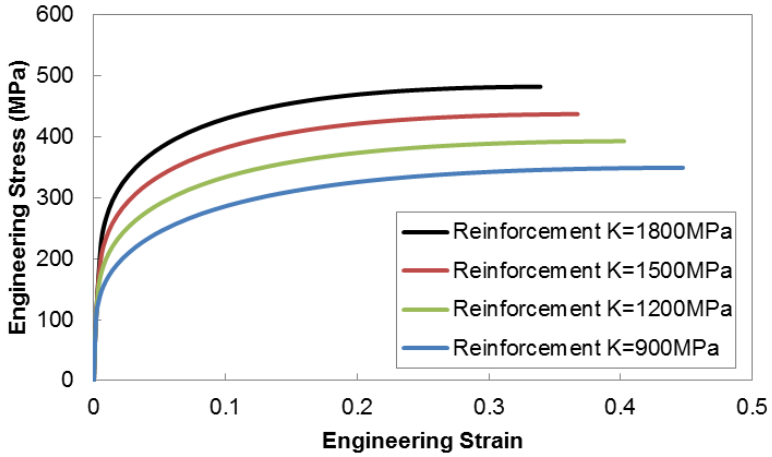


**Figure 3-57: FEM generated stress-strain curves of straight reinforced composites with power-law hardening component materials under plane strain tension. Each curve corresponds to a different reinforcement hardening coefficient (K).**

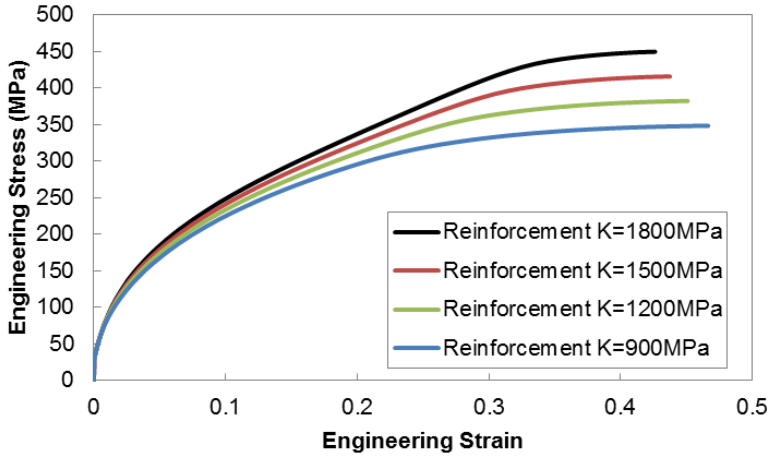


**Figure 3-58: FEM generated stress-strain curves of corrugation reinforced composites with power-law hardening component materials under plane strain tension. Each curve corresponds to a different reinforcement hardening coefficient (K).**

The final set of simulations that explores the reinforcing material focuses on the reinforcement yield strength. The values of the parameters used in this parametric study are highlighted in Table 3-28. In this case the reinforcement yield strength is varied from 100-500MPa between

simulations while the rest of the material parameters for both components are kept constant. These simulations led to the sets of stress strain curves that were unaffected by the values of reinforcement yield strength and thus were not included below.

**Table 3-27: Material parameters of power-law hardening materials with variable reinforcement hardening exponent, n.**

| | *Matrix* | | | *Reinforcement* | | |
|---|---|---|---|---|---|---|
| **Simulation #** | **Yield Strength (MPa)** | **Hardening Coefficient, K (MPa)** | **Hardening Exponent, n** | **Yield Strength (MPa)** | **Hardening Coefficient, K (MPa)** | **Hardening Exponent, n** |
| 1 | 25 | 540 | 0.53 | 100 | 1200 | **0.05** |
| 2 | 25 | 540 | 0.53 | 100 | 1200 | **0.12** |
| 3 | 25 | 540 | 0.53 | 100 | 1200 | **0.15** |
| 4 | 25 | 540 | 0.53 | 100 | 1200 | **0.25** |
| 5 | 25 | 540 | 0.53 | 100 | 1200 | **0.35** |

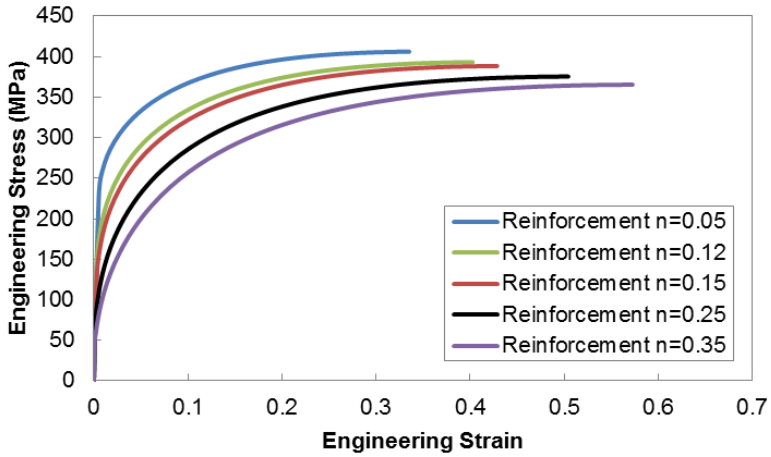


**Figure 3-59: FEM generated stress-strain curves of straight reinforced composites with power-law hardening component materials under plane strain tension. Each curve corresponds to a different reinforcement hardening exponent (n).**

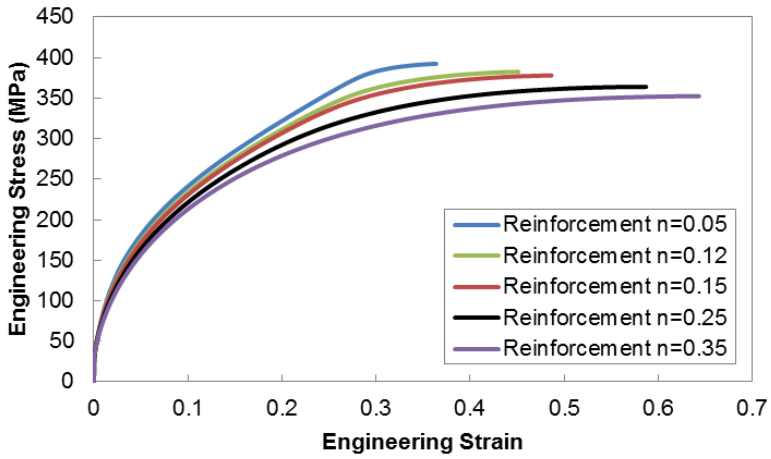


**Figure 3-60: FEM generated stress-strain curves of corrugation reinforced composites with power-law hardening materials under plane strain tension. Each curve corresponds to a different reinforcement hardening exponent (n).**

**Table 3-28: Material parameters of power-law hardening components with variable reinforcement yield strength.**

| | *Matrix* | | | *Reinforcement* | | |
|---|---|---|---|---|---|---|
| **Simulation #** | **Yield Strength (MPa)** | **Hardening Coefficient, K (MPa)** | **Hardening Exponent, n** | **Yield Strength (MPa)** | **Hardening Coefficient, K (MPa)** | **Hardening Exponent, n** |
| 1 | 25 | 540 | 0.53 | **100** | 1200 | 0.12 |
| 2 | 25 | 540 | 0.53 | **200** | 1200 | 0.12 |
| 3 | 25 | 540 | 0.53 | **300** | 1200 | 0.12 |
| 4 | 25 | 540 | 0.53 | **350** | 1200 | 0.12 |
| 5 | 25 | 540 | 0.53 | **400** | 1200 | 0.12 |
| 6 | 25 | 540 | 0.53 | **500** | 1200 | 0.12 |

# 4 Discussion

## 4.1 Introduction

This chapter will present a discussion and analysis of the modeling results that were reported in the previous chapter. This will involve identifying trends in the effects of properties and developing a framework for predicting the behaviour of corrugation reinforced composite materials. The ultimate purpose of this section will be to tie together the results in such a way as to gain a general understanding of the conditions for which the use of a corrugated architecture is beneficial. This chapter will be divided into sections, beginning with a focus on isolated corrugations, followed by that of corrugation reinforced composites.

## 4.2 Isolated Corrugation in Plane Strain Tension

### 4.2.1 Generalized Behaviour of Isolated Corrugation

To begin with, it is of some benefit to discuss the generalized behaviour of an isolated corrugation subject to plane strain tension. This general behaviour is exemplified by the FEM simulation results of the isolated copper corrugation whose shape, stress and strain maps were displayed in Figure 3-10-Figure 3-15. It is important to first clarify the general behaviour of an isolated corrugation before one explores the impact of alterations to the geometry or the material.

It is clear looking at the FEM calculated big picture progression of the isolated corrugation, seen in Figure 3-10, that the sample undergoes an unbending process. The amplitude of the peaks and troughs that define the corrugated architecture lessen in height with additional horizontal strain until the sample straightens out and thereby undergoes relatively simple deformation. This unbending behaviour is the source of the benefits in ductility that the corrugated architecture promises. It is evident that the deformation of this structure is first dominated by a bending

process concentrated at the peaks and troughs followed by a transition towards stretching dominated behaviour that takes precedence as the geometry straightens out.

Looking at the stress maps in Figure 3-11-Figure 3-13, showing the von Mises, longitudinal and transverse stresses respectively, it is clear that at lower values of overall strain, the stresses of interest are concentrated in the regions around the peaks and troughs. The straighter regions of the sample between peaks and troughs on the other hand show very low stresses. Looking at a peak of the corrugation in the longitudinal stress map in Figure 3-12, it can be seen that the outer surface of the peak is under compressive strains and the inner surface is under large tensile strains. As one traverses the thickness of the peak there is a transition from the high tensile stresses towards the high compressive stresses. This is exactly the opposite of the stress profile that would be expected for the bending of a straight sheet, as discussed in Hosford and Caddell's Metal Forming textbook.[66] This suggests that there is clearly an unbending process occurring at lower values of initial strain. The strain maps seen in Figure 3-14-Figure 3-15 also show localized variations in strain that suggest an unbending process initially.

It is also beneficial to attempt to tie this observed deformation behaviour to the associated overall stress-strain response of this material. The stress-strain curve corresponding to the simulation of an isolated corrugation discussed above can be found in Figure 4-1 along with the stress-strain curve of a straight strip for comparative purposes. The main difference between the simulation with the corrugated geometry and that of the straight geometry is that for the corrugated sample there is a delay in reaching the ultimate tensile strength of the material and the related necking of the material. This delayed necking strain manifests itself in essentially a shift of the stress-strain curve of the straight sample to higher values in strain. This shift is of course the result of the unbending process described above for the corrugation.

At low values of strain, Point A in Figure 4-1, the corrugation is undergoing this unbending process which is accompanied by relatively low values of stress and a significantly reduced hardening rate. This association between bending (or unbending) dominated behaviour and low hardening rates is a well-known relationship that has been best described by Ashby[10] for cellular materials. When the connectivity between the struts of a cellular material is such that bending dominated behaviour is observed during compression, the foam will have a low structural efficiency. This low structural efficiency is embodied in a material that suffers large amount of deformation at low values of stress, as seen in Figure 4-2, which is ideal for energy absorption applications. On the other hand, when a cellular architecture exhibits stretch dominated behaviour it will have high structural efficiency and tends to be a stiffer, stronger and less ductile material.

Looking again at Figure 4-1 it is clear that at low values of strain the behaviour of the corrugation looks similar to that of a bending-dominated cellular structure with high strains sustained at low values of stress. However, in this corrugated material there is a transition, around Point B in Figure 4-1, towards stretch dominated behaviour or essentially simple plastic stretching, similar to that seen for the straight strip. This transition is linked to the straightening of the corrugation. As shown in Figure 3-10, as the corrugation unbends it transitions towards an alignment that is aligned longitudinally to the loading direction and thus its stress-strain response transitions towards that of a straight material. This manifests itself in the form of an increase in strain hardening of the sample as its geometry evolves, giving it a characteristic sigmoid-type shape. This is what was described by Bouaziz[31] as *geometrically induced strain hardening*. Finally, once the sample is straightened its stress-strain curve behaves similar to a straight sample, as evident at Point C in Figure 4-1. For the purposes of describing the stress-strain

curves of these isolated corrugations in the subsequent discussion, the curve can roughly be broken down into three regions. The first region, Point A, will be called the unbending region, and is characterized by low stresses over sustained strains. The second region, Point B, will be called the transition region, and is characterized by a rise in the work hardening rate. The final region, Point C, will be called the stretching region, and is characterized by the expected stress-strain response of a straight sample of the given material.

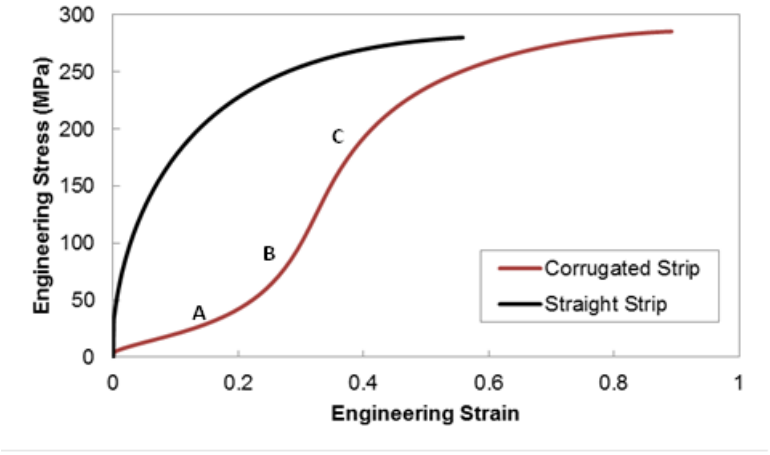


**Figure 4-1: FEM generated stress-strain curves of an isolated copper corrugation and a straight copper strip, both under plane strain tension.**

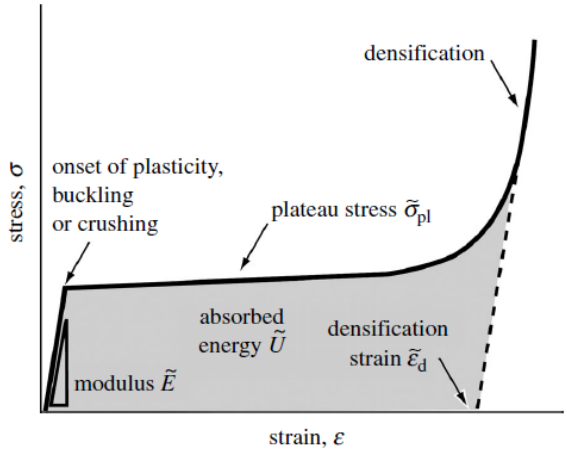


**Figure 4-2: A generic stress-strain curve of a cellular solid under compression showing important parameters and the characteristic sustained deformation at low stresses of a bending dominated structure (Ashby).**[10]

The increasing work hardening behaviour discussed above is most obvious when presented in the form of a Considere plot, as seen below in Figure 4-3. In this plot both a true stress-true strain curve and a work-hardening versus true strain curve are included for both geometries. At the point when the stress is equal to the work-hardening, Considere's criterion is met and necking will occur. Not only does this plot show a much later intersection of these two values for the corrugated geometry compared to the straight geometry, it also clearly shows that the reason for this delay in intersection for the corrugated case is the introduction of increasing work hardening. This increasing work hardening manifests itself as the peak seen in work hardening for the corrugated curve.

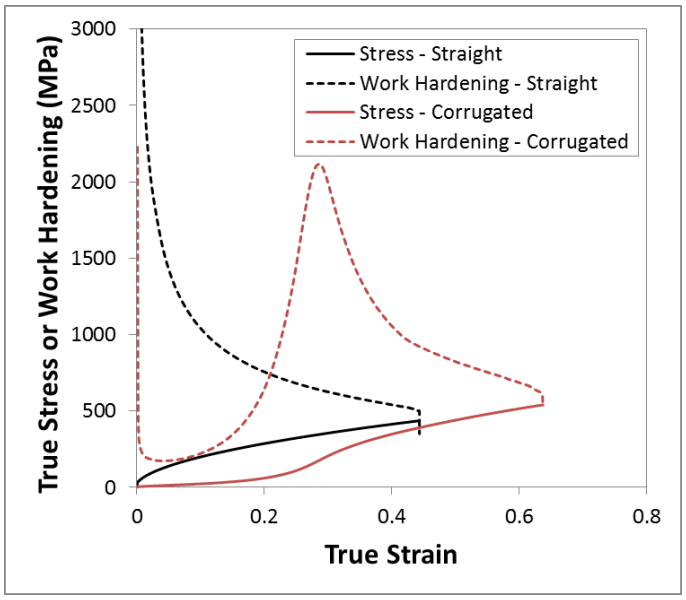


**Figure 4-3: Considere plot of FEM generated true stress-true strain and work hardening curves of an isolated copper corrugation and a straight copper strip, both under plane strain tension.**

### 4.2.2 Effect of Geometry

Now that the general behaviour of an isolated corrugation has been understood, the next step is to discuss the effect that a change in geometry has on the stress-strain response.

#### *4.2.2.1 Effect of Corrugation Height*

Looking at Figure 3-16 it is clear that the larger the height of the corrugation, the larger the unbending region of the stress-strain curve, and ultimately, the larger the necking strain of the sample. A larger corrugation height means that the degree of corrugation is higher and the initial corrugation angle is larger. A larger initial corrugation angle necessitates the corrugation to unbend a larger amount in order to straighten out. Therefore, it is clear that a larger corrugation height should lead to a larger unbending region of the stress-strain curve, which is what is observed for all three materials examined. This larger unbending region for larger corrugation heights leads to a larger boost in work hardening that is initiated later at larger values of strain, as seen from the work hardening curves for the copper strips seen in Figure 4-4. This increase in the size of the boost and the delay of its onset is what leads to the improvement in necking strain with increased corrugation height.

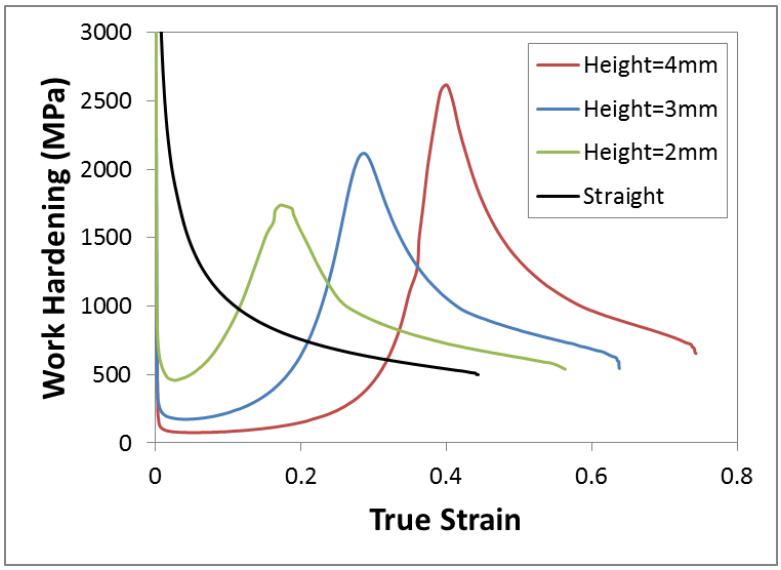


**Figure 4-4: Work hardening as a function of true strain from FEM of isolated copper corrugations with various corrugation heights and also a straight copper strip under plane strain tension.**

The general trends seen in Figure 3-16 for copper were also observed for the other material systems simulated with the main differences from one material system to another being in the stretching region of the graph. This is as expected as the stretching region of the stress-strain curve is intimately related to the material itself and the behaviour of a straight sample. For a ductile material like copper with a high hardening exponent, n=0.53, it would be expected that a large stretching region exists. On the contrary, the less ductile 4130 steel, with a smaller hardening exponent, n=0.12, would be expected to show a much smaller stretching region, which is what was observed. Finally, due to the more abrupt changes in hardening rate seen in linear hardening materials, it would be expected that the stress-strain curves for LinMat1 would be more abrupt and angular, which is what was seen for all the geometries tested. It is important to note that in looking at Figure 3-16 that changing the height of the corrugation has little to no effect on the ultimate tensile strength of these samples.

As one of the main attractions of this corrugated architecture is its promise of improved ductility without significant sacrifice in strength, it is of interest to track the effects of all of the parameters being explored on the necking strain. With this in mind, Figure 4-5 shows how the necking strain of the samples varies with the corrugation's height for all three materials. Note that a corrugation height of zero is just a straight sample. It is clear that regardless of the material the same trend, increasing corrugation height leads to higher necking strain, is observed. In fact, the points for the different materials seem to follow parallel paths that just differ from one another based on the necking strain of the base material.

#### *4.2.2.2 Effect of Corrugation Period*

Similar to the height of the corrugation, altering the period of the corrugation also shifts the stress-strain curve horizontally. As can be seen in Figure 3-17 for copper, as the period of the

corrugation is decreased the stress-strain curves shift to the right and ultimately neck at a higher value of strain. Once again, it is the initial unbending region of the stress-strain curve that becomes larger, in this case as the period of the corrugation is decreased. Similar to the effect of increasing the height of the corrugation, decreasing the period of the corrugation results in a structure with a larger degree of corrugation and therefore a larger initial corrugation angle. This means that the corrugation must unbend to a greater degree and hence the shifting of the curves to the right. The main differences between the curves for the three different materials were the same as those discussed above for the corrugation height and can be attributed to the ductility and hardening behaviour of the base material themselves.

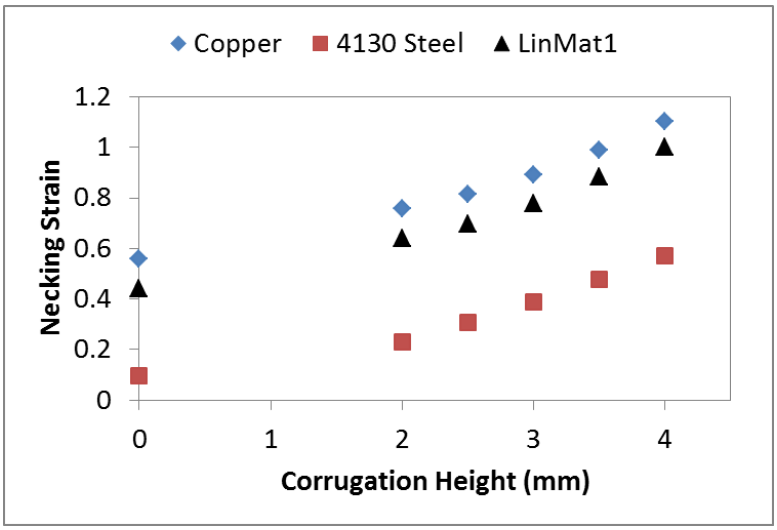


**Figure 4-5: Effect of corrugation height on necking strain for FEM simulations of isolated corrugations of copper, 4130 steel and LinMat1.**

One can get a better idea of the effect of the period of the corrugation on the ductility of the sample by plotting the necking strain as a function of corrugation period. This is done for copper, 4130 steel and LinMat1 in Figure 4-6 below. Unlike the case for corrugation height, there is no point representing the straight case on this plot as the period in the straight case is undefined. It is fairly clear looking at Figure 4-5 and Figure 4-6 that there is direct relationship between necking

strain and corrugation height and an inverse relationship between necking strain and corrugation period. For this reason it appears that there may be some benefit to defining a new variable called the corrugation steepness, representing the ratio of the height of the corrugation to its period (h/P). The corrugation steepness can be thought of as a measure of the degree of corrugation. If one takes all of the data points from Figure 4-5 and Figure 4-6 and plots the necking strain versus the corrugation steepness instead, one gets a new curve as seen in Figure 4-7. Both the simulations where the height was varied and those where the period was varied seem to lie along the same curve for each material. It is clear that this corrugation steepness is a good indicator to be used to predict the ductility of the sample.

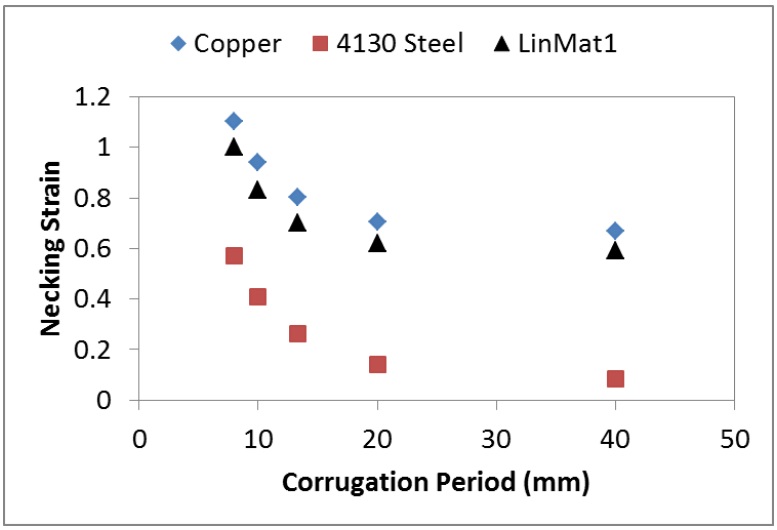


**Figure 4-6: Effect of corrugation period on necking strain for FEM simulations of isolated corrugations of copper, 4130 steel and LinMat1.**

Similar to the idea of corrugation steepness, another measure of the degree of corrugation, the tortuosity, can be used. The tortuosity is a measure of the deviation of a curve from its most direct path. It is calculated as the ratio of the arc length of the curve to that of the shortest distance between its endpoints. This concept was introduced earlier to calculate the thickness of a corrugated reinforcement in order to maintain the same volume fraction as that of a straight

reinforcement. The tortuosity, τ, of the corrugations of the simulations just discussed was calculated using:

$$\tau = \frac{L_{arc}}{L_{hor}} = \frac{\int_0^{L_{hor}} \left( \sqrt{\left(\frac{\pi h}{P}\right)^2 \left(cos\left(\frac{2\pi}{P}x\right)\right)^2 + 1} \right) dx}{L_{hor}} \quad (4\text{-}1)$$

Using this as a measure of the degree of corrugation, one can plot the necking strain versus the initial tortuosity of the corrugation for all of the simulations just discussed as seen in in Figure 4-8. In this case there is an almost linear relationship between necking strain and tortuosity, especially if one ignores the points at a tortuosity of 1, which represent the straight case. All of these plots point towards a strong relationship wherein there is an increase in the necking strain of a corrugated strip as the degree of corrugation is increased. This relationship will be discussed further when introducing an analytical model of the stress-strain response of isolated corrugations.

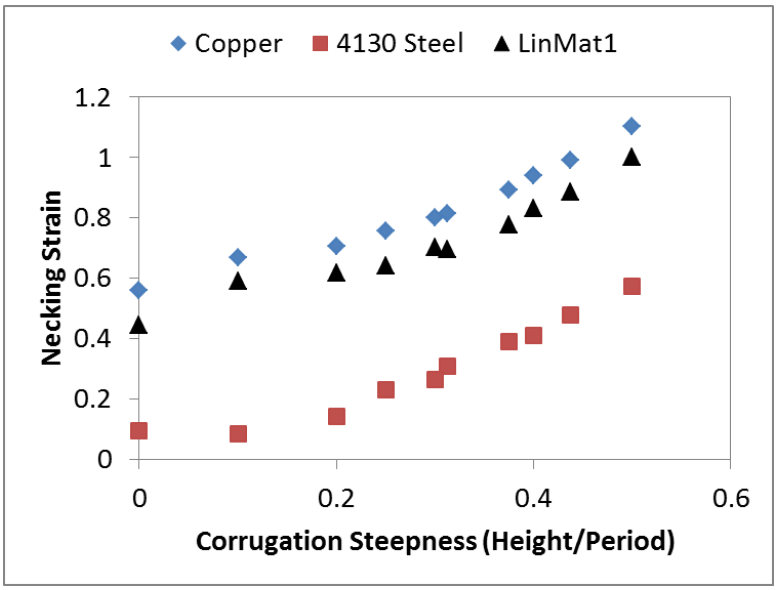


**Figure 4-7: Effect of corrugation steepness (height/period) on necking strain for FEM simulations of isolated corrugations of copper, 4130 steel and LinMat1.**

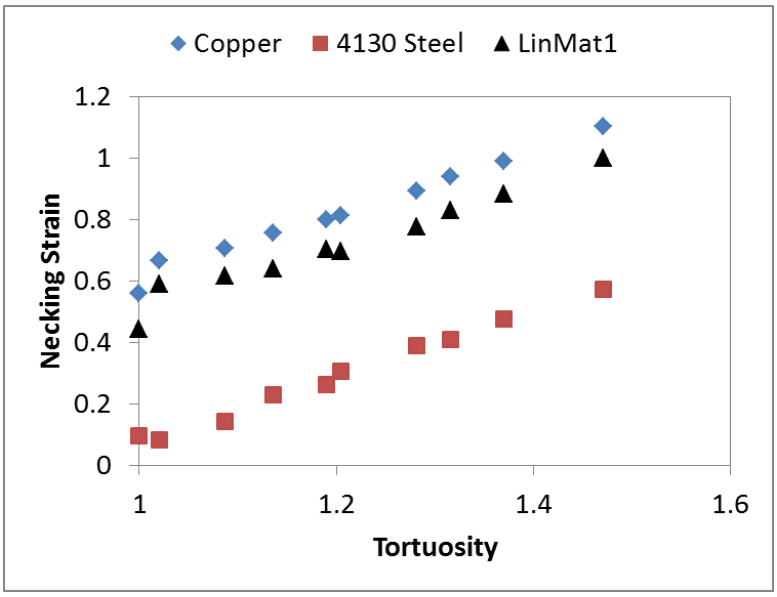


**Figure 4-8: Effect of corrugation tortuosity on necking strain for FEM simulations of isolated corrugations of copper, 4130 steel and LinMat1.**

#### *4.2.2.3 Effect of Percentage Corrugated*

The next component of the geometry that was explored was the percentage corrugated. Looking at the curves for copper in Figure 3-18 there is a clear trend that as the percentage corrugated increases, the size of the unbending section of the stress-strain curves also increases and ultimately the sample peaks at a higher necking strain. Given the trends that were observed for corrugation height and period, it seems fairly logical that if a larger percentage of the sample is corrugated then the gains in ductility through corrugation will be larger. In the cases where the percentage corrugated is less than 100%, there are sections of the sample that have a straight, aligned geometry. Due to the fact that bending dominated processes are structurally inefficient, the unbending process occurs at a low value of applied stress, as seen in section A of Figure 4-1. During unbending, this low amount of applied stress is not high enough to cause any significant plastic stretching in the straight regions of the sample. Therefore, the strain in the sample that is observed during the early stages of deformation is localized into the corrugated regions of the

sample, with the straight regions showing no deformation. Since, the total length of the sample includes the straight regions, and the deformation is only in the corrugated regions, the total strain of the sample will be higher the larger the proportion of the sample that is corrugated. The straight regions of the sample only begin to deform once the stresses required to continue unbending become high enough and the stress-strain curve enters into the transition region. If during the unbending stage one compares the strain in the corrugated region of an 80% corrugated sample to the strain in the corrugated region of a 40% corrugated sample, the strains will be the same, however, the total strain will be lower in the 40% corrugated sample due to the fact that it has a larger portion that is essentially undeformed. Using the stress-strain curves for all three material systems one can extract the necking strains of these samples and plot them versus the percentage corrugated, as seen in Figure 4-9. All three material systems show similar dependence on the percentage corrugated. Although there is a fairly direct relationship between percentage corrugated and necking strain it is not as linear as would be expected to be observed. The reason for this is not clear at this time, though could perhaps be attributed to differences in thickness between samples in order to ensure the same amount of material was used in one sample as the next.

#### *4.2.2.4 Effect of Corrugation Thickness*

This effect of sample thickness was the last geometric parameter to be explored for these isolated corrugations. As can be seen in Figure 3-19, Figure 3-20 and Figure 3-21, corresponding to simulations using copper, 4130 steel and LinMat1, respectively, the effect of the sample thickness is more complicated than the effects of height, period and percentage corrugated discussed previously. Looking at these figures, the first thing that is evident is that the sustained stress during the unbending stages is higher if the thickness of the samples is greater. The second

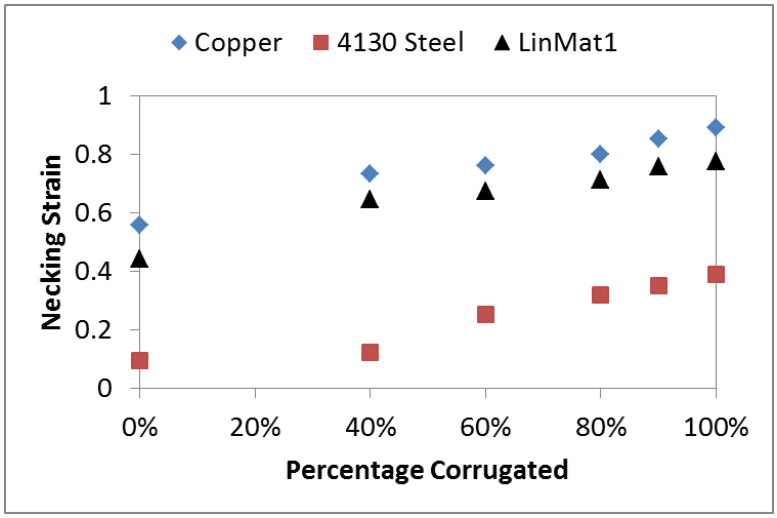


**Figure 4-9: Effect of percentage corrugated on necking strain for FEM simulations of isolated corrugations of copper, 4130 steel and LinMat1.**

is that the thicker samples show a less distinct unbending region and a larger transition region. This suggests that the thicker samples require a larger amount of stress to begin unbending and because of this larger stress they begin to stretch very soon afterwards and thus experience a larger transition region in which both unbending and stretch dominated behaviour is occurring. The reason for this larger initial stress could be due to the fact that the further one is from the midline of a sheet the larger the local strain needed to achieve unbending. Therefore, the thicker samples require a larger stress to achieve the same degree of unbending. This hypothesis is supported by looking at a stress map of the 0.39mm thick copper sample, Figure 4-10, and comparing it to the 1.56mm thick copper sample, Figure 4-11, at a total strain of 0.1. As is clear the range of stresses present for the thicker sample through its thickness is much larger than that for the smaller sample, hence when integrated through the thickness the total stress is higher for the thicker sample during the unbending stage.

The idea that the thinner samples have a larger unbending region and a smaller transition region is borne out if one investigates the evolution of the corrugation angle with overall strain. The

corrugation angle, θ, is defined as the angle between the corrugation diagonal and the horizontal, as illustrated in Figure 4-12. This corrugation diagonal is formed by drawing a line from the midpoint of a trough to the midpoint of the adjacent peak. As the corrugation unbends, these points will move and by tracking the location of these points throughout the simulation one can find the evolution of the corrugation angle. This was done for the simulations with varying thicknesses for all three materials and can be seen in Figure 4-13 for the copper system. The other systems show similar corrugation angle evolution behaviour.

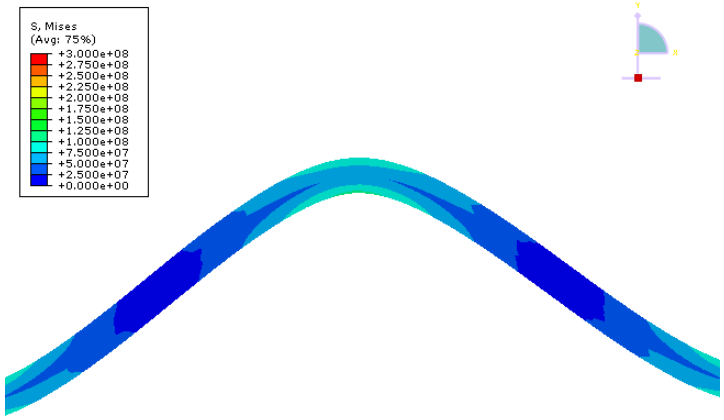


**Figure 4-10: Von Mises stress map of isolated copper corrugation with thickness of 0.39mm at a total strain of 0.1.**

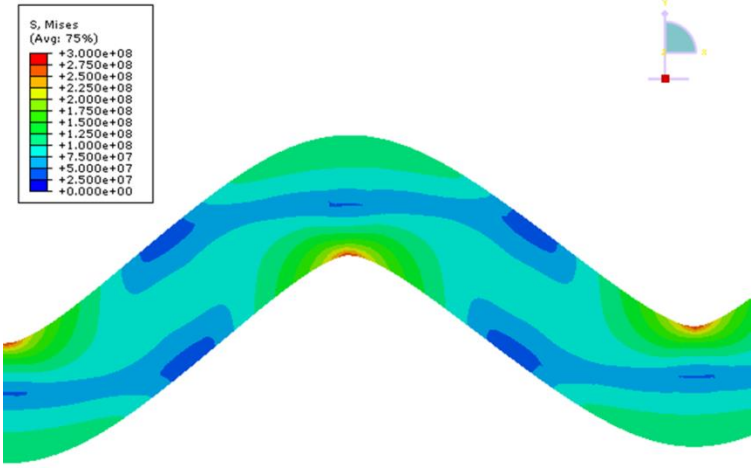


**Figure 4-11: Von Mises stress map of isolated copper corrugation with thickness of 1.56mm at a total strain of 0.1.**

Looking at this plot, it is evident that initially the angles reduce at the same rate in the unbending stage. However, when the corrugation is thinner the deformation continues to be dominated by unbending and the angle drops quickly, whereas for the thicker samples the unbending is less dominant and the angle decreases more slowly. This suggests that the thicker corrugations begin to stretch at an earlier point leading to a more gradual increase in stress in the stress-strain response as they are undergoing both stretching and unbending simultaneously over a larger portion of the total deformation. The thinner samples on the other hand show a more abrupt change from unbending to stretching as they are able to unbend more completely, due to the lower stresses involved, before they begin to stretch. Note that the corrugation angles fall below zero degrees for these samples which would imply bending past the point of being straight. This is likely an aberration in the simulations due to the constraint offered by the boundary conditions and any angle below zero can just be thought of as a straightened sample with an angle of zero.

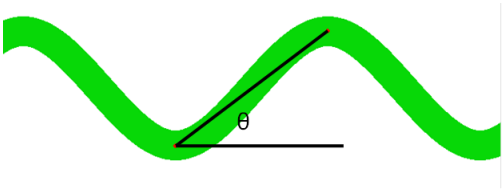


**Figure 4-12: Definition of corrugation angle, θ.**

Overall, it seems that the thickness of the sample has a less significant effect on the final necking strains of the corrugations compared to the other geometric parameters. The thickness tends to affect the path of the stress-strain curve, but does not significantly affect the end point. This is clear in looking at the stress-strain curves for the copper and LinMat1 materials in Figure 3-19 and Figure 3-21. There does seem to be an effect of the thickness on the necking strain for the 4130 steel samples, Figure 3-20, with a trend showing that necking strain increases with corrugation thickness. This trend can likely be attributed to the fact that the steel is not

particularly ductile in and of itself, with a hardening exponent of n=0.12, and the actual unbending process results in local areas of large strain that do not allow subsequent stretching, and hence the material necks. Therefore, with this material, when the corrugation is thinner and it undergoes complete unbending at lower overall strains, it will neck quickly after unbending is complete at a relatively lower strain compared to a thicker sample that takes larger overall strains to complete its unbending process.

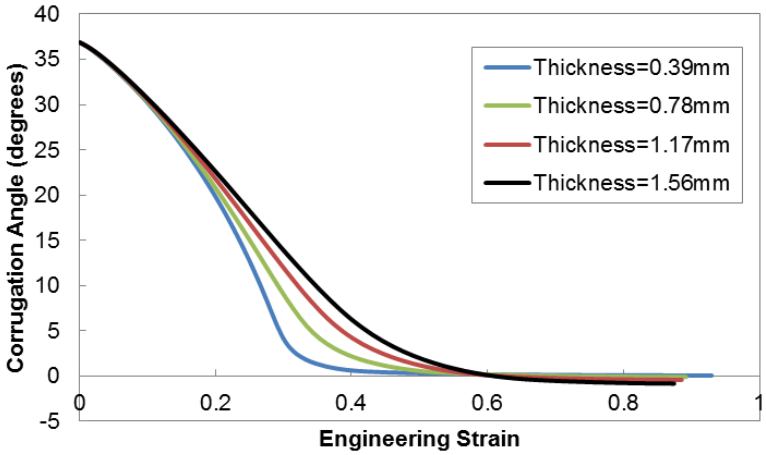


**Figure 4-13: Effect of corrugation thickness on the evolution of the corrugation angle during deformation for FEM simulations of isolated corrugations of copper.**

The trends that were observed with regards to the effects of corrugation height, period and percentage corrugated on the stress-strain response of isolated corrugations agree with those seen in literature, particularly with the work done by Boke.[32] The effect of the corrugation thickness on the initial stress levels and subsequent work hardening observed in this work is similar to that seen in the simulations of Khatam and Pindera[49] for corrugated multilayers.

### 4.2.3 Effect of Material Parameters

It was discussed earlier that the main difference between the stress-strain curves of isolated corrugations of copper and 4130 steel was related to the response of the material during the

stretching stage of the deformation. However, only looking at these two materials does not provide a complete picture as to the effect of the material being used and therefore a more systematic study of the effect of material parameters was performed. This study focused individually on both power-law hardening materials and linear hardening materials and performed parametric studies on both straight and corrugated geometries to determine whether there was any interaction between the material properties and the geometry of interest.

#### *4.2.3.1 Power-Law Hardening Materials: Effect of Yield Strength*

Beginning with the power-law hardening materials, it was observed in the previous chapter that the yield strength of these materials has essentially no effect on the stress-strain response of the sample, regardless of its geometry. This result seems somewhat puzzling, however, the reason for this lack of effect stems from the fact that once yielding of the material occurs, all of the materials used will have identical plastic mechanical behaviour, as defined by their power-law hardening parameters. This means that they have the same level of stress for the same levels of plastic strain. Since, the deformation is dominated by plastic deformation, it is to be expected that the overall response be unaffected by changes in yield strength.

#### *4.2.3.2 Power-Law Hardening Materials: Effect of Hardening Coefficient, K*

Moving on to the hardening coefficient, K, looking at Figure 3-22 and Figure 3-23 for the straight and corrugated geometries, respectively, it is clear that an increase in the hardening coefficient K strictly has the effect of increasing the strength of the material at every given value of strain. Both the straight and corrugated geometries show similar stress-only effects of the hardening coefficient, K, with the necking strains of the samples being essentially unaffected. In fact, if the engineering stress from each of the stress-strain curves for the isolated corrugations in

Figure 3-23 is normalized by dividing by the corresponding hardening coefficient, K, the curves practically collapse onto one another as seen in Figure 4-14.

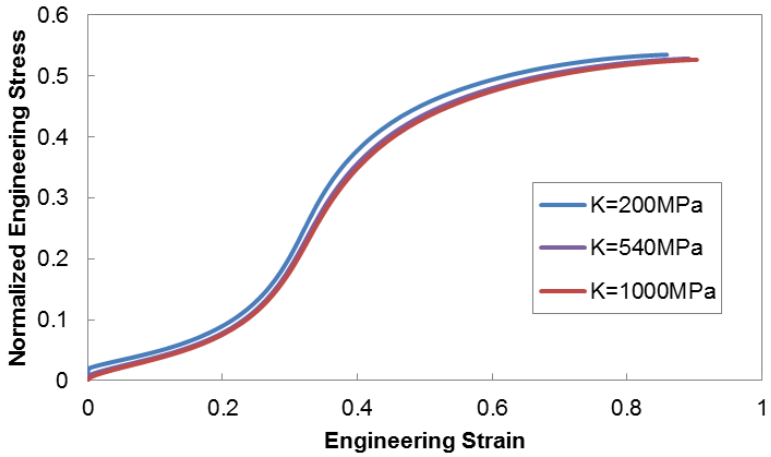


**Figure 4-14: FEM generated normalized stress-strain curves of isolated power-law hardening corrugations with variable hardening coefficient, K, under plane strain tension. Normalization is done by dividing the stress by the appropriate hardening coefficient, K.**

#### *4.2.3.3 Power-Law Hardening Materials: Effect of Hardening Exponent, n*

The final material parameter that was explored for the power-law hardening materials was the hardening exponent, n. As seen in Figure 3-24 for the straight strip and in Figure 3-25 for the corrugated strip, the effect of this hardening exponent is more complicated than the yield strength or the hardening coefficient. For both geometries increasing the hardening exponent leads to higher necking strains and lower ultimate tensile strengths, which is the expected effect of the hardening exponent. Regardless of the hardening exponent, the stress-strain response of the corrugated samples still included an unbending region, followed by increasing hardening in the transition phase, and ending with typical stretching behaviour until necking. It appears that the amount of unbending, prior to stretching can once again be tied to the stress at which unbending is occurring. In the case of lower n values, the stress of unbending is higher and thus the transition region occurs at lower overall strains as stretching is initiated earlier. Also, the

amount of stretching after the transition is highly dependent on the hardening exponent n, with lower values of n leading to much shorter stretching regions. This is as expected as lower n values are tied to less ductility. If one plots the stretching strain as a function of the hardening exponent for both the straight and corrugated samples, as seen in Figure 4-15, it is clear that regardless of geometry the effect of the hardening exponent is similar. Looking closely at these points, the necking strain of the corrugated samples seems to increase slightly more with increasing value of hardening exponent than that of the straight samples, suggesting that greater improvements in ductility can be achieved if materials with higher hardening exponents are used. That being said, the difference seems to be relatively minor.

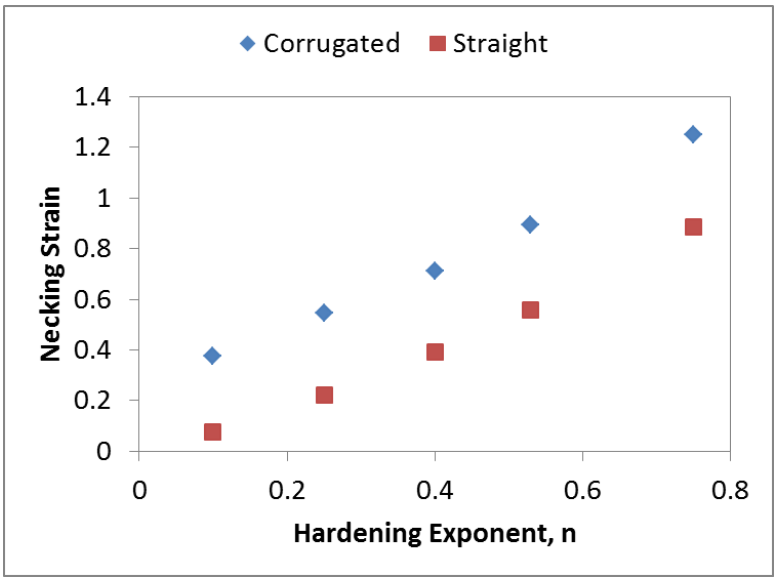


**Figure 4-15: Effect of the hardening exponent, n, on necking strain for FEM simulations of both straight and corrugated geometries with power-law hardening materials.**

It can be concluded based on the three parametric studies just discussed, that for power-law hardening materials there is very little difference between the effect of yield strength, hardening coefficient and hardening exponent on the stress-strain response of straight samples compared to their effect on isolated corrugations.

#### *4.2.3.4 Linear Hardening Materials: Effect of Yield Strength*

A similar study was also performed on linear hardening materials, looking at the effects of the yield strength and hardening coefficient on the stress-strain response of straight and corrugated geometries. Starting with the yield strength, Figure 3-26 and Figure 3-27 show the stress-strain curves for straight and corrugated samples, respectively, with various yield strengths. Looking at these figures it is evident that a lower yield strength has a similar effect to that of a higher hardening exponent in power-law hardening materials. The stress-strain curves with lower yield strengths have lower ultimate tensile strengths and higher ductility in the form of a larger necking strain. This trend can be understood by applying Considere's criterion to a linear hardening material model. Considere's criterion states that the onset of necking will occur when the work hardening rate, $\frac{d\sigma}{d\varepsilon}$, is equal to the stress, $\sigma = \sigma_{YS} + K\varepsilon$, in the sample. Deriving this for a linear hardening material, one can get the necking strain, $\varepsilon_n$;

$$\boldsymbol{\sigma = \sigma_{YS} + K\varepsilon} \qquad \boldsymbol{\frac{d\sigma}{d\varepsilon} = K} \tag{4-2}$$

$$\boldsymbol{\sigma = \frac{d\sigma}{d\varepsilon}} \qquad \rightarrow \qquad \boldsymbol{\sigma_{YS} + K\varepsilon_n = K} \tag{4-3}$$

$$\boldsymbol{\varepsilon_n = 1 - \frac{\sigma_{YS}}{K}} \tag{4-4}$$

Therefore, according to this equation, as the yield strength is decreased the necking strain of these materials is increased. This corresponds well to what is observed. One thing that is very clear when comparing Figure 3-26 to Figure 3-27 is that through the introduction of a corrugated geometry, one can achieve huge improvements in ductility for samples with high yield strengths. It seems that regardless of the yield strength the sample will undergo unbending, and thus improve the ductility. Plotting the necking strain as a function of yield strength, Figure 4-16 , shows this improvement in necking strain. With that in mind it is evident that this improvement

in necking strain through corrugation is consistent regardless of the yield strength, as the two lines are essentially parallel.

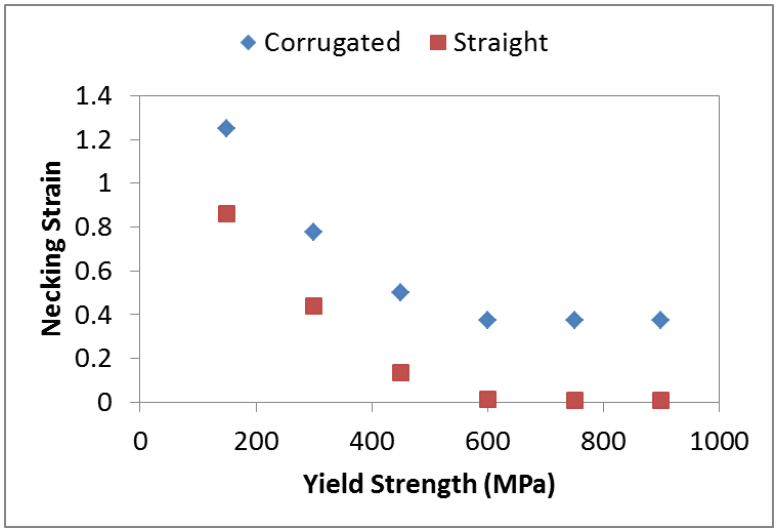


**Figure 4-16: Effect of the yield strength on the necking strain for FEM simulations of both straight and corrugated geometries with linear hardening materials.**

#### *4.2.3.5 Linear Hardening Materials: Effect of Hardening Coefficient, K*

The final material parameter of interest is the linear hardening coefficient, K. The effect of the hardening coefficient can be seen in Figure 3-28 for straight samples and in Figure 3-29 for corrugated samples. Looking at both of these figures it is clear that increasing the value of the hardening coefficient both increases the necking strain and the ultimate tensile strength, regardless of the geometry. In fact, the behaviour observed in Figure 3-29 after the unbending and transition phases are complete seems to exactly mirror that of the straight sample in Figure 3-28. Looking at a plot of necking strain versus hardening coefficient, Figure 4-17, this similarity in the trends for straight and corrugated geometries is evident, with a slightly increasing improvement in necking strain as the coefficient is increased. The hardening coefficient seems to have little effect on the unbending process itself, as all of the curves in Figure 3-29 follow the same stress-strain path during unbending. However, if one zooms in closer and focuses on this

unbending stage, as seen in Figure 4-18, it is clear that an increase in the hardening coefficient results in a larger value of stress and an earlier introduction to the increasing work hardening behaviour. It also appears that the effect of this hardening coefficient becomes more pronounced as the unbending progresses, as demonstrated by the divergence of the curves with increasing strain. The general positive trend relating hardening coefficient and necking strain can also be explained using the Considere criterion derived above. It is clear from this expression that the necking strain will increase as the value of K increases.

Overall, it appears that there is minimal interplay between the parameters of the material used and the geometry of the sample. For all of the parameters explored the effect on the stress-strain response of the sample was comparable regardless of whether the sample had a straight or corrugated architecture. Nevertheless, it is still important to know details of both the geometry and the material in order to be able to predict the complete stress-strain response of an isolated corrugated strip.

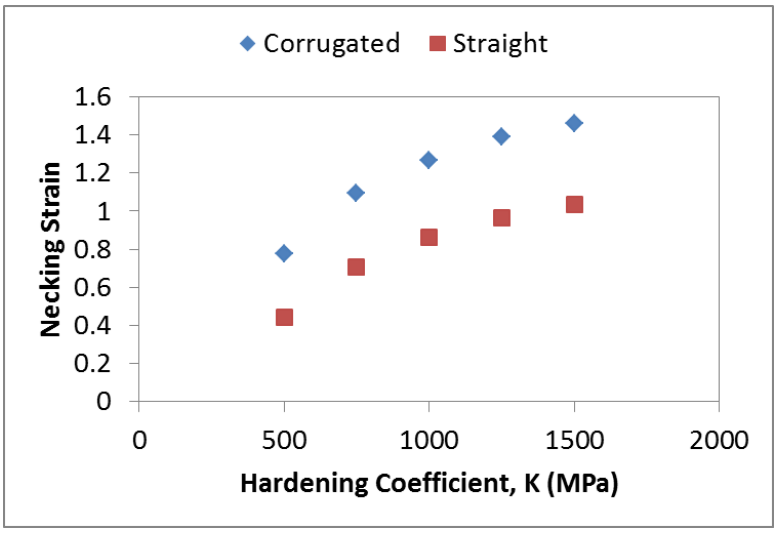


**Figure 4-17: Effect of the linear hardening coefficient, K, on the necking strain for FEM simulations of both straight and corrugated geometries with linear hardening materials.**

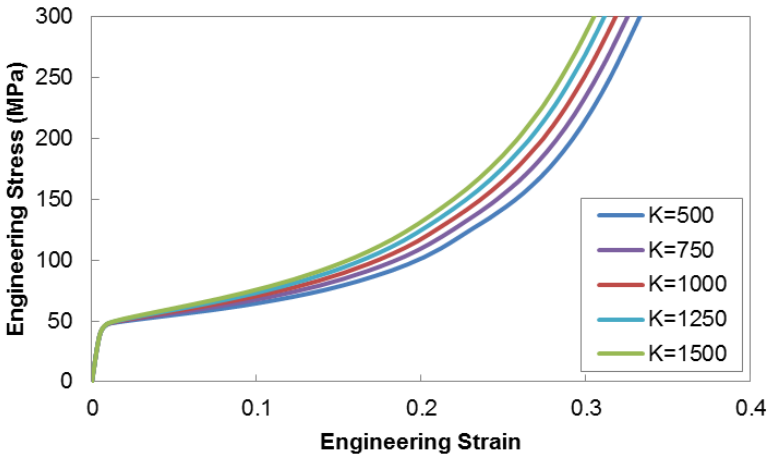


**Figure 4-18: Zoom in of unbending stage of Figure 3-29. FEM generated stress-strain curves of isolated linear hardening corrugations with variable hardening coefficient, K under plane strain tension.**

### 4.2.4 Analytical Model of Unbending of Isolated Corrugation

Although having a qualitative understanding of the effects of geometric and material parameters on the stress-strain behaviour of isolated corrugations is valuable, it would be more helpful to be able to have a model that is capable of predicting this stress-strain response given any arbitrary values of these parameters. In order to meet this need an analytical model was developed by the author.[67] The idea behind this analytical model is to capture the stress-strain response of unbending through the modification of simple sheet bending models and adding this to the concurrent stretching that occurs throughout the deformation of these corrugated strips. The model will assume uniaxial tensile loading and will be compared to FEM simulation data of plane strain tension that has been appropriately transformed to effective stress and strain for comparison purposes.

To begin, the geometry of the corrugated strip used in this model is defined, as depicted in Figure 4-19a. The corrugated strip has a width, w, a thickness, t, and has a wave structure, whose midline is described using a sine function, with a corrugation height of $h_0$ and a period of $P_0$. In

order to capture the variable of percentage corrugated, two lengths will also be defined, total initial length, $L_0$, and corrugated length, $L_c$, as seen in Figure 4-19a. These are strictly horizontal lengths and should not be confused with the arc length. In addition to this sinusoidal corrugation, there will be instances in the derivation of this model for which geometric simplification is required, and a triangular corrugation will be used instead. A simple depiction of this triangular corrugation can be found in Figure 4-19b, with the period and corrugation height defined.

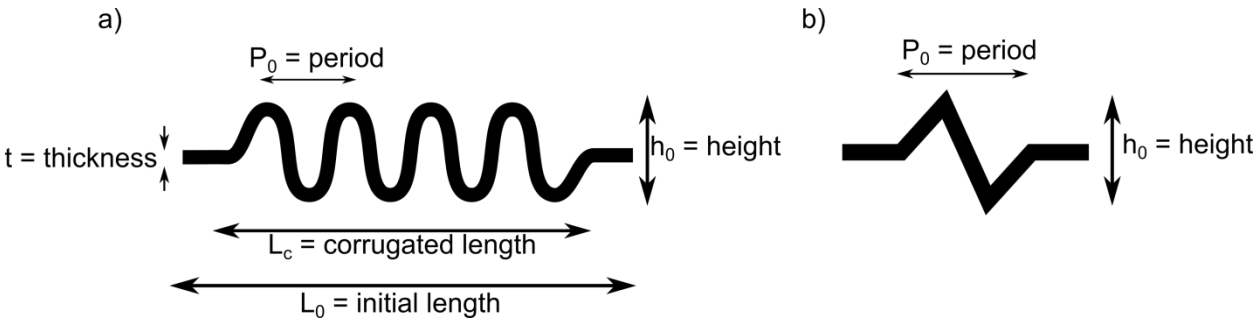


**Figure 4-19: a) Diagram defining key geometric parameter of an isolated corrugated strip for the analytical model and b) triangular geometric simplification of corrugation.**

For the purposes of this model, the stress-strain behaviour of a corrugated strip under uniaxial tension in the longitudinal direction is divided into an unbending component and a stretching component. These two components will be modelled concurrently, although the majority of the modelling effort focuses on the unbending behaviour. As mentioned before, the unbending behaviour is modeled by taking a simple expression for the bending of a sheet and modifying it to model the unbending of a corrugation. There are a number of assumptions that are made in order for this unbending model to be effective.

1. First, it is assumed that the local strains found when unbending a curved sheet from an initial radius of curvature, $r_0$, to a radius of curvature, r, are equal to the difference between the local strains in bending a flat sheet to a radius of curvature of $r_0$ and in

bending a flat sheet to a radius of curvature of r (i.e. $e_{unbend,\ r0 \rightarrow r} = e_{bend,\ r} - e_{bend,\ r0}$). This inaccurately assumes that the engineering strain in tension equals that in compression; however, it is a necessary assumption for maintaining a simple model and is not a grievous error.

2. The second assumption is that there are no residual stresses present in the corrugated sheet prior to the tensile loading. This is not an outrageous assumption as this could be obtained through an annealing process.
3. It is also assumed that the corrugation will maintain a shape that can be described using a sinusoidal function throughout the unbending process. Although, the height and period of the corrugation will change during unbending, it is being assumed that this is still a sinusoidal wave present. Also, it is assumed that during this modeling of the unbending processes that no stretching is taking place and that the arc-length of the corrugation is staying constant. The stretching strains that occur are handled separately and the strains added together at the end.

Keeping these assumptions in mind, the goal of this unbending model is to provide a prediction of the stress-strain response of an unbending corrugation. This means that the output of this model should be the macroscopic stress as a function of macroscopic strain. In order to achieve this output, first the local microscopic strains observed during unbending are related to the macroscopic strains. This is accomplished using the constant arc-length assumption and geometric relationships. Next, the microscopic stresses are determined based on the microscopic strains using an appropriate material model of plastic behaviour. This is done initially with a power-law hardening model. The microscopic stresses are then used in an integration across the thickness of the arc to get a bending moment, which divided by its lever arm gives an applied

force. The applied force is then simply divided by the cross-sectional area to give the macroscopic stress. Tying all these things together gives the macroscopic stress of unbending as a function of macroscopic strain. The stretching strains will then be calculated using this macroscopic stress and added to the unbending strains to get a complete model of the stress-strain response of the corrugated strip during unbending. The full model will be divided into two stages, an unbending stage, as just described, and a stretch dominated stage, that begins after the unbending process is complete. A detailed, step-by-step derivation of the process just described will now be provided, starting with the unbending behaviour in the first stage. This model description will be for a sample that is 100% corrugated.

To begin, the macroscopic strain, $e_{mac}$, is defined in terms of the change in the period, P, of the sine wave:

$$\boldsymbol{e_{mac} = \frac{P - P_0}{P_0}} \tag{4-5}$$

Equation 4-5 can be rearranged in terms of the period;

$$\boldsymbol{P = P_0(1 + e_{mac})} \tag{4-6}$$

At this point, it is required to relate the macroscopic strain of unbending to the microscopic strain. To do this, first consider the microscopic strain in the x-direction, of bending a flat sheet to a radius of curvature, r. This microscopic strain can be found as a function of the distance from the midplane of the sheet, z. It is acquired by comparing the arc-length of the sheet at a distance z from the midplane, to the arc-length of the sheet at the midplane, z=0. This gives the local strain at a point z because the arc-length of the sheet at the midplane stays constant throughout the bending process and is therefore equivalent to the starting arc-length at a point z, when the sheet is flat. Using the definitions of variables provided in Figure 4-20, the microscopic

strain, $e_{mic,b}$, of a point a distance of z from the midplane, after being bent to a radius of curvature, r, is:

$$\boldsymbol{e_{mic,b}} = \frac{(\boldsymbol{z+r})\boldsymbol{\theta}-\boldsymbol{r\theta}}{\boldsymbol{r\theta}} = \frac{\boldsymbol{z}}{\boldsymbol{r}} \tag{4-7}$$

where θ is the angle of the bend, as seen in Figure 4-20. For the purposes of this model it is assumed that the engineering strain, $e_{mic,b}$, is equal to the true strain, $\varepsilon_{mic,b}$. Although not strictly true it is a reasonable assumption, especially at low values of strain. This leads to;

$$\boldsymbol{\varepsilon_{mic,b}} \approx \boldsymbol{e_{mic,b}} = \frac{\boldsymbol{z}}{\boldsymbol{r}} \tag{4-8}$$

The microscopic strain just provided does not give the value of strain desired for an unbending process, but rather a bending process. Therefore, to acquire a microscopic strain for unbending from a radius of $r_0$ to a radius of r, the following adjustment is made in accordance with the second assumption listed above;

$$\boldsymbol{\varepsilon_{mic}} = \boldsymbol{\varepsilon_{mic,b}} - \boldsymbol{\varepsilon_{mic,b,0}} = \boldsymbol{z}\left(\frac{\boldsymbol{1}}{\boldsymbol{r}} - \frac{\boldsymbol{1}}{\boldsymbol{r_0}}\right) \tag{4-9}$$

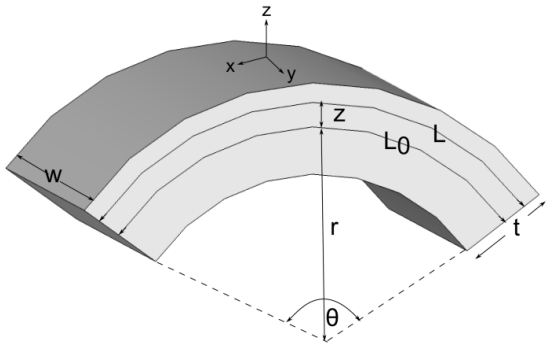


**Figure 4-20: Depiction of a bent sheet that defines the key variables involved in the bending process.**

Before relating this microscopic strain to the macroscopic strain through the use of the corrugation period, the radius of curvature must first be defined in terms of the corrugation period. This can be accomplished through the calculation of the radius of the sine wave at a point

lying on its peak. The corrugation itself is represented by a sine wave with the following equation;

$$\boldsymbol{z = \frac{h}{2} sin\left(\frac{2\pi}{P} x\right)} \tag{4-10}$$

where h is the height of the corrugation and P is the period. The radius of curvature of a function can be calculated using the following expression;

$$\boldsymbol{r = \frac{\left(1+(z')^2\right)^{3/2}}{|z''|}} \tag{4-11}$$

Calculating the appropriate derivatives of Equation 4-10 and plugging them into Equation 4-11 and then evaluating the expression at x=P/4 (i.e. the location of the peak), the radius of the sine wave at its peak is equal to;

$$\boldsymbol{r = \frac{P^2}{2\pi^2 h}} \tag{4-12}$$

As required, Equation 4-12 gives a relationship for the radius of curvature as a function of period; however it also contains height as a variable. Therefore, it is necessary to find an equation that relates the height of the corrugation to either the macroscopic strain or to the period. For the purposes of this model, this is accomplished by using the constant arc-length assumption and a temporary geometric simplification. The geometric simplification that is employed is a conversion to a triangular corrugation, as depicted in Figure 4-19b, such that it has the same period and height as the sinusoidal corrugation. This geometric simplification for this step in the derivation results in minimal error and greatly simplifies the mathematics involved. If instead the sinusoidal corrugation was assumed, then the model would have to make use of an elliptic integral for the calculation of the arc length of the sine wave, significantly complicating the derivation. Using this triangular arrangement, simple trigonometry and a constant arc-length, a, the following expression for the corrugation height is derived;

$a_0 = a$

$$\left(\frac{P_0}{4}\right)^2 + \left(\frac{h_0}{2}\right)^2 = \left(\frac{P}{4}\right)^2 + \left(\frac{h}{2}\right)^2$$

$$\boldsymbol{h = \sqrt{h_o^2 + \frac{P_0^2}{4} - \frac{P^2}{4}}} \tag{4-13}$$

Since Equation 4-13 shows height as a function of period, and initial geometric parameters, initial height, $h_0$, and initial period, $P_0$, one can plug in Equation 4-6 for period as a function of macroscopic strain to get height as function of macroscopic strain;

$$\boldsymbol{h = \sqrt{h_o^2 + \frac{P_0^2}{4}(1 - (1 + e_{mac})^2)}} \tag{4-14}$$

Now that there are two equations, Equation 4-6 and Equation 4-14, that are in terms of macroscopic strain, they can be inserted into Equation 4-12 to get the radius of curvature as a function of macroscopic strain;

$$\boldsymbol{r = \frac{(P_0(1+e_{mac}))^2}{2\pi^2\sqrt{h_o^2+\frac{P_0^2}{4}(1-(1+e_{mac})^2)}}} \tag{4-15}$$

Finally, if Equation 4-15 is plugged into Equation 4-9, one gets an expression for the microscopic strain in terms of macroscopic strain and the initial corrugation height and period;

$$\boldsymbol{\varepsilon_{mic} = \frac{z2\pi^2}{{P_0}^2}\left(\frac{\sqrt{h_o^2+\frac{P_0^2}{4}(1-(1+e_{mac})^2)}}{(1+e_{mac})^2} - h_0\right)} \tag{4-16}$$

Moving forward in the derivation, the next step is to obtain an expression that gives the microscopic stress as a function of microscopic strain. This is a fairly simple step and involves inserting Equation 4-16 into whatever material model is being used to describe the plastic behaviour of the material. For this particular version of the model a power-law hardening expression will be used;

$$\boldsymbol{\sigma_{mic,unbending} = K\varepsilon_{mic}{}^{n}} \quad (4\text{-}17)$$

where K is the hardening coefficient, n is the hardening exponent and $\sigma_{mic,unbending}$ is the local microscopic value of stress. This leads to the following expression when Equation 4-16 is inserted in Equation 4-17;

$$\boldsymbol{\sigma_{mic} = K\left(\frac{z2\pi^2}{P_0{}^2}\left(\frac{\sqrt{h_0^2+\frac{P_0^2}{4}(1-(1+e_{mac})^2)}}{(1+e_{mac})^2}-h_0\right)\right)^{n}} \quad (4\text{-}18)$$

The next step in the derivation is to relate the microscopic stress to the macroscopic stress. The first step in achieving this is to calculate the bending moment, M, related to this unbending process. The macroscopic bending moment is found by multiplying the microscopic stress by the distance, z, from the midplane, and the width of the sheet, w, and then integrating this product across the thickness, t, of the corrugation. It is important to note that Equation 4-18 calculates a true stress and the bending moment requires an engineering stress. However, it is an acceptable assumption to assume their equivalence as the bending strains involved are relatively small and the difference between them not significant. Once the bending moment is calculated it can be used to calculate the applied force of unbending, $F_x$, by dividing the moment by the lever arm. In this case, since the force is in the longitudinal x-direction, the lever arm is the corrugation height, h, divided by two. Finally, if the applied force is multiplied by the cross-sectional area of the sheet, the macroscopic engineering stress, $S_{mac,x}$, is calculated. All of this is shown in the following derivation;

$$dM = w\sigma_{mic}zdz$$

$$M = \int_{-t/2}^{t/2} w\sigma_{mic}zdz = 2w\int_{0}^{t/2}\sigma_{mic}zdz$$

$$M = 2w\int_0^{t/2} K\left(\frac{z2\pi^2}{{P_0}^2}\left(\frac{\sqrt{h_0^2+\frac{P_0^2}{4}(1-(1+e_{mac})^2)}}{(1+e_{mac})^2}-h_0\right)\right)^n zdz$$

$$M = 2wK\left(\frac{2\pi^2}{{P_0}^2}\left(\frac{\sqrt{h_0^2+\frac{P_0^2}{4}(1-(1+e_{mac})^2)}}{(1+e_{mac})^2}-h_0\right)\right)^n \frac{t^{n+2}}{(n+2)2^{n+2}}$$

$$F_x = \frac{2M}{h} = \frac{wKt^{n+2}}{h(n+2)}\left(\frac{\pi^2}{{P_0}^2}\left(\frac{\sqrt{h_0^2+\frac{P_0^2}{4}(1-(1+e_{mac})^2)}}{(1+e_{mac})^2}-h_0\right)\right)^n$$

$$\boldsymbol{S_{mac,x} = \frac{F_x}{wt} = \frac{Kt^{n+1}}{h(n+2)}\left(\frac{\pi^2}{{P_0}^2}\left(\frac{\sqrt{h_0^2+\frac{P_0^2}{4}(1-(1+e_{mac})^2)}}{(1+e_{mac})^2}-h_0\right)\right)^n} \quad (4\text{-}19)$$

Equation 4-19 is the most important equation in this model as it provides the macroscopic stress of unbending of a corrugated sheet as a function of the macroscopic strain, with the only other parameters being the material and geometric parameters that define the system. This equation can be used up until the point at which the sheet has straightened.

It was mentioned earlier that during the unbending stage of the model both unbending and stretching were occurring. Therefore, at this point it is now necessary to incorporate the stretching contribution to the model. The stress that is needed to cause the unbending of the corrugation will simultaneously result in some stretching of the sample. In order to determine the resulting stretching strain the model once again employs the use of the triangular geometric simplification. With this simplification, the stretching strain that will happen will essentially take the form of the elongation of the straight sections, struts, of the sheet between peaks and troughs. The stress that was calculated in Equation 4-19 was in the horizontal, x-direction. Therefore, in order to determine how much stretching of the struts will occur it is necessary to determine how

large the stress will be aligned in the direction of the struts. This aligned stress will be called the parallel stress, $S_{par}$. There will also be a component of the stress that is perpendicular to the struts. This component of stress will cause the height of the corrugation to increase slightly, however, due to the small impact it has on the geometry it will be ignored moving forward. In order to calculate this parallel stress component, the angle of the corrugation must be determined. Note that this angle is defined differently than the corrugation angle used earlier in the thesis. This angle can be found using the following expression;

$$\frac{\theta}{2} = \boldsymbol{tan^{-1}}\left(\frac{P}{2h}\right) = \boldsymbol{tan^{-1}}\left(\frac{P_0(1+e_{mac})}{2\sqrt{h_o^2+\frac{P_0^2}{4}(1-(1+e_{mac})^2)}}\right) \tag{4-20}$$

The parallel stress component can then be calculated as:

$$\boldsymbol{S_{par} = S_{mac,x}cos\left(\frac{\pi}{2}-\frac{\theta}{2}\right)} \tag{4-21}$$

Again, if it is assumed the material behaves according to a power-law hardening expression, the parallel stretching strain can be calculated for this material as;

$$\boldsymbol{\varepsilon_{stretching,par}} = \left(\frac{\sigma}{K}\right)^{\frac{1}{n}} \tag{4-22}$$

Notice, that once again there is an expression that uses true stress and the stress in Equation 4-21 is engineering stress. In order to convert the engineering stress to true stress the strain must be known a priori, which in this case it is not. Therefore, it is assumed that the engineering stress in Equation 4-21 is not significantly different from the related true stress, and this value is inserted into Equation 4-22.

$$\boldsymbol{\varepsilon_{stretching,par}} = \left(\frac{S_{par}}{K}\right)^{\frac{1}{n}} \tag{4-23}$$

Again, due to the small strains involved, the error resulting from this assumption is minimal. This stretching strain can then be resolved into its horizontal and vertical components, again using the angle. The vertical component again causes an increase in the corrugation height that will be ignored due to its relative insignificance. The horizontal component is calculated as follows;

$$\boldsymbol{\varepsilon_{stretching,x}} = \frac{\boldsymbol{\varepsilon_{stretching,par}}}{\boldsymbol{cos}\left(\frac{\boldsymbol{\pi}}{\boldsymbol{2}}-\frac{\boldsymbol{\theta}}{\boldsymbol{2}}\right)} \quad (4\text{-}24)$$

In order to properly add the strains from unbending and stretching together, they must both be in the form of true strain. Once the total true strain is calculated it can then be converted into engineering form for the purposes of predicting an engineering stress-strain curve.

$$\boldsymbol{e_{total}} = \boldsymbol{exp}\left(\boldsymbol{\varepsilon_{stretching,x}} + \boldsymbol{\varepsilon_{unbending}}\right) - \mathbf{1} \quad (4\text{-}25)$$

To summarize the modeling of the unbending portion;

1. The macroscopic unbending strain is used to calculate the unbending stress, according to Equation 4-19.
2. The unbending stress is used to calculate the stretching strain, using Equations 4-20, 4-21 and 4-23.
3. The total strain is calculated by summing the macroscopic unbending strain and the stretching strain, according to Equation 4-25.
4. A plot of engineering stress vs. strain for the unbending portion of the deformation can be made using the results of Equation 4-19 and Equation 4-25.

The final stage in modeling the deformation of these corrugated samples is to capture the behaviour of the sample after unbending has completed. Once the corrugation has unbent to such a degree, it no longer becomes useful to consider the contribution of unbending behaviour. The

amount of stress required to unbend the corrugation further by any meaningful amount becomes prohibitively high and thus the unbending process should be ignored. At this point, the sample is almost completely straightened and the deformation is dominated by the stretching behaviour anyways, so the sample is assumed to be completely straight from this point forward. Instead of incrementing the unbending strain to calculate further increases in stress, the stretching strain is incremented and the stress is calculated based on the simple plastic stretching behaviour. It is necessary to select a transition point for which the model transfers from the unbending model to the stretching model. For the purposes of this model this point has been selected to be when the value of the parallel engineering stretching strain, $e_{stretching,par}$, exceeds the increment observed in the unbending strain, $e_{unbending}$, for a given level of stress.

The model for the stretch dominated stage is very simple. The total strain still consists of adding the unbending strain, which is now fixed as the value at the transition point, and the stretching strain in the x-direction, as in Equation 4-25. The stress is now calculated by inserting the stretching strain into the plastic hardening model of the material (i.e. the power-law hardening model).

The complete model for the corrugated strip under uniaxial tension is determined by tying together the model for the unbending stage and that for the stretching stage. This provides an engineering stress strain curve for the entire stress-strain response of a corrugated sheet. If a model for a corrugated strip that is only partially corrugated is desired, then the strains from this model can be multiplied by the percentage corrugated and added to strains calculated using the simple power-law behaviour that are multiplied by the percentage that is straight.

In order to validate this model, one can compare the predictions of the model to those found in FEM models of the same system. This can be done for a corrugated copper sample that follows the power-law hardening model, with the material parameters given in Table 3-2. The geometry of this corrugated sample has a period of 8mm, a corrugation height of 3mm, a thickness of 0.78mm and is 100% corrugated. This exact system was modeled earlier with the FEM generated stress-strain curve being presented as the corrugated curve in Figure 4-1. Using the above analytical model, inputting the material and geometric parameters just discussed, a stress-strain curve is determined and can be plotted compared to the FEM generated curve for validation as seen in Figure 4-21. It is apparent that there is a small discrepancy between the curves, with the analytical model under-predicting the amount of strain when compared to the FEM results. This is a trend that is consistent for all model predictions of this analytical model when compared to FEM simulations. That being said, the model clearly predicts the general behaviour of the unbending corrugation quite well, as the shapes of the two curves are quite similar.

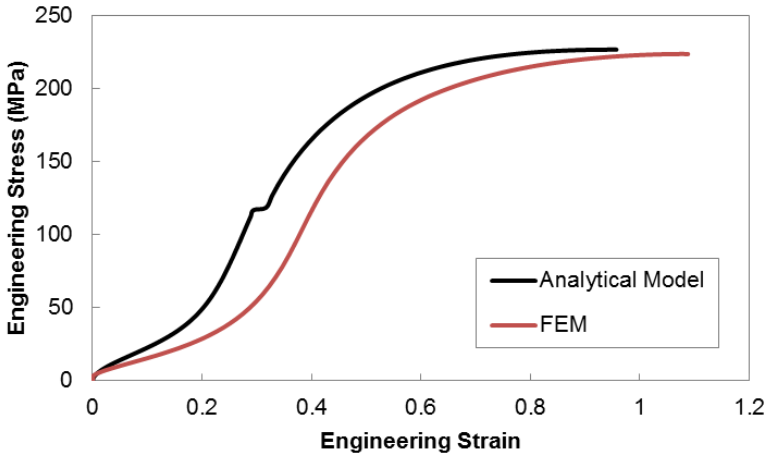


**Figure 4-21: Comparison of FEM and analytical model generated stress-strain curves of an isolated copper corrugation under uniaxial tension.**

It is possible that some of the assumptions and geometric simplifications used in the analytical model are responsible for the analytical stress-strain curve appearing to be shifted to lower values of strain. Regardless, this model is clearly still an effective tool for predicting the stress-strain response of an isolated corrugation. There is also a small abrupt change in the analytically modelled stress-strain curve that is due to the transition from the unbending phase of the model to the stretch-dominated phase. This disjointedness is minor and has little effect on the final prediction.

It is possible to perform parametric studies of the geometric and material input parameters into this model to see if the trends are similar to those trends seen from the FEM studies. To begin, the effect of corrugation height is analytically modelled for a copper corrugation using some of the same conditions listed in Table 3-3 for the FEM study. The stress-strain predictions of the analytical model for these systems can be seen in Figure 4-22. Similarly, using the conditions in Table 3-5 and Table 3-6, the analytical model can be used to show the effect of percentage corrugated, and corrugation thickness, respectively. The stress-strain curves generated by the model for these two parameters are found in Figure 4-23 for percentage corrugated and Figure 4-24 for corrugation thickness. It has already been shown that the effect of increasing corrugation height is similar to that of decreasing corrugation period, so there is no need to show the analytical model's predictions for the effect of period. It is clear that by comparing the trends observed in the FEM studies, Figure 3-16, Figure 3-18 and Figure 3-19, and the trends from the analytical modelling, Figure 4-22, Figure 4-23 and Figure 4-24, that the model successful incorporates the effects of the different geometric parameters.

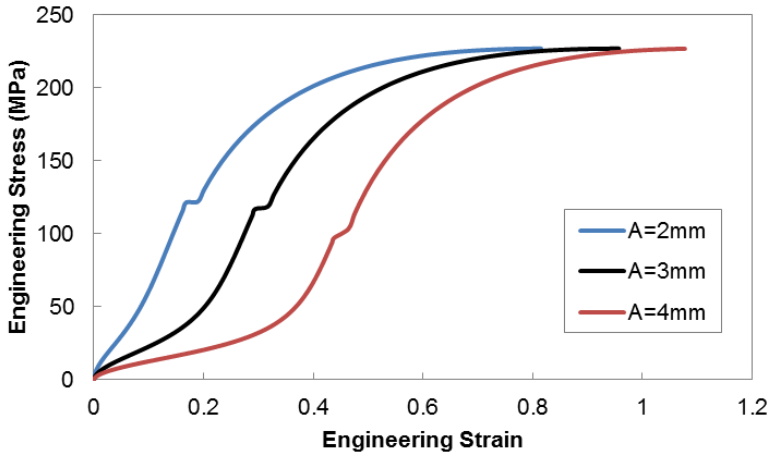


**Figure 4-22: Analytical model predictions of the effect of corrugation height (A) on the stress-strain response of an isolated corrugated copper strip under uniaxial tension.**

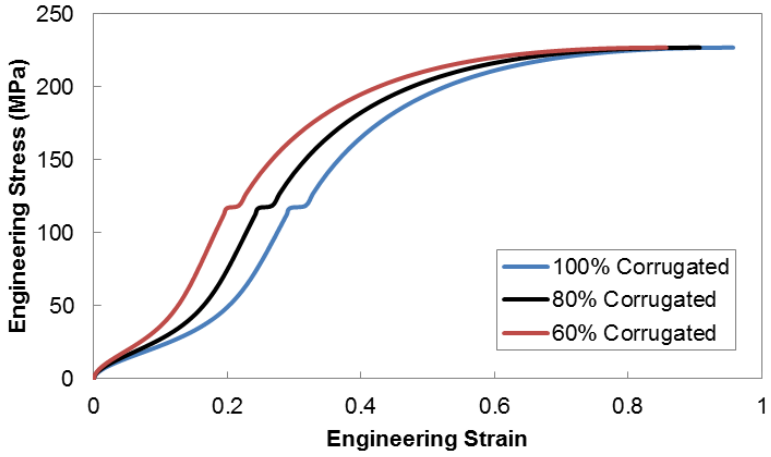


**Figure 4-23: Analytical model predictions of the effect of percentage corrugated on the stress-strain response of an isolated corrugated copper strip under uniaxial tension.**

In addition to the geometric input parameters, it is also beneficial to explore the effect of the material parameters on the predictions of the model. Since the model is derived for power-law hardening materials, this involves looking at the effect of the hardening coefficient K, and the hardening exponent, n. Maintaining a corrugation geometry that has a height of 3mm, period of 8mm, thickness of 0.78mm and length of 40mm, the effect of the hardening coefficient, K, is explored using the conditions listed for the FEM parametric study in Table 3-8 and the effect of

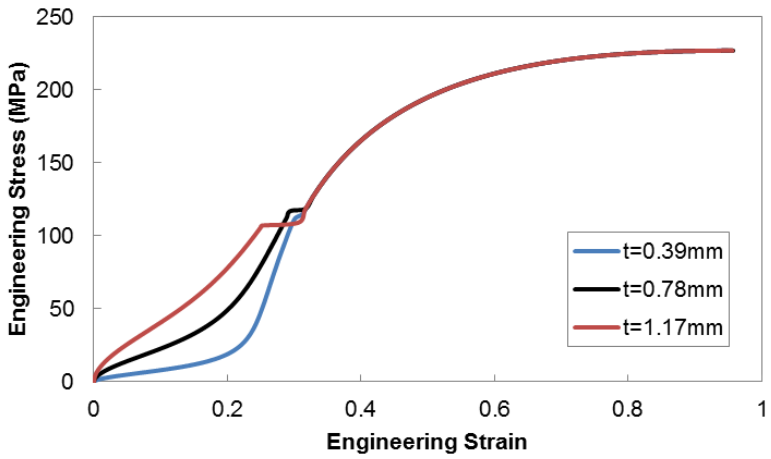


**Figure 4-24: Analytical model predictions of the effect of corrugation thickness on the stress-strain response of an isolated corrugated copper strip under uniaxial tension.**

the hardening exponent, n, is modelled using the conditions listed in Table 3-9. The analytical model predictions showing the effect of K and n are found in Figure 4-25 and Figure 4-26, respectively. Comparing Figure 4-25 to Figure 3-23 and Figure 4-26 to Figure 3-25, it is clear that the analytical model shows the correct trends for these two material parameters.

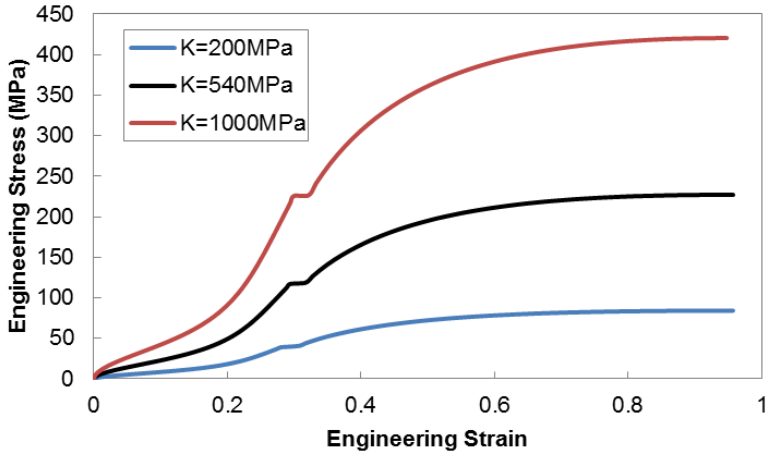


**Figure 4-25: Analytical model predictions of the effect of the hardening coefficient, K, on the stress-strain response of an isolated, corrugated, power-law hardening strip under uniaxial tension.**

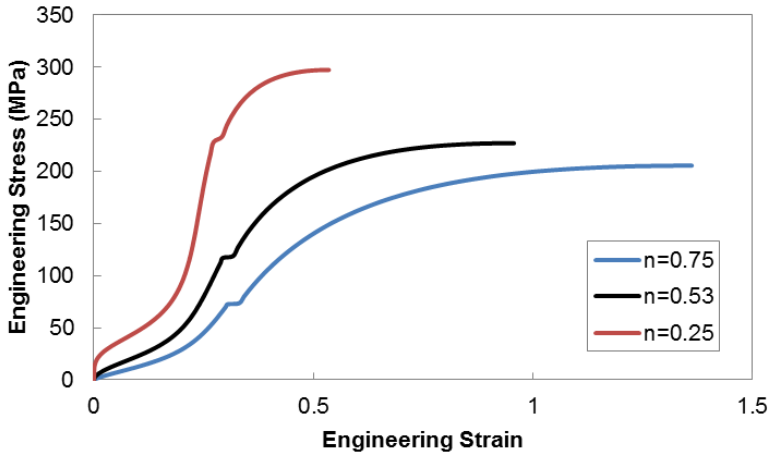


**Figure 4-26: Analytical model predictions of the effect of the hardening exponent, n, on the stress-strain response of an isolated, corrugated, power-law hardening strip under uniaxial tension.**

The model as it is currently, derived is only capable of predicting the stress-strain response of a corrugated strip made from a power-law hardening material. However, it is fairly simple to derive the model for another hardening model. Since, the linear hardening model has been a large part of the FEM modelling effort, it would be valuable to derive the analytical model using this type of hardening expression. It is not worthwhile to go through the entire derivation again, so instead the changes to the main equations will be highlighted. First of all, Equation 4-17 needs to be changed to represent the correct hardening expression of the material;

$$\boldsymbol{\sigma_{mic,unbending} = K\varepsilon_{mic}{}^{n} \quad \rightarrow \quad \sigma_{mic,unbending} = \sigma_{YS} + K\varepsilon} \tag{4-26}$$

This change will affect the next steps of the derivation and result in a modified expression of Equation 4-19 for the macroscopic stress as a function of macroscopic strain;

$$\boldsymbol{S_{mac,x} = \frac{t}{2h}\left(\sigma_{YS} - \frac{2Kt\pi^2}{3P_0{}^2}\left(\frac{\sqrt{h_o^2+\frac{P_0^2}{4}\left(1-(1+e_{mac})^2\right)}}{(1+e_{mac})^2} - h_0\right)\right)} \tag{4-27}$$

Finally, for the stretching contribution, Equation 4-23 is modified to become;

$$\varepsilon_{stretching,par} = \left(\frac{S_{par}}{K}\right)^{\frac{1}{n}} \quad \rightarrow \quad \varepsilon_{stretching,par} = \frac{S_{par}-\sigma_{YS}}{K} \tag{4-28}$$

Using this modified version of the analytical model, the stress-strain response of a linear hardening corrugated strip can be predicted. This was done for a sample that had a geometry defined by a corrugation height of 3mm, period of 8mm, thickness of 0.78mm and length of 40mm. The linear hardening model was used with a yield strength of 300MPa and a hardening rate of 500MPa, exactly the same in geometry and material as the FEM simulation #2 from Table 3-10. Comparing the analytical model to the FEM simulation of the same system, as seen in Figure 4-27, it is clear that similar to the model for power-law hardening materials that the analytical model under-predicts the strains when compared to the results of the FEM simulations. Once again this under prediction is apparent for all analytically modelled linear hardening corrugations. The overall shape of the curves however is very similar and the predictive ability of the model is reasonably good, though not quite as good as that seen for the power-law hardening analytical model.

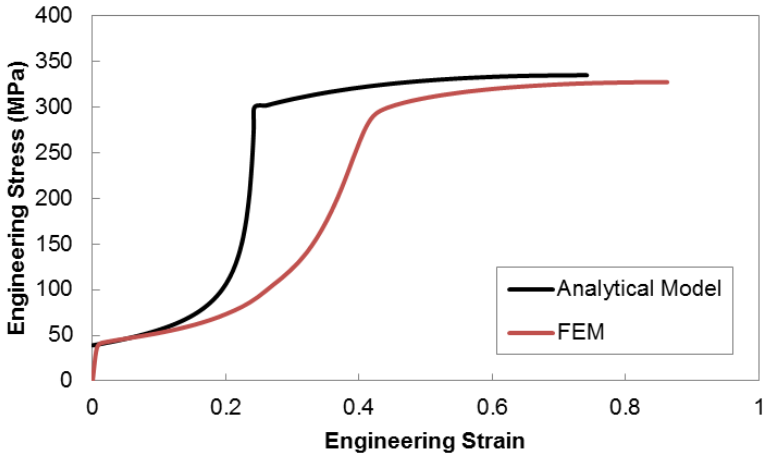


**Figure 4-27: Comparison of FEM and analytical model generated stress-strain curves of an isolated linear hardening corrugation under uniaxial tension.**

Using this linear hardening analytical model, the effects of the geometric parameters are as expected and similar to those seen for the power-law hardening material. The effects of the material parameters themselves however, should still be explored and compared to the trends observed in the FEM simulations. Looking at the effect of the yield strength first, stress-strain curves were predicted using the parameters given in Table 3-10 that were used for the FEM study. The geometry was the same as used above to generate Figure 4-27. The analytically modelled stress-strain response of these systems with variable yield strength is seen in Figure 4-28. These trends are very similar to those seen in the FEM study also looking at the effect of yield strength seen in Figure 3-27. Similarly, the analytical model's predictions of the effect of hardening rate, K, can be compared to those seen from FEM. Using the same geometry as above and the material parameters shown in Table 3-11, the model's predictions are seen in Figure 4-29. These show the same trends as predicted in the FEM study as shown in Figure 3-29.

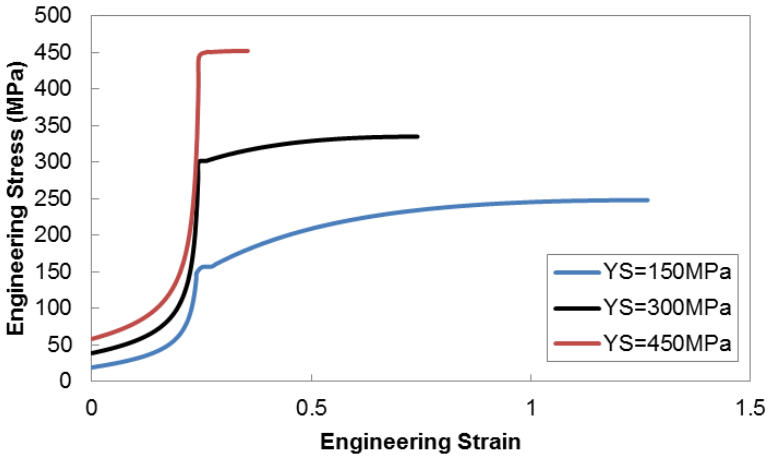


**Figure 4-28: Analytical model predictions of the effect of the yield strength, YS, on the stress-strain response of an isolated, corrugated, linear hardening strip under uniaxial tension.**

Overall, this analytical model shows promise in predicting the stress-strain response of a corrugated strip. It has the flexibility to handle different material hardening models and does an

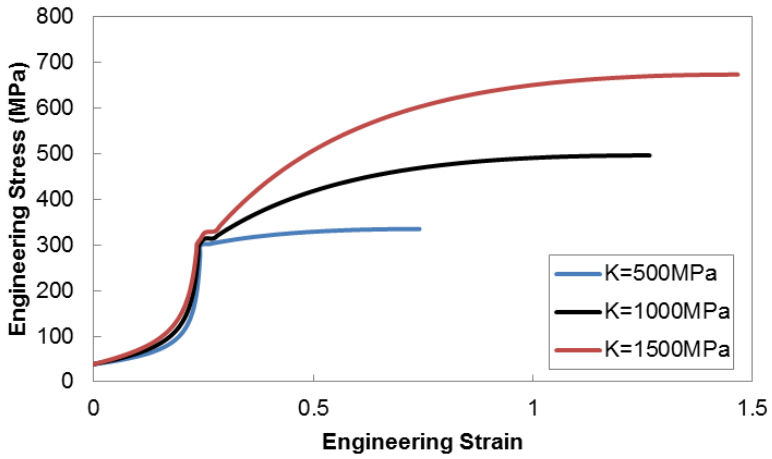


**Figure 4-29: Analytical model predictions of the effect of the hardening rate, K, on the stress-strain response of an isolated, corrugated, linear hardening strip under uniaxial tension.**

excellent job predicting the effects of the different geometric and material parameters. When compared to the FEM simulations, however, it reliably under-predicts the strains involved in the unbending process. Therefore, without further modifications the predictions of this model should be treated as rough predictions with excellent ability to show trends related to changing the input parameters.

The FEM models and the analytical model have clearly demonstrated the benefit with regards to ductility that the corrugated architecture provides. They have also been valuable in illuminating the relationships between the key geometric and material parameters and the response of the corrugated strip. These can be summarized as follows:

1. Increasing the height or decreasing the period of the corrugation will lead to a larger unbending stage and ultimately a higher amount of ductility. This can also be explained using the concepts of corrugation steepness (height/period) or tortuosity.
2. The effect of the percentage corrugated can be explained using a rule of mixtures model combining the corrugated behaviour with that of the straight geometry.

3. Thicker corrugations require larger stresses to unbend and do not experience unbending as rapidly as thinner corrugations.
4. The material parameters effect the corrugations in the same way as they do the straight geometry.

Additionally, the FEM models have provided information on local stresses and strains and overall geometry evolution that has allowed for the identification of a transition from a bending dominated process towards a stretching dominated process. The next section will explore whether these same trends occur once the corrugation is embedded in a matrix material and to what degree.

## 4.3 Corrugation Reinforced Composites

At the outset, it is helpful to discuss the behaviour of a single composite system that employs the corrugation reinforced composite. This will provide a framework with which one can explore the effects of the important parameters. This can be done by using a model system of a copper matrix and 4130 steel reinforcement. To begin with, one can explore the effect of combining these two materials together with a simple, straight reinforcement geometry. Looking at the stress-strain curves for copper, 4130 steel and a straight reinforced composite with a 20% volume fraction of reinforcement, seen in Figure 3-30, it is clear that in creating this hybrid, material, the end result is a material that exhibits a mechanical response that is intermediate to that of the components. The ultimate tensile strength and the necking strain for this composite are a non-linear combination of the component materials themselves. This is evident by extracting the values for ultimate tensile strength and necking strain from these curves and mapping the results onto a material property chart as seen in Figure 4-30. In addition to the 20% volume fraction, additional simulations were conducted that spanned the entire range of volume

fractions by changing the thickness of the straight reinforcement. The results from these simulations were also plotted on the property chart in Figure 4-30. What is evident in looking at this property chart is that the combination of the two component materials into a composite does not lead to a rule-of-mixtures type relationship for both of these two properties, as the composite does not lie along a straight line between the two components. Plotting both the necking strain and the ultimate tensile strength versus the volume fraction, Figure 4-31, it appears that the ultimate tensile strength is a relatively linear function of volume fraction, but the necking strain is non-linear.

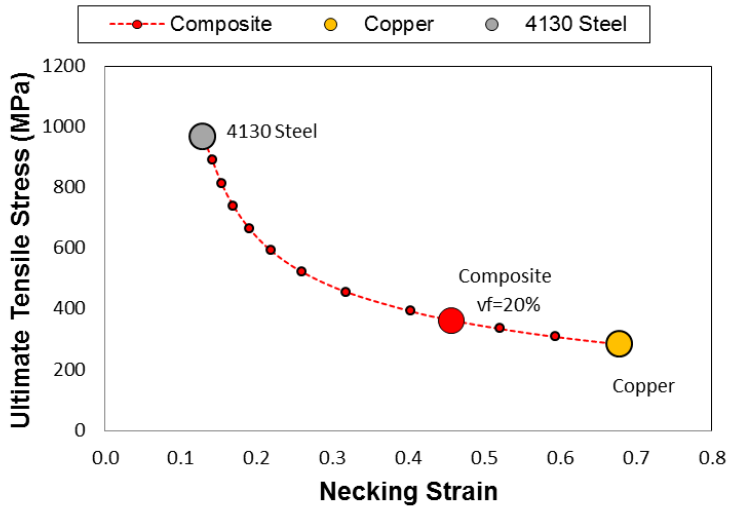


**Figure 4-30: Materials property chart of ultimate tensile strength versus necking strain for copper, 4130 steel and straight reinforced composites of various volume fractions of the 4130 steel reinforcement.**

In order to improve on the straight reinforcement geometry, it is desirable to increase the necking strain without sacrificing the ultimate tensile strength for a given volume fraction. What this means in terms of the material property chart is that it is desirable to try and populate the top right section of this plot. The goal of this thesis is determine whether this can be done using a corrugated reinforcement geometry and if so why and under what constraints.

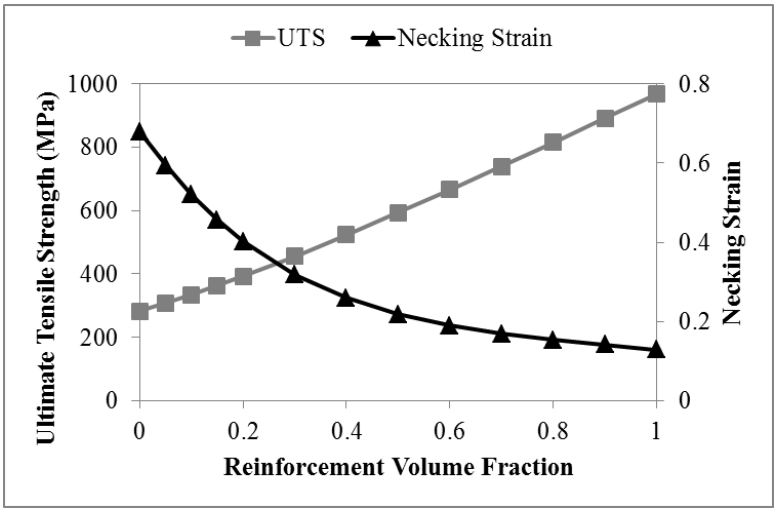


**Figure 4-31: Effect of volume fraction of straight reinforced composites on ultimate tensile strength and necking strain for system of copper (matrix) and 4130 steel (reinforcement).**

First, to understand the potential of a corrugated reinforcement, one need only look at the stress-strain curves in Figure 3-31, comparing a copper matrix and 4130 steel reinforcement composite with a straight reinforcement to one with a corrugated reinforcement. Although, the stress-strain curve for the corrugated reinforcement does not show the same drastic change in shape towards a sigmoidal profile, as it did for the isolated corrugation, there is still clearly an effect in the behaviour of the corrugated composite compared to the standard straight composite. There exists a lowering of the flow stress at lower values of strain when compared to the straight case followed by the emergence of increasing work hardening as the strain reaches higher levels. In this particular case this leads to a composite that reaches its peak stress and necks at a higher value of strain, thus improving the ductility in comparison to the straight reinforced composite. This lower flow stress value that increases as deformation continues echoes that seen for the isolated corrugation as a result of its unbending. In the case of the composite, this is not as severe; however, this muting of the effect could be expected due to the presence of the constraint of the surrounding matrix material.

In order to understand the reason for the delay in necking strain observed for this corrugated composite, one can look at a Considere plot for the straight and corrugated composite systems and look at how the work hardening evolves throughout the deformation process. This plot can be seen for this model system in Figure 4-32. It is clear that in the case of the corrugated composite there is a jump in the work hardening rate that leads to a delayed intersection with the stress curve. Similar to the isolated corrugation, it is believed that the source of this jump in the work hardening rate can be attributed to the evolving geometry of the material and not a change in the behaviour of dislocation storage of the material itself.

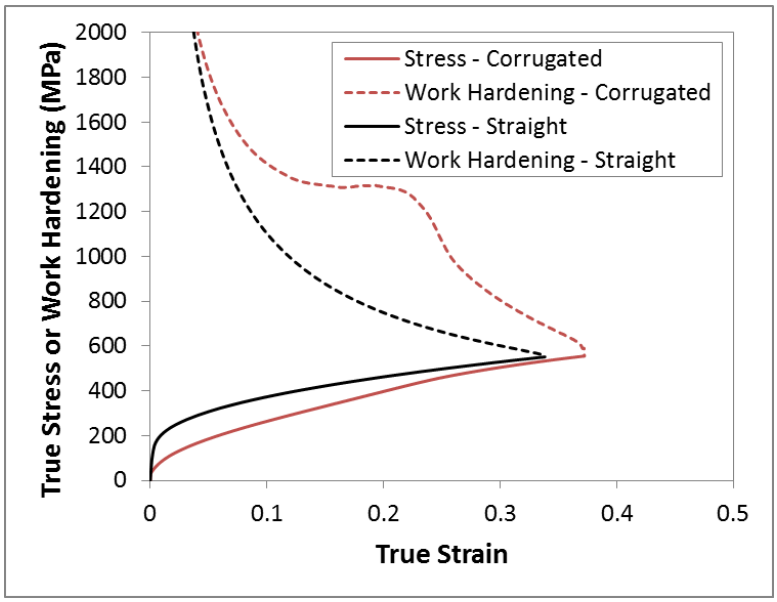


**Figure 4-32: FEM generated Considere plot of work hardening and stress-strain curves of copper-matrix, 4130 steel reinforcement composites with straight and corrugated geometries.**

To understand the reason for the existence of this increasing work hardening behaviour it is beneficial to apply a simple geometry based argument. To begin, consider two simple geometric systems as illustrated in Figure 4-33. System 1 consists of a composite with a straight reinforcement that is positioned at angle to the horizontal loading direction. System 2 consists of a straight composite that is positioned such that it is aligned along the horizontal loading

direction. For both cases assume that the reinforcement is a stronger and stiffer material than the surrounding matrix. It is well established in composite science that the strength and stiffness of a composite is higher for a system in which the reinforcement is aligned in the direction of loading compared to an off-axis reinforcement alignment. The stiffness and strength in the aligned system are often modeled using the iso-strain formulation, which is an upper-bound measure of these properties. A transversely loaded composite will have much lower stiffness and strength, and can roughly be represented using an iso-stress model as a lower bound. An off-axis alignment will have behaviour that lies between these extremes.

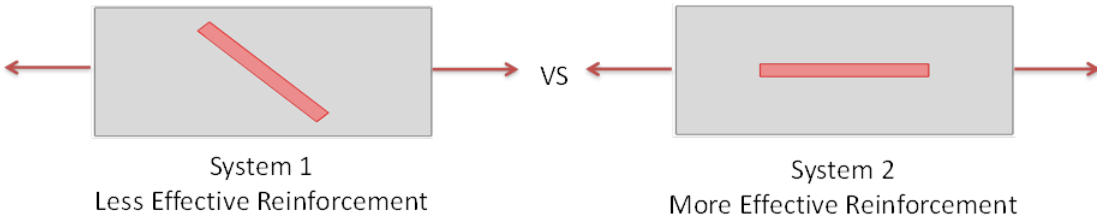


**Figure 4-33: Schematic of two different reinforcement alignments. System 1 shows an off-axis alignment that is less efficient at carrying load and System 2 shows an aligned geometry that is more structurally efficient.**

If one simplifies the geometry of corrugated reinforcement, into a triangular geometry, such that it is a series of off-axis struts connected at peaks and troughs, it is possible to develop an explanation of the increasing work hardening behaviour observed in these composites using the two simple systems just introduced. When a corrugation reinforced composite is loaded in tension it starts out with the less efficient reinforcement alignment as represented by System 1. As the loading continues, the corrugation undergoes an unbending process whereby the angle of misalignment decreases and the reinforcement essentially rotates towards the more efficient reinforcement alignment represented by System 2. This unbending process, as depicted schematically in Figure 4-34, causes a transition from less efficient loading alignment towards more efficient loading alignment and in the process results in a strengthening, or hardening

process that is strictly attributed to an evolving geometry. Using this simple geometry based argument one can explain how the unbending of a corrugated reinforcement introduces the increasing work hardening that is the key to improving necking strain in these composites.

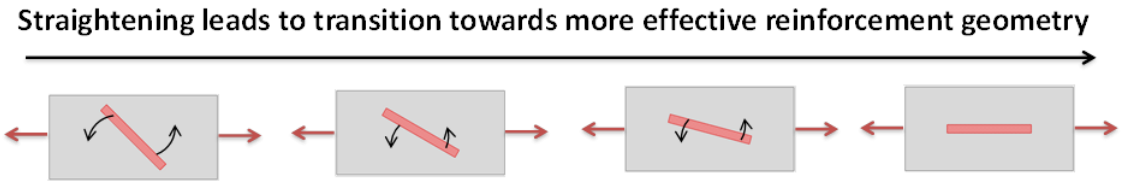


**Figure 4-34: Schematic illustrating the change in reinforcement alignment as loading continues and unbending progresses.**

In order for this simple geometric argument to be an effective descriptor it needs to be established that some degree of unbending occurs in the corrugation reinforced composite material. First, this can be seen qualitatively by looking at Von Mises stress maps at increasing values of overall strain, as depicted in Figure 4-35. It is clear in looking at these stress maps that the corrugation undergoes an unbending process as the overall deformation progresses. To obtain a more quantitative confirmation of the angle evolution one can use the measure of the corrugation angle introduced for the isolated corrugations in Figure 4-12, and apply this measure to the corrugation angle of the copper-4130 steel sample case, as seen in Figure 4-36. Also included in this plot is the evolution of the corrugation angle for an isolated corrugation with an identical geometry to that of the reinforcement and made of the same material. This isolated corrugation represents one extreme in the angle evolution as it expresses the behaviour of an unconstrained corrugation subject to tensile loading. Another extreme is also included in this plot and is labeled as 'Homogenous'. The homogenous curve essentially captures the evolution of a fictional angle for a scenario in which only a single, homogenous material is present. Alternatively, it can be thought of as calculating the corrugation angle as deformation proceeds for a system in which the corrugation is the same material as the surrounding matrix.

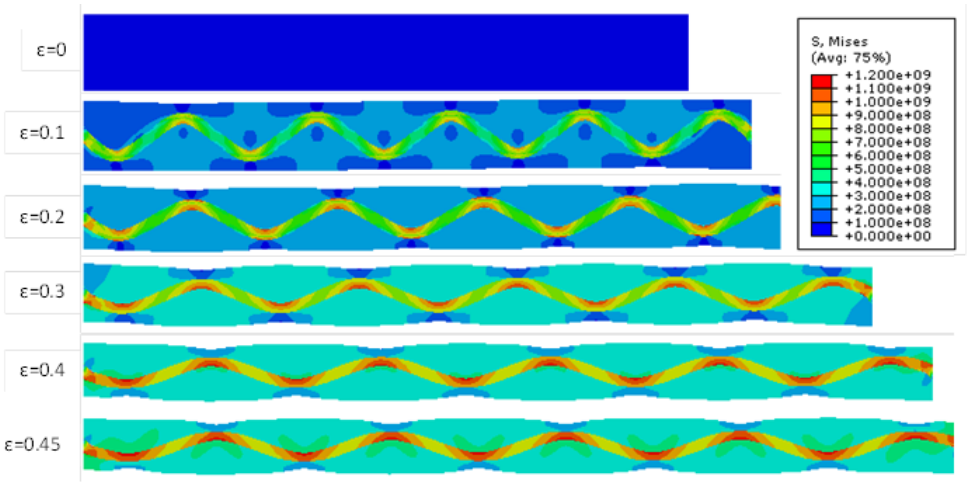


**Figure 4-35: FEM generated Von Mises stress maps of copper-matrix, corrugated 4130 steel reinforcement composite at increasing values of overall strain.**

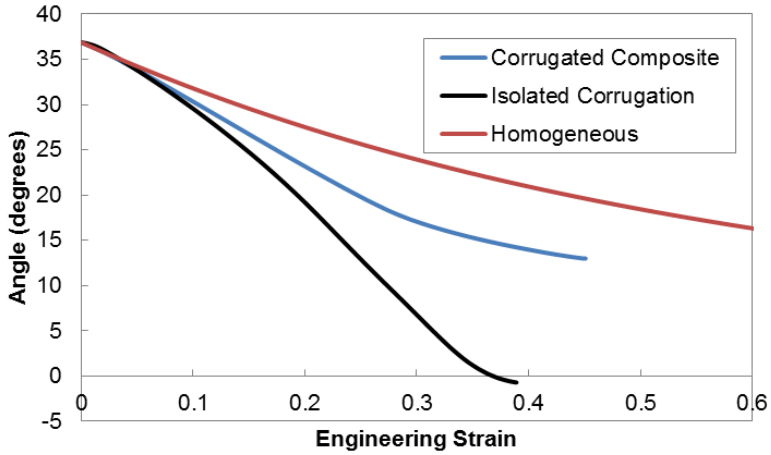


**Figure 4-36: Evolution of corrugation angle with overall strain for a homogenous material, an isolated corrugated strip, and a corrugation reinforced composite. The material of the corrugation is 4130 steel and for the composite case the matrix material is copper.**

The calculation used here is strictly based on the shape change of the homogenous material when it is subject to plane strain loading. What is clear when looking at this plot in Figure 4-36 is that the angle evolution behaviour of this corrugated composite lies somewhere intermediate to that of the isolated corrugation and the homogenous material. This means that the corrugation unbends to a lesser extent when compared to the isolated corrugation but unbends more rapidly in comparison to the change in angle caused by the plane strain shape change. Due to the

constraint offered by the matrix the corrugated reinforcement is not able to unbend as quickly or as completely as it does when it is isolated. However, there is clearly some significant unbending that still happens in the case of the composite, which can be used to explain the increasing work hardening behaviour seen in the Considere plot in Figure 4-32.

Although the corrugation has clearly undergone some unbending it is evident that the matrix impedes this unbending to some degree. This can be attributed to the fact that there will be some stress transfer from the weaker matrix to the stronger reinforcement as loading progresses. As was mentioned earlier, for an isolated corrugation, the stress and strain are concentrated in the peaks and troughs of the sample as it undergoes the unbending process. When this corrugation is embedded in a matrix and stress is transferred to the corrugation from the matrix, there will also emerge larger stresses in the regions connecting the peaks and the troughs. The process of unbending will be hindered and eventually significantly curtailed once the stresses in the rest of the corrugation reach the yield point and begin to plastically deform. At this point the deformation of the corrugation transitions from a bending dominated process to a stretching dominated process. Once this stretching process has begun any further improvements in ductility due to the corrugated architecture are unlikely to occur, as the corrugation will not unbend much and will now stretch with the reinforcements basically fixed at an angle to the loading direction.

In order to identify whether this transition towards stretching dominated behaviour is occurring in a given sample, one can track the plastic stretching strain present in the reinforcement. In particular it is helpful to consider the plastic strain of the reinforcement at the midpoint between a peak and adjacent trough. This plastic strain can be extracted from the FEM simulation output and calculated in the direction that is aligned with the reinforcement at that midpoint. The location and orientation of this plastic strain can be seen depicted in Figure 4-37. Note that due to

the unbending process, the direction of alignment with the reinforcement will change with the overall deformation. Therefore, in order to get the stretching strain along the direction of the reinforcement, the coordinate system that defines the direction of the plastic strain will also evolve with the overall deformation. This concept is illustrated in Figure 4-38 below.

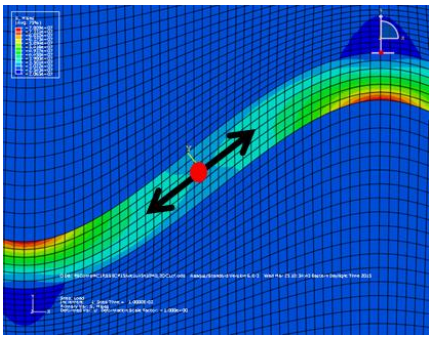

**Figure 4-37: Schematic defining the location (red point) and the direction (black arrow) of the plastic stretching strain of a corrugation.**

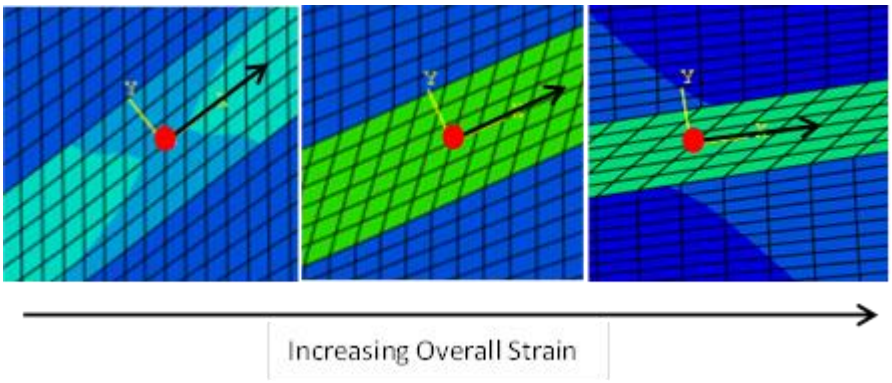


**Figure 4-38: Schematic showing the progression of the coordinate system with increasing overall deformation that is used to define the plastic stretching strain of the corrugation.**

Using this definition for the stretching strain of the corrugation, a plot of the stretching strain of the sample copper-4130 steel corrugated composite and the related 4130 steel isolated corrugation is presented in Figure 4-39. What is clear from this plot is that both samples have an initial region whereby no plastic stretching occurs followed by the emergence of a plastic stretching strain after some amount of total deformation. This first region is the stage at which

unbending is occurring, as the region between the peaks and troughs is not plastically deforming. In both cases there is a transition period whereby the stretching strain begins to ramp up followed by the stretching dominated behaviour where the stretching strain increases linearly as a function of overall strain. In comparing the two curves it is evident that the corrugated composite deviates from the unbending behaviour earlier than the isolated corrugation and begins to stretch. This earlier emergence of stretching behaviour can be attributed to the stress-transfer from the matrix causing the reinforcement to yield in this region at an earlier point. In this particular system it is clear that enough unbending occurred prior to stretching to provide the work hardening behaviour that allowed for an improvement in necking strain as a result of corrugating the reinforcement. In fact a plot that shows both the evolution of the corrugation angle and the reinforcement plastic stretching strain as a function of overall strain, see Figure 4-40, shows that the initiation of stretching stress coincides with a change in the pattern of the angle evolution. For this system this occurs at an overall strain of around 0.15. This is perhaps clearer looking at the plot seen in Figure 4-41, which plots the first derivative of the corrugation angle with regards to total strain on the same plot as the stretching strain. The minima of the first derivative plot, representing a change in the rate of change of the angle, lies at around the same point as the emergence of the plastic stretching strain, as highlighted by the blue box.

Due to the fact that the constraint of the matrix clearly restrains the unbending process and that the deformation in the matrix is highly heterogeneous, as shown later in Figure 4-42, it is not possible to create a simple analytical model to predict the stress-strain response of the composite. Unfortunately, this simple model that just uses a volume fraction weighted average of the analytical model for the isolated corrugation presented earlier with the simple stress-strain behaviour of the matrix material would not capture the effect of the matrix and reinforcement

components on their opposite component. The system is too complex with too many interrelated effects for a simple rule-of-mixtures model to work.

One of the consequences of the unbending of the corrugated reinforcement is the emergence of a very heterogeneous and periodic deformation pattern in the matrix of the composite. Looking at maps of the horizontal and vertical logarithmic strains of this corrugation reinforced composite

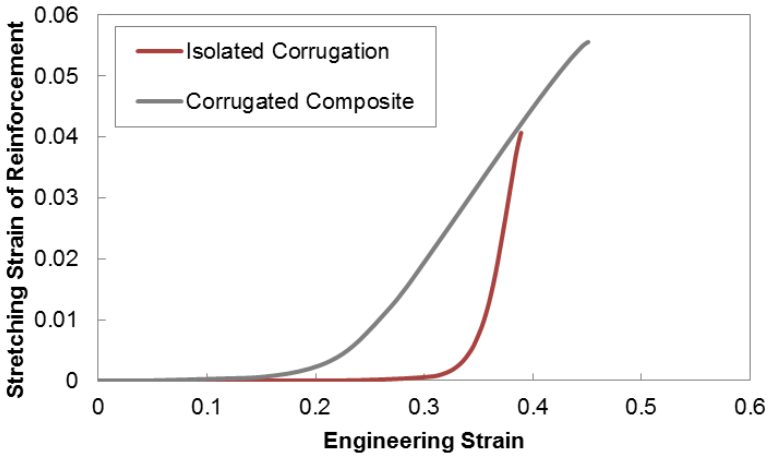


**Figure 4-39: Stretching strain of the reinforcement as a function of overall strain for an isolated corrugated strip and a corrugation reinforced composite. The material of the corrugation is 4130 steel and for the composite case the matrix material is copper.**

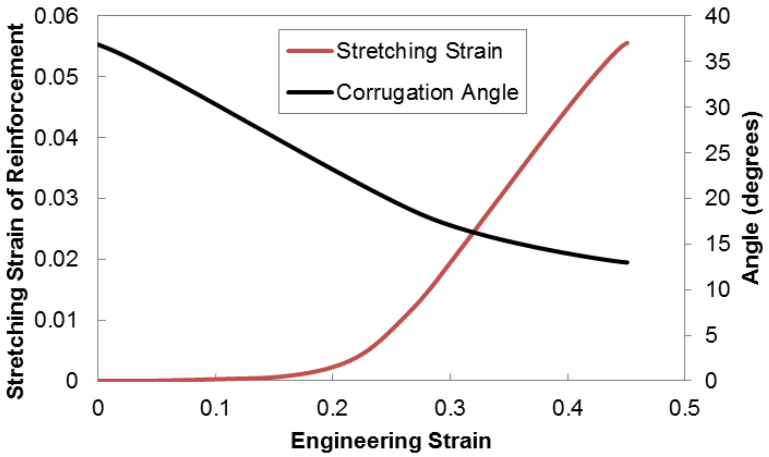


**Figure 4-40: Reinforcement stretching strain and corrugation angle as a function of overall strain for a corrugation reinforced composite. The reinforcement is 4130 steel and the matrix material is copper.**

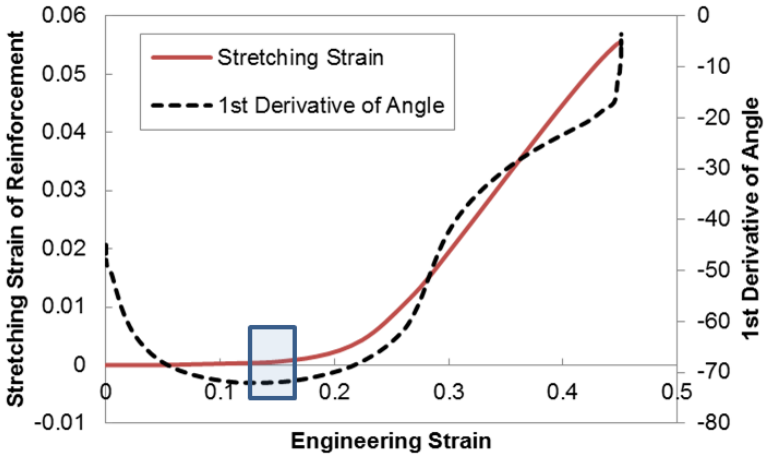


**Figure 4-41: Reinforcement stretching strain and the first derivative of the corrugation angle with respect to overall strain for a corrugation reinforced composite. The reinforcement is 4130 steel and the matrix material is copper.**

after 20% deformation, as shown in Figure 4-42a and Figure 4-42b, respectively, it is clear that there are regions in the matrix that undergo large amounts of deformation and other regions that undergo very minimal deformation. First looking at the horizontal strain map, it can be seen that the regions that are in the matrix underneath a peak, labeled as 1 in Figure 4-42, undergo a large amount of tensile strain, as evidenced by their red colour. This is highly contrasted by the regions above peaks, labeled as 2 in Figure 4-42, which show very minimal deformation in the horizontal direction, and have a blue colour. Looking at the vertical strain map these trends are similar; however there are now large compressive strains underneath peaks and small compressive strains above peaks. Due to the periodic nature of the corrugated reinforcement these patterns appear in a very regular, periodic fashion throughout the material. The emergence of this large amount of tensile strain observed below peaks, and also above troughs, can be explained by considering the unbending process. When a corrugation is unbent, this leads to high tensile strains at its inner interface and high compressive strains on its outer interface. Since in this scenario the corrugation is embedded in a matrix material, the high tensile strains on its inner interface are

transferred to the adjacent matrix in that region and large deformation is therefore observed in the matrix underneath a peak. Using this same justification, the compressive strain at the upper interface of the corrugation peak, constrains the surrounding matrix to have a much lower horizontal strain. The vertical strains are related to the horizontal strains through a conservation of volume and the plane strain nature of the deformation.

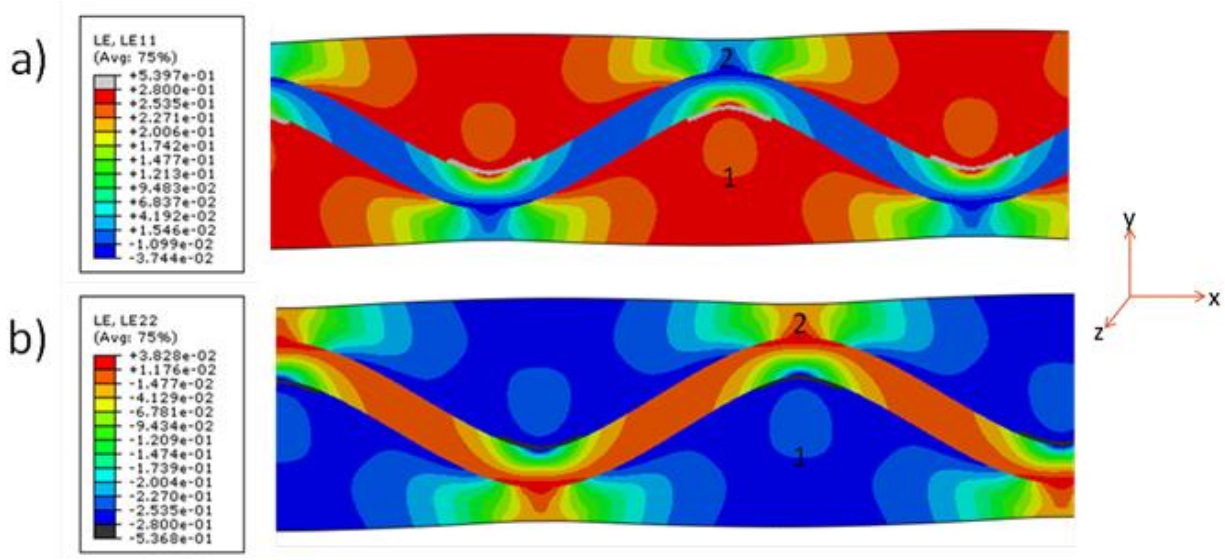


**Figure 4-42: FEM generated logarithmic strain maps of copper-matrix, corrugated 4130 steel reinforcement composite at an overall tensile strain of 0.2. a) Map of strain in horizontal direction and b) map of strain in vertical direction.**

These patterns can also be justified by considering the global deformation that is expected for a plane-strain tensile load. In general, as a sample is loaded in plane strain tension it is expected to stretch in the horizontal direction and contract in the vertical direction. Also, when a corrugation is loaded it begins to unbend. This unbending leads to an increase in the distance between adjacent peaks of the corrugation, i.e. the period, and a decrease in the vertical distance between peaks and troughs, i.e. the corrugation height. Now, consider the vertical strains in a system with the corrugation embedded in a matrix and subject to plane strain tension, as depicted schematically in Figure 4-43. The whole sample is contracting vertically, but in addition there is

also a driving force for the corrugation to unbend. Therefore, in the region underneath the corrugation peak, there are vertical compressive strains as the entire sample contracts, but there are additional compressive strains in this region as there is the driving force for the corrugation height to decrease through unbending, leading to overall large compressive strains in this region. This is contrasted to the region above the corrugation peak that will be subject to the overall compressive strains due to the plane strain tension in addition to a tensile vertical strain caused by the decreasing corrugation height. Therefore, what are observed are large compressive strains underneath corrugation peaks and much smaller compressive strains above corrugation peaks, as labeled in Figure 4-43c. The interrelatedness of vertical and horizontal strains results in the high horizontal tensile strains underneath peaks and low horizontal tensile strains above peaks.

The existence of these strain patterns is important for a number a reasons. First of all, the emergence of this characteristic pattern is indicative of a composite system that is undergoing an unbending process. Therefore, if this pattern is observed, it can be inferred that the parameters of the system are such that they allow unbending to occur. Under what conditions this unbending process leads to an improvement in ductility compared to a straight geometry will be discussed later in this chapter. Secondly, comparing the localized strain patterns observed in these simulations to experiments can be a method of validating the modeling work. This can then allow one to use more modeling to evaluate a given system under altered circumstances of loading or geometry. For example, if one could show similar strain patterns in plane strain compression for FEM simulations and experimental tests, then one could run simulations in plane strain tension of the same system to get information concerning theoretical ductility, which could otherwise be difficult to achieve experimentally. This idea will be discussed further in the experiment chapters of the thesis. Thirdly, knowing that the deformation of a corrugated

composite leads to a very heterogeneous and periodic deformation pattern could allow one to use corrugated composites as an intermediate fabrication step. If a material with a spatially periodic pattern in properties is desired, one could start with a corrugated composite, and then deform the material to obtain this periodic structure. It could also then be subject to further treatments such as recrystallization to further solidify the spatial differences in properties. Finally, the heterogeneous deformation pattern coupled with the end result of an increase in necking strain, suggests that there may be some redundant work being done in these materials that could lead to an improvement in energy absorption in some cases.

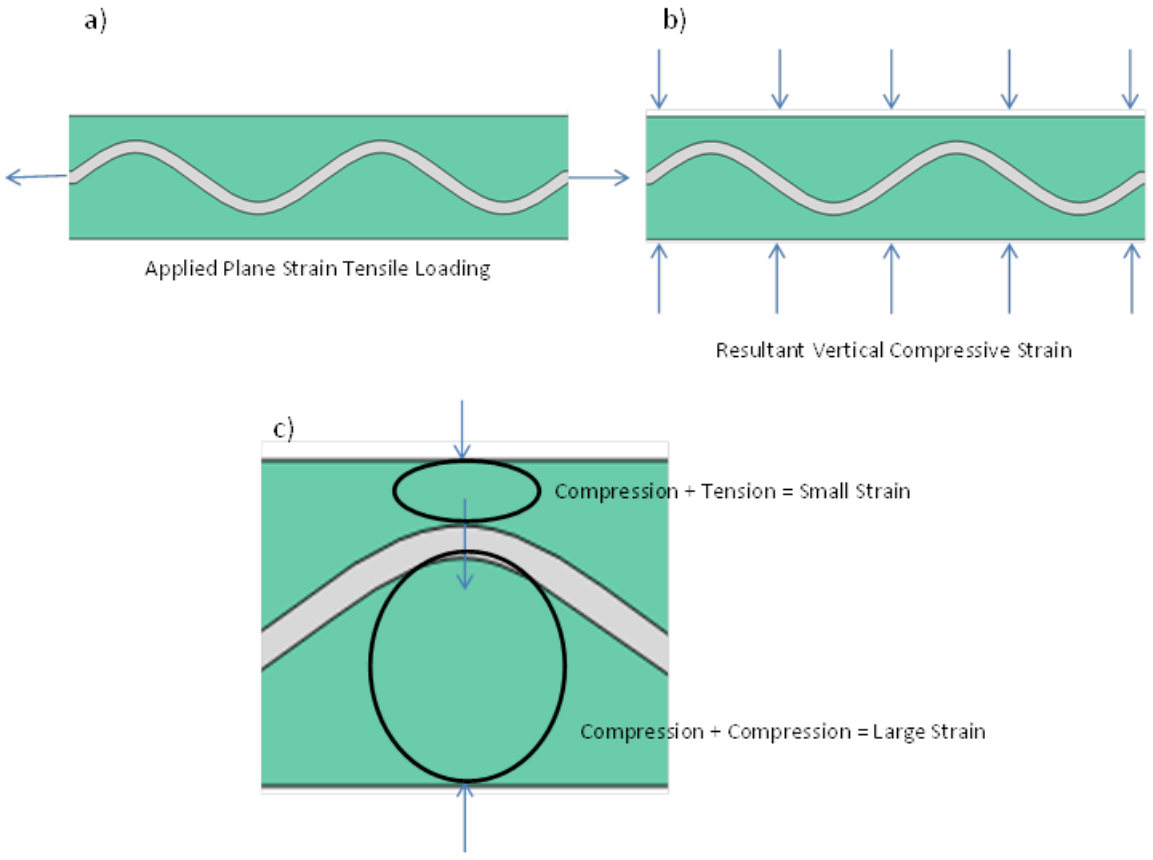


**Figure 4-43: Schematic for explaining the deformation patterns observed in corrugated composites. a) A plane strain tensile load is applied to the composite, which in addition to horizontal tensile strain also leads to b) vertical compressive strain. c) The vertical compressive strain coupled with the driving force for corrugation unbending leads to regions of high and low compressive strains.**

Now that the local and overall behaviour of the corrugation reinforced composite has been introduced for a sample system, it is of interest to discuss the effects of changing the different parameters related to these corrugated composite systems. This involves discussing the effect of the different geometric, material, spatial and arrangement parameters of these systems.

### 4.3.1 Effect of Geometry

#### *4.3.1.1 Effect of Corrugation Height*

Starting with the geometric parameters, one can look at the effect of corrugation height on the stress-strain response of these materials, as seen in Figure 3-32 for the copper matrix, 4130 steel reinforcement system with 20% volume fraction. It appears that introducing a corrugation with a small height, i.e. 1mm or 2mm, actually results in the composite performing worse with regards to its necking strain than the straight reinforced composite of the same volume fraction. However, when the reinforcement is a corrugation with a larger corrugation height, i.e. 3mm or 4mm, the corrugated composite outperforms the straight composite. In fact, the trend that is observed is that as the corrugation height is increased the improvement in necking strain over the straight geometry becomes larger. Therefore, there appears to be a threshold with regards to corrugation height that needs to be exceeded, in this case between 2mm and 3mm, in order for the benefits of corrugation to be realized and after exceeding this threshold further increases in corrugation height lead to larger improvements in necking strain. This is seen in the plot of necking strain versus corrugation height in Figure 4-44 below. The ultimate tensile strength and necking strain for these composite systems with different corrugation heights can also be plotted on a materials property chart as seen below in Figure 4-45. It is clear that the cases with the larger corrugation heights begin to fill the desirable hole in the right portion of the property space.

At first glance, it is not entirely clear why the cases with the lower corrugation heights do not show improvements in necking strain compared to the straight case. In order to understand this it is necessary to look at the work hardening behaviour of one of these systems. Figure 4-46 below is a Considere plot for the case with the corrugation height of 2mm in comparison to that for the straight reinforced case. The boost in work hardening that is characteristic of an unbending corrugation is still present in this case, however it appears to occur too early in the overall deformation and the work hardening rate returns to that of the straight case around the point at which it equals the stress and necking occurs. Therefore, for this particular combination of materials, a corrugation height of 2mm is not sufficiently high to provide the required boost in work hardening that would lead to an increase in necking strain. A similar conclusion can be made for the case with a height of 1mm. This is an important finding as it suggests that the benefit of corrugation is not universally applicable and that for a given material system a certain degree of corrugation is required in order to obtain any benefit in ductility.

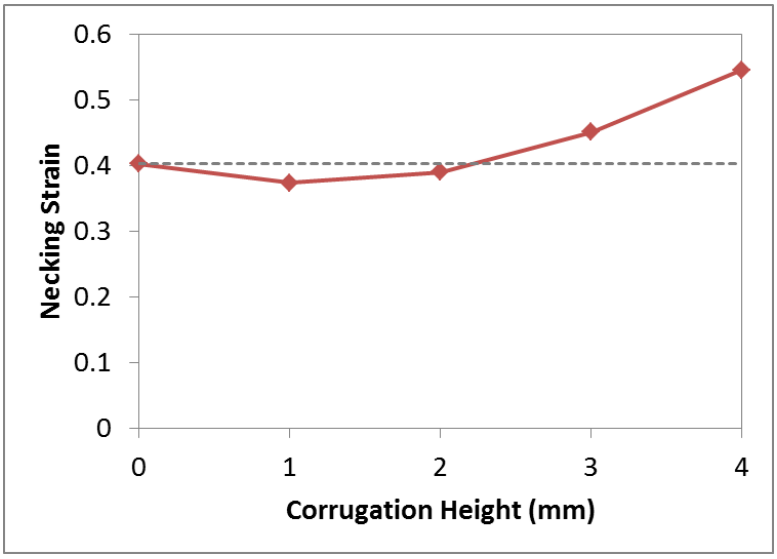


**Figure 4-44: Effect of corrugation height on necking strain for FEM simulations of corrugation reinforced composites with copper matrix and 4130 steel reinforcement. The dashed line represents the necking strain of a straight reinforced composite with a volume fraction of 20%.**

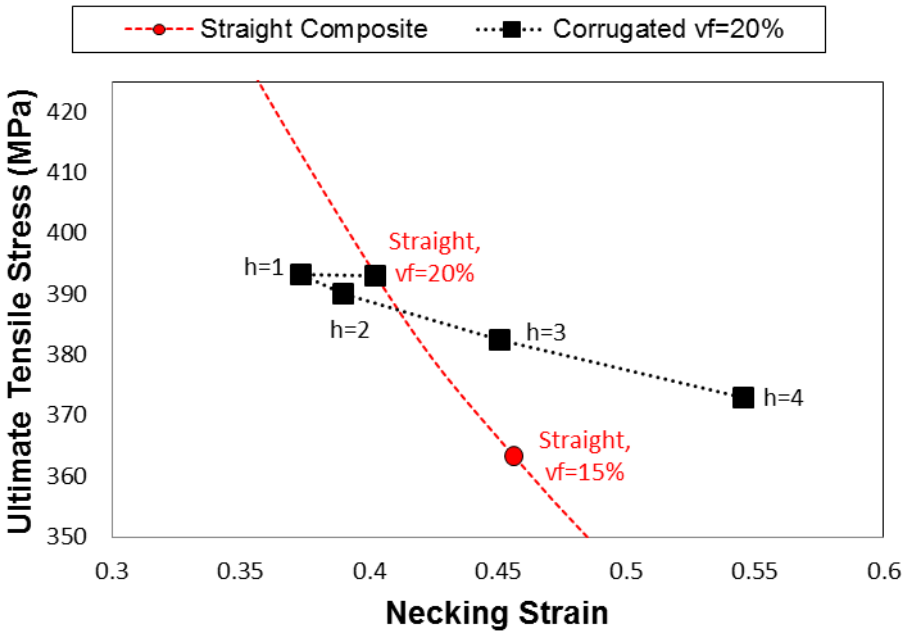


**Figure 4-45: Materials property chart of ultimate tensile strength versus necking strain for both straight reinforced composites and for corrugation reinforced composites of various corrugation heights, h. All the composites consist of a copper matrix and 4130 steel reinforcement.**

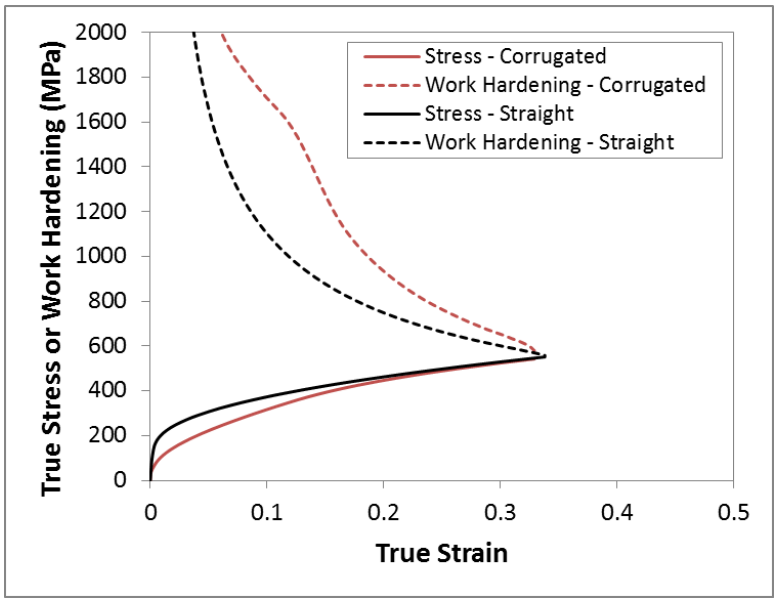


**Figure 4-46: FEM generated Considere plot of work hardening and stress-strain curves of copper-matrix, 4130 steel reinforcement composites. Included are curves for both straight and corrugation reinforced composites.**

#### *4.3.1.2 Effect of Corrugation Period*

Related to corrugation height, the corrugation period has a similar but opposite effect on corrugated composites. Looking at the stress strain curves in Figure 3-33, it is clear that once the period is below a certain threshold value, between 8mm and 10mm, improvement of the necking strain compared to the straight geometry is possible with the improvement increasing as the period is further reduced. Due to the fact that both increasing the height and decreasing the period increase the degree of corrugation, this finding is logical. For the cases when the period is greater than 8mm the corrugation reinforced composite has lower necking strain than the straight case, as seen in the plot of necking strain versus corrugation period in Figure 4-47.

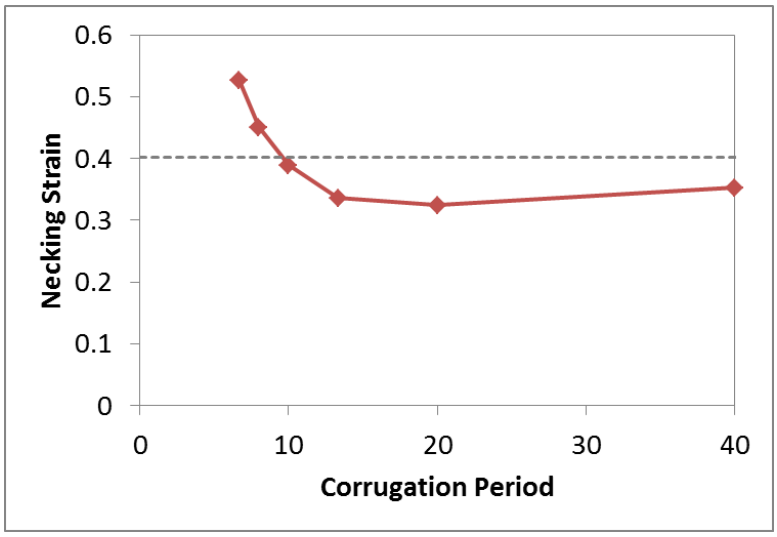


**Figure 4-47: Effect of corrugation period on necking strain for FEM simulations of corrugation reinforced composites with copper matrix and 4130 steel reinforcement. The dashed line represents the necking strain of a straight reinforced composite with a volume fraction of 20%.**

A materials property chart of ultimate tensile stress and necking strain for these scenarios with different corrugation period would look very similar to that in Figure 4-45 for corrugation height. In fact plotting the necking strain versus the corrugation steepness (height/period), as seen in Figure 4-48, it is clear that it is not the height or period alone that determine the necking strain

but rather this degree of corrugation. This is clear as both the cases with variable corrugation height and variable period approximately follow the same trend. From this plot it can be concluded that in this particular system the threshold for corrugation steepness is around 0.35, and above this value benefits in terms of ductility are achievable through corrugation.

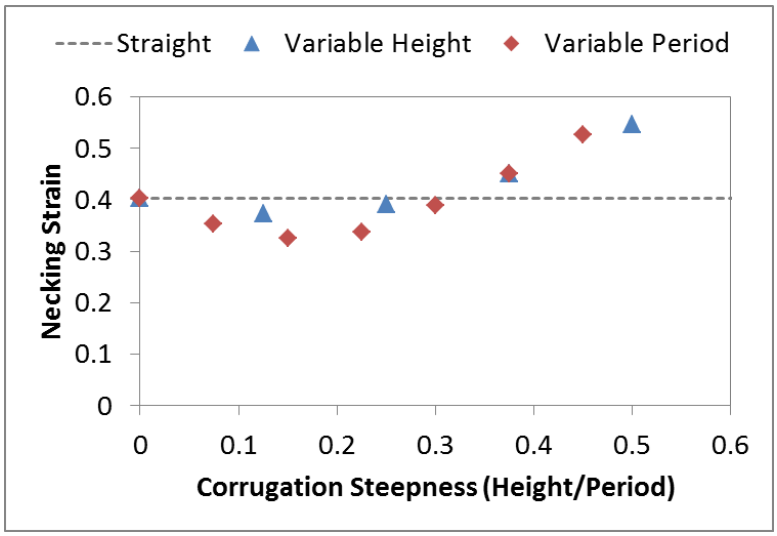


**Figure 4-48: Effect of corrugation steepness (ratio of corrugation height/period) on necking strain for FEM simulations of corrugation reinforced composites with copper matrix and 4130 steel reinforcement. Each of the series represents a set of simulations in which only one geometric variable was changed.**

#### *4.3.1.3 Effect of Corrugation Thickness*

Looking at Figure 3-34, which varies the thickness of straight reinforcements and comparing it to Figure 3-35, which varies the thickness in corrugated composites, it appears that the thickness has a similar effect regardless of the geometry. This effect can be thought of as the volume fraction effect. As the thickness of a reinforcement is increased, and hence the volume fraction increases, the resulting stress-strain response of the composite is to have a higher strength and a lower ductility. This is sensible as the increase in the volume fraction of the reinforcement means that the system now has a larger contribution from the component that is stronger and less ductile. However, if one examines Figure 3-36, which compares both the straight and corrugated

geometries of composites with 10% and 40% volume fractions of reinforcement, it appears that the corrugation is more effective at improving the ductility in systems with larger reinforcement thicknesses, and volume fractions. This idea is shown more convincingly in Figure 4-49, which plots the necking strain as a function of reinforcement volume fraction for both straight and corrugated reinforcement geometries.

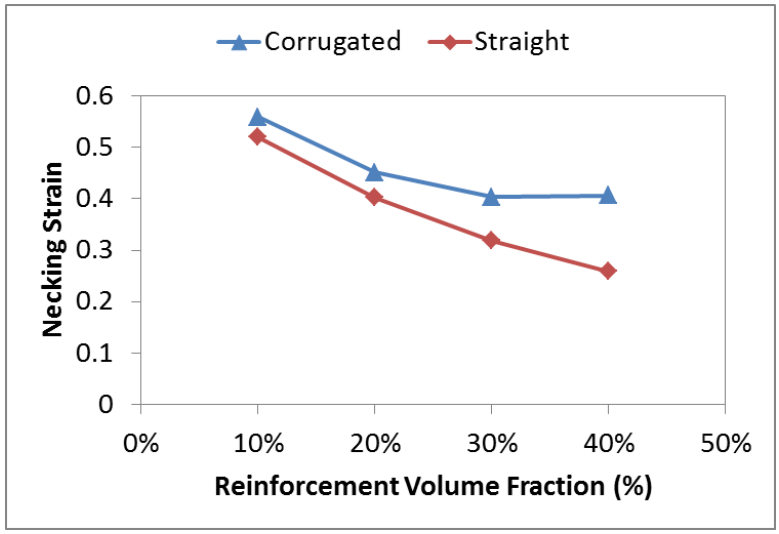


**Figure 4-49: Effect of reinforcement volume fraction (or thickness) on necking strain for FEM simulations of straight and corrugation reinforced composites with copper matrix and 4130 steel reinforcement.**

The reason for this behaviour can possibly be explained by looking at the work hardening behaviour of two different corrugated composites with different volume fractions and thicknesses, as seen in Figure 4-50. The work hardening curve of the sample with the thinner reinforcement has a smaller jump that occurs at lower strains compared to the thicker reinforced sample. The smaller increase in work hardening can likely be attributed to the lower volume fraction as the contribution from the reinforcement in this case would be lower. The reason that this increase in work hardening happens at a lower strain for smaller thickness scenario is not as clear, however one potential reason is that a thicker corrugation leads to a smaller radius of curvature at the peaks and troughs and subsequently requires a larger amount of unbending

compared to the thinner samples with the larger radius of curvature. This larger amount of unbending for the thicker reinforcements leads to the increase in work hardening resulting from the straightening of the corrugation to be delayed to higher values of strain.

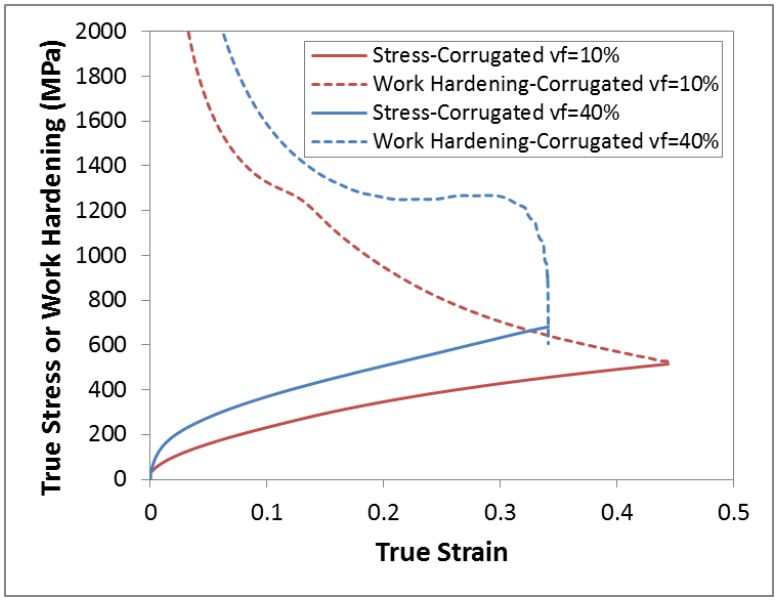


**Figure 4-50: FEM generated Considere plot of work hardening and stress-strain curves of copper-matrix, corrugated 4130 steel reinforcement composites. The 'vf=10%' curves are for a 0.39mm thick reinforcement and the 'vf=40%' curves are for a 1.56mm thick reinforcement.**

#### *4.3.1.4 Effect of Percentage Corrugated*

Finally, the effect of the last geometric parameter that was investigated, the percentage corrugated, can be seen by looking at Figure 3-37. The trends that are observed with regards to the percentage corrugated for these corrugated composites are very different than those seen for isolated corrugations. For isolated corrugations there was a direct relationship between percentage corrugated and ductility, with the necking strain increasing progressively with increases in percentage corrugated. When these corrugations are embedded in a matrix material they behave very differently. In both cases the highest necking strain comes from the sample that is 100% corrugated. However, for the composite cases when the percentage is reduced to 80% corrugated there is a large reduction in necking strain. Further reductions in the percentage

corrugated actually increase the necking strain which is the opposite of what is seen for an isolated corrugation. The trends in terms of necking strain as a function of percentage corrugated for both the isolated and composite systems are summarized in Figure 4-51 below. The reason for this behaviour is not exactly clear.

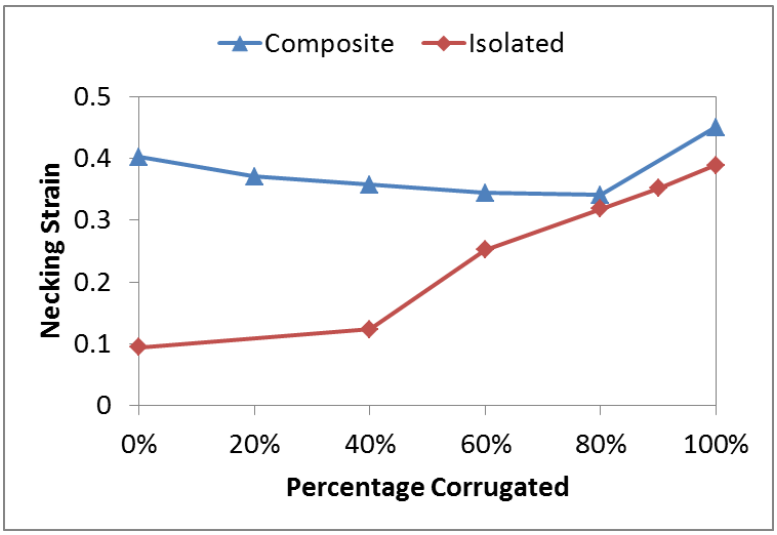


**Figure 4-51: Effect of percentage corrugated on necking strain for FEM simulations of isolated corrugated 4130 steel strips and corrugation reinforced composites with copper matrix and 4130 steel reinforcement.**

It could be expected that the behaviour of a composite with two distinct regions, corrugated and straight, could be explained by thinking of the system as two separate competing subsystems in an iso-stress arrangement. The first subsystem would consist of the straight sections of the reinforcement and the second subsystem would consist of the corrugated sections of the reinforcement. When a load is applied to the overall system, both subsystems would experience the same stress. This stress would initially cause stretching of the first subsection and unbending of the second subsystem. Once this stress causes the necking of either subsystem, no further deformation can occur in the remaining subsystem. The overall strain would be a weighted average of the strains reached in each of the subsystems up to the point of necking. This behaviour however is not observed as there is not a direct relationship between the percentage

corrugated and the necking strain. If this were the case it would be expected that the necking strain of a 50% corrugation composite would lie halfway between that of 100% corrugated composite and a straight reinforced composite. As shown in Figure 4-51 this is clearly not the case.

One hypothesis for this behaviour is that the introduction of a transition from corrugated to straight influences the ability of the corrugation to deform. For this particular system, this transition lowers the strain achievable in the corrugated region to below that of a straight composite and thus the weighted average between the strains in the straight and corrugated regions is a weighted average using a different value for the corrugated contribution. This is why the 80% corrugated case has a lower necking strain than that of the 20% corrugated case as the contribution from this 'worse' corrugation value is weighted more highly in the 80% corrugated case. This however is only a partial explanation as it does not provide a reason why this transition leads to a lower value of strain for the corrugated contribution. One possible explanation for why the transition lowers the corrugated strain contribution is that the transition creates a corrugation geometry locally with a smaller height. In this case instead of having a corrugation that goes from a peak at +1.5mm to a trough at -1.5mm, for a height of 3mm, the corrugation goes from a peak at +1.5mm to the straight portion at the midpoint, 0mm. The corrugation height is locally cut in half and thus the system must be considered to have a height of 1.5mm instead of 3mm. As was shown earlier in Figure 4-44, a corrugation height between 1mm and 2mm will produce worse than a straight reinforced case and should have a necking strain around 0.33. This value for the contribution from the corrugated region agrees nicely with an extrapolation of the trend in Figure 4-51 if the 100% corrugated scenario is ignored, see Figure 4-52.

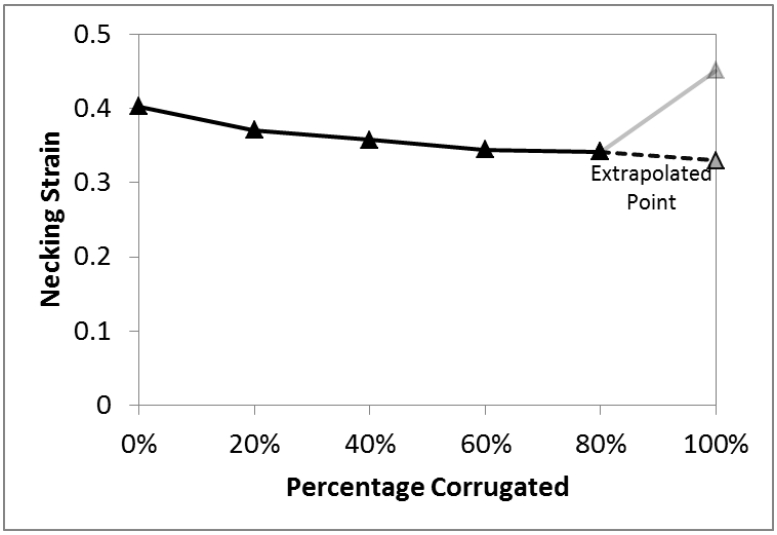


**Figure 4-52: Effect of percentage corrugated on necking strain for FEM simulations of corrugation reinforced composites with copper matrix and 4130 steel reinforcement. The extrapolated point is added to show that the data fits a trend for a sample with a corrugation height of 1.5mm better than the actual height of 3mm.**

### 4.3.2 Effect of Reinforcement Volume Fraction and Spacing

#### *4.3.2.1 Effect of Reinforcement Volume Fraction*

Now that the effect of the different geometric parameters has been established, the next step is to explore the effect of volume fraction of the reinforcing component. Again staying with the copper-matrix, 4130 steel reinforcement system, the effect of the volume fraction can be seen in Figure 3-38 for a straight geometry and in Figure 3-39-Figure 3-43 for composites with corrugated reinforcements of different heights. For all plots there is the obvious trend that as the volume fraction of the stronger reinforcement component is increased, the ultimate tensile strength of the materials increases. The trends that are observed with regards to the necking strain as a function of volume fraction are less predictable. In order to view these trends in a more constructive manner, the ultimate tensile strength and necking strain can be taken from each curve in Figure 3-38-Figure 3-43 and plotted as a point in materials property space. Starting with the data for the straight geometry from Figure 3-38 and the corrugated geometry with a

height of 1.25mm from Figure 3-43, a materials property chart of ultimate tensile strength and necking strain can be generated that shows the trends as the volume fraction is increased for each geometry. This property chart is seen below in Figure 4-53.

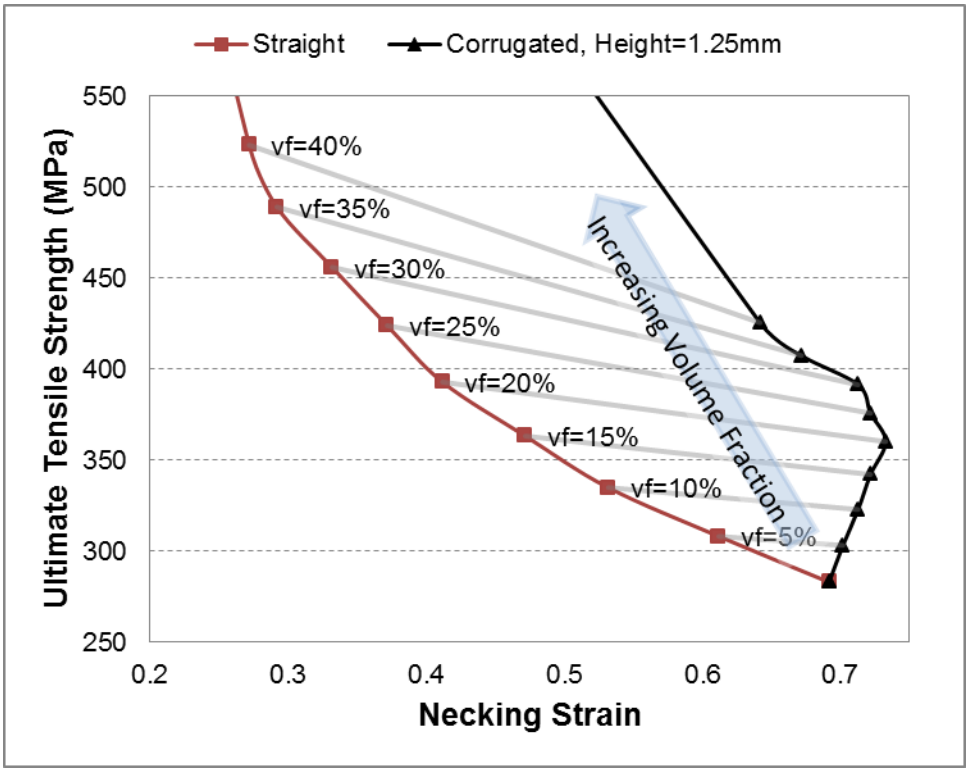


**Figure 4-53: Materials property chart of ultimate tensile strength versus necking strain for composites with copper matrix and 4130 steel reinforcement at various levels of reinforcement volume fraction as a result of different numbers of reinforcements. The 'Straight' points correspond to composites with straight reinforcements and the 'Corrugated' curve corresponds to a corrugated reinforcement geometry with a height of 1.25mm.**

Looking at this plot it is clear that for the straight reinforcement geometry, as the reinforcing volume fraction is increased the necking strain of the composite decreases. For the corrugated case this behaviour is not observed and initial increases in the volume fraction actual lead to improvements in necking strain. Not only is there an improvement in necking strain for the corrugated geometry over the straight geometry at a given volume fraction, but for low values of volume fraction, increasing the volume fraction of the reinforcement offers further gains in

ductility over that of pure copper. The curve corresponding to the corrugated composite is traversing through a very desirable hole in materials property space defined by high strength and ductility. It is intuitive that in going from a pure copper sample to a sample with 5% corrugated reinforcement that a gain in necking strain is possible. In order for this improvement in necking strain to occur there is the prerequisite that the corrugated geometry is such the loading of an isolated corrugation of the same geometry would have a necking strain greater than that of the pure matrix material, in this case copper. If this is true then further increases in volume fraction lead to a larger contribution from the reinforcement and can lead to larger overall necking strains. Eventually the volume fraction of the reinforcement will reach a level such that the corrugations are too close together and they begin to constrain the matrix and ultimately lead to a reduction in necking strain. In this case, this occurred around the 20% volume fraction.

Additional curves corresponding to other corrugated geometries with smaller heights, with the data taken from Figure 3-39-Figure 3-42, can be added to this property chart, as seen in Figure 4-54. Looking at this map it is clear that as the corrugation height is lowered the composite begins to transition towards behaviour more reminiscent of the straight reinforced composites, where increases in volume fraction lead to reductions in necking strain. This transition is logical as the degree of corrugation is being reduced and the reinforcement geometry is nearing that of the straight arrangement. However, the benefit of corrugation is still apparent for most of the corrugated geometries at the volume fractions investigated.

There are a couple of key takeaways from these plots. The first takeaway is that using corrugated reinforcements instead of straight reinforcements allows one to access a desirable region of materials property space. The second takeaway is that the path between 100% matrix and 100% reinforcement that is taken by corrugated samples does not necessarily follow the same general

trend as straight samples, and can actually see increases in necking strain with an increased volume fraction of the less ductile reinforcing material. This could be very advantageous as it unexpectedly allows one to potentially improve on ductility through the addition of less ductile reinforcement materials.

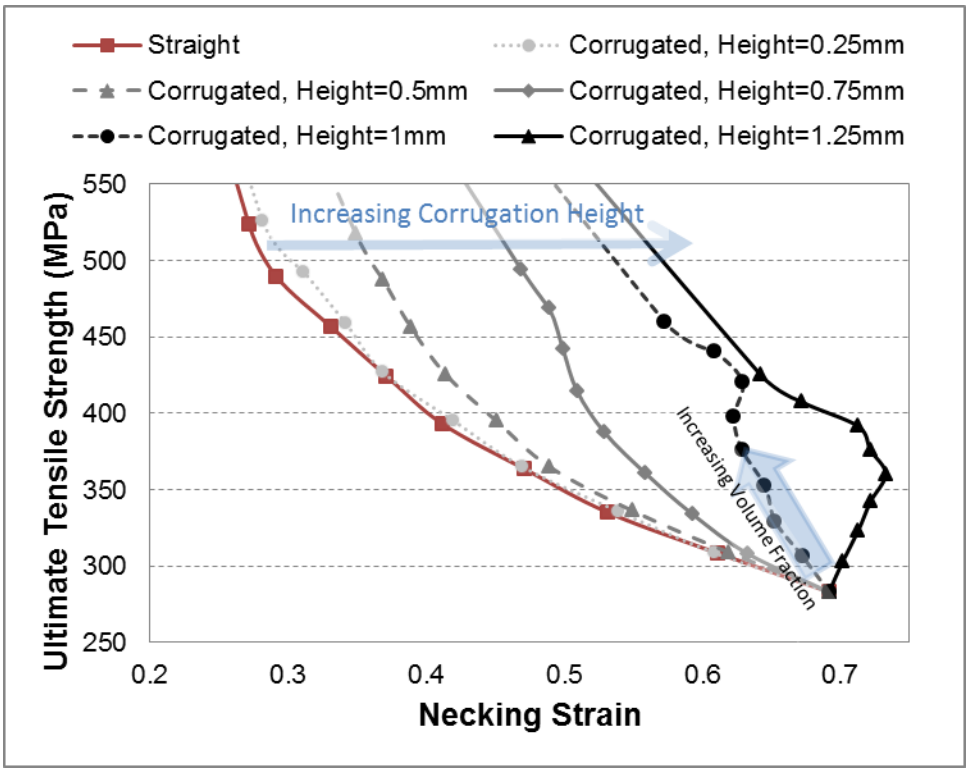


**Figure 4-54: Materials property chart of ultimate tensile strength versus necking strain for composites with copper matrix and 4130 steel reinforcement at various levels of reinforcement volume fraction as a result of different numbers of reinforcements. The 'Straight' points correspond to composites with straight reinforcements and the 'Corrugated' curves each correspond to a corrugated reinforcement geometry with a different corrugation height.**

#### *4.3.2.2 Effect of Reinforcement Spacing*

In addition to exploring the effect of the volume fraction of the reinforcement it is also important to understand what affect the arrangement and spacing of the reinforcements might have on the response of the composite. It was established in the previous chapter that both the straight geometry and the smaller height, 0.75mm, show almost no effect from changing the spacing of

the reinforcements. However, looking at Figure 3-44 for the case with corrugated reinforcements with a larger height of 1.25mm, it is clear that as the spacing between the corrugations is reduced the necking strain is reduced. This can be seen clearly on a plot of necking strain versus reinforcement spacing in Figure 4-55. The reason for this behaviour is not completely clear. It is possible that the constraint that emerges as a result of the reinforcement spacing becomes important only at large values of strain, in the range of where the matrix material would begin to neck if on its own. The matrix in this case is copper, which necks around a strain of 69% when on its own. The spacing may not be important for the straight and small height corrugation geometries as they neck at strains well below this level, whereas the large height corrugation is necking in the range around that of the copper by itself.

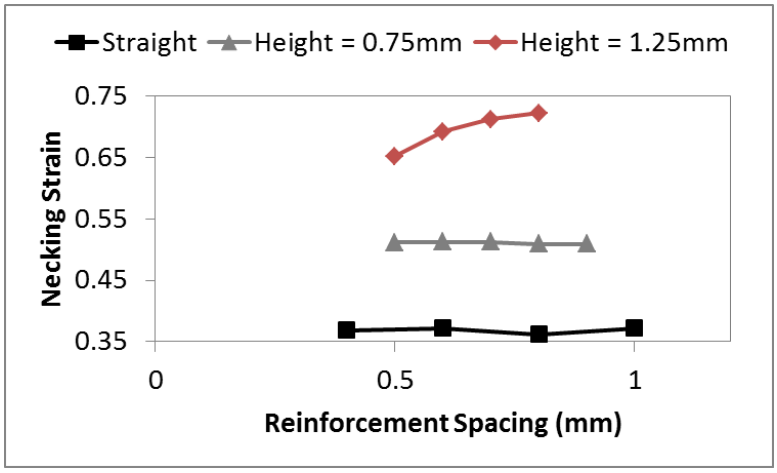


**Figure 4-55: Effect of reinforcement spacing on necking strain for FEM simulations of straight and corrugation reinforced composites of different heights with copper matrix and 4130 steel reinforcement.**

In order to better understand this spacing effect, an additional set of simulations were run that varied the number of corrugated reinforcements and hence the volume fraction, but always maintained the same spacing of 0.5mm. Similar to the simulations run to generate the property chart in Figure 4-53, these corrugations all had the same geometry; a corrugation height of 1.25mm and period of 2mm. This spacing was selected as it is a small spacing that should

impose constraint on the system. The stress-strain curves for these simulations can be seen in Figure 4-56. The data from these curves was extracted and plotted on the same materials property chart, Figure 4-53, that was used before to show the straight case and the corrugated case that had variable spacing. The new version of the chart is seen below in Figure 4-57. It is clear that in this case the tighter spacing between the reinforcements has led to an earlier reduction in necking strain with increasing volume fraction compared to the case with the larger spacing between reinforcements. This suggests, as proposed earlier, that it was the spacing of the corrugations at higher volume fractions that resulted in subsequent reductions in necking strain with increases in volume fraction. When the scenario is changed such that the spacing is fixed this reduction in necking strain when the volume fraction is increased is almost immediate. Therefore, when the space between the corrugations is too small some form of constraint is occurring that is resulting in earlier necking than might be otherwise expected for that specific geometry.

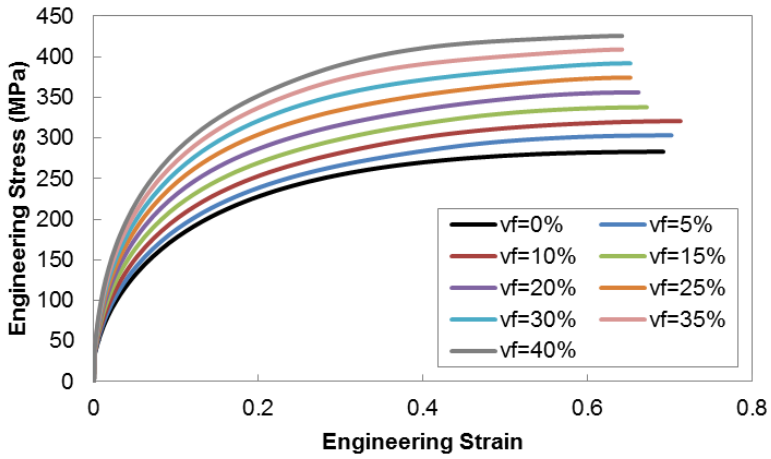


**Figure 4-56: FEM generated stress-strain curves of copper-matrix, corrugated 4130 steel reinforcement composites with variable numbers of reinforcements and hence volume fraction, vf. The reinforcements had a corrugation height of 1.25mm and a spacing of 0.5mm between reinforcements.**

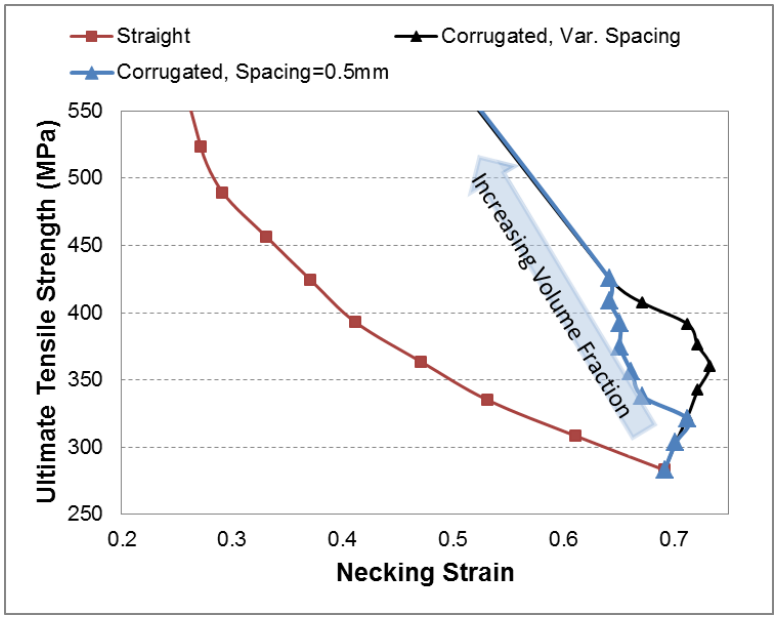


**Figure 4-57: Materials property chart of ultimate tensile strength versus necking strain for composites with copper matrix and 4130 steel reinforcement at various levels of reinforcement volume fraction as a result of different numbers of reinforcements. The 'Straight' points correspond to composites with straight reinforcements and the 'Corrugated' curves correspond to a corrugated reinforcement geometry with a height of 1.25mm. The curve labeled 'Var. Spacing' used different spacing between reinforcements for each of the volume fractions simulated whereas the curve labeled 'Spacing=0.5mm' used a fixed spacing for all volume fractions.**

Finally, in addition to examining the spacing between the reinforcements, it was also important to investigate whether there would be any effect from horizontal offset of the corrugations. This can be thought of as testing the effect of the wave being in phase compared to various degrees of out of phase. Based on the results of the simulations outlined in the previous chapter it seems that the same result is obtained ranging from completely in-phase to completely out of phase with a 180° offset. It would be desirable to look at composites with a larger corrugation height, as these are the ones in which the spacing and arrangement seem to matter most but due to the need to avoid overlapping of reinforcements it is not possible to make corrugated composites with significant volume fractions and large corrugation heights. Therefore, based on the results generated for this system it appears that the horizontal offset of the corrugations has little effect on the stress-strain behaviour of the composite.

### 4.3.3 Effect of Materials

Given the understanding of the effect of geometry, volume fraction and arrangement just presented, it is now sensible to explore the effect of the material properties of the matrix and reinforcement components.

#### *4.3.3.1 Linear Hardening Materials*

The simulations that were first conducted to explore this topic utilized simple linear hardening material models for the components. This allows one to use parametric studies to easily explore the effect of the two key components that comprise a material's plasticity; yield strength and work hardening rate. The first parametric study looked at the effect of matrix yield strength, the results of which can be found in Figure 3-45 and Figure 3-46 for the straight and corrugated reinforcement geometries respectively. Looking at the curves for the straight geometry it is evident that as the matrix yield strength is decreased the ultimate tensile strength of the material decreases and more relevant to this study, the necking strain of the material increases. This behaviour is expected and can be substantiated by doing a fairly simple Considere type calculation, that was presented by Semiatin and Piehler[27] for a sandwich structure. The maximum load condition is:

$$\frac{d}{d\varepsilon}(\boldsymbol{A_m\sigma_m} + \boldsymbol{A_r\sigma_r}) - (\boldsymbol{A_m\sigma_m} + \boldsymbol{A_r\sigma_r}) = \mathbf{0} \qquad (4\text{-}29)$$

where $A_m$ is the cross-sectional area of the matrix, $A_r$ is the cross-sectional area of the reinforcement, $\sigma_m$ is the stress in the matrix and $\sigma_r$ is the stress in the reinforcement. Rearranging the above equation 4-29 and plugging in the linear hardening definitions for stress of the components and dividing by the total cross-sectional area, $A_T$, one gets the following expression:

$$\frac{\boldsymbol{A_m}}{\boldsymbol{A_T}}\left(\frac{\boldsymbol{d}}{\boldsymbol{d\varepsilon}}\left(\boldsymbol{\sigma_{YS,m}}+\boldsymbol{K_m\varepsilon}\right)-\left(\boldsymbol{\sigma_{YS,m}}+\boldsymbol{K_m\varepsilon}\right)\right)+\frac{\boldsymbol{A_r}}{\boldsymbol{A_T}}\left(\frac{\boldsymbol{d}}{\boldsymbol{d\varepsilon}}\left(\boldsymbol{\sigma_{YS,r}}+\boldsymbol{K_r\varepsilon}\right)-\left(\boldsymbol{\sigma_{YS,r}}+\boldsymbol{K_r\varepsilon}\right)\right)=\mathbf{0}$$

Evaluating the derivatives and solving for the necking strain, $\varepsilon_n$:

$$(1-\mathrm{f})\left(\mathrm{K_m}-\sigma_{\mathrm{YS,m}}-\mathrm{K_m}\varepsilon_\mathrm{n}\right)+\mathrm{f}\left(\mathrm{K_r}-\sigma_{\mathrm{YS,r}}-\mathrm{K_r}\varepsilon_\mathrm{n}\right)=0$$

$$\boldsymbol{\varepsilon_n}=\frac{\boldsymbol{(1-f)(K_m-\sigma_{YS,m})+f(K_r-\sigma_{YS,r})}}{\boldsymbol{(1-f)K_m+fK_r}}=\mathbf{1}-\frac{\boldsymbol{f\sigma_{YS,r}+(1-f)\sigma_{YS,m}}}{\boldsymbol{fK_r+(1-f)K_m}} \qquad (4\text{-}30)$$

It is clear in looking at this equation that if the yield strength of the matrix is decreased there should be an increase in necking strain if all else is kept constant. The effect on the necking strain of a straight reinforced composite of increasing each of the material parameters in the equation above is summarized in Table 4-1 below.

**Table 4-1: Summary of the effects of changing linear hardening material parameters on the necking strain of a straight reinforced composite based on a simple Rule of Mixtures model.**

| Variable Change | | Effect |
|---|---|---|
| Increase Matrix Yield Strength ($\uparrow\sigma_{ys,m}$) | Leads to $\rightarrow$ | Decrease in Necking Strain ($\downarrow\varepsilon_n$) |
| Increase Matrix Hardening Rate ($\uparrow K_m$) | | Increase in Necking Strain ($\uparrow\varepsilon_n$) |
| Increase Reinforcement Yield Strength ($\uparrow\sigma_{ys,r}$) | | Decrease in Necking Strain ($\downarrow\varepsilon_n$) |
| Increase Reinforcement Hardening Rate ($\uparrow K_r$) | | Increase in Necking Strain ($\uparrow\varepsilon_n$) |

Looking at Figure 3-46 for the corrugated geometry, this same trend appears whereby a decrease in matrix yield strength results in an increase in necking strain. The effect of the matrix yield strength however is more complicated than just this simple trend, especially when looking at the necking strain of the corrugated geometry relative to that of the straight geometry. Plotting the necking strain as a function of the matrix yield strength for both the straight and corrugated geometries yields an interesting result, as seen in Figure 4-58. Although the necking strains of both the corrugated and straight cases decreases with increasing matrix yield strength, the manner in which they decrease is very different. In fact, the difference in necking strain between

the two geometries shows an interesting response to matrix yield strength. Also plotted in Figure 4-58 is this difference, or improvement, in necking strain that the corrugated geometry offers compared to the straight geometry as a function of matrix yield strength. It appears that at low matrix yield strengths the improvement is minimal with the improvement increasing as the yield strength increases. This improvement peaks at some intermediate value of matrix yield strength and further increases in yield strength lead to a reduction in the gains in necking strain through corrugation. This suggests that there may be a finite zone of matrix yield strengths that allow for benefit through corrugation, given the other fixed parameters of the system. This idea of a desirable range of material properties will be explored further later in the thesis.

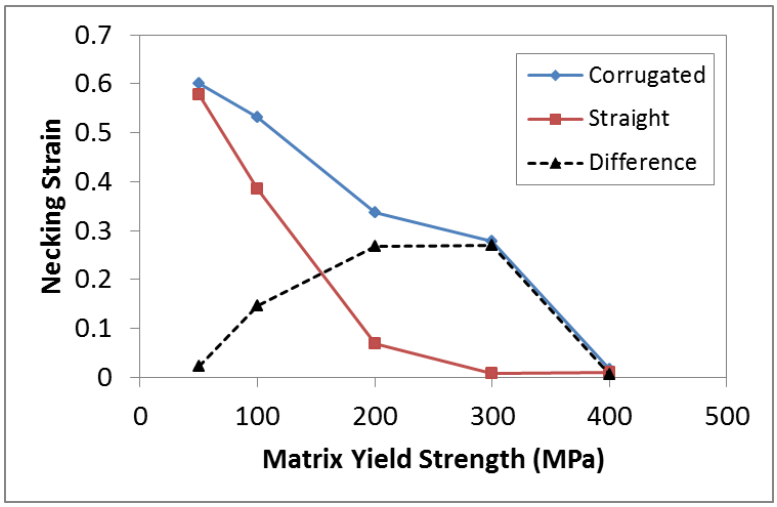


**Figure 4-58: Effect of matrix yield strength on necking strain of FEM simulations of composites with linear hardening component materials under plane strain tension. The 'Difference' points represent the improvement in necking strain of the corrugated composite compared to the straight composite for each matrix yield strength tested.**

The next material parameter of interest is the matrix hardening rate. The effect of the matrix hardening rate on the stress-strain response can be seen in Figure 3-47 and Figure 3-48 for the straight and corrugated geometries, respectively. Looking at the different stress-strain curves in Figure 3-47 it is clear that increasing the matrix hardening rate will lead to an increase in the

necking strain of the straight reinforced composites. This improvement in necking strain as a result of increasing the matrix hardening rate once again matches well with the Considere derivation presented above and summarized in Table 4-1. Now focusing on the curves in Figure 3-48, increasing the matrix hardening rate leads to increases in the necking strain of the corrugation reinforced materials. Once again both the straight and corrugated materials see a similar correlation between the material property and the necking strain, but it is an incomplete picture. Taking the necking strains from these stress-strain curves and plotting them as a function of matrix hardening rate, as seen in Figure 4-59, it is clear that increasing the matrix hardening rate can result in very different improvements in necking strain for the different geometries.

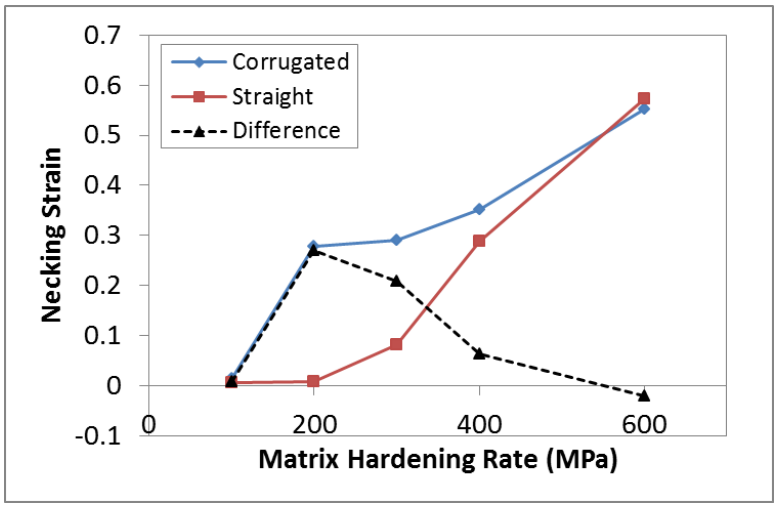


**Figure 4-59: Effect of matrix hardening rate on necking strain of FEM simulations of composites with linear hardening component materials under plane strain tension. The 'Difference' points represent the improvement in necking strain of the corrugated composite compared to the straight composite for each matrix hardening rate tested.**

At low hardening rates both geometries show almost no ductility, but as the hardening rate is increased there is observed a rapid jump in the necking strain of the corrugated arrangement compared to a more gradual increase for the straight geometry. As the matrix hardening rate is further increased the necking strain of the straight composites begins to increase more rapidly

and approaches that of the corrugated composites. Superimposing a plot of the difference in necking strains between the corrugated and straight geometries, shows a maxima of improvement through corrugation at intermediate hardening rates and again suggests a range of material property for which there is benefit through corrugation.

Shifting the focus to the properties of the reinforcement, the next material property of interest is the reinforcement yield strength. Looking at the stress-strain curves that each represent a scenario with a different reinforcement yield strength, Figure 3-49 for the straight geometry and Figure 3-50 for the corrugated geometry, it is evident that the reinforcement yield strength has a very different effect on the necking strain depending on the geometry. Starting with the straight geometry, increasing the reinforcement yield strength leads to a reduction in the necking strain of the composite. This behaviour agrees well with the predictions of the simple Considere calculation above. This trend is followed in the case of the corrugated geometry for the situations in which the reinforcement yield strength is low, in this case below 450 MPa. However, when the yield strength is above 450 MPa, increases in yield strength actually lead to increases in the necking strain. All of this is summarized below in the plot of necking strain versus reinforcement yield strength found in Figure 4-60. Also included in this figure is the improvement in necking strain for the corrugated geometry compared to the straight geometry at each reinforcement yield strength. For this particular property it appears that below some threshold value of reinforcement yield strength, a corrugated sample will achieve a lower necking strain than a straight sample. Above this threshold value, increases in yield strength appear to lead to improvements in the benefit observed from corrugation. As the reinforcement yield strength is further increased the increases in benefit level off and reach a constant value.

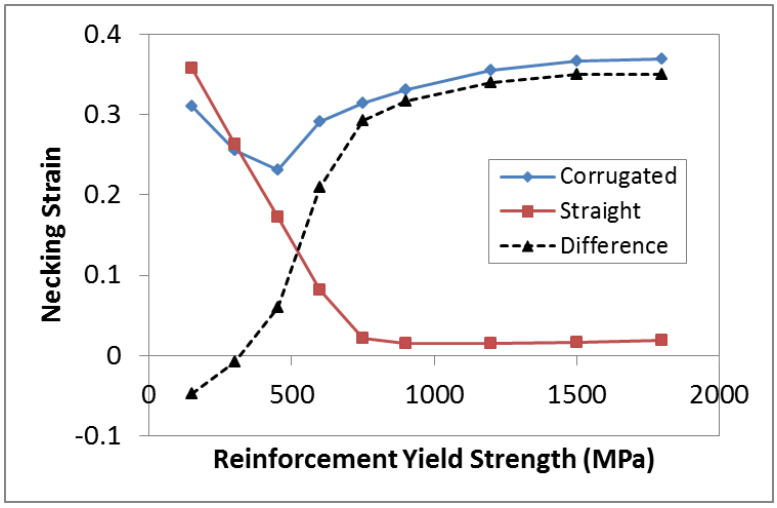


**Figure 4-60: Effect of reinforcement yield strength on necking strain of FEM simulations of composites with linear hardening component materials under plane strain tension. The 'Difference' points represent the improvement in necking strain of the corrugated composite compared to the straight composite for each reinforcement yield strength tested.**

The final material property that was explored in these simplified linear hardening materials was the reinforcement hardening rate. For this property, looking at the relevant stress-strain curves in Figure 3-51 for the straight geometry and Figure 3-52 for the corrugated geometry, it is clear that regardless of geometry increasing the reinforcement hardening rate leads to higher necking strains and ultimate tensile strengths. The trends for the necking strains can be seen clearly in Figure 4-61 for both the straight and corrugated geometries. Also included in this figure is the difference in necking strain between the corrugated and straight scenarios which can be seen to increase as the hardening rate increases due to the more drastic increases in necking strain observed for the corrugated samples. As the reinforcement hardening rate is further increased the increases in necking strain for both the corrugated and straight geometries begin to level off and the benefit of corrugation reaches a plateau value of around 0.3.

Taking into consideration the four plots just presented outlining the effect of the matrix and reinforcement material properties, one can generate a more comprehensive view of the effect of

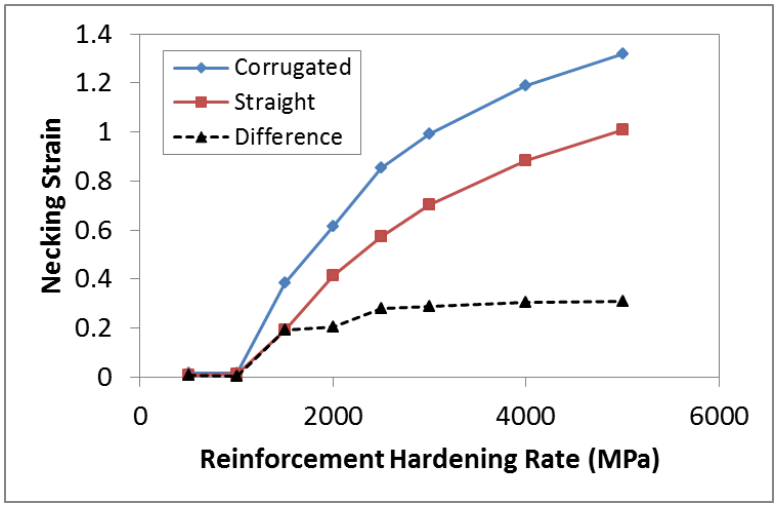


**Figure 4-61: Effect of reinforcement hardening rate on necking strain of FEM simulations of composites with linear hardening component materials under plane strain tension. The 'Difference' points represent the improvement in necking strain of the corrugated composite compared to the straight composite for each reinforcement hardening rate tested.**

the materials on the behaviour of corrugated composites. First off, looking at Figure 4-60 it is clear that as long as the reinforcement possesses a high enough strength relative to the matrix, there is the option to improve the necking strain of a composite through adding a corrugated reinforcement architecture. In order to benefit from corrugation the yield strength of the reinforcement must be high enough such that the transfer of stress occurring from the matrix to the reinforcement during unbending is not high enough to cause significant yielding of the reinforcement in the regions between peaks and troughs. In other words the reinforcement yield strength must be sufficiently high such that the deformation can be dominated by unbending of the peaks and troughs instead of stretching of the regions between peaks and troughs. This can be better understood by looking at the corrugation angle evolution, Figure 4-62, and the stretching strain of the midpoint between peaks and troughs, Figure 4-63, for a couple of different reinforcement yield strengths that span the range of behaviour. The curves corresponding to a yield strength of 300MPa represent a scenario in which there is not benefit from corrugation, whereas the 600MPa and 900MPa yield strength curves represent scenarios in which using a

corrugated geometry improved the composite ductility. Looking at the corrugation angle in Figure 4-62, it is clear that the corrugation angle for the 300MPa yield strength follows an evolution that is almost equivalent to a homogenous material, suggesting that minimal corrugation unbending is actually occurring. This lack of unbending is accompanied by some significant stretching behaviour for the 300MPa yield strength case as seen in Figure 4-63. It is clear that a reinforcement yield strength of 300MPa is too low to prevent stretching and thus minimal corrugation unbending occurs leading to no improvement in ductility compared to the straight case. This is contrasted with the more drastic reductions in corrugation angle seen for the 600MPa and 900MPa yield strength cases. This larger amount of unbending is possible due to the minimal stretching observed in these cases as presented in the stretching strain curves in Figure 4-63. For these scenarios the yield strength of the reinforcement was sufficiently high to prevent the initiation of stretching, allowing the unbending process to occur and ultimately leading to an improvement in necking strain compared to the straight case.

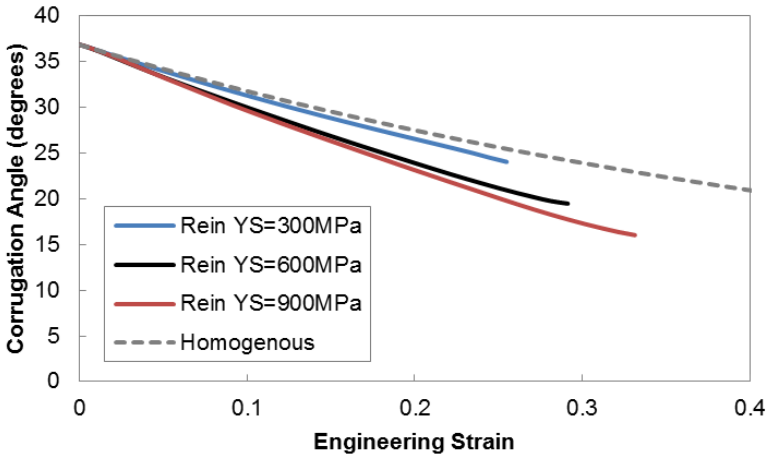


**Figure 4-62: Evolution of corrugation angle with overall strain for a homogenous material, and linear hardening corrugation reinforced composites with variable reinforcement yield strengths.**

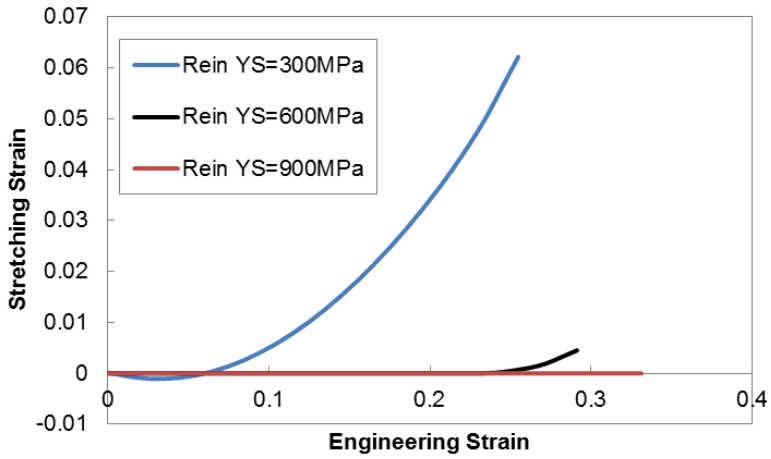


**Figure 4-63: Stretching strain of the midpoint of the corrugated reinforcement, as defined in Figure 4-37, as a function of overall strain for linear hardening corrugation reinforced composites with variable reinforcement yield strengths.**

Still focusing on the reinforcement, it appears that the hardening rate of the reinforcement is really only important insofar as it must be high enough such that it does not lead to early necking, regardless of the geometry. If the reinforcement and matrix hardening rates together lead to an overall hardening rate that is too low, the material will neck early on as the hardening rate is not able to match the stress present in the material. This will happen regardless of the geometry present. Therefore, a sufficiently high reinforcement hardening rate is required for benefit through corrugation as without it the composite will neck quickly regardless of the geometry. This explains why both the corrugated and straight curves in Figure 4-61 show negligible ductility for values of reinforcement hardening rate below a threshold value. Above this threshold, meaningful ductility can be achieved for both geometries and in this case the other properties are such that improvement through corrugation is achievable. It is possible to envision a scenario, where the other properties are such that improvement through corrugation does not occur even as the reinforcement hardening rate is changed.

Shifting the focus to the matrix component, as discussed earlier there appears to exist a range of matrix yield strengths that enable improved ductility through a corrugated reinforcement geometry. If the yield strength of the matrix is below the lower limit of this range, then the benefit from corrugation narrows, as seen in Figure 4-58, and likely disappears altogether. As the matrix yield strength is lowered the composites with a straight geometry are able to achieve necking strains that approach those of their corrugated counterparts. Consider two hypothetical materials with the same hardening rate; material A has a high yield strength and material B a low yield strength. If both materials are stretched to the same amount of plastic strain, the stress in material A will be higher than that in material B. The work hardening in both materials, however, is identical. Therefore, as the materials are further strained, material A will reach a stress which can no longer be matched by the work hardening at an earlier value of strain than material B and thus material A will neck at a lower strain value. Therefore, lower values of yield strength lead to higher values of necking strain as they are at lower values of stress for equivalent values of strain. Returning to the case of straight reinforced composites, when a system has a lower matrix yield strength, it will neck at a larger value of strain. A corrugated reinforcement is only beneficial when its unbending causes a boost in work hardening that delays the strain of necking. For cases when the yield strength is on the low end, the boost in work hardening occurs too early in the deformation process relative to the necking strain it could achieve if a straight geometry were used. The boost in work hardening occurs and then the work hardening rate returns to a level comparable to that of a straight composite, and ultimately little to no gain in ductility occur. When the matrix yield strength is in the intermediate range the boost in work hardening occurs at a level of strain that results in a delaying of the necking strain. Work hardening curves for a low matrix yield strength of 50MPa can be seen in Figure 4-64, and

compared to those of an intermediate matrix yield strength of 200MPa, seen in Figure 4-65, which illustrates this idea of the importance of the timing of the work hardening boost.

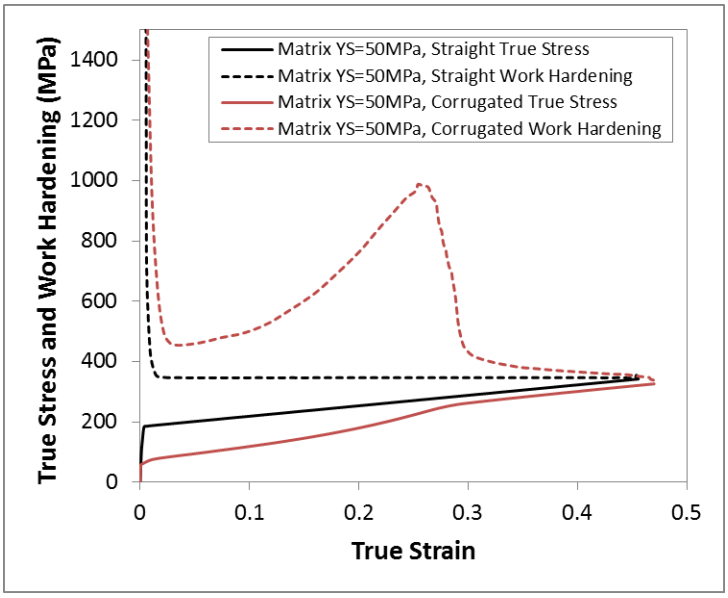


**Figure 4-64: FEM generated Considere plot of work hardening and stress-strain curves of linear hardening composites with either straight or corrugated reinforcements. These curves are for systems with a low matrix yield strength, 50MPa.**

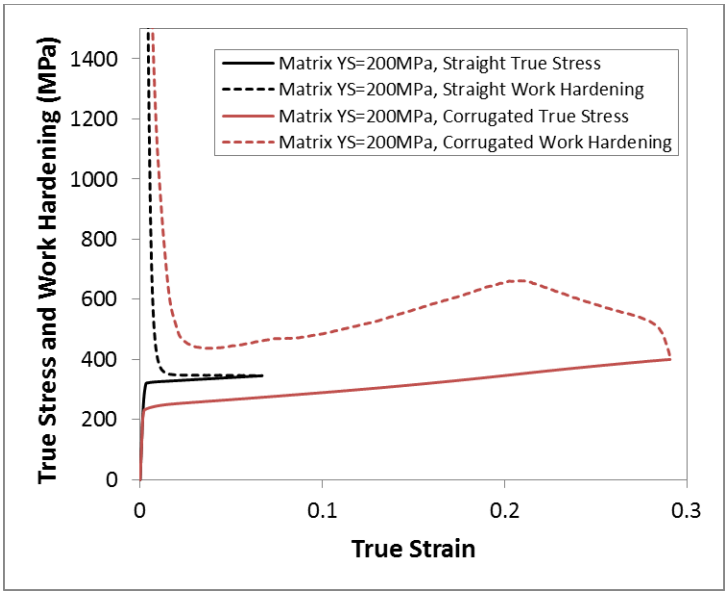


**Figure 4-65: FEM generated Considere plot of work hardening and stress-strain curves of linear hardening composites with either straight or corrugated reinforcements. These curves are for systems with an intermediate matrix yield strength, 200MPa.**

In addition to this concern of a matrix yield strength being too low to take advantage of a corrugated architecture, there is also the concern of the matrix yield strength being too high, as illustrated in Figure 4-58. In order for any unbending to occur the matrix must be deformed and accommodate the movement of the reinforcement. When the matrix yield strength is too large it essentially leads to a condition whereby its plastic hardening rate is almost immediately insufficient to accommodate the stresses present and the material will begin to neck. This will happen regardless of the geometry and since no significant unbending has occurred there is no benefit through corrugation. Any boost in work hardening that could have aided the ductility of the sample would have come in too late to address the high stresses caused by the larger matrix yield strength.

The second matrix material property of interest is the matrix hardening rate. Similar to the matrix yield strength, there seems to be a range of matrix hardening rates that result in a gain in ductility through the use of a corrugated architecture. This is evident in looking at Figure 4-59. When the matrix hardening rate is too low, it results in a similar situation to when the matrix yield strength was too high. That is too say, after the matrix yields the low hardening rate is not high enough to accommodate the high level of stress and the material will neck prior to unbending. The boost in work hardening for a corrugated sample would come in too late to be of use in postponing the necking of the material.

When the matrix yield strength was too low the boost in work hardening came in too early and there ended up being no overall increase in necking strain for the corrugated sample compared to the straight sample. For similar reasons, when the matrix hardening rate is too high, the work hardening of the matrix is sufficiently high to achieve a large necking strain in the straight geometry. This large necking strain is not improved on through a corrugated geometry because

the boost in work hardening that comes from the corrugation unbending occurs too early in the deformation process and the work hardening rate returns to a level similar to that of the straight sample. Thus no gain in ductility is achieved through corrugation under these circumstances.

The trends observed for the matrix properties suggest that it is likely the ratio of the matrix yield strength to its hardening rate (i.e. $\sigma_{ys}/K$) that is the key factor in determining whether there is to be a gain in ductility through corrugation. In fact if the necking strain for the corrugated and straight geometries is plotted as a function of this ratio for both the case with variable matrix yield strength and the case with variable matrix hardening rate, as seen in Figure 4-66, it is clear that this ratio does indeed seem to be the important factor. In this figure both sets of data roughly follow the same trends. It should be kept in mind that the absolute values of the matrix properties relative to those of the reinforcement also likely play a role in determining a set of parameters that can take advantage of a corrugated geometry. This relativity of the matrix properties to those of the reinforcement could possibly be responsible for the differences between the cases observed in Figure 4-66. This relativity is important in determining the stress transfer to the reinforcement and the possibility of early stretching if the reinforcement yield strength is low relative to the matrix properties.

In addition to looking into the corrugation angles and stretching strains to evaluate the unbending processes occurring, there is benefit in looking at the strain maps of these systems. As an example, strain maps after 30% strain can be found in Figure 4-67 for systems with a matrix with a yield strength of 300MPa and hardening rate of 400MPa, a fixed reinforcement hardening rate of 500MPa, and different reinforcement yield strengths. The map for the case with high reinforcement yield strength, 750MPa, shows the heterogeneous, periodic strain pattern that is

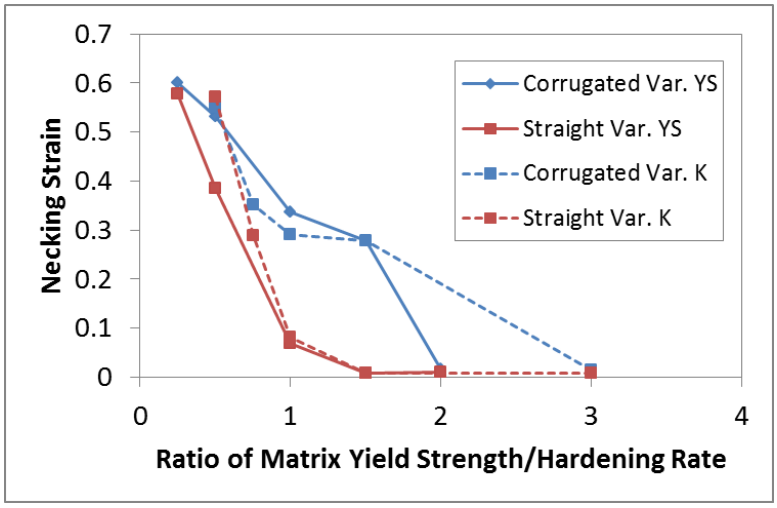


**Figure 4-66: Effect of ratio of matrix yield strength to hardening rate on necking strain of FEM simulations of straight and corrugation reinforced composites with linear hardening component materials. For the curves labeled 'Var. YS' the matrix yield strength was varied while the matrix hardening rate was kept constant at 200MPa and for the curves labeled 'Var. K' the matrix hardening rate was varied while the matrix yield strength was kept constant at 300MPa.**

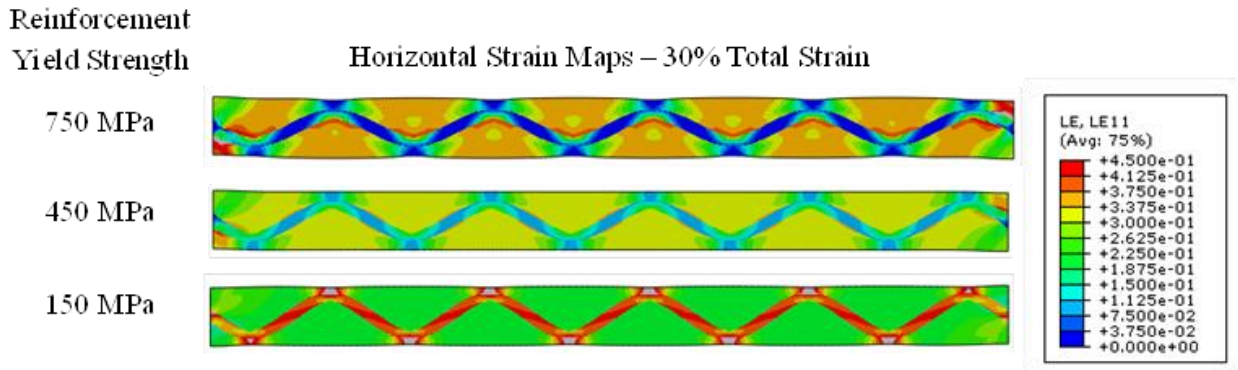


**Figure 4-67: Horizontal strain maps after 30% strain for three systems with linear hardening materials and different reinforcement yield strengths.**

indicative of an unbending corrugation, introduced earlier. This case showed improvement in necking strain through corrugation. As the reinforcement yield strength is reduced, for the 450MPa case, the degree of heterogeneity between high and low strain regions is reduced. In this case minimal gain in necking strain through corrugation was achieved. Finally, for the case with a low reinforcement yield strength, 150MPa, the reinforcement shows higher strains than the matrix and no unbending is occurring. In this case the straight reinforced geometry has higher

necking strains than the corrugated geometry. The variations in these strain maps suggest that the acquisition and analysis of strain maps can be useful in identifying when a system is likely to not show benefit through corrugation. When the characteristic strain pattern emerges, it is predictive of an unbending corrugation. This in itself is not sufficient to conclude that there is improved ductility through corrugation; however, the absence of this pattern conclusively suggests no benefit through corrugation will occur.

The reason that these strain maps cannot be used to definitively confirm that benefit through corrugation will occur can be depicted by looking at strain maps of systems with different matrix hardening rates. Consider three systems with different matrix hardening rates, 100MPa, 200MPa and 600MPa and fixed matrix yield strength, 300MPa, fixed reinforcement yield strength, 750MPa, and fixed reinforcement hardening rate, 500MPa. The first system necks early for both corrugated and straight geometries due to the low hardening rate. The second system shows large improvement in necking strain through corrugation. The third system shows no improvement in ductility through corrugation, though both the straight and corrugated systems have large necking strains. In this third system the boost in work hardening from the unbending corrugation comes in too early, and necking is not delayed at all. Looking at strains maps, Figure 4-68, of the second and third system after 30% strain, the first system being excluded due to its early necking, it is difficult to predict that the third system will show no improvement through corrugation. Both systems show strain maps with the characteristic patterns, and therefore unbending is occurring for both systems. However, in the third system the unbending does not lead to improvement in necking strain. It is for this reason that although the strain maps can be used to determine whether unbending is occurring they cannot be used to definitively predict whether the corrugated architecture leads to an improvement in necking strain.

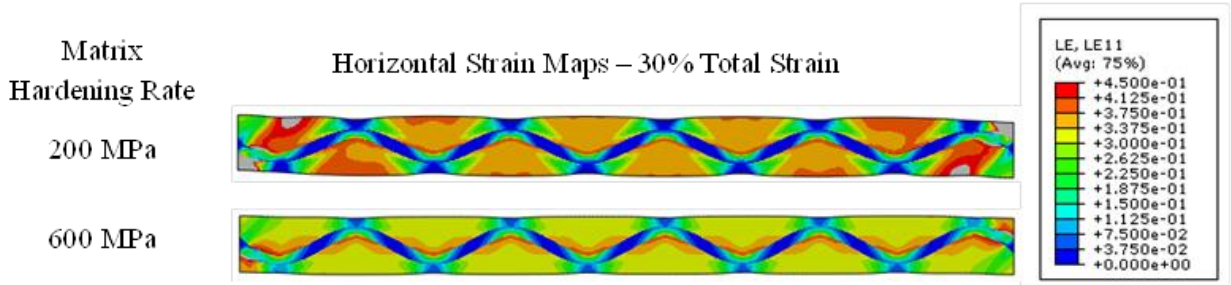


**Figure 4-68: Horizontal strain maps after 30% strain for two systems with linear hardening materials and different reinforcement yield strengths.**

#### *4.3.3.2 Power-Law Hardening Materials*

Thus far, all of the discussion with regards to the effect of the materials on the composite behaviour has focused on the linear hardening materials. These linear hardening materials are simpler in their formulation due to the straightforwardness in separating the contributions of yield strength and hardening rate. This allows for an easier examination on the effects of these key material properties on the mechanical response of corrugated composites. Although these linear hardening materials are very useful in parsing out the important influences of yield strength and hardening rate, in reality, metals are more likely to exhibit plastic deformation behaviour that follows a power-law hardening model. It is for this reason, that composite systems using power-law hardening components were also considered and the effects of their material parameters explored.

Focusing first on the matrix material, and in particular the matrix hardening coefficient, K, it is apparent in looking at the stress-strain curves in Figure 3-53 for straight reinforced composites and in Figure 3-54 for corrugation reinforced composites, that the matrix K value acts a stress multiplier, regardless of the geometry. Increasing the value of the matrix K, increases the flow stress in the material at all values of strain. In addition, there is a trend present for both the straight and corrugated geometries in which the necking strain decreases with a reduction in matrix K. This is clearer in a plot of necking strain versus matrix K for the straight and

corrugated geometries, seen in Figure 4-69 below. Also, included in this figure is the difference in necking strain between the corrugated and straight geometries for the different values of matrix K. It is clear that the necking strain of the corrugation reinforced composites is less sensitive to changes in matrix K than the straight reinforced composites. This leads to a scenario in which the benefit in necking strain through corrugation increases as the matrix K value is reduced. Reducing the value of the matrix K reduces the flow stress in the matrix, and thus the corrugated reinforcement is under less constraint and can unbend to a larger degree. This would result in a boost in work hardening that partially combats the reduction in work hardening that accompanies a reduction in matrix K. This explains why the benefit through corrugation increases as the matrix K value is reduced, as the reduction in the work hardening for the straight geometry is more pronounced than for the corrugated geometry.

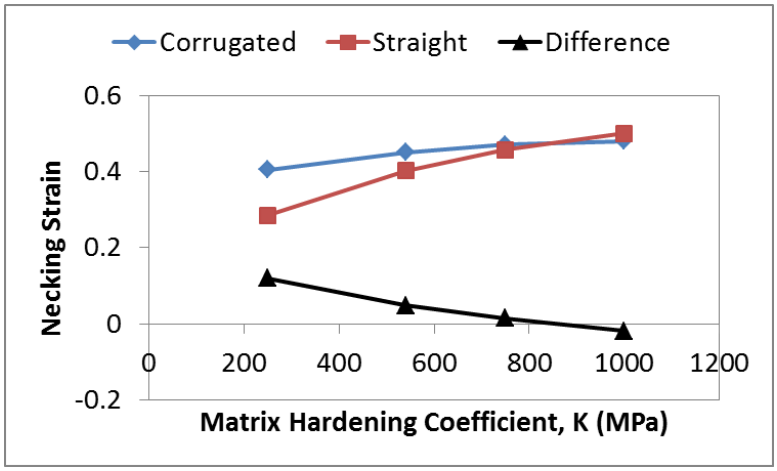


**Figure 4-69: Effect of matrix hardening coefficient, K, on necking strain of FEM simulations of straight and corrugation reinforced composites with power-law hardening component materials. The 'Difference' points show the improvement in necking strain of the corrugated composite compared to the straight composite for each matrix K tested.**

The next material parameter of interest is the matrix hardening exponent, n. Figure 3-55 and Figure 3-56, show the effect of the matrix n parameter on the stress-strain curves for straight and corrugated composite systems, respectively. The general effect of reducing the value of the

matrix n is an increase in the stress of the composite, culminating in an increase in ultimate tensile strength, and a reduction in the necking strain of the composite. This occurs for both the straight and corrugated composites. A closer look at the comparative effect of the matrix n on the necking strain for the two geometries however yields a more interesting result. This is seen in a plot of necking strain versus matrix n for both geometries, with the difference in necking strain between the geometries also included, as seen in Figure 4-70. At low values of matrix n the straight and corrugated composites have similar necking strains, however as the value of matrix n is increased the necking strain of the corrugated composite begins to outpace that of the straight composite. This benefit in necking strain through corrugation initially increases with increasing values of matrix n, but eventually decreases and the benefit through corrugation recedes. The lack of benefit through corrugation at low values of matrix n is logical. Low values of matrix n lead to a rapid reduction in work hardening rate as strain is increased and ultimately neck at lower values of strain. This lack of matrix hardening coupled with high matrix flow stress during the early stages of deformation results in large stresses transferred to the reinforcement, which initiates stretching and hinders unbending, and also leads to a matrix material unable to accommodate the deformation required for unbending without necking. Thus, low values of matrix n lead to low necking strains for both the straight and corrugated geometries. As the matrix n is increased, not only does the necking strain of the straight composite improve due to lower flow stresses and higher hardening rates, but it also leads to conditions that are more amenable to the corrugation unbending. The ability of the corrugation to unbend to a larger degree allows the composite to take advantage of the boost in work hardening and ultimately leads to a larger necking strain and thus a larger benefit through corrugation. However, the increases in matrix n value will reach a point wherein the improved ductility

provided by the higher matrix n value is such that there is no need to have a corrugation to increase the necking strain. In these cases the boost in work hardening that comes from an unbending corrugation occurs too early in the deformation process and the work hardening returns to the level of a straight composite prior to the initiation of necking. This explains why the benefit from corrugation reaches a peak value and further increases in matrix n lead to a reduction in the benefit from corrugation. This same concept was discussed earlier with regards to linear hardening systems and is illustrated in Figure 4-59.

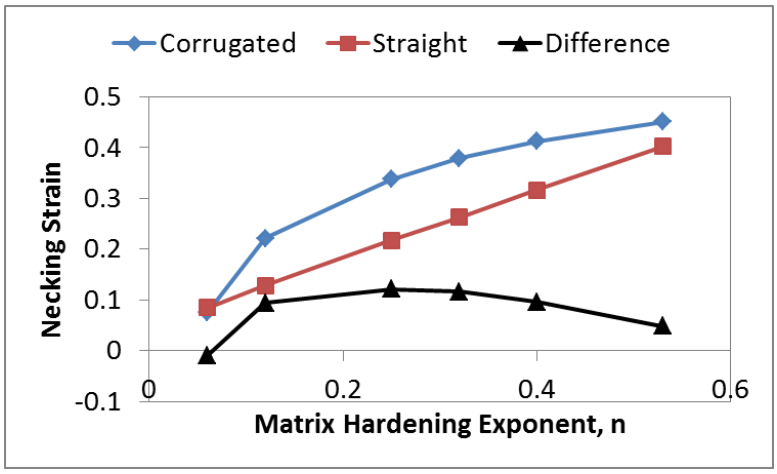


**Figure 4-70: Effect of matrix hardening exponent, n, on necking strain of FEM simulations of straight and corrugation reinforced composites with power-law hardening component materials. The 'Difference' points show the improvement in necking strain of the corrugated composite compared to the straight composite for each matrix n tested.**

The next matrix property explored was the matrix yield strength. The matrix yield strength was shown to have very minimal impact on the behaviour of these materials. This may seem somewhat surprising given the effect of yield strength observed earlier for the linear hardening materials, however, this lack of an effect is due to the fact that the yield strength in the power-law hardening materials only dictates the onset of plastic behaviour and has nothing to do with the subsequent stress levels as a function of plastic strain.

In addition to looking at the effect of the matrix material parameters, the material parameters of the reinforcement were also investigated. The series of stress strain curves shown in Figure 3-57 and Figure 3-58 show the effect of changing the reinforcement hardening coefficient, K for straight and corrugated composites, respectively. Similar to the matrix K value, increasing the reinforcement K value leads to increases in the flow stresses of the composite and the ultimate tensile strength for both the straight and corrugated geometries. However, unlike the trend seen for the matrix K parameter, decreases in the reinforcement K value actually lead to increases in the necking strain of the composite for both geometries, as illustrated in the plot in Figure 4-71. Also included in this plot is the difference in necking strain between corrugated and straight composites as a function of reinforcement K.

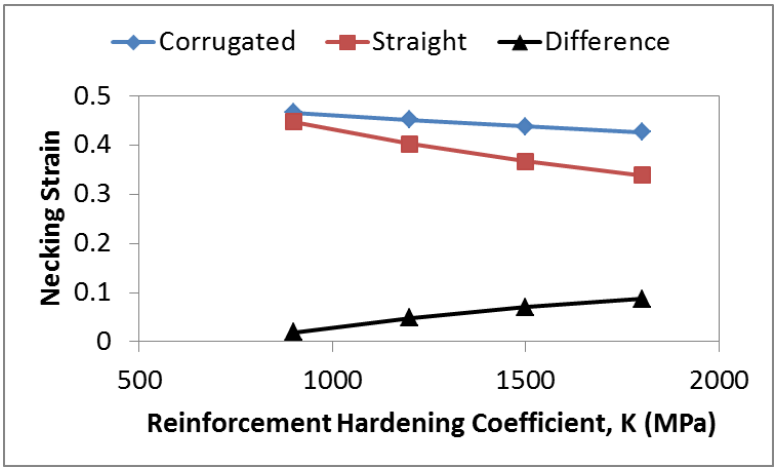


**Figure 4-71: Effect of reinforcement hardening coefficient, K, on necking strain of FEM simulations of straight and corrugation reinforced composites with power-law hardening component materials. The 'Difference' points show the improvement in necking strain of the corrugated composite compared to the straight composite for each reinforcement K tested.**

Looking at this plot it is evident that increasing the reinforcement K value leads to larger increases in the benefit in necking strain through corrugation. Increasing the reinforcement K value increases the stress required to deform this material to the same amount of strain. This means that a larger amount of stress transfer from the matrix is required to cause stretching of the

reinforcement, which means that the reinforcement should be capable of unbending to a larger degree prior to the emergence of stretching dominated behaviour. This unbending results in a boost in work hardening for the corrugated composites that is absent for the straight composites, which can act to counteract the increase in flow stress that accompanies a higher reinforcement K value, and lead to an improvement in necking relative to the straight composites.

The next reinforcement parameter of interest is the reinforcement hardening exponent, n. The effect of reinforcement n is illustrated in the series of stress strain curves presented in Figure 3-59 for straight composites and Figure 3-60 for corrugated composites. Similar to the trends observed with regards to the matrix n value, these figures show that increasing the reinforcement n value leads to larger stresses and smaller necking strains. The relationship between the necking strain and the reinforcement n value is better illuminated in Figure 4-72, which takes the necking strain values from the stress-strain curves and plots them versus reinforcement n for the straight and corrugated cases. Once again, the difference in necking strain is also included. The effect of reinforcement n on the necking strain seems to be fairly similar for the straight and corrugated geometries. The difference in necking strains increases slightly as reinforcement n is increased initially, followed by a peak and subsequent reduction. This behaviour is similar to that for matrix n, though it has a more muted effect. It is likely that the matrix n value has more importance in dictating the necking strain of the corrugated composite materials. Perhaps, a more dramatic trend would emerge if the matrix n value itself was lower, allowing for larger benefit through corrugation when attainable.

The final reinforcement parameter that was studied was the reinforcement yield strength which for similar reasons to those discussed above for the matrix yield strength shows no effect on the stress-strain behaviour of these composites.

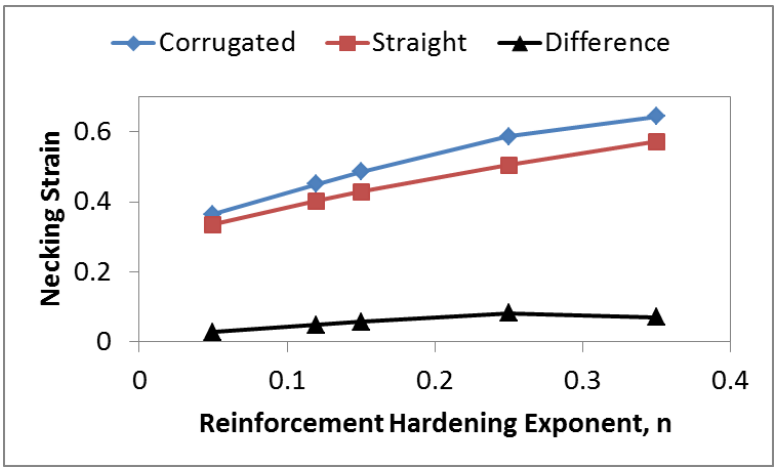


**Figure 4-72: Effect of reinforcement hardening exponent, n, on necking strain of FEM simulations of straight and corrugation reinforced composites with power-law hardening component materials. The 'Difference' points show the improvement in necking strain of the corrugated composite compared to the straight composite for each reinforcement n tested.**

### 4.3.4 Benefit Maps and Surfaces

It was concluded earlier that for isolated corrugations the properties of the material had the same effects on stress-strain behaviour regardless of the geometry that was present. This however is not the case when the corrugation is embedded in the matrix material. There is significant interplay between material properties and geometry that affects the stress-strain behaviour of these composite materials. Given the analysis above, it is clear that some combinations of material and geometric parameters result in systems that achieve higher necking strains when using a corrugated reinforcement geometry and other combinations of parameters achieve higher necking strains when using a straight corrugation geometry. If one is looking to design a composite that has improved ductility it would be beneficial to have a more comprehensive method of identifying potential corrugated systems. A useful tool for these purposes would be a set of maps that identify regions of property space that are capable of improving ductility by replacing a straight reinforcement geometry with a corrugated geometry. For the purposes of this work, these maps will be termed 'benefit maps'. In an ideal situation these maps would fill a

property space that is n-dimensional, where n is the number of material and geometric parameters being varied. This unfortunately would be impossible to visualize and extremely difficult to generate. Therefore, instead of creating a map of n-dimensional space, work was completed to create 2 and 3 dimensional slices of this space that would require fixing the values of some of the parameters. Although not quite as comprehensive, these slices still provide valuable information for the selection of material and geometric parameters in the design of these composite systems.

Focusing on the simpler linear hardening material systems, based on the trends observed above for the different material parameters, it was resolved that the most valuable definition of property space for these benefit maps would consist of matrix hardening rate on one axis and reinforcement yield strength on the other axis. This requires the corrugation geometry, matrix yield strength and reinforcement hardening rate to be fixed for a given benefit map. However, the effect of these other parameters can still be captured by observing how changing their values, shifts the boundaries of the benefit map. The matrix hardening rate was chosen as a variable for the map because there is clearly a finite range of values of this variable in which a benefit in ductility is achieved from corrugation. The matrix yield strength could also have been chosen for this reason, but due to their interrelatedness only one of them needed to be selected for this map. The reinforcement yield strength was selected as a variable for the map, as there exists a threshold value of this parameter below which benefit through corrugation is not possible. The reinforcement hardening rate was not selected due to the fact that its value has similar effects on both straight and corrugated geometries.

Before explaining how these maps were generated it is useful to define exactly what these maps are showing and what the different regions will represent. The map will be defined using matrix

hardening rate on the y-axis and reinforcement yield strength on the x-axis. These maps will consist of two regions; one region represents a set of conditions for which the ductility can be improved through the use of a corrugated geometry, called the 'benefit' region, and a second region in which the conditions are such that corrugation will yield no real improvement in ductility over a straight geometry, called the 'no benefit' region. In order for a set of properties to be designated as belonging to the benefit region, the improvement in necking strain of the composite with the corrugated geometry must be at least 0.05 over that of the necking strain for the straight composite. This is an arbitrary limit that was selected for convenience sake and changing its value would only serve to slightly shift the boundaries between the two regions on the map.

The maps were generated by determining sets of properties that correspond to points along the boundaries between the two regions. These boundaries will be referred to as 'benefit boundaries'. For a given map, the corrugation geometry, matrix yield strength and reinforcement hardening rate are fixed. The points along the benefit boundaries were determined by selecting a value for the reinforcement yield strength and then running simulations of both corrugated and straight composite systems with different values of matrix hardening rate, similar to the process used to generate the stress-strain curves in Figure 3-47 and Figure 3-48, and the necking strain plot in Figure 4-59. Initially, the values of matrix hardening rates were selected to span a large range of values to give a rough idea of where the benefit boundaries will lie. In order to illustrate the procedure for determining these boundaries, the system used to generate Figure 4-59 will be taken as an example. It should be reiterated that for this system, the matrix yield strength is fixed at 300MPa, the reinforcement yield strength and hardening rate are fixed at 600MPa and 500MPa, respectively, and the geometry of the corrugation is constant with a corrugation height

of 3mm, period of 8mm, thickness of 0.78mm and volume fraction of 20%. Looking at the plot in Figure 4-59, it could be estimated that there will be a point on an upper benefit boundary that has a matrix hardening rate value between 400-600MPa. Using this information, additional simulations would be run with a matrix hardening rate value of 500MPa to try and narrow the range in which the upper benefit boundary point lies. Based on the result of this, further simulations with different matrix hardening rates would be conducted until the benefit boundary point was bounded by a 10MPa gap in matrix hardening rates. In order words, a matrix hardening rate of X MPa was found to give an improvement in necking strain through corrugation greater than 0.05 and a matrix hardening rate of X+10 MPa was found to give an improvement in necking strain less than 0.05. If this is the case the point on the upper benefit boundary would be selected as X+5 MPa. For the example described above, a plot of the necking strains for corrugated and straight geometries, and the difference between them was generated in Figure 4-73, with the new points corresponding to this pinpointing exercise added to the plot. Also included in this plot is a line at a strain of 0.05, representing the cut-off point used to determine the benefit boundary point. Zooming in on the region of the upper benefit boundary and focusing on the difference in necking strain between the corrugated and straight cases, as seen in Figure 4-74, it is evident that for this particular case the value for the upper benefit boundary point is 435MPa.

Again looking at Figure 4-59, it is clear for the system with reinforcement yield strength of 600MPa that there should be a point on a lower benefit boundary with a matrix hardening rate value between 100-200MPa. Using a similar pinpointing technique to that described for the upper benefit boundary point, the point can be identified that lies on the lower benefit boundary. The main difference in the technique used for the lower boundary is that the necking strain for

the straight case is not required in order to pinpoint the matrix hardening rate at the boundary, as the necking strain is negligible (<0.01) for all values. This is in contrast with the necking strain for the corrugated case, which is either very small (<0.05), when there is no benefit from corrugation or it is significant (>0.1) when there is a benefit from corrugation.

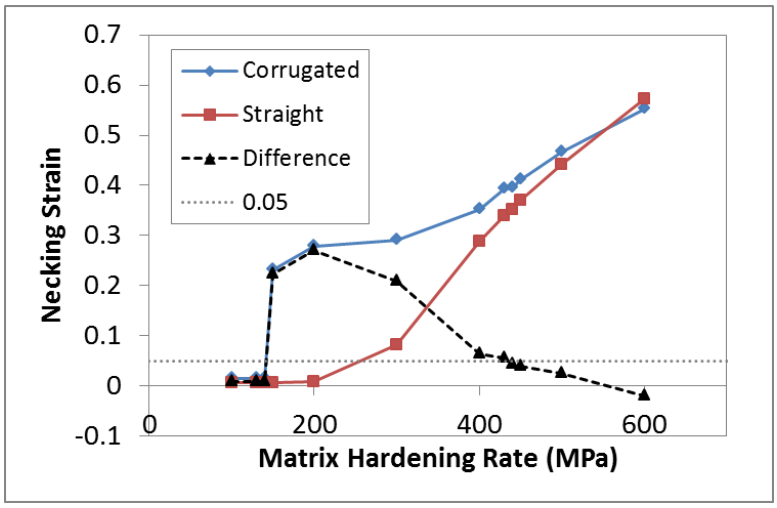


**Figure 4-73: Updated version of Figure 4-59 with additional data points used for generating benefit boundary points. This plot shows the effect of matrix hardening rate on necking strain of FEM simulations of straight and corrugation reinforced composites with linear hardening component materials. The 'Difference' points represent the improvement in necking strain of the corrugated composite compared to the straight composite for each matrix hardening rate tested.**

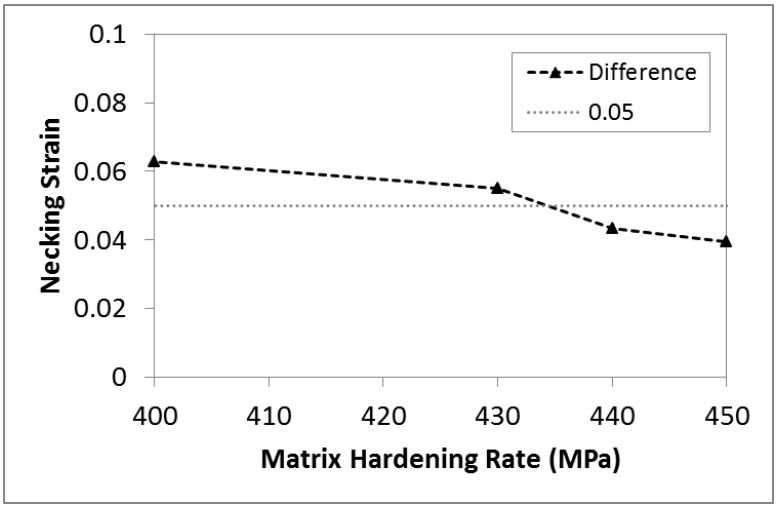


**Figure 4-74: Zoomed in version of Figure 4-73, focusing on the region of the upper benefit boundary point.**

Therefore, in order to reduce the number of simulations required only the corrugated geometry was tested when pinpointing the location of the lower benefit boundary points. This procedure was applied to the example system with the reinforcement yield strength of 600MPa and additional points were added to the plot of Figure 4-59, in the region around the lower benefit boundary, as seen in the new plot in Figure 4-73. This region is blown up in Figure 4-75, and focuses only on the corrugated necking strain, which for these systems is almost equivalent to the difference in necking strains. Looking at this figure it can be determined that the value of the matrix hardening rate for the lower benefit boundary is 145MPa.

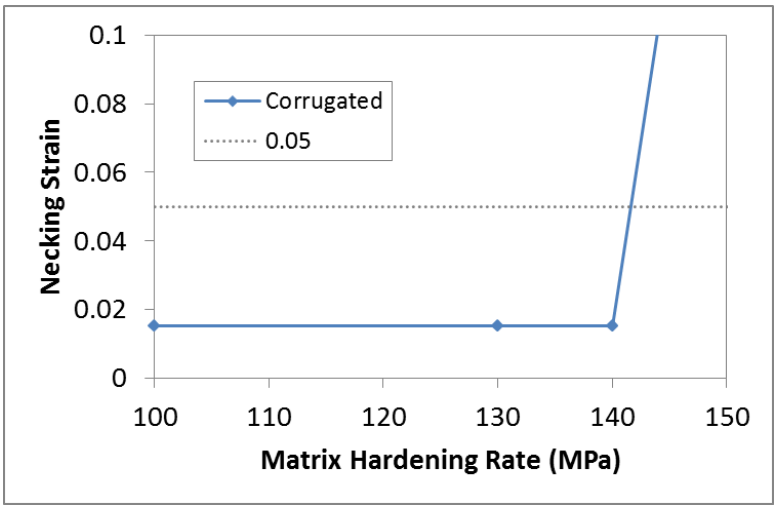


**Figure 4-75: Zoomed in version of Figure 4-73, focusing on the region of the lower benefit boundary point.**

This process can then be repeated for different values of reinforcement yield strength in order to obtain other points along the upper and lower benefit boundaries and thus complete the benefit map. Continuing with this sample system, the upper and lower benefit boundaries were determined by completing this process for a number of reinforcement yield strengths spanning the range between 375MPa-900MPa. The result of using this technique is a complete benefit map, seen in Figure 4-76 below.

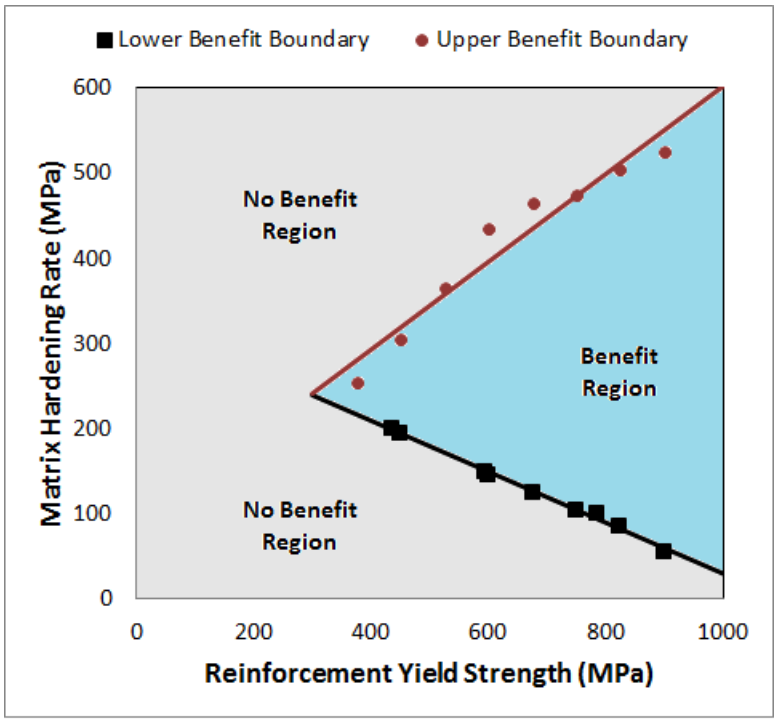


**Figure 4-76: Benefit map showing regions of material property values in which gains in necking strain are achieved through corrugation. This map represents a system with fixed matrix yield strength at 300MPa and reinforcement hardening rate at 500MPa along with a constant corrugation geometry with corrugation height of 3mm, period of 8mm, thickness of 0.78mm and volume fraction of 20%. The solid boundary lines outlining the benefit region are fitted lines for the benefit boundary points.**

Also, included on this benefit map are fitted lines that can be used to roughly define the benefit boundaries. For this system the equation of the upper benefit boundary is;

$$K_{M,upper} = 0.52\sigma_{YS,r} + 87 \quad (4\text{-}31)$$

And the equation for the lower benefit boundary is;

$$K_{M,lower} = -0.30\sigma_{YS,r} + 329 \quad (4\text{-}32)$$

where $K_M$ is the matrix hardening rate and $\sigma_{ys,r}$ is the reinforcement yield strength. These equations are only valid for reinforcement yield strengths above 300MPa, and could be used to estimate the upper and lower benefit boundary points for a given reinforcement yield strength. Any value of $K_M$ between these values represents a system for which corrugation will lead to gains in ductility.

Now that the method for the creation of the benefit maps has been established, it is of value to examine the effect of changes to the previously fixed parameters on the map. The first parameter to be explored is the geometry of the corrugation. It has been established previously that increasing the height of a corrugation and decreasing the period of a corrugation have similar effects on the behaviour of corrugated composites. Therefore, for the purposes of these benefit maps only the effect of changing the corrugation height will be explored. The process for creating a benefit map was repeated for systems with corrugation heights of 2mm and 4mm, keeping all else the same. The benefit boundaries for systems with corrugation height of 2mm, 3mm and 4mm are all included in Figure 4-77.

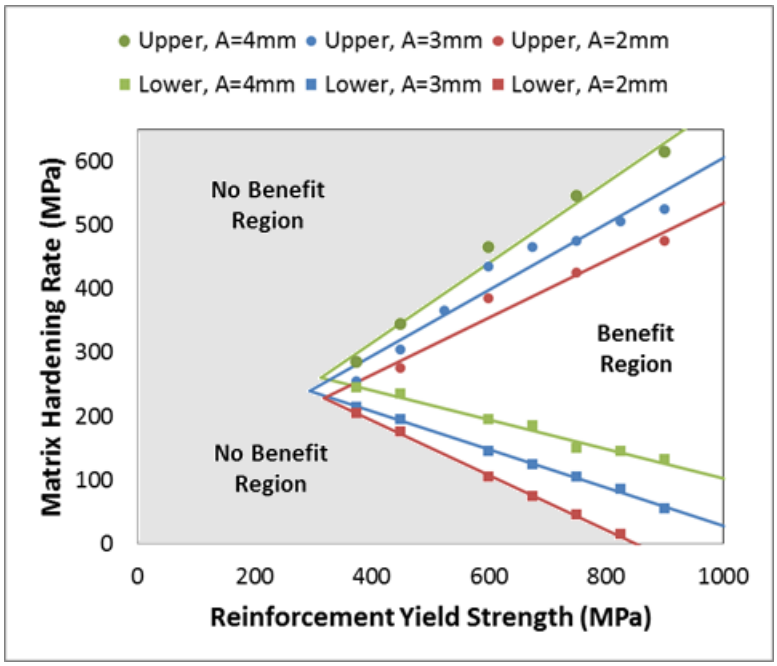


**Figure 4-77: Benefit map showing regions of material property values in which gains in necking strain are achieved through corrugation, for systems with different corrugation heights, A. This map represents a system with fixed matrix yield strength at 300MPa and reinforcement hardening rate at 500MPa along with a constant corrugation period of 8mm, thickness of 0.78mm and volume fraction of 20%. The solid boundary lines outlining the benefit region are fitted lines for both the upper and lower benefit boundary points.**

Looking at this figure it is evident that increasing the height of the corrugation has effects on the upper and lower benefit boundaries. An increase in corrugation height moves the upper benefit

boundary upwards towards higher values of matrix hardening rate, expanding the benefit region. This means that all else constant, systems with larger corrugation heights are capable of achieving improvements in ductility through corrugation at values of matrix hardening rate that are greater than those possible for systems with smaller corrugation heights.

Shifting the focus to the lower boundaries in Figure 4-77, it appears that as the height of the corrugation is increased the lower boundary shifts upwards, reducing the size of the benefit region on the lower end. Essentially, this means that composites with a larger corrugation height require the matrix to have a higher minimum hardening rate in order to take benefit from corrugation.

Moving on from the effect of geometry on the benefit maps, the next parameter that was explored was the matrix yield strength. In this case the steps for creating the benefit boundaries were repeated for three scenarios with different matrix yield strengths; 100MPa, 200MPa, and 300MPa. The geometry was fixed between the cases with a corrugation height of 3mm and period of 8mm, and the reinforcement hardening rate was constant at 500MPa. The upper and lower benefit boundaries for all three scenarios with different matrix yield strengths can be seen together in Figure 4-78.

Focusing on the upper benefit boundaries first, it is evident that an increase in the matrix yield strength leads to an expansion of the upper benefit boundary upwards to higher values of matrix hardening rate. Shifting the focus to the lower benefit boundaries in Figure 4-78, it can be seen that there is a trend in which lowering the matrix yield strength results in an expansion of the area of benefit, shifting the lower benefit boundary to lower values of matrix hardening rate. The final item of note in the benefit map in Figure 4-78 is that as the matrix yield strength is lowered,

the intersection of the upper and lower benefit boundaries translates to the lower left portion of the map represented by lower matrix hardening rates and lower reinforcement yield strengths. This intersection point can be thought of as a minimum reinforcement yield strength, below which no benefit through corrugation is achievable regardless of the matrix hardening rate. It appears that this minimum reinforcement yield strength is around the value of the matrix yield strength, at least for the 200MPa and 300MPa matrix yield strength cases. This is fairly logical, as if the reinforcement yield strength is lower than that of the matrix, then the corrugation is likely to stretch, especially initially at low values of strain, and not likely to unbend and thus there will likely be no benefit to use a corrugated architecture, as no boost in work hardening will come from a sample that does not unbend.

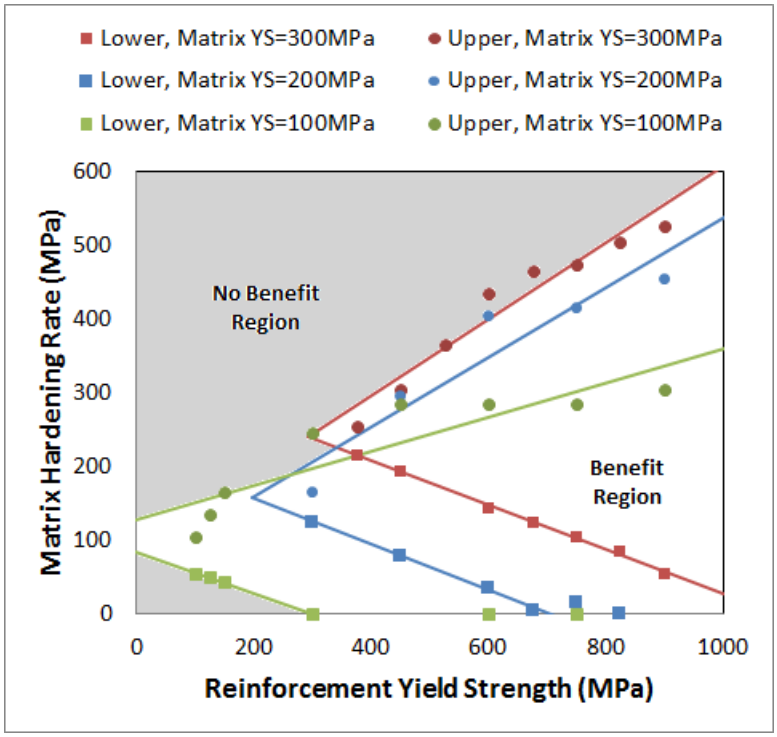


**Figure 4-78: Benefit map showing regions of material property values in which gains in necking strain are achieved through corrugation, for systems with different matrix yield strengths, YS. This map represents a system with fixed reinforcement hardening rate at 500MPa along with a constant corrugation period of 8mm, height of 3mm, thickness of 0.78mm and volume fraction of 20%. The solid boundary lines outlining the benefit region are fitted lines for both the upper and lower benefit boundary points.**

The final parameter that was varied was the reinforcement hardening rate. The process for creating benefit maps was repeated for reinforcement hardening rates of 500MPa, 1000MPa and 1500MPa, with the matrix yield strength kept constant at 300MPa and the corrugation geometry fixed with a corrugation height of 3mm and period of 8mm. A single plot was created with the upper and lower benefit boundaries for the three scenarios included in the same map, as seen in Figure 4-79. It should be noted that the linear fitted line for the upper benefit boundary of the reinforcement hardening rate of 1500MPa, clearly begins to deviate from the data points at lower values of reinforcement yield strength, and thus this line is only a rough guideline in this region. Beginning with the lower benefit boundary, there is a clear trend that as the reinforcement hardening rate is increased the boundary shifts down to lower values of matrix hardening rate, expanding the benefit region on the lower end.

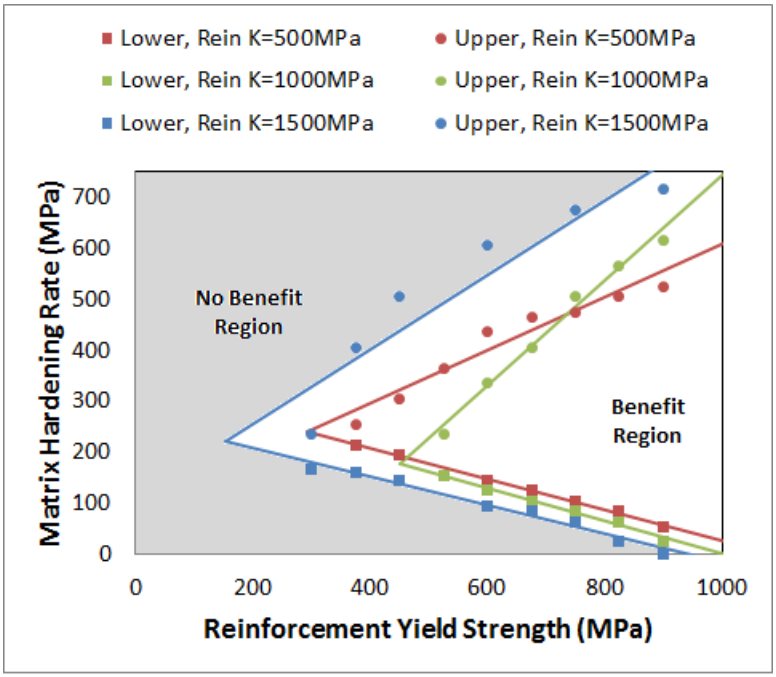


**Figure 4-79: Benefit map showing regions of material property values in which gains in necking strain are achieved through corrugation, for systems with different reinforcement hardening rates, K. This map represents a system with fixed matrix yield strength at 300MPa along with a constant corrugation period of 8mm, height of 3mm, thickness of 0.78mm and volume fraction of 20%. The solid boundary lines outlining the benefit region are fitted lines for both the upper and lower benefit boundary points.**

Switching focus to the upper benefit boundary, the effect of changing the reinforcement hardening rate appears to be more complicated. At high values of reinforcement yield strength, near the right edge of the map, increasing the reinforcement hardening rate leads to an expansion of the benefit range upwards, shifting the upper benefit boundaries to higher values of matrix hardening rate. However, as the reinforcement yield strength is lowered, the boundary corresponding to the reinforcement hardening rate of 1000MPa, crosses over that for 500MPa, while the 1500MPa boundary stays higher than both. This behaviour is unexpected and difficult to explain at first glance. However, upon investigation is appears that it may be the result of the arbitrary selection of the cut-off value at 0.05 and a more prototypical set of boundaries can be seen if the cut-off is set at 0.02 as shown in Figure 4-80. This cross-over of boundaries is unique to the benefit maps with different reinforcement hardening rates and is due the fact that composites with higher values of reinforcement hardening rates are able to achieve small but finite amounts of benefit through corrugation over a larger range of matrix hardening rates.

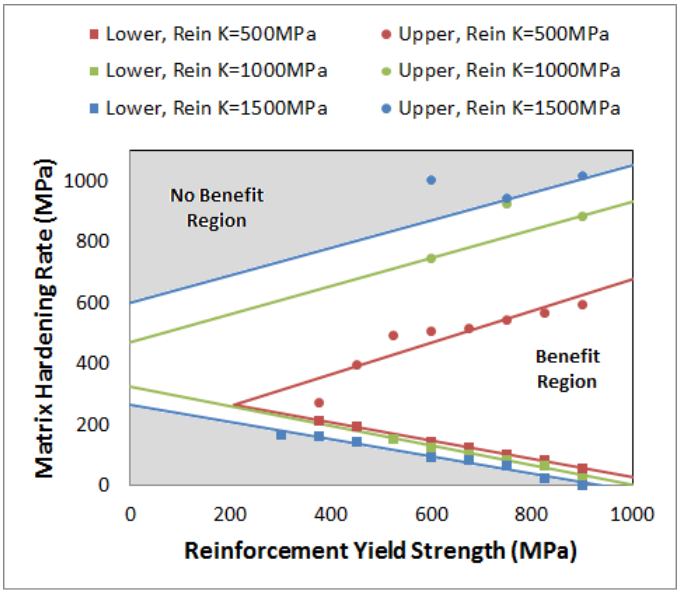


**Figure 4-80: Benefit map showing regions of material property values in which gains in necking strain are achieved through corrugation, for systems with different reinforcement hardening rates, K. This map is similar to Figure 4-79, but the upper benefit boundary cut-off is set at 0.02.**

Although these benefit maps are useful tools it may be of value to supplement them with some additional information. These benefit maps are very useful for predicting whether a given system will exhibit gains in ductility by using a corrugated architecture, however, they do not provide information as to how large of an improvement can be expected. In order to predict this behaviour it would be beneficial to create 'benefit surfaces' that visually show the improved ductility that is achievable for given combinations of parameters.

The creation of these benefit surfaces was accomplished by running a number of simulations that span a range of material parameter values for both corrugated and straight geometries and then for each combination of material parameters calculating the difference in necking strain between the corrugated and straight scenarios. A 3-D surface and corresponding 2-D colour map were then created using the gnuplot graphing software. Each plot consists of a surface that is generated based on x-y-z coordinates with interpolation between the points. The x-coordinate is the matrix hardening rate, the y-coordinate is the reinforcement yield strength and the z-coordinate is the difference in necking strain. The surface plots and colour maps were created for all of the different scenarios discussed above for the benefit maps, with each plot corresponding to a fixed corrugation geometry, matrix yield strength and reinforcement hardening rate. Each plot has both a three dimensional surface on the top, with the topography representing the difference in necking strain and a corresponding colour map at the bottom, with the colour spectrum representing the range of necking strain differences.

The first set of 3-D plots, Figure 4-81, shows the effect of corrugation height, with three plots at different corrugation heights, 2mm, 3mm and 4mm, with a fixed matrix yield strength of 300MPa and a fixed reinforcement hardening rate of 500MPa. The main trend that is clear in looking at these plots is that the improvement in necking strain through the use of a corrugated

reinforcement increases as the height of the corrugation is increased. This is evident in looking at the height of the 3-D surface and the colour map showing colours towards the high end of the spectrum with regards to difference in necking strain. This trend matches observations made earlier with regards to the effect on necking strain of increasing the height of a corrugation. There is also a shift in the region that is showing benefit towards higher values of matrix hardening rate, which agrees with the trend observed above in the benefit map in Figure 4-77.

The second set of 3-D plots, Figure 4-82, highlights the effect of the matrix yield strength, with three plots, each for a different value of the matrix yield strength, 100MPa, 200MPa, and 300MPa, with a fixed reinforcement hardening rate of 500MPa and a constant corrugation height of 3mm. Looking at this plot, the maximum improvement in necking strain achievable does not seem to change significantly with the matrix yield strength. This can be concluded by looking at the peak height of the surface and the most extreme colour present on the colour map, which seems to be fairly constant for all three plots. The main effect of decreasing the matrix yield strength is a shift in the region of benefit and maximum improvement in necking strain towards lower values of matrix hardening rate and lower values of reinforcement yield strength. These observations agree with those seen in the benefit map presented earlier in Figure 4-78.

The final set of 3-D plots, Figure 4-83, shows the effect of the reinforcement hardening rate, with three plots, each using a different reinforcement hardening rate, 500MPa, 1000MPa, and 1500MPa, with a constant matrix yield strength of 300MPa and a constant corrugation height of 3mm. Focusing on the peak benefit first, it is clear that increasing the reinforcement hardening rate results in a shifting of the value of peak benefit towards lower matrix hardening rate as well as a slight increase in magnitude of that peak value. The shifting is evident in looking at the movement of the peak in the 3-D surface and the shifting of the orange region in the colour map.

The increase in the value of the peak improvement in necking strain is apparent in the deepening of the orange colour as the reinforcement hardening rate is increased. The maximum value of improvement in necking strain is going to occur at the maximum value of matrix hardening rate for which a straight composite still has an insignificant necking strain, close to zero, and a corrugated composite is capable of achieving a boost in work hardening as a result of unbending. When the reinforcement hardening rate is increased, this increases the necking strain of straight reinforced composites, and perhaps more importantly requires a compensatory lower matrix hardening rate in order to achieve conditions of a near-zero necking strain. This explains why the peak value shifts to lower values of matrix hardening rate as the reinforcement hardening rate increases. The slight increase in the peak improvement in necking strain, with the increased reinforcement hardening rate, is due to the fact that higher reinforcement hardening rates lead to larger potential necking strains for both straight and corrugated composites and thus a larger peak improvement when comparing the corrugated composite with a significant necking strain to a near-zero necking strain of a straight composite. In addition to movement of the peak improvement value, the plots in Figure 4-83 also show a broadening of the region of potential benefit through corrugation as the reinforcement hardening rate increases. This is most evident in the form of the larger spreading green region for the 1500MPa case, which shows a much larger range of modest benefit compared to the 1000MPa case. Composites with larger reinforcement hardening rates appear to show an ability to achieve small improvements in necking strain through corrugation, between 0 and 0.05, over a very large range of matrix hardening rates and reinforcement yield strengths. The reason for this is related to the discussion earlier with regards to the cut-off values selected for the benefit maps. When the matrix hardening rate is increased the increase in necking strain of a straight composite is more drastic when the reinforcement

hardening rate is lower and thus the gap in necking strain between corrugated and straight composites is reduced more quickly. Therefore, systems with larger reinforcement hardening rates will be able to capitalize on relatively small gains in necking strain through corrugation over a larger range of matrix hardening rates.

In summary, the creation of benefit maps and benefit surfaces allows one to gain valuable information with regards to the potential benefits achievable through the use of a corrugated reinforcement architecture. By compiling numerous maps representing variations in geometric and material parameters, it is possible to estimate whether a given scenario will be able to benefit through the use of corrugations and if not, what adjustments could be made with regards to geometry or component materials in order to realize a benefit through corrugation.

As an example for using these benefit surfaces consider a hypothetical system that has linear hardening matrix and reinforcement materials, with properties given by System 1 in Table 4-2. Looking at the values of matrix yield strength, reinforcement hardening rate and corrugation height, the closest 3D surface available is that given in Figure 4-82 for the matrix yield strength of 200MPa. For this particular plot, a matrix hardening rate of 350MPa and reinforcement yield strength of 500MPa corresponds to a blue region in the colour map with no significant benefit through corrugation. However, the matrix yield strength of System 1 is actually 160MPa, so one should compare to the 100MPa plot in Figure 4-82 to estimate the effect of moving the yield strength to 160MPa. It is seen that this makes it more unlikely that there is benefit from corrugation. The next step would be to look at how increasing the reinforcement hardening rate from 500 to 700MPa affects the benefit surface. This can be done by looking at Figure 4-83 and looking at the movement of the surface from the 500MPa plot to the 1000MPa plot.

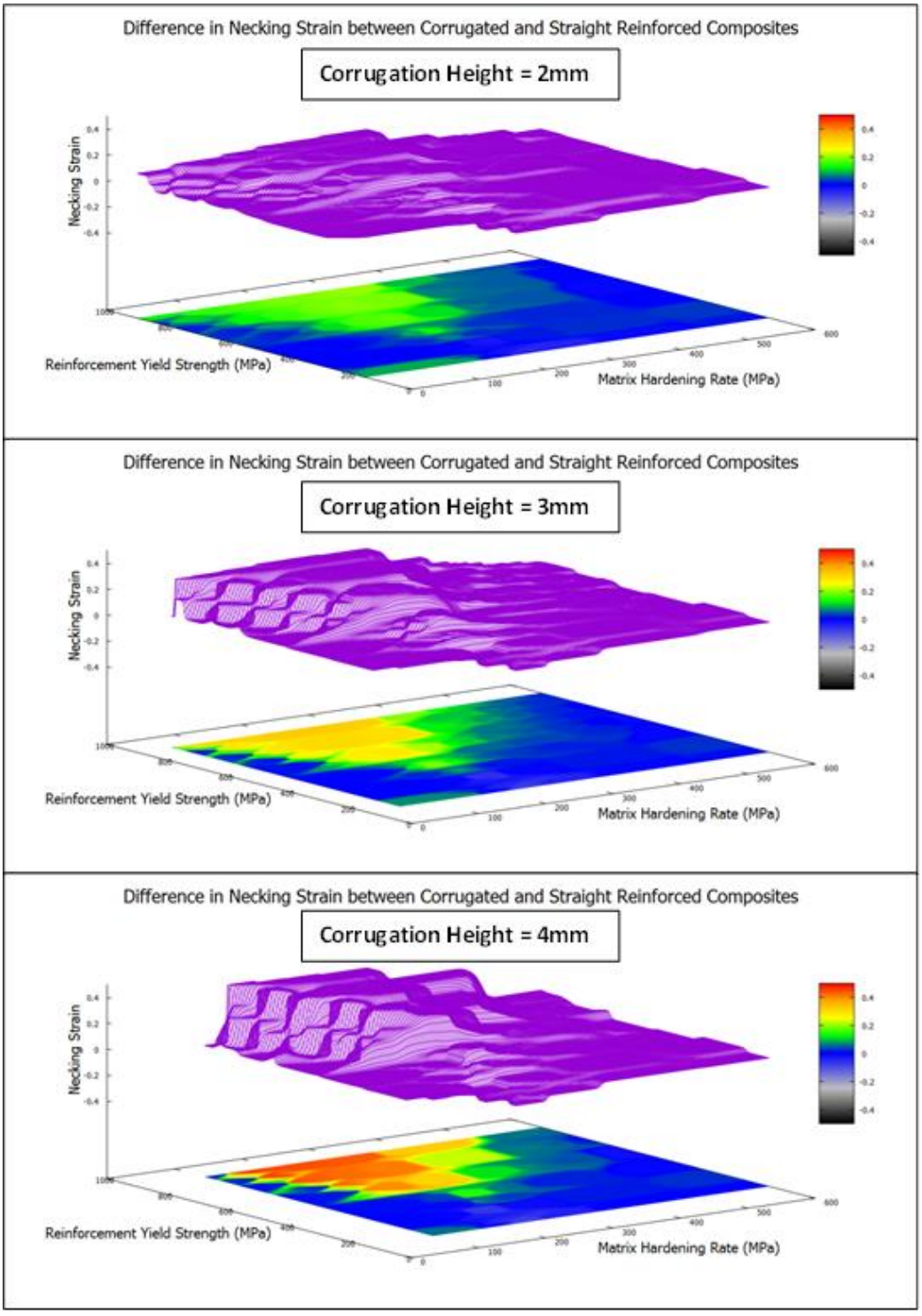


**Figure 4-81: 3-D surfaces and colour plots of the difference in necking strain between corrugation and straight reinforced composites over a range of values of reinforcement yield strength and matrix hardening rate. Each plot corresponds to a different corrugation height; (top) 2mm, (middle) 3mm and (bottom) 4mm. The matrix yield strength was kept constant at 300MPa and the reinforcement hardening rate was fixed at 500MPa. The corrugation geometry had a fixed period of 8mm and a volume fraction of 20%.**

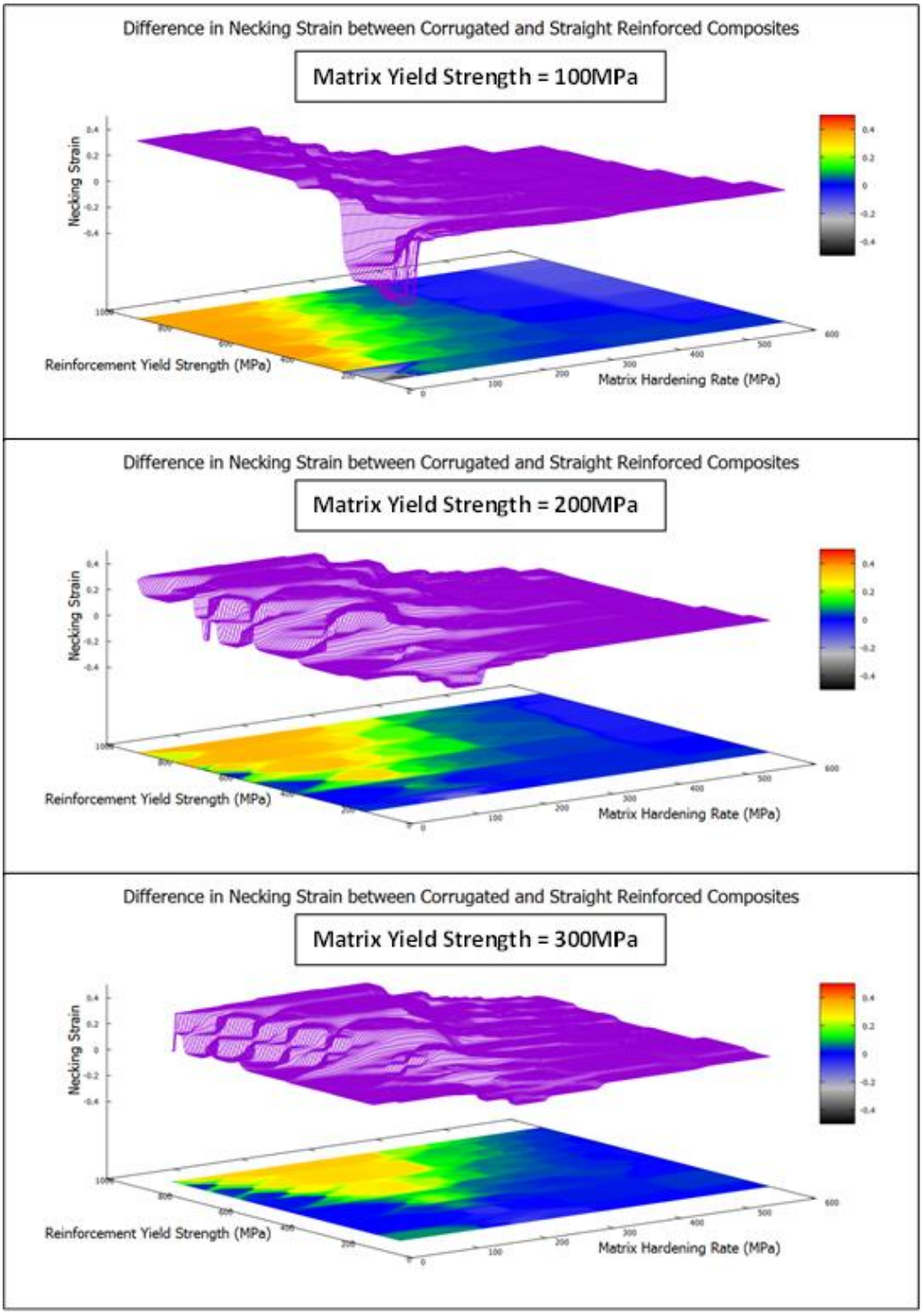


**Figure 4-82: 3-D surfaces and colour plots of the difference in necking strain between corrugation composites and straight reinforced composites over a range of values of reinforcement yield strength and matrix hardening rate. Each plot corresponds to a different matrix yield strength; (top) 100MPa, (middle) 200MPa and (bottom) 300MPa.The reinforcement hardening rate was fixed at 500MPa and the corrugation geometry had a fixed period of 8mm, height of 3mm and a volume fraction of 20%.**

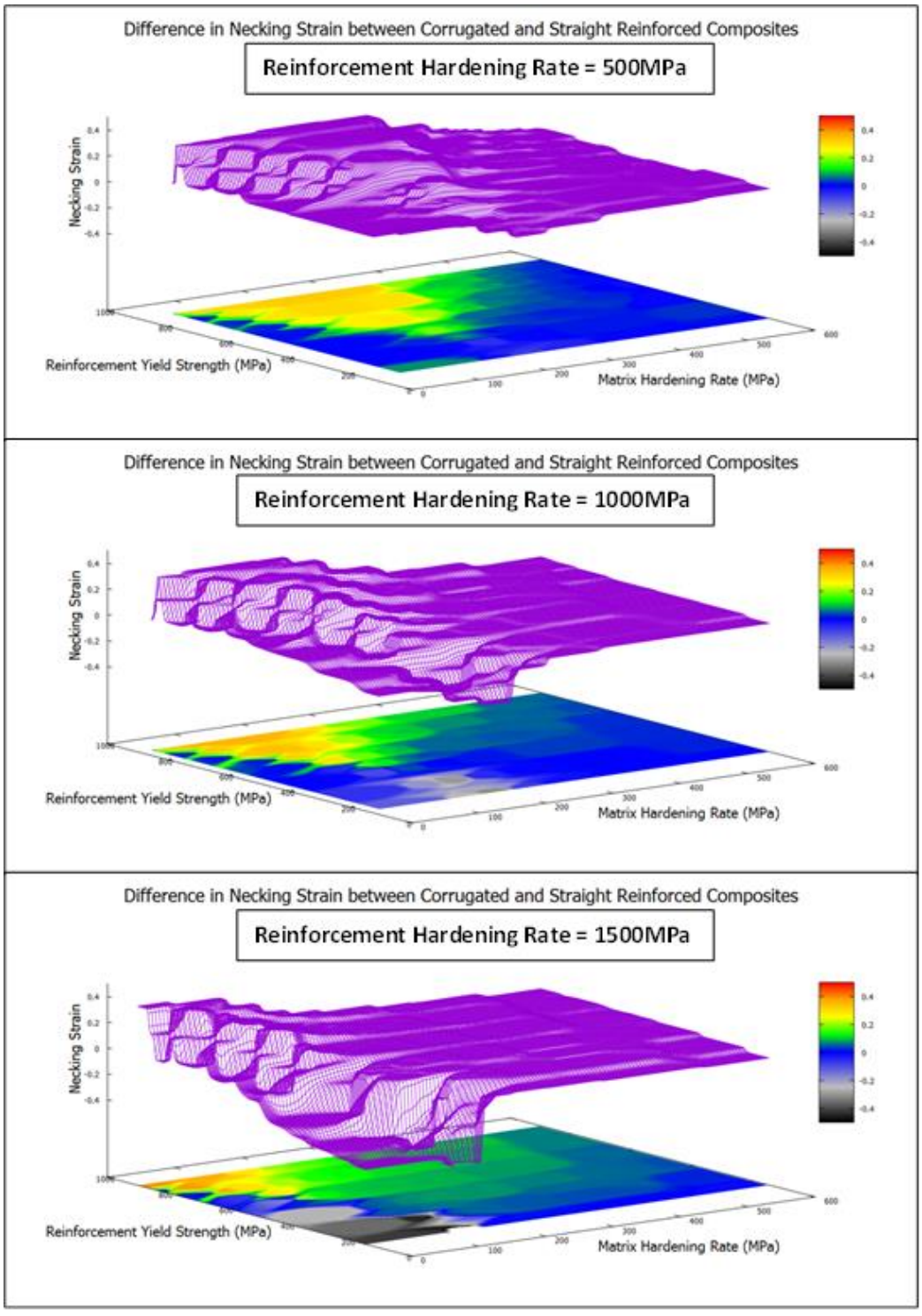


**Figure 4-83: 3-D surfaces and colour plots of the difference in necking strain between corrugation and straight reinforced composites over a range of values of reinforcement yield strength and matrix hardening rate. Each plot corresponds to a different reinforcement hardening rate; (top) 500MPa, (middle) 1000MPa and (bottom) 1500MPa. The matrix yield strength was fixed at 300MPa and the corrugation geometry had a fixed period of 8mm, height of 3mm and a volume fraction of 20%.**

This move appears to also reduce the likelihood of there being a benefit through corrugation. Finally, since the corrugation height in System 1 is 3.5 mm, one needs to look at Figure 4-81 and compare the 3mm height plot to the 4mm height plot. Increasing the height from 3mm to 3.5mm will slightly increase the chance of there being a benefit through corrugation and will increase that benefit if it does indeed happen. Based on the fact that most of these interpolations point towards a system that is less likely to benefit from corrugation, and the starting point was a system with little benefit from corrugation, it is likely that System 1 will not take advantage of a corrugated reinforcement geometry.

This same method of extrapolating behaviour between maps in order to estimate whether a given change in variable would increase or decrease the likelihood of benefit through corrugation was applied to the four other hypothetical systems in Table 4-2 in order to provide a prediction as to the size of benefit through corrugation for each system. A summary of these predictions for all five systems can be found in Table 4-3 below. In order to test these predictions, FEM simulations were performed for both straight and corrugated composites using the material parameters of the matrix and reinforcement components provided in Table 4-2. For the corrugated composites the corrugation period was fixed at 8mm for all systems and the volume fraction of the reinforcement was set at 20% for both the straight and corrugated geometries. A summary of the necking strains calculated in these simulations is provided in Table 4-3, along with the difference in necking strain between the corrugation reinforced composite and its related straight reinforced composite. In comparing the difference in necking strain to that of the predictions it was found that the predictions were fairly accurate, with them being quite accurate in the cases of systems 2,3 and 5 and somewhat accurate for systems 1 and 4. In the cases of both system 1 and 4, the lack of accuracy stems from the fact that near the upper benefit boundary, as the matrix

hardening rate is increased, the necking strain of the straight composite gradually approaches that of the corrugated composite and it can be difficult to predict whether a system will have a small benefit or no benefit in this space of material properties. In general however, these test systems have shown that the benefit maps and surfaces can be effective tools at predicting the viability of a given system to show improvement in necking strain through corrugation.

**Table 4-2: Summary of material and geometric parameters used in test systems for evaluating the predictive ability of benefit maps and surfaces for determining whether a system can take advantage of a corrugated reinforcement geometry.**

| System # | Matrix Yield Strength | Matrix Hardening Rate | Reinforcement Yield Strength | Reinforcement Hardening Rate | Corrugation Height |
|---|---|---|---|---|---|
| 1 | 160 MPa | 350 MPa | 500 MPa | 700 MPa | 3.5 mm |
| 2 | 275 MPa | 220 MPa | 720 MPa | 1200 MPa | 2.5 mm |
| 3 | 320 MPa | 160 MPa | 800 MPa | 800 MPa | 3.8 mm |
| 4 | 240 MPa | 400 MPa | 620 MPa | 450 MPa | 3.2 mm |
| 5 | 260 MPa | 120 MPa | 580 MPa | 750 MPa | 2.7 mm |

**Table 4-3: Summary of the necking strains obtained from FEM simulations of the test systems presented in Table 4-2, along with the predictions for these systems and evaluations of the accuracy of those predictions.**

| System # | Prediction | Necking Strain | | | Evaluation of Prediction |
|---|---|---|---|---|---|
| | | Corrugated | Straight | Difference | |
| 1 | Minimal Benefit | 0.740 | 0.679 | 0.061 | Somewhat accurate |
| 2 | Small Benefit | 0.366 | 0.272 | 0.094 | Accurate |
| 3 | Large Benefit | 0.440 | 0.011 | 0.429 | Accurate |
| 4 | Moderate Benefit | 0.445 | 0.383 | 0.062 | Somewhat accurate |
| 5 | Large Benefit | 0.280 | 0.010 | 0.270 | Accurate |

## 4.4 Summary of Discussion

A range of FEM studies have been conducted that examine the behaviour of isolated and embedded corrugations and explore effects of the different geometric, material and arrangement parameters that define a given composite system. In particular, a focus has been placed on the

ductility of these materials as represented by the necking strain. First off, some of the main findings with regards to isolated corrugations are:

a) The use of a corrugated geometry can provide an improvement in necking strain that is the result of an unbending of the corrugation. This unbending was confirmed through the measurement of the corrugation angle and the stress profile present across the thickness of a corrugation peak.
b) The stress-strain curve of an isolated corrugation can be divided into three main regions; unbending region, transition region, and stretching region. In the unbending region, bending dominated behaviour is occurring and in the stretching region, stretch dominated behaviour is occurring.
c) The unbending process causes an evolution of the geometry that leads to geometrically induced work hardening, taking the form of a boost in the work-hardening curves.
d) The ultimate tensile strength is unaffected by the corrugation geometry.
e) Increasing the height or decreasing the period of the corrugation (i.e. increasing the degree of corrugation) results in higher necking strains due to a lengthening of the unbending region in the stress-strain curve.
f) The corrugation percentage of a sample scales linearly with the necking strain as it dictates how much of the sample supplies the boost in strain that comes from unbending.
g) Increasing the thickness of the corrugation leads to higher stresses due to fact that for an unbending peak, local stress increases with distance from the midline. These higher stresses lead to an earlier initiation of the transition region of the stress-strain response.
h) The material properties of the isolated corrugation have very little effect on the unbending region of the stress-strain curve, or the boost in necking strain that comes from

corrugation, and mainly impact the stretching region of the stress-strain curve. In fact changing the material properties has the same effect on straight and corrugated samples.

i) The use of a corrugated architecture can lead to significant ductility in materials for which a straight geometry would achieve almost no ductility.

j) An analytical model was developed that uses both material and geometric input parameters and is capable of predicting the stress-strain response of a corrugated strip with good qualitative sensitivity and decent quantitative accuracy for both power-law hardening and linear hardening materials.

In addition to the results observed for the isolated corrugation, the findings concerning the corrugation reinforced composites are:

k) The increasing work hardening effect observed for the unbending of an isolated corrugation can be attained when embedding the corrugation in a matrix material. This effect however, is muted somewhat, due to the presence of the surrounding matrix material. The constraint of the matrix can lead to stress transfer to the corrugated reinforcement that leads to the emergence of stretching dominated behaviour prior to complete unbending of the corrugation.

l) The unbending of the corrugated reinforcement can be compared to that of an isolated corrugation using the evolution of the corrugation angle and the stretching strain in the corrugation to determine the degree to which unbending has occurred.

m) Due to the interplay between the matrix and the corrugation, it is not possible to create a rule-of-mixtures model for the stress-strain response that uses the analytical model of the isolated corrugation and a material model of the matrix material.

n) The heterogeneous and periodic strain patterns that emerge in the matrix during deformation can be explained using a simple thought experiment concerning the overall shape change and the driving force for unbending of the corrugation.

o) Changing the height or period of the corrugation has similar effects on necking strain as those observed for isolated corrugations. However, there exist threshold values that need to be exceeded in order for an improvement in necking strain over that of the straight reinforcement to be achieved. The boost in work hardening from the corrugation unbending needs to be large enough and occur at the right strain value in order to delay necking.

p) Increasing the thickness of the reinforcement leads to a larger benefit in necking strain when using a corrugated reinforcement. This is due to the fact that a larger volume fraction is taking advantage of the potential for improvement in necking strain.

q) Unlike for the isolated corrugations, increasing the percentage corrugated can actually lead to a reduction in necking strain, with the exception of 100% corrugation. This is due to the fact that a transition zone is introduced when less than 100% corrugation is present.

r) Focusing on the copper-4130 steel system, depending on the degree of corrugation used, it is possible to increase the necking strain of a corrugated composite by increasing the volume fraction of the reinforcement, even though the reinforcing material itself has ductility much lower than that of the matrix material.

s) The use of the corrugation reinforcement architecture enables one to traverse through desirable regions of material property space defined by both high strength and ductility.

t) When multiple reinforcements are used, the spacing between the corrugations can be important, as when it is too small, the constraint of the matrix that emerges can lead to a reduction in the necking strain.

u) When looking at linear hardening materials, there is a range of matrix yield strength or matrix hardening rate, outside of which benefit through corrugation is not possible. Additionally, there is a minimum value of reinforcement yield strength that must be exceeded for benefit through corrugation to be achieved. Similar ranges and trends exist for power-law hardening materials as well.

v) There exists interplay between material properties and geometric parameters in determining the necking strain of a corrugated composite and its relative value compared to a straight composite.

w) The generation of benefit maps and benefit surfaces allows one to predict under what circumstances it is possible to improve the necking strain of a composite through the use of a corrugated reinforcement geometry. These tools can also be used to give rough estimates as to the absolute value of that benefit in necking strain.

# 5 Experimental Work

This chapter describes the experimental work that was completed in an effort to validate some of the modeling work on isolated corrugations and corrugation reinforced composites described in the previous chapters. Not only was the experimental work meant to validate the modeling efforts but was also aiming to develop feasible techniques for fabricating and testing these materials. This experimental work met with a number of challenges along the way, resulting in changes to material systems, fabrication techniques and testing methods, all of which will also be addressed in this chapter. The chapter will be organized into two main sections; the first focusing on isolated corrugations and the second focusing on corrugation reinforced composites. Each of these sections will group the discussion of the methods and results of each experimental approach together in order to explain how the results of one approach led to the changes used in the next approach. When appropriate the results will be compared to the modeling work previously presented.

## 5.1 Isolated Corrugations

The first section will focus on the experiments conducted on isolated corrugated strips. The purpose of these experiments was to see if the stress-strain behaviour characteristic of an unbending corrugation, which was found in FEM modeling and analytical modeling, could be replicated in practice. With this in mind, the desired output from these experiments is the stress-strain curve of an isolated corrugated strip, subject to tensile loading.

### 5.1.1 Copper

The first set of experiments that were conducted used copper sheet as the material of interest. All of the samples were fabricated from strips of copper sheet with starting dimensions of 170mm

length, 20mm width and 1.18mm thickness. In order to create the corrugated geometry a two-piece anvil and cylinder apparatus was employed as described in Bouaziz et al[68] and illustrated in Figure 5-1. Steel cylindrical pins with a diameter of 0.25mm were placed in grooves on the inner surfaces of the anvils. They were arranged with spacing between cylinders that would determine the period of the corrugation and in such a way that the cylinders in the top piece of the anvil were shifted by half the spacing distance compared to those of the bottom piece of the anvil. The copper strip was then placed between the two pieces of the anvil with only the cylindrical pins in contact with the strip as illustrated below in Figure 5-1. The entire apparatus was then placed in a hydraulic press and based on the amount of pressure applied a corrugation with a certain height was created. By varying the spacing of the cylinders the period was changed. And by varying the number of cylinders used the percentage corrugated was changed.

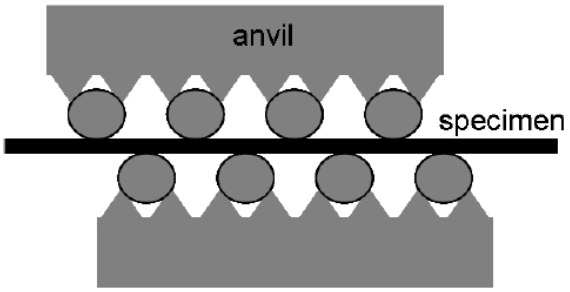


**Figure 5-1: Illustration of apparatus used to create corrugated strips (Bouaziz).**[31]

This method was used to create corrugated copper strips, an example shown in Figure 5-2 below, with the geometric parameters listed in Table 5-1 with Sample 1 being the base case of a straight, uncorrugated strip. There are two almost identical samples, A and B, for each geometry. It should be noted that the corrugation height is measured as the vertical distance from the top of a peak to the bottom of the adjacent trough minus the thickness of the sheet, giving the distance from the midplane of the sheet. These dimensions were measured using a caliper.

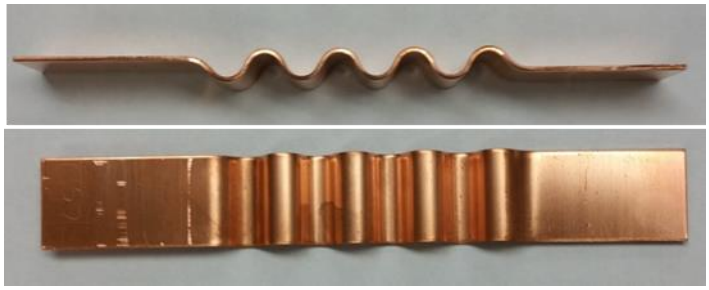

**Figure 5-2: Corrugated copper strip.**

**Table 5-1: Geometric parameters of corrugated copper strips for experimental testing.**

| Sample | Period | Height | % Corrugated | Sample | Period | Height | % Corrugated |
|---|---|---|---|---|---|---|---|
| 1A | NA | 0 | 0% | 1B | NA | 0 | 0% |
| 2A | 15mm | 5.97mm | 60% | 2B | 15mm | 5.98mm | 60% |
| 3A | 15mm | 4.98mm | 60% | 3B | 15mm | 4.95mm | 60% |
| 4A | 15mm | 4.02mm | 60% | 4B | 15mm | 4.05mm | 60% |
| 5A | 15mm | 2.99mm | 60% | 5B | 15mm | 2.98mm | 60% |
| 6A | 15mm | 1.95mm | 60% | 6B | 15mm | 1.93mm | 60% |
| 7A | 15mm | 4.78mm | 90% | 7B | 15mm | 4.78mm | 90% |
| 8A | 15mm | 5.16mm | 30% | 8B | 15mm | 5.11mm | 30% |
| 9A | 15mm | 3.86mm | 90% | 9B | 15mm | 3.85mm | 90% |
| 10A | 30mm | 4.13mm | 90% | 10B | 30mm | 4.12mm | 90% |
| 11A | 45mm | 4.02mm | 90% | 11B | 45mm | 4.03mm | 90% |

By comparing samples 1, 2, 3, 4, 5 and 6, the effect of height can be examined as the period and percentage corrugated is kept approximately constant. Similarly, by comparing samples 1, 9, 10 and 11 the effect of period can be explored as the height and percentage corrugated are constant in these cases. Finally by comparing samples 1, 3, 7 and 8 the effect of the percentage corrugated can be tested as the height and period of these samples are approximately constant.

Before tensile tests could be conducted on the samples an annealing process was used to remove any internal stresses present due to the deformation process. The samples were placed in a tube furnace at 600 °C for 15 minutes in Argon gas. Tensile tests were then conducted on the samples

using an MTS 50 kN machine and were setup such that the grips were a distance of 100mm apart (i.e. gauge length of 100mm). This allowed for consistency between samples as the total length was variable due to different amounts of corrugation in each sample. The rate of extension was set at 10mm/min which corresponds to an initial strain rate of around 0.0017 /s. During testing the machine recorded the force and the crosshead displacement. The engineering stress was calculated by dividing the force by the initial cross sectional area and the engineering strain was calculated by dividing the crosshead displacement by the initial gauge length of the sample, i.e., 100mm. It was observed that there was some slippage of the samples in the tensile grips during testing and for this reason the strain that was calculated based on the cross-head displacement was multiplied by a factor that represented the percentage of the deformation that occurred in the region denoted by the initial gauge length. For example, in one sample it was measured that the grips slipped 4mm during a total deformation of 48.1mm. Therefore, in this case the strain that was calculated was multiplied by a factor of:

$$\textbf{Slippage Factor} = \frac{\Delta \mathbf{d_{total}} - \Delta \mathbf{d_{slippage}}}{\Delta \mathbf{d_{total}}} = \frac{\mathbf{48.1 - 4}}{\mathbf{48.1}} = \mathbf{0.917} \quad (5\text{-}1)$$

The calculated experimental engineering stress-strain curves showing the effect of corrugation height, percentage corrugated and corrugation period are found in Figure 5-3, Figure 5-4 and Figure 5-5, respectively. Each curve in the plots corresponds to a single sample, and only one curve for each geometry is included in the plots, due to the similarity between curves of identical geometries. The stress-strain curves were plotted up to the point of reaching the maximum stress, with the data at higher values of strain being left out in order to present a cleaner plot.

The trends demonstrated from these tensile tests on the annealed copper strips are similar to those observed earlier from the FEM simulations. It can be seen that increasing the height, decreasing the period or increasing the percentage that is corrugated, all result in an initial

reduction of stress carried by the sample, a shifting of the stress strain curves towards higher values of strain, and in general lead to an increase in the necking strain of the material. These trends can be seen more clearly in Figure 5-6, Figure 5-7 and Figure 5-8, which plot the necking strain as a function of corrugation height, percentage corrugated and period, respectively.

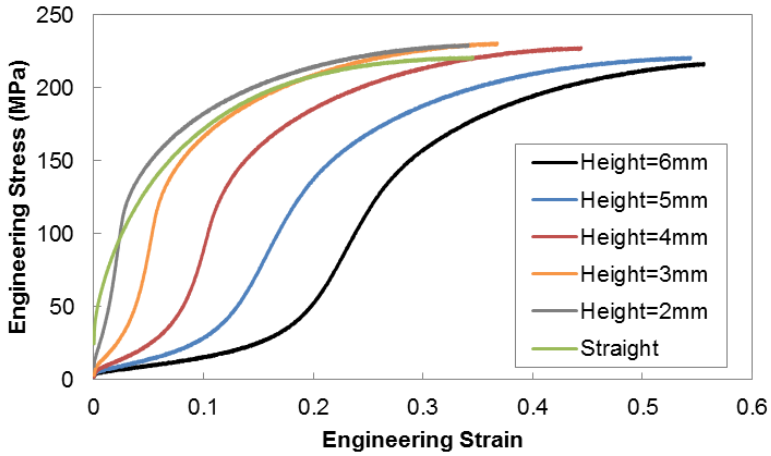


**Figure 5-3: Experimental stress-strain curves of isolated corrugated copper strips with variable corrugation height. The stress-strain curve for a straight strip of copper was included for comparison purposes.**

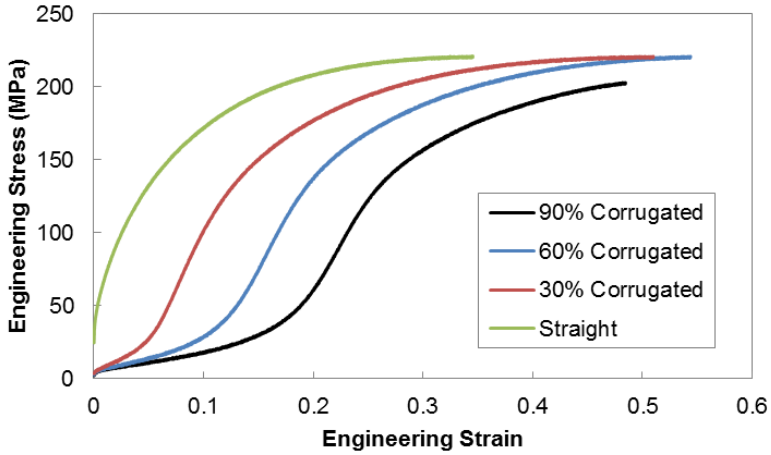


**Figure 5-4: Experimental stress-strain curves of isolated corrugated copper strips with variable percentage corrugated. The stress-strain curve for a straight strip of copper was included for comparison purposes.**

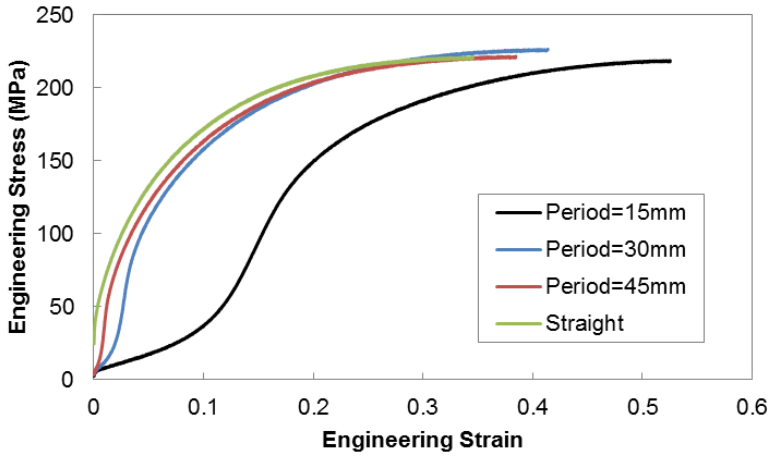


**Figure 5-5: Experimental stress-strain curves of isolated corrugated copper strips with variable corrugation period. The stress-strain curve for a straight strip of copper was included for comparison purposes.**

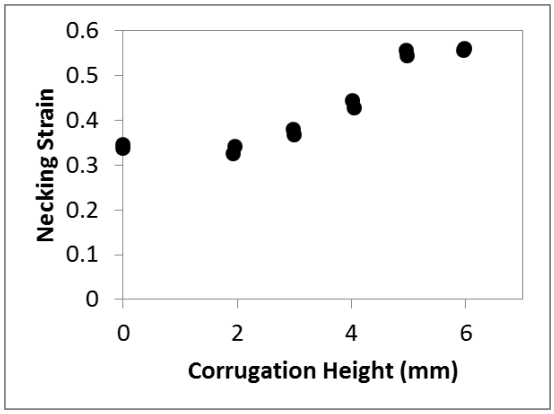


**Figure 5-6: Necking strain as a function of corrugation height for isolated corrugated copper strips.**

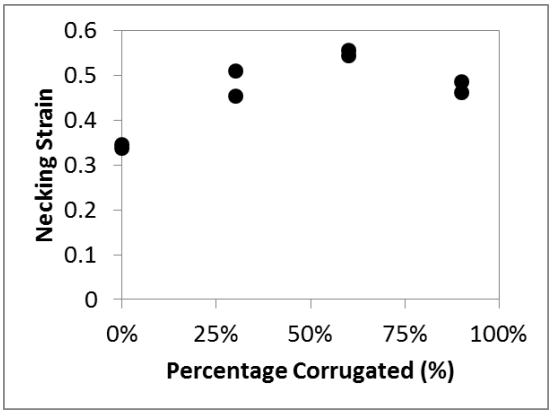


**Figure 5-7: Necking strain as a function of percentage corrugated for isolated corrugated copper strips.**

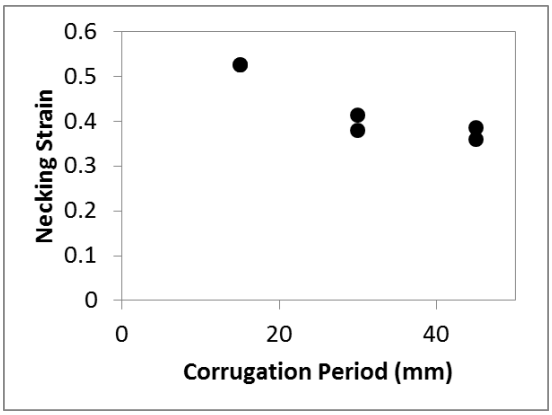


**Figure 5-8: Necking strain as a function of corrugation period for isolated corrugated copper strips.**

There are two slight variations from the trend that should be noted. First, looking at Figure 5-3, when the corrugation height is very low, i.e. 2mm, no improvement in necking strain is observed when compared to the straight case. This could be a result of minor differences in annealing between the samples or errors in measuring the amount of slippage that occurred for these samples, or simply be due to the fact that a corrugation with a period of 15mm and height of 2mm is almost straight. The second variation involves the behaviour of the strip with 90% corrugation seen in Figure 5-4. As the percentage corrugated is increased the necking strain would be expected to increase, however in this case it does not. Looking at this curve it appears that it may have failed prematurely as the stress of the sample had not reached the plateau seen in all the other samples. This is likely due to the fact that there is a transition region from the corrugated part of a sample to the straight part, as can be seen by looking at Figure 5-2 above, and for a 90% corrugated sample this transition region is right around where the sample is gripped. Therefore, perhaps the sample was being gripped in a slightly bent region of the sample, which led to it failing earlier than would be expected. Regardless of these two minor deviations, in all cases, as the degree of corrugation is increased the curves are characterized by a larger unbending section and a delayed onset of the increasing work hardening behaviour and the

subsequent stretching section. Similar tests performed by Bouaziz[31], illustrated earlier in Figure 2-9, for interstitial free steel showed similar trends that matched well with the FEM predictions.

### 5.1.2 Steel

In order to ensure the observed behaviour of isolated corrugated strips was not limited to the copper system, additional experiments were conducted that looked at different material systems. In particular, tensile tests were performed on straight and corrugated strips of interstitial free (IF) steel and 304 stainless steel. Starting with the IF steel strips, samples were prepared in a similar fashion, beginning with strips with starting dimensions of around 150mm in length, 20mm in width and 1mm in thickness. The strips were then corrugated using the anvil and cylinder technique to provide samples with the geometries outlined in Table 5-2. In this case a pair of samples were made and tested for each geometry of interest. Comparing samples 2 and 3 should give an idea of the effect of changing the corrugation height, as the period and number of corrugations is kept constant for the corrugated samples. Comparing samples 1, 2 and 4 should provide information on the effect of changing the percentage corrugated, as the period is constant for the corrugated samples and the corrugated heights are close enough that the comparison is still valid.

**Table 5-2: Geometric parameters of corrugated IF steel for experimental testing.**

| Sample | Period | Height | Number of Corrugations |
|---|---|---|---|
| 1A | NA | 0 | 0 |
| 1B | NA | 0 | 0 |
| 2A | 15.2mm | 4.04mm | 4 |
| 2B | 15.3mm | 4.13mm | 4 |
| 3A | 15.2mm | 2.46mm | 4 |
| 3B | 15.1mm | 2.65mm | 4 |
| 4A | 15.1mm | 4.59mm | 2 |
| 4B | 15.2mm | 4.65mm | 2 |

For this system, after the samples were corrugated, all of the strips were annealed in a tube furnace at 950°C for 10 minutes in Argon gas in order to remove any residual stresses and ensure comparable starting conditions for the straight and corrugated samples. The tensile tests were completed using a 50kN MTS machine, this time with the grips spaced 80mm apart for the gauge section, and a rate of extension of 1mm/min or an initial strain rate of around 0.0002 /s. The stress was calculated in a similar manner to that used for the copper system. Similar to the copper system the strain was calculated taking into consideration the slippage in the grips.

The stress strain curves showing the effect of the corrugation height from the tensile tests of IF steel can be seen in Figure 5-9. Figure 5-10 displays the stress-strain curves showing the effect of the number of corrugations, or alternatively, the percentage corrugated. The trends exhibited for IF steel closely resemble those that were seen in the literature and in the modeling results, with the necking strain increasing as the degree of corrugation is increased, with no loss in the strength of the materials. This is even clearer in the plot of necking strain versus corrugation height seen in Figure 5-11, and necking strain versus number of cycles seen in Figure 5-12.

As mentioned earlier some tensile tests were also performed on corrugated samples of 304 stainless steel. Beginning with sheet metal, the steel was cut into strips with initial dimensions of around 170mm long, 20mm wide and 0.9mm thick. They were then corrugated using the anvil and cylinder technique. In this case only three samples were tested, one straight, and two corrugated samples with different heights. The geometries of these samples are summarized in Table 5-3. After corrugation, all of the samples were heat treated in a tube furnace at 900°C for 1 hour in Argon gas. The samples were then pulled in tension, using a 50kN MTS machine, with the grips separated by a distance of 100mm. The samples were pulled at a rate of 5mm/min or an initial strain rate of around 0.0008 /s. Similar to the previous samples, some slippage was

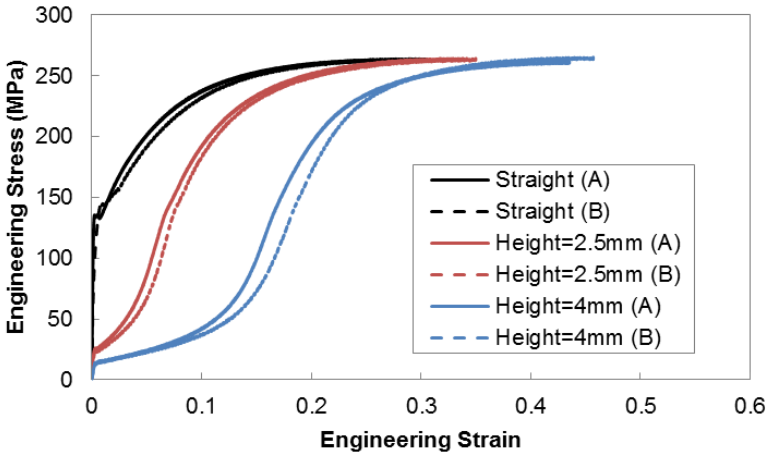


**Figure 5-9: Experimental stress-strain curves of isolated corrugated IF steel strips with variable corrugation height. There are two curves for each sample geometry, labeled A and B. The stress-strain curve for a straight strip of IF steel was included for comparison purposes.**

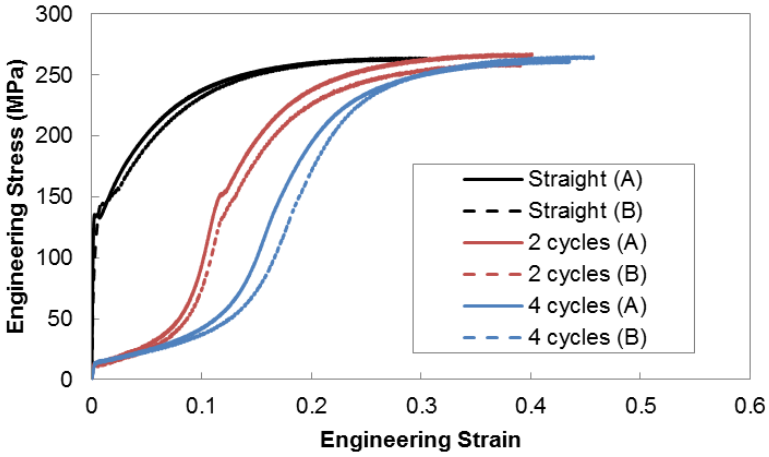


**Figure 5-10: Experimental stress-strain curves of isolated corrugated IF steel strips with variable number of corrugation cycles (or percentage corrugated). There are two curves for each sample geometry, labeled A and B. The stress-strain curve for a straight strip of IF steel was included for comparison purposes.**

observed in the grips and therefore the strain was calculated in a similar fashion using the slippage factor. The stress-strain curves from the tensile tests of these stainless steel samples can be seen in below Figure 5-13. Similar to the previous samples, the trends observed for the stainless steel samples match those expected for corrugated samples. Both materials exhibit the improvement in necking strain with increasing degree of corrugation as a result of a larger

unbending portion of the deformation behaviour and a delay in the onset of increasing work hardening behaviour and subsequent stretching behaviour.

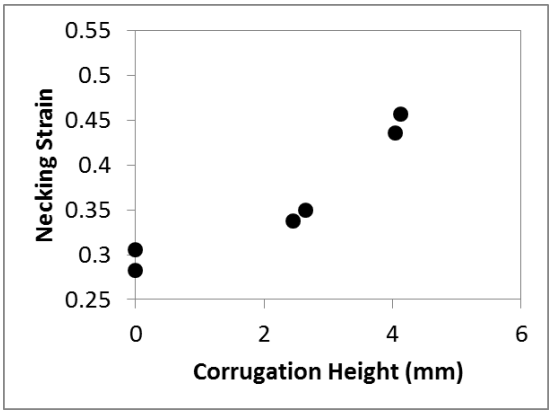


**Figure 5-11: Necking strain as a function of corrugation height for isolated corrugated IF steel.**

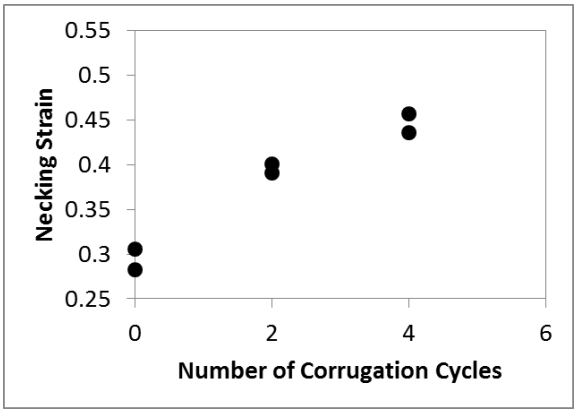


**Figure 5-12: Necking strain as a function of the number of corrugation cycles for isolated corrugated IF steel.**

**Table 5-3: Geometric parameters of corrugated 304 stainless steel for experimental testing.**

| Sample | Period | Height | Number of Corrugations |
|---|---|---|---|
| 1 | NA | 0 | 0 |
| 2 | 15mm | 3.65mm | 5 |
| 3 | 15mm | 2.8mm | 5 |

### 5.1.3 Comparison with FEM and Analytical Model

Based on the results of the tensile experiments shown thus far, there is a clear qualitative validation of the modeling work that was presented earlier. That being said, it would be desirable

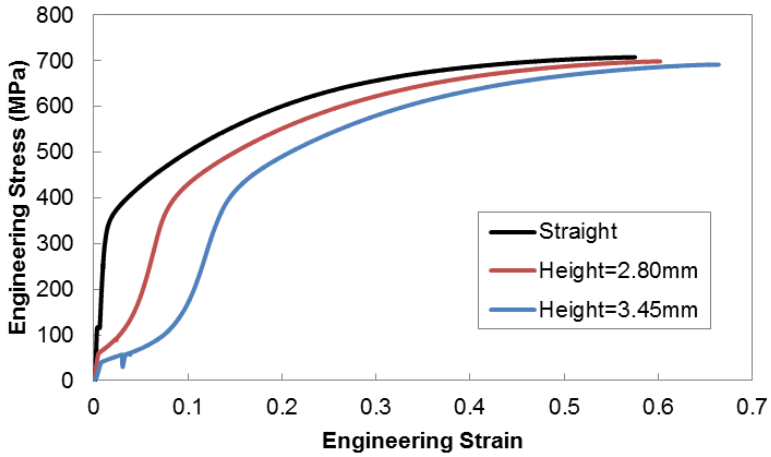


**Figure 5-13: Experimental stress-strain curves of isolated corrugated 304 stainless steel strips with variable corrugation height. The stress-strain curve for a straight strip of stainless steel was included for comparison purposes.**

to obtain some quantitative validation of the modeling approach by modeling the exact geometries and systems that were tested experimentally using both FEM simulations and the analytical model developed in the previous chapter. The first step in modeling these systems is to obtain a fairly accurate representation of the stress-strain response of the material itself. This can be done by taking the stress-strain curve generated from the experiments of a straight strip and fitting an equation to these curves. Based on the shape of the stress-strain curves shown above it is reasonable to use a power-law hardening model ($\sigma=K\varepsilon^n$) to describe the behaviour of these materials. This is done by first converting the engineering stress, S, and engineering strain, e, values to true stress, σ, and true strain, ε, using the following equations;

$$\boldsymbol{\sigma = S(1 + e)} \quad (5\text{-}2)$$

$$\boldsymbol{\varepsilon = ln(1 + e)} \quad (5\text{-}3)$$

In order to determine the values of the hardening coefficient, K, and the hardening exponent, n, a logarithmic plot of ln(σ) versus ln(ε) is employed. A linear line can then be fitted to the data and the value of K is extracted from the y-axis intercept, which is equal to ln(K) and the value of n is equal to the slope of the line. It is often necessary to only select a section of the data in order to get a good fit between the linear line and the data. The yield strength of the material is taken using a 0.2% offset method. This process was completed for the three materials of interest with their values of K, n and $\sigma_{ys}$ shown in Table 5-4.

**Table 5-4: Power law hardening material parameters fitted to tensile test experimental data**

| Material | Hardening Coefficient, K | Hardening Exponent, n | Yield Strength, $\sigma_{ys}$ |
|---|---|---|---|
| Copper (1) | 540 MPa | 0.53 | 25 MPa |
| Copper (2) | 430 MPa | 0.30 | 25 MPa |
| IF Steel | 480 MPa | 0.25 | 130 MPa |
| 304 Stainless Steel | 1600 MPa | 0.45 | 130 MPa |

Note that are two sets of parameters listed for copper. The first copper parameters were based on the stress-strain curves from earlier experiments of copper strips prior to the consideration of the slippage factor. The second set of parameters is based on the experiment explained above using the slippage correction factor. Additionally, the first set of parameters matches the shape of the majority of the stress-strain curve of copper, but deviates when the experimental curve nears the ultimate tensile strength. This set of parameters was used to represent copper for the FEM simulation work presented in the previous chapters. However, it was noticed that this set of parameters does a poor job of representing the necking strain for copper and over-predicts this value. For that reason the second set of parameters were selected to have much better fit with the later strain stages of the experimental curve and accurately predicted the necking strain. This came at the expense of deviations at smaller values of strain. Due to the fact that the goal of the

FEM work presented in the previous chapters was not to necessarily replicate a specific material system, but rather to show the trends of changing different parameters, the use of the first set of copper parameters was deemed acceptable. Since the goal of this chapter is validation of modeling work, the second set of copper parameters will be used in the models when comparing to the experimental results. A plot of the stress-strain curves for all four sets of material parameters is included below in Figure 5-14, with the experimental curves included for comparison purposes.

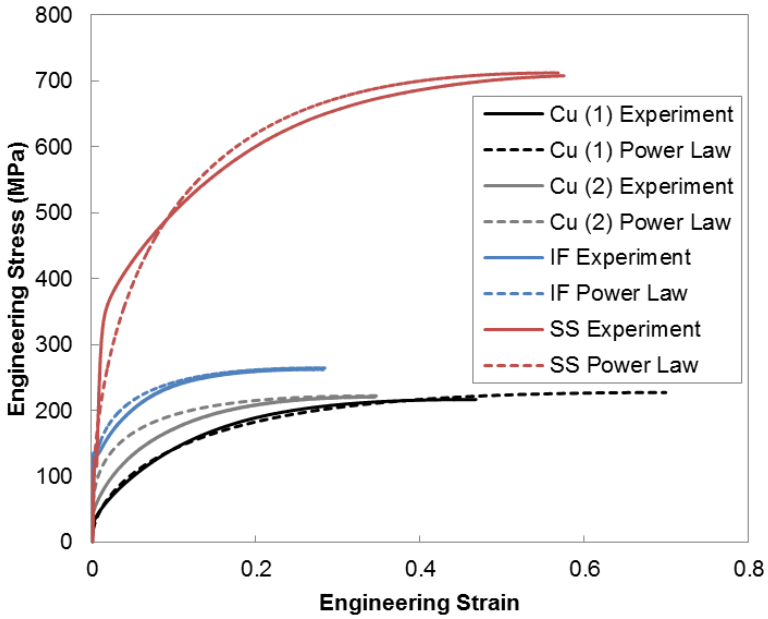


**Figure 5-14: Experimental stress-strain curves and their corresponding power-law hardening representations, using the parameters listed in Table 5-4 for copper (Cu), interstitial free steel (IF), and 304 stainless steel (SS).**

Using the material parameters given in Table 5-4, with Copper (2) used for copper, FEM simulations and predictions using the analytical model were performed to model the behaviour of each of the tensile tests performed for the three materials. In order to compare the stress-strain curve generated from the plane strain FEM simulation to the stress strain curve from the uniaxial experiment and analytical model it is necessary to apply a multiplication factor to the stresses of

the FEM curve. This factor is calculated by substituting effective stress and strain in the power law equation with their plane strain equivalents:

$$\boldsymbol{\sigma_{eff}} = \frac{\sqrt{3}}{2}\boldsymbol{\sigma_1} \tag{5-4}$$

$$\boldsymbol{\varepsilon_{eff}} = \frac{2}{\sqrt{3}}\boldsymbol{\varepsilon_1} \tag{5-5}$$

This leads to a power law material response in plane strain that follows the following expression:

$$\boldsymbol{\sigma_1} = \left(\frac{2}{\sqrt{3}}\right)^{\boldsymbol{n+1}} \boldsymbol{K{\varepsilon_1}^n} \tag{5-6}$$

The factor in front of the power-law is dependent on the material due to the inclusion of the n value. This means that it will not be possible to apply a simple conversion factor for plane strain simulations of composite systems due to the more complicated stress-strain response of the materials. However, the factor works well for the isolated corrugations and was confirmed by running a 3D simulation of a corrugated strip and comparing the resulting stress-strain curve to the adjusted stress-strain curve of a plane strain simulation with the same corrugation geometry. Both curves overlapped when this was performed.

Plots comparing the stress-strain curves generated by the analytical model, the plane strain FEM simulation and the experimental tensile tests are shown below for copper sample 3A in Figure 5-15, IF steel sample 2A in Figure 5-16, and stainless steel sample 2 in Figure 5-17. Similar plots were made for the rest of the samples but the plots were comparable. What is evident in looking at these plots is that there is a good qualitative match in terms of the unbending behaviour of the corrugations. All three methods predict similar increasing work hardening behaviour that is characteristic of an unbending corrugation. Additionally, the levels of stress present in these curves show very good agreement between the techniques, in particular with regards to the ultimate tensile strength. The main differences between the curves provided by each of the

technique lies in the duration of the unbending period and the strain at which the increasing work hardening behaviour takes off. In all cases the analytical model shows the smallest unbending region and the earliest onset of stretching behaviour, and it is commonly found that the experimental curve has the largest unbending region and the latest onset of stretching behaviour. It is possible that this could be a result of errors in estimating the geometric parameters found experimentally, in particular the corrugation height. In fact, if the corrugation height used in the analytical model is increased by a value comparable to the thickness of the strip, a good match can be found between the analytical model and the experimental results. An example of this is seen in Figure 5-18, for IF steel sample 2, in which the height of the corrugation is increased from 4mm to 5mm in the model. It is also possible that the shapes of the corrugations in the various techniques differ slightly from one another. For example, the spline based corrugation in the FEM simulations is different from the sinusoidal/triangular corrugation used in the analytical model, which in turn may be different from that generated using the anvil and cylinder technique experimentally. These slightly different shapes may lead to different amounts of unbending occurring and thus result in different onsets of stretching behaviour.

Another common trend seen in these comparison plots is that the FEM curves reach their peak stress and neck earlier than that observed for the model or experimentally. If one looks at a Considere plot for these FEM samples it becomes apparent that something is causing these samples to neck prematurely. An example can be seen in Figure 5-19 again for the IF steel sample 2. It is clear that at high strains the work hardening is decreasing at a predictable rate, and then it suddenly drops causing the work hardening rate to equal the stress and triggering the necking of the sample. If the work hardening continued along the path it was going, it appears that it would intersect the stress curve at a value closer to that seen for the analytical model. It is

not clear what causes this early necking in the FEM simulations, but it is consistent for all isolated corrugated samples, and occurs even if a 3D model is used instead. Perhaps it is due to the local constraint caused by the boundary conditions, as the necking seems to initiate at the sample ends for these simulations.

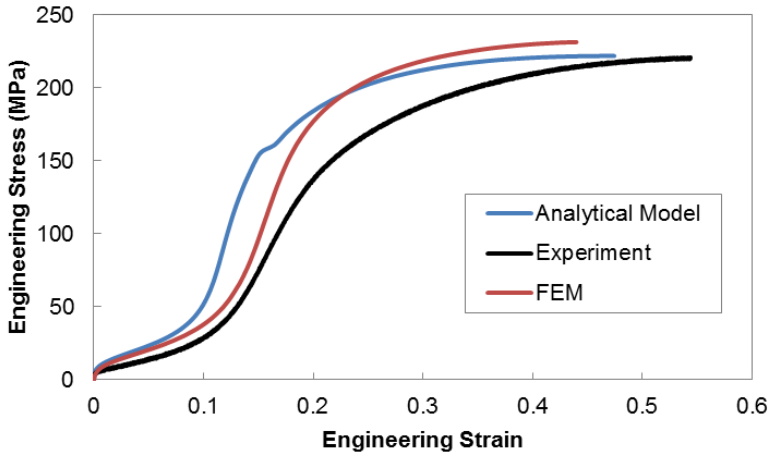


**Figure 5-15: Comparison of stress strain curves from the analytical model, experimental tensile tests and FEM simulations of corrugated copper sample 3A from Table 5-1.**

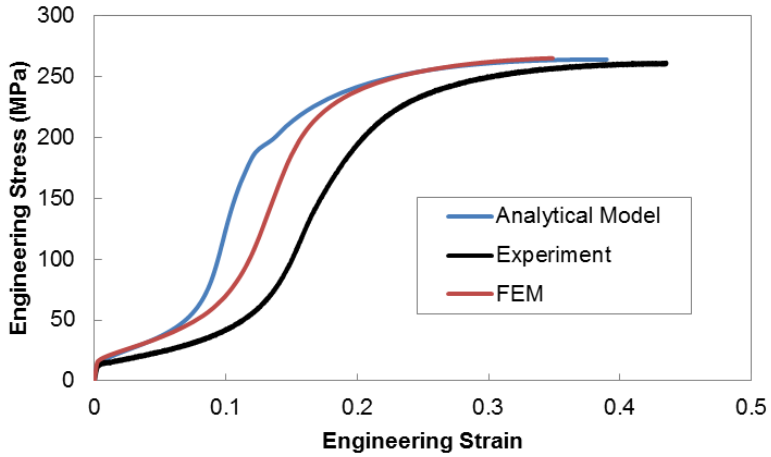


**Figure 5-16: Comparison of stress strain curves from the analytical model, experimental tensile tests and FEM simulations of corrugated IF steel sample 2A from Table 5-2.**

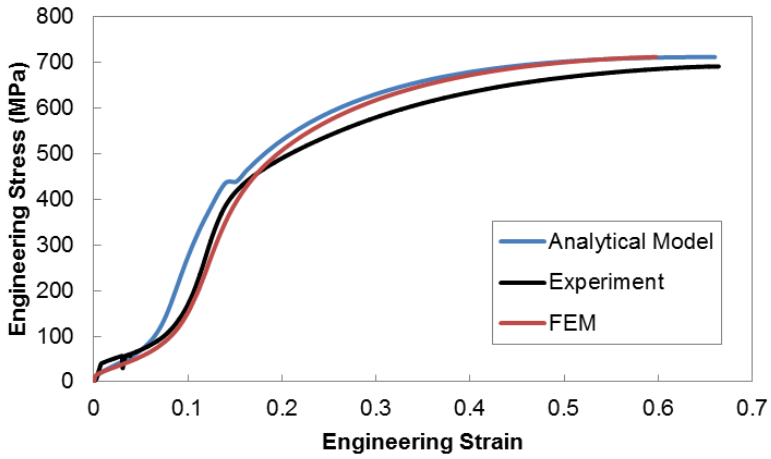


**Figure 5-17: Comparison of stress strain curves from the analytical model, experimental tensile tests and FEM simulations of corrugated stainless steel sample 10 from Table 5-3.**

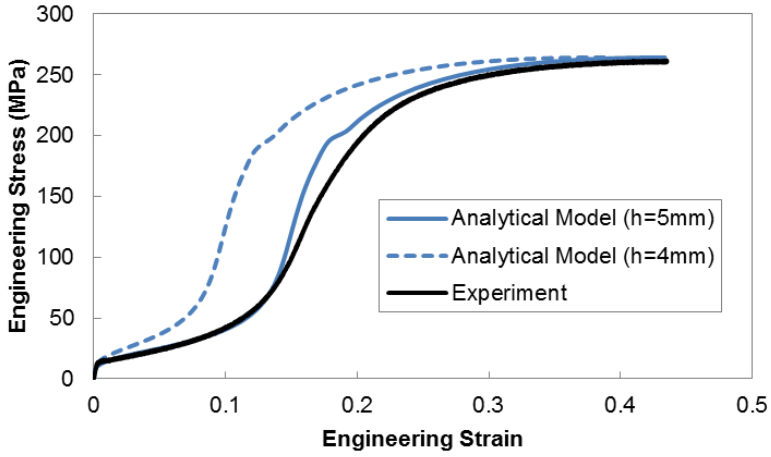


**Figure 5-18: Comparison of stress strain curves from the analytical model and experimental tensile test of corrugated IF steel sample 2A from Table 5-2. This geometry consists of a corrugation height of 4mm. Also included is an analytical model curve in which the height is increased to 5mm.**

In general, there is good qualitative agreement with regards to the stress strain response seen experimentally and in the modeling efforts. The unbending, transition and stretching regions of the stress strain curves that were observed in the modeling efforts were found in the experimental testing, and the general trends with regards to the effect of geometric parameters were also observed. The levels of stress seen in the experiments match those in the modeling as well. The main difference seems to be the length of the unbending region of the stress-strain curve, which

is likely due to the differences in corrugation shape and the measurement of geometric parameters experimentally. Now that the modeling of the isolated corrugations has been experimentally validated, the experimental work pertaining to the corrugation reinforced composites will be discussed.

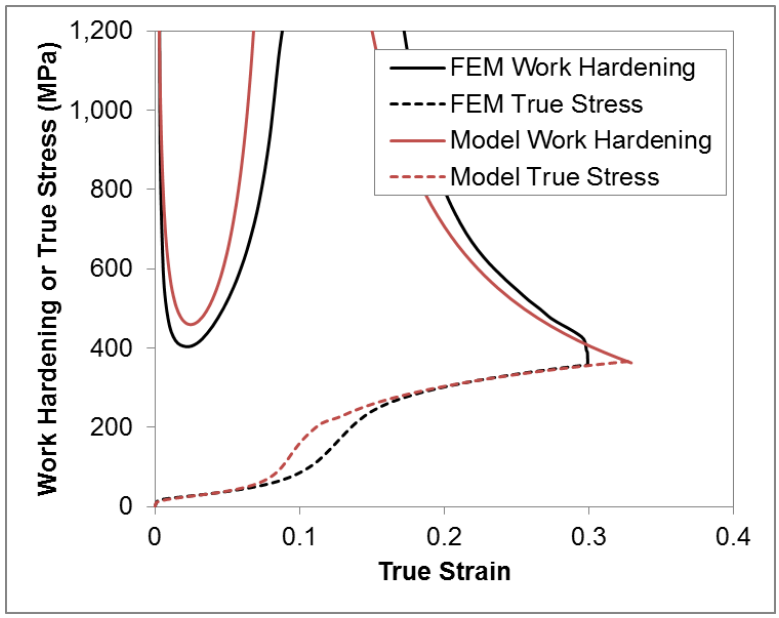


**Figure 5-19: Considere plot showing work hardening and stress based on the stress strain curves from the analytical model and FEM simulations of corrugated IF steel sample 2A from Table 5-2.**

## 5.2 Corrugation Reinforced Composites

The purpose of this section is to present the experimental work that was completed that focused on making and testing corrugation reinforced composites. This section will discuss the efforts made for a number of different material systems, but will start with, and mainly focus on, the system that yielded the best results; the solder matrix – copper reinforcement system.

### 5.2.1 Solder Matrix – Copper Reinforcement System

#### *5.2.1.1 Uniaxial Tension Samples*

The initial goal of these experiments was to develop a method for making corrugation reinforced composites and then test their stress-strain response to see whether the gains in ductility observed in theory were obtainable in practice. Therefore, the preliminary attempts at making these composites focused on creating samples for tensile testing. The component materials were selected to be a eutectic lead-tin solder matrix and a copper reinforcement. The low melting point of the solder was attractive as it would allow sample fabrication to be done at relatively lower and safer temperatures compared to other options. Additionally, copper and solder were found to form a relatively strong interface, with good contrast in terms of the strengths of the materials. Also, copper has good formability, which made it attractive in terms of easily corrugating the reinforcement material. The casting process that was used to make these samples will now be described.

The first step in the fabrication of these composite materials was to create a corrugated strip of copper to be used as the reinforcement. The same process as that use for the isolated corrugation, using the anvil and cylinders, was used for these purposes. After the copper strip was corrugated and annealed, a pre-coating process was performed. First, the surface of the copper strip was prepared for coating by cleaning it in a solution of phosphoric acid and water in an ultrasonic bath for 15 minutes. As this was happening, small pieces of solder were cut from an ingot and placed in a tall, thin, steel tube that was closed on the bottom end. This tube was then placed in a box furnace at 270°C and the solder was melted. Once the solder was completely molten, the tube was removed from the furnace and the cleaned copper strip was dipped into the solder. It was then cooled by dipping it in a pail of water. In order to aid in the wetting process, a

phosphoric acid flux was applied to the surface of the copper just prior to the dipping process. This enabled the formation of a thin solder layer on the surface of the copper, as seen in Figure 5-20. This pre-coating process was found to aid in the formation of a better interface during the casting process.

**Figure 5-20: Copper strip after pre-coating of solder has been applied.**

After this pre-coating process, the actual casting process was performed. First, the die into which the solder was to be cast was coated using a boron nitride spray in order to minimize sticking to the die wall. The die was a split-piece steel die in which the cavity of the die was in the shape of a dog-bone style tensile sample as seen in Figure 5-21. Also included in this die were notches on each end to hold the reinforcement strip centered in place. After the coating dried, the pre-coated corrugated strip was placed in the die, the die was screwed shut and then placed in a box furnace at 270°C along with a ceramic crucible loaded with pieces of solder. This melting of the solder and preheating of the die were done for 30 minutes, after which the die was removed from the furnace. The molten solder was then poured out of the crucible into the casting hole of the die until the die cavity was filled. The die was then tapped and hit periodically over the next 10 minutes to remove bubbles and prevent cavity formation during solidification. After the 10 minutes, the solder had solidified and it was quenched in a pail of water. The corrugated composite sample was then removed from the die and any surface cavities that were present were filled using solder wire and a torch. An example of a sample can be seen in Figure 5-22 below.

After this point, the sample underwent machining to clean up the surfaces and ready it for mechanical testing.

**Figure 5-21: Die used for casting dog-bone composite samples in assembled (left) and open (right) configurations.**

**Figure 5-22: Solder matrix, copper reinforcement cast dog-bone sample.**

The samples were machined to dimensions similar to those given in Figure 5-23 below giving an effective gauge length of 60mm. For the initial set of tensile tests, three samples were created. The first sample was entirely solder. The second sample had a single straight copper reinforcement of thickness 1.18mm. And the third sample consisted of corrugated copper reinforcement with a period of 15mm, a height of 4mm, and a reinforcement thickness of 1.18mm. These samples were pulled in tension using a 100kN tensile testing machine at a deformation rate of 2 mm/min or an initial strain rate of around 0.0003 /s. The strain was measured using an extensometer and the stress was calculated by dividing the measured force by

the initial cross sectional area of the gauge section. The stress-strain curves for the solder and corrugation reinforced copper samples can be seen in Figure 5-24. Unfortunately, the data from the straight reinforced sample was not captured. The discontinuity seen in the solder curve is a result of unloading and reloading the sample in order to reposition the strain gauge, which was reaching its limit. Without a straight reinforced composite curve for comparison it is difficult to judge whether the corrugation reinforced sample would provide an improvement in ductility.

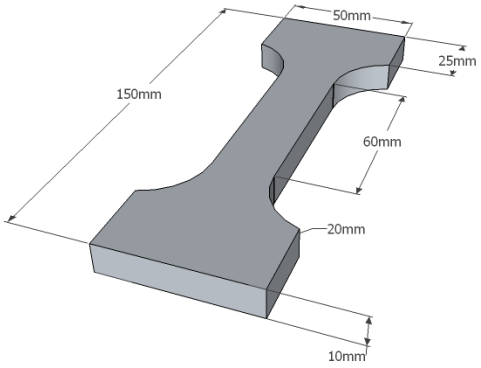


**Figure 5-23: Dimensions of dog-bone samples after machining for tensile tests.**

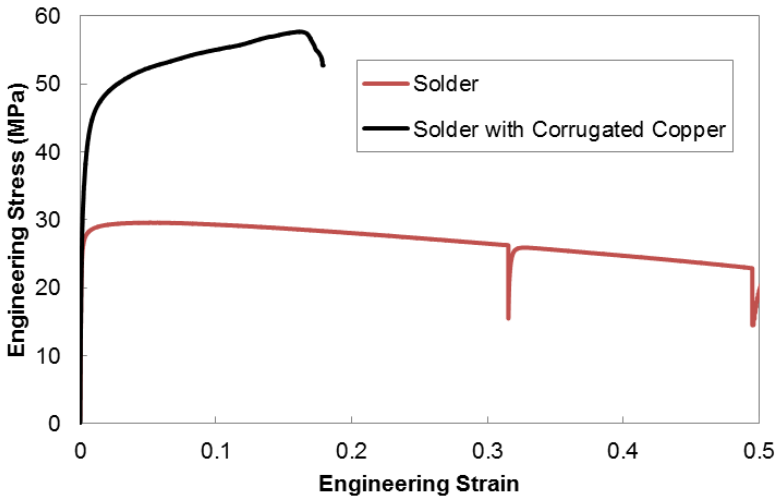


**Figure 5-24: Experimental stress-strain curves from uniaxial tension test of cast dog-bone samples. One sample was entirely solder and the other had a solder matrix and corrugated copper reinforcement.**

With that in mind it is possible to view the work hardening behaviour of the corrugated composite to see if it exhibits the characteristic boost in work hardening typical of an unbending corrugated geometry. The work hardening for the corrugated sample was calculated from the stress-strain data, sampling every 400$^{th}$ data point in order to minimize the noise, and can be seen in the Considere plot in Figure 5-25. The characteristic boost in work hardening is present in this curve. Whether this would have led to a delay in the necking of the sample compared to a straight case is unknown. One can perform a simple calculation using the expression from Semiatin and Piehler[27] discussed earlier for the necking strain of a sandwich structure under uniaxial tension to estimate this necking strain. In order to perform this calculation it is necessary to have material models for both the solder matrix and the copper reinforcement. A power law representation for the copper has already been determined from the isolated copper strip tests and is found in Table 5-4. A similar power-law expression can be found for the solder material based on the tensile test just performed for the solder dog-bone sample. The power-law parameters for the solder are summarized in Table 5-5 below. Using these parameters the necking strain for a solder-copper composite with a 10% volume fraction can be determined by numerically solving the following equation for strain, ε;

$$(\mathbf{1}-\mathbf{f})\left(\mathbf{n_{So}K_{So}\varepsilon^{(n_{So}-1)}}-\mathbf{K_{So}\varepsilon^{n_{So}}}\right)+\mathbf{f}\left(\mathbf{n_{Cu}K_{Cu}\varepsilon^{(n_{Cu}-1)}}-\mathbf{K_{Cu}\varepsilon^{n_{Cu}}}\right)=\mathbf{0} \quad (5\text{-}7)$$

For this particular system, this gives a true necking strain value of 0.17 or an engineering necking strain of 0.185. This is compared to the necking strain value of 0.161 seen experimentally for the corrugated copper reinforcement sample. Therefore, in this particular case the corrugation did not boost the ductility of the sample. This lack of improvement in necking strain however, may not have been due to the corrugated geometry, but rather because imperfections in the sample interface resulted in premature failure.

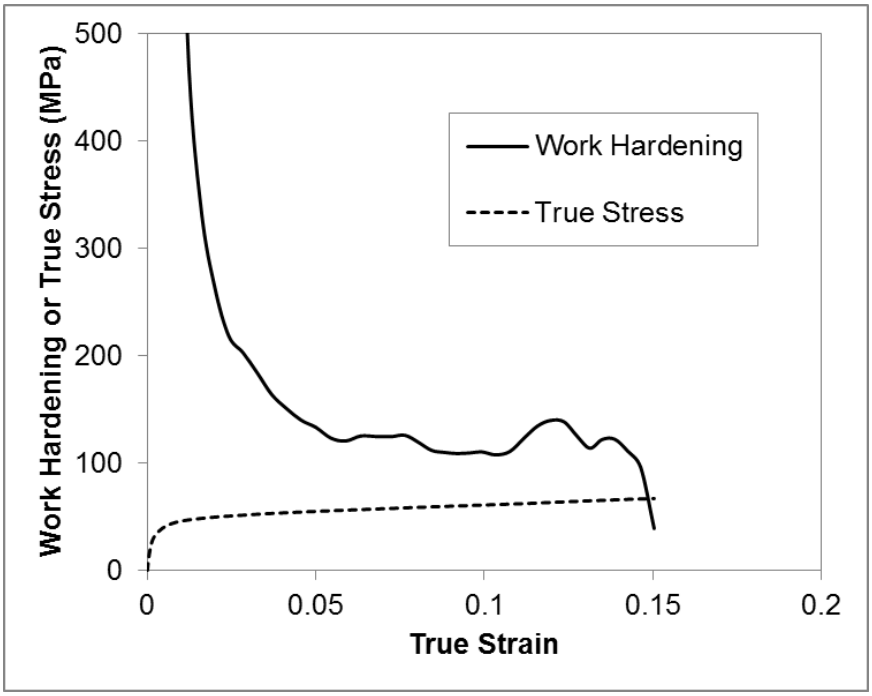


**Figure 5-25: Considere plot calculated from experimental stress-strain curves of uniaxial tension test of a solder matrix reinforced with a copper corrugation.**

**Table 5-5: Power law hardening material parameters fitted to tensile test experimental data for solder**

| Material | Hardening Coefficient, K | Hardening Exponent, n | Yield Strength, $\sigma_{ys}$ |
|---|---|---|---|
| Solder | 37 MPa | 0.06 | 25 MPa |

Looking at the sample after the completion of the tensile test it is obvious that there was some serious interfacial decohesion occurring. This can be seen in the pictures of this sample shown in Figure 5-26. Similar decohesion was observed in the sample with the straight copper reinforcement. All of the FEM modeling work that was described in the previous chapters for these corrugated composites assumed a perfect, cohesive interface that would never break. This assumption was used to simplify the analysis and to focus on the effect of the geometry itself. However, in practice the strength of the interface of the composite plays a very important role in determining the mechanical response of the material. When the interface is weak and it decoheres, stress can no longer be transmitted across the interface at those points, making the

composite less structurally efficient. This can force the matrix to carry much higher loads than it otherwise would with a strong interface and leads to significant deformation and perhaps early necking in these regions. These areas of interface decohesion are often the sources of the ultimate failure of the composite. It is likely that for these samples the interfacial decohesion was caused by the presence of an oxide at points along the surface of the copper which may have formed during the preheating stage of the fabrication process. The lack of a strong interface in these solder-copper composites poses a problem in evaluating the ability of the corrugated architecture to improve the ductility of the composite, as it leads to incomplete load transfer and alters local deformation patterns. The detrimental effect of this weak interface is particularly evident under tensile loading conditions as it leads to local weaknesses that can trigger early necking. The issues concerning interfacial strength will be discussed more later in this section.

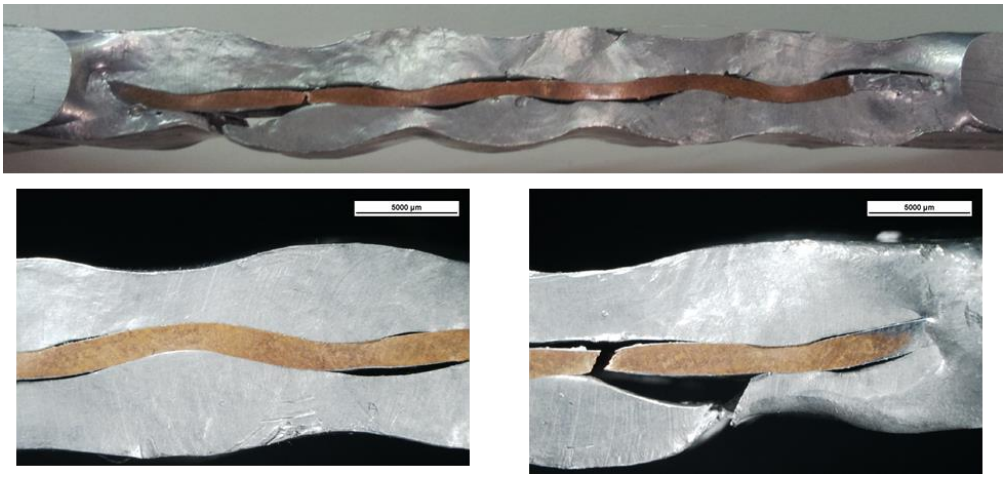


**Figure 5-26: Pictures of composite with corrugated copper reinforcement embedded in a solder matrix. Images were taken after approximately 16% deformation under uniaxial tension.**

Before discussing the next experiments that were performed, there are some other interesting things seen in Figure 5-26 to point out. The first item that is of interest is the fact that the copper reinforcement has clearly straightened out to a large degree. In fact, looking at the top image, it appears that the copper has almost completely unbent. This straightening of the corrugated

reinforcement is a desirable outcome as it is through unbending that the boost in work hardening occurs. The unbending of the copper observed visually supports the claim that the boost in work hardening seen in Figure 5-25 is a result of an evolving geometry. The second item of interest in Figure 5-26 is the presence of what appears to be multiple, periodic necks along the sample surface. This multiple necking phenomenon matches that seen in the FEM stress map for the copper-steel system seen earlier in Figure 4-35. This wavy, periodic surface is likely a result of the movement of the peaks and troughs towards the middle of the sample as the corrugation straightens out. When the corrugation unbends it brings the nearby matrix material with it and thus the matrix above a peak or below a trough moves towards the centerline. This would create an indent shape in these regions near the surface. In an opposite fashion the matrix below a peak or above a trough is being pushed outwards by the unbending corrugation, creating a bulge shape in these regions near the surface. Due to the periodic nature of the corrugation this unbending process leads to alternating bowl and bulge shapes at the surface creating that wavy structure. This makes it appear as if multiple necks are forming. However, every bowl shape created above a peak is coupled with a bulge shape below that same peak. This is not truly a neck being formed which is characterized by a narrowing on both the top and bottom surfaces. Instead the tensile loading of these corrugation reinforced composites seems to transfer the corrugated architecture from the reinforcement to the overall material as unbending progresses.

Due to the interfacial decohesion and early necking seen in the samples above, additional samples were fabricated and machined for tensile testing. For these samples, in addition to acquiring overall stress-strain data from the tensile test, local strain data was also collected. This was done using the technique of Digital Image Correlation (DIC) using the Aramis software. Similar to the grid method used in Poole's[24] work on copper tungsten composites, DIC calculates

local strains by tracking the movement of a random pattern of dots on the surface of the sample. This is done by using a camera to take pictures of the pattern on the surface of the sample. These pictures are taken while the tensile test is being performed and they are taken at given time intervals. The software then calculates the strain in a region by tracking the location of the random spots relative to their neighbours. This will give a set of strain maps, each map at a different stage of overall total deformation. In order to apply a random pattern of dots, the surface of the sample was spray painted, first with a white paint to give a clean background followed by a light misting of a black paint such that a random pattern of dots was created. Such a pattern can be seen in Figure 5-27 below.

**Figure 5-27: Spray paint generated, random pattern used for Digital Image Correlation.**

Unfortunately, these new samples had similar problems with regards to interface decohesion and early necking, and often failed at even earlier strains than the sample shown above. For this reason, the stress-strain curves of these tests will not be shown. With that being said, there is still some information with regards to the strain maps generated through DIC that is interesting to inspect. In particular, the strain maps of a solder-copper corrugated composite with a corrugation height of 5mm, period of 15mm and thickness of 1.18mm is of interest. These tests were performed on a 10kN tensile machine at a deformation rate of 1mm/min. The sample was

machined to the same dimensions as the previous dog-bone samples. Maps of the local strain in the vertical (or longitudinal) direction can be seen in Figure 5-28 for this sample at different levels of overall deformation. Note that the colour legend changes at each level of strain. Looking at the first strain map representing a total strain of 0.024, there is a pattern that has emerged along the right side which consists of periodic regions of high local strain. These regions correspond to the regions underneath a corrugation peak for which high strains are predicted according to the FEM simulations performed earlier. However, if this material was deforming as expected for a corrugation reinforced composite, there would exist similar periodic regions of high strain on the left side of the sample, offset from those on the right side of the sample. These regions would correspond to areas that are above a corrugation trough. For this sample, this pattern is only seen near the bottom of the sample. Looking at the other strain maps at higher levels of strain the reason for this lack of pattern on the right side becomes apparent as the strain begins to localize closer to the top of the sample and data begins to be lost in this region. This was caused by the decohesion of the interface in this region and the subsequent matrix failure. Once again, the weak interface is the source of problems in evaluating these composites. With that being said the initial local deformation of these corrugated solder-copper composites showed promise in displaying the behaviour expected of these materials based on what was observed in the FEM simulations.

Although, some interesting information was obtained from this set of tensile test experiments there were a number of issues that prevented the acquisition of complete stress-strain curves and local strain maps. First, the interfacial strength between the solder and copper is not strong enough to withstand the stresses imposed on it during loading. Tensile testing is particularly sensitive to small defects at the interface as it triggers local decohesion. This decohesion at the

interface led to loss of local strain data and early necking. Second, the solder material was very soft and it tended to flow in the grips during the loading. This would affect the amounts of strain calculated and would also affect the load required for a given amount of deformation. For these reasons, it was decided that it may be advantageous to change the manner of loading used to test these composites.

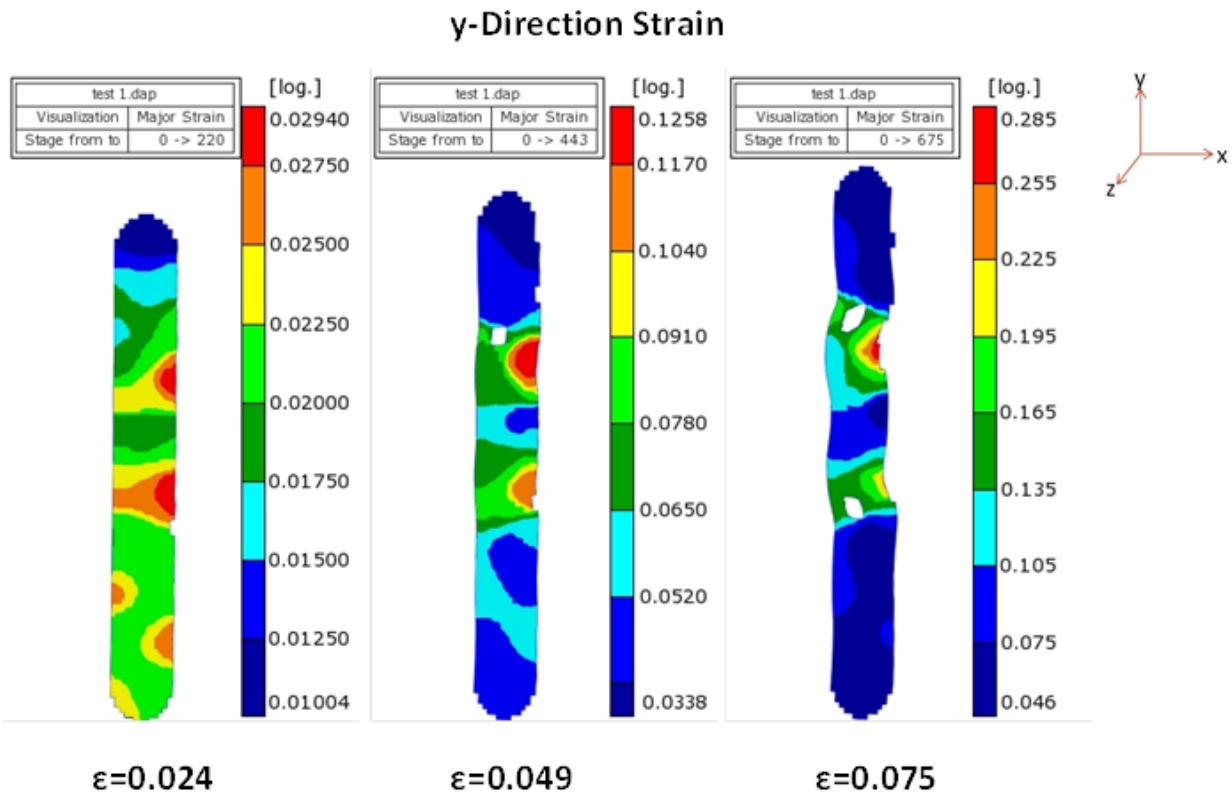


**Figure 5-28: Maps of y-direction strain (vertical) calculated using DIC from the tensile test of solder-copper composite with a corrugated reinforcement.**

### *5.2.1.2 Transverse Compression Samples*

In particular, it was decided that these samples would be tested in plane strain compression in the transverse direction, as illustrated in Figure 5-29, using a channel die setup. By testing the samples in compression the concerns of a weak interface leading to interface decohesion and subsequent early necking of the matrix would be avoided. In addition, since no grips are used in

these tests, the problems surrounding the solder flowing in the grips would be avoided. The use of channel die compression comes with its own set of concerns including the need for small samples due to the large forces required and also the requirement that an interrupted test be performed in order to perform DIC. The sample would have to be deformed a small amount, removed from the channel to take a picture of the speckle pattern, returned to the channel and the process repeated. Additionally, frictional effects become important for compressive loading, in particular when the compression is done in a channel.

#### 5.2.1.2.1 Justification for Transverse Compression Testing

Before performing these channel die compression tests it was important to establish that deformation of these corrugated composites in the transverse direction in plane strain compression was comparable to tensile deformation in a couple of key ways. First off, it needs to be established whether the overall stress-strain curve generated from a transverse compression test is at all predictive of what would occur for tensile loading of the same composite. In particular, can the transverse plane strain compression curve provide any predictions on the expected necking strain under tensile loading. The second thing that needs to be determined is whether the local deformation patterns are similar for both loading geometries. If it can be shown using FEM modeling that similar strain maps are generated under transverse plane strain compression, as under plane strain tension, then it can be inferred that any strain patterns measured experimentally in transverse plane strain compression are indicative of what would occur for tensile samples if the interfacial issues were not occurring. In order to test the usefulness of using transverse plane strain compression loading, FEM simulations were conducted for various loading states.

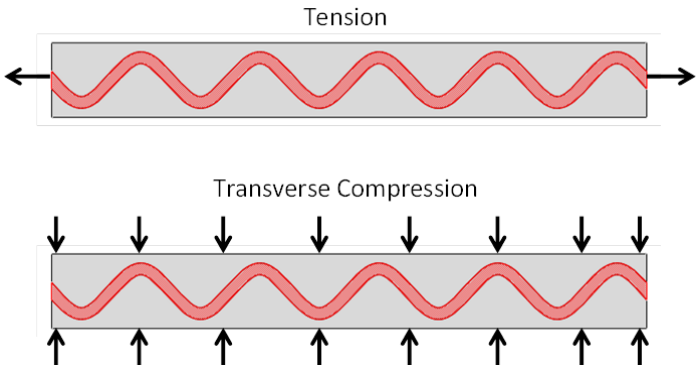


**Figure 5-29: Comparison of loading under tension (top) and transverse compression (bottom).**

To begin, similar to a lot of the previous FEM work performed earlier, the material system that was explored was a copper matrix – 4130 steel reinforcement system. As will be explained later, experimental tests using this system were also conducted. In this particular study, four different loading conditions were examined;

1. Plane strain tension
2. Uniaxial tension
3. Transverse plane strain compression
4. Transverse uniaxial compression

The boundary conditions for these simulations were set as described earlier in section 3.3.6. For each of these loading conditions, five different reinforcement geometries were simulated, as outlined in Table 5-6. This consisted of one straight reinforcement geometry and four corrugated reinforcement geometries with different corrugation heights. The samples were 15mm long, 10mm high and for the uniaxial tension and compression simulations, which require 3D modeling, the sample width was 10mm.

The stress strain curves generated from these simulations are divided into plots for each loading condition and can be seen in Figure 5-30 for plane strain tension, Figure 5-31 for uniaxial

tension, Figure 5-32 for transverse plane strain compression and Figure 5-33 for transverse uniaxial compression. The strain for the compressive loading is calculated by dividing the vertical displacement of the top surface by the initial height of the composite and the stress is calculated by dividing the sum of the reaction forces on the bottom surface by the initial cross sectional area. Upon first inspection of Figure 5-32 and Figure 5-33, there does not seem to be significant differences between the curves representing different reinforcement geometries under compressive loading. The main variations among the curves in a given plot seem to be a slight decrease in stress values at low strains as the corrugation height is increased and slight changes in inflection points and curvature.

**Table 5-6: Geometric parameters of composites used in simulations with various loading conditions.**

| Sample | Corrugation Height | Corrugation Period | Reinforcement Thickness | Volume Fraction |
|---|---|---|---|---|
| 1 (straight) | NA | NA | 1.32 mm | 13.2% |
| 2 | 2 mm | 15 mm | 1.26 mm | 13.2% |
| 3 | 4 mm | 15 mm | 1.13 mm | 13.2% |
| 4 | 6 mm | 15 mm | 1.00 mm | 13.2% |
| 5 | 8 mm | 15 mm | 0.87 mm | 13.2% |

It is possible, however, to extract some useful information from these curves by converting the stress-strain data towards effective stress and strain formulations. For example, given the values of engineering stress, $S_y$, and engineering strain, $e_y$, for plane strain compression from a curve in Figure 5-32, one can calculate the effective true stress, $\sigma_{eff}$, and true strain, $\varepsilon_{eff}$, using the following equations:

$$\boldsymbol{\varepsilon_{eff} = -\frac{2}{\sqrt{3}}\ln\left(1 + e_y\right)} \quad (5\text{-}8)$$

$$\boldsymbol{\sigma_{eff} - \frac{\sqrt{3}}{2}S_y\left(1 + e_y\right)} \quad (5\text{-}9)$$

Similar equations could be used for uniaxial compression samples that do not have the $2/\sqrt{3}$ and$\sqrt{3}/2$ factors. Using these values one can then estimate what the engineering stress, $S_x$, and strain, $e_x$, would be for a sample loaded in uniaxial tension:

$$\boldsymbol{e_x = exp(\varepsilon_{eff}) - 1} \tag{5-10}$$

$$\boldsymbol{S_x = \frac{\sigma_{eff}}{(1+e_x)}} \tag{5-11}$$

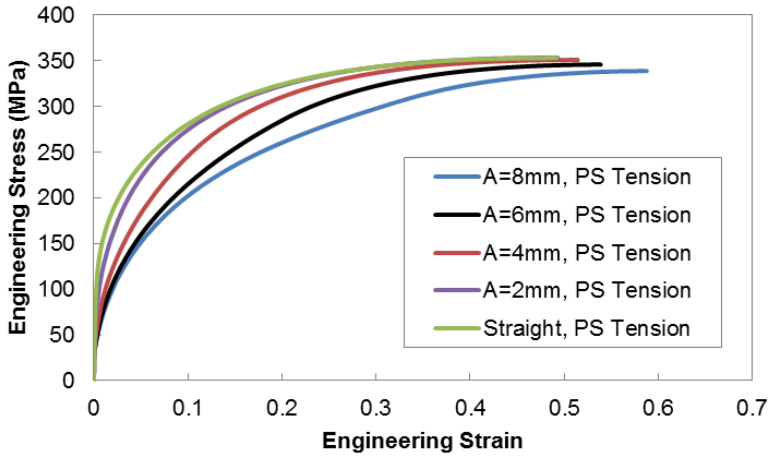


**Figure 5-30: Stress-strain curves from FEM simulations of straight and corrugation reinforced composites under plane strain (PS) tension loading showing the effect of corrugation height. The composites had a copper matrix and 4130 steel reinforcement.**

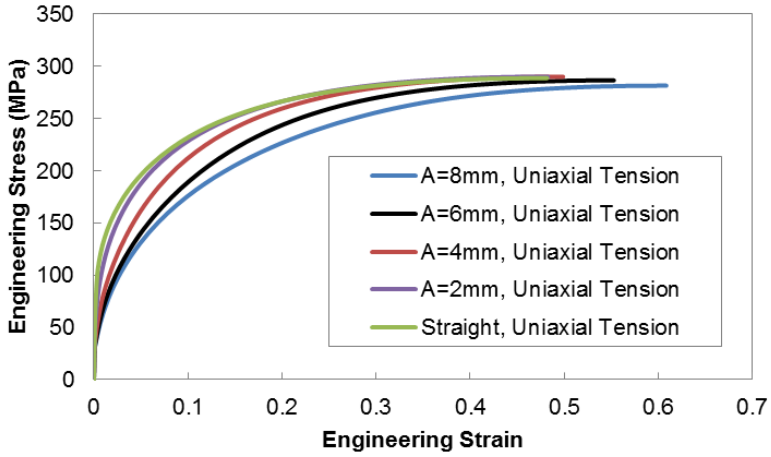


**Figure 5-31: Stress-strain curves from FEM simulations of straight and corrugation reinforced composites under uniaxial tension loading showing the effect of corrugation height. The composites had a copper matrix and 4130 steel reinforcement.**

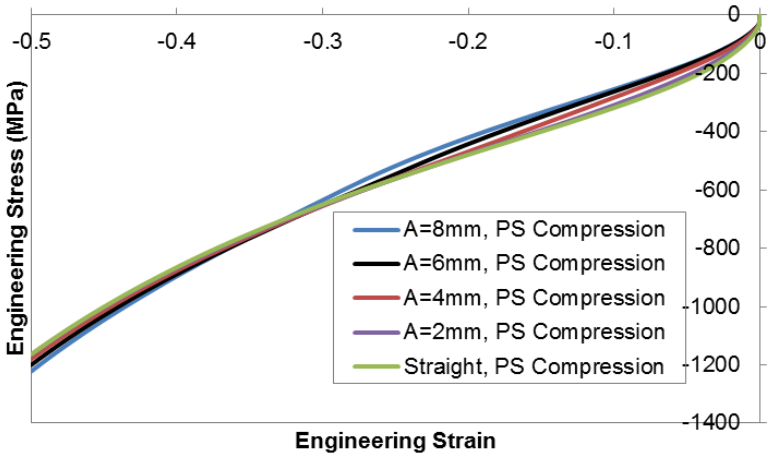


**Figure 5-32: Stress-strain curves from FEM simulations of straight and corrugation reinforced composites under plane strain (PS) compression loading showing the effect of corrugation height. The composites had a copper matrix and 4130 steel reinforcement.**

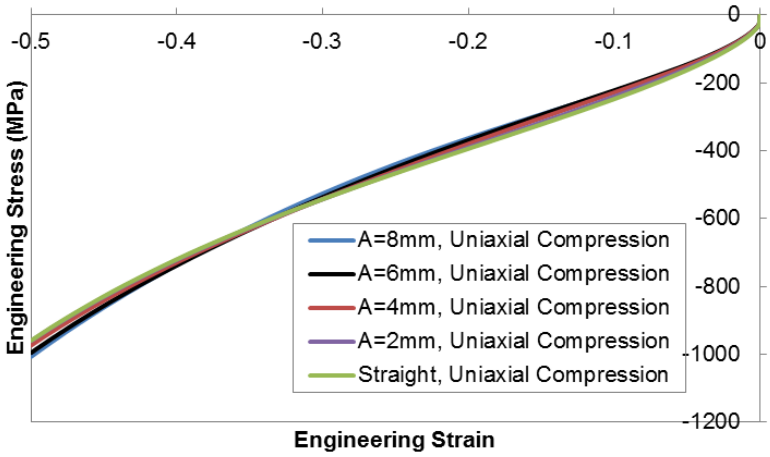


**Figure 5-33: Stress-strain curves from FEM simulations of straight and corrugation reinforced composites uniaxial compression loading showing the effect of corrugation height. The composites had a copper matrix and 4130 steel reinforcement.**

This technique works best in going from transverse plane strain compression to plane strain tension, as the relationship between longitudinal and transverse strains remains consistent. It is less accurate when done for transverse uniaxial compression to uniaxial tension, as the deformation in the width direction makes it more complicated than is covered by the simple

calculation. Performing these operations on the stress-strain data for the curves in Figure 5-32 and Figure 5-33, one can acquire a set of indirect stress-strain curves representing predictions for uniaxial tension behaviour. The indirect stress-strain curves based on the plane strain compression data can be seen in Figure 5-34, and the indirect stress-strain curves based on uniaxial compression data are displayed in Figure 5-35. These curves were terminated when the calculated engineering stress reached its peak value at a point when necking would be expected under tensile loading. Looking at these sets of indirectly calculated curves, behaviour and trends similar to that seen for tensile loading emerge, with no effect on the ultimate tensile strength and an increased necking strain as the height of the corrugation is increased. Plotting the necking strain (or indirectly calculated necking strain) as a function of corrugation height for all four loading geometries, as seen in Figure 5-36, demonstrates that approximately the same values for necking strain occur regardless of the loading geometry and the trends of increasing necking strain with corrugation height are present for all four cases. This suggests that transverse compressive loading, either plane strain compression or uniaxial compression, may be useful for predicting the necking behaviour of corrugated composites under tensile loading conditions.

There is still some concern as to whether the indirectly calculated stress-strain curves will capture the situations wherein there is no benefit through corrugation and the "necking" strain of the corrugated case is less than or equal to that of the straight reinforced case. In order to test this idea, benefit surfaces were generated for loading geometries of uniaxial tension and uniaxial compression. These surfaces were made for linear hardening materials and compare the necking strains (or indirectly calculated necking strains) for a corrugated geometry with a corrugation height of 6mm, period of 15mm and reinforcement thickness of 1mm, to an equivalent volume fraction for the straight geometry with a thickness of 1.32mm. As described earlier in the FEM

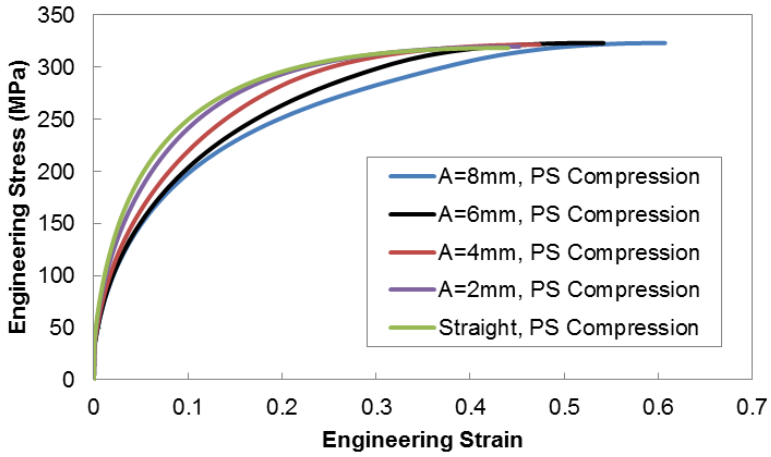


**Figure 5-34: Indirectly calculated stress-strain curves for uniaxial tension loading showing the effect of corrugation height based on FEM simulations of straight and corrugation reinforced composites under plane strain (PS) compression loading. The composites had a copper matrix and 4130 steel reinforcement.**

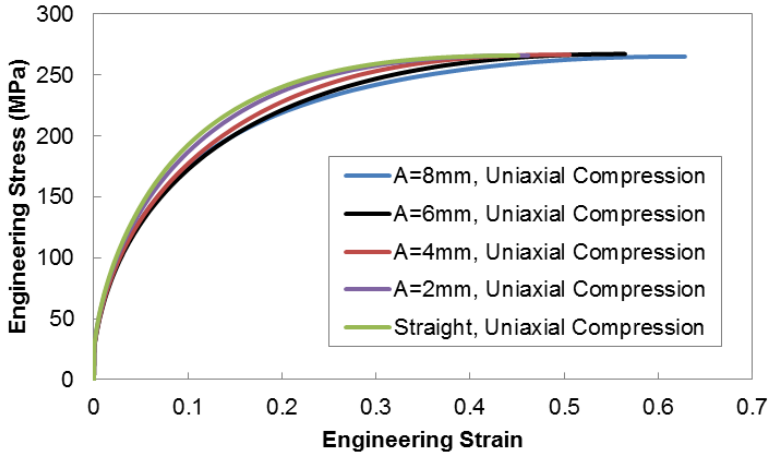


**Figure 5-35: Indirectly calculated stress-strain curves for uniaxial tension loading showing the effect of corrugation height based on FEM simulations of straight and corrugation reinforced composites under uniaxial compression loading. The composites had a copper matrix and 4130 steel reinforcement.**

discussion, this consisted of performing a large number of simulations with matrix hardening rates varying from 100-600MPa and reinforcement yield strengths varying from 150-900MPa. For all simulations the matrix yield strength was constant at 300MPa and the reinforcement hardening rate was fixed at 500MPa. The resultant benefit surfaces for the uniaxial tension and uniaxial compression loading conditions are seen below in Figure 5-37. Comparing the two maps

it is shown that the compression map under-predicts the benefits obtainable through corrugation and slightly shifts the area of benefit towards higher values of matrix hardening rate. This under-prediction in benefit comes from a combination of slightly higher predictions of necking strain for straight reinforced composites and lower predictions of necking for corrugated composites.

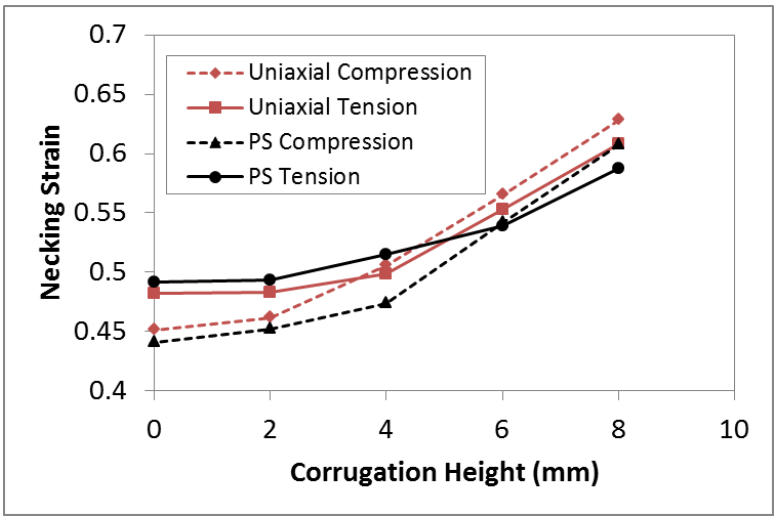


**Figure 5-36: Necking strain (tension) or indirectly calculated necking strain (compression) for copper matrix – 4130 steel reinforcement corrugated composites under uniaxial and plane strain (PS) loading conditions versus corrugation height.**

This suggests that indirectly calculated stress-strain curves obtained from compression testing should only be used to give a conservative estimate for the necking strain of corrugation reinforced composites. In addition, the trends observed with regards to the effect of corrugation height and materials properties seem to also occur for these indirectly calculated stress-strain curves. For these reasons it was deemed that valuable information may be obtained from the stress-strain curves of transverse compression of corrugation reinforced composites.

In addition to the stress-strain data, it would be desirable to obtain useful information pertaining to local strain patterns from these transverse plane strain compression tests. In order to determine whether the strain patterns that occur in plane strain compression are indicative of the

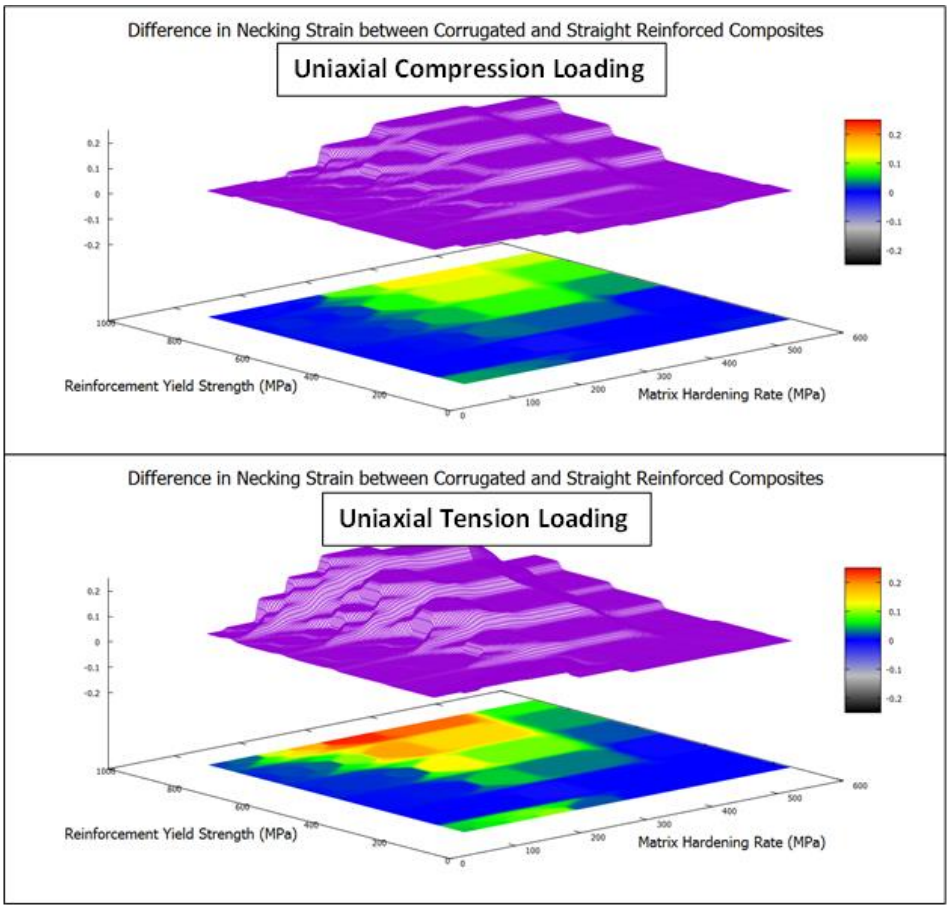


**Figure 5-37: Benefit surfaces showing the improvement in necking strain for a corrugated composite compared to a straight composite for different combinations of reinforcement yield strength and matrix hardening rate. The top plot represents a system in which the loading was uniaxial compression and the necking strains were indirectly calculated necking strains and the bottom plot represents a system in which the loading was uniaxial tension.**

deformation patterns seen under plane strain tensile loading, comparisons of FEM simulation results under these different loading conditions can be used. For this purpose, FEM simulations of a corrugated composite with a copper matrix and 4130 steel reinforcement were performed for both plane strain tension and plane strain compression. The corrugation had a height of 3mm, period of 8mm and thickness of 0.78mm, corresponding to a 20% volume fraction. The total composite itself had a length of 40mm and a height of 5mm. Horizontal (x-direction) strain maps at different levels of overall horizontal strain were collected for both plane strain tension and compression, as seen in Figure 5-38. The colour legend is identical for both loading types. A

similar set of vertical (y-direction) strain maps were also collected, as seen in Figure 5-39. Looking at these strain maps it appears that similar strain patterns emerge in both the matrix and the reinforcement for both plane strain tension and compression, particularly at lower levels of overall strain. As the deformation proceeds, the local extremes of high strain under peaks and above troughs seem to be higher under plane strain tension, as evidenced by the emergence of red colouring in Figure 5-38 and blue colouring in Figure 5-39. In contrast, the regions of extreme low strain above peaks and below troughs seem to be lower under plane strain compression. This slight deviation in the strain patterns is likely due to the lack of constraint on the top and bottom surfaces that is present under tensile loading. The lack of constraint results in the formation of surface waviness as unbending progresses as described earlier and also larger local deformation under peaks and above troughs.

In addition to these strain maps, the evolution of the corrugation angle under both loading conditions was also calculated, as seen in Figure 5-40. Also included in this plot is the angle evolution for a homogenous material. Under both plane strain tension and compression unbending is occurring as evidenced by the faster reduction in angle than the homogenous case. During early deformation both tension and compression show similar angle evolution, however as deformation progresses the corrugation angle under plane strain tension begins to unbend slightly more rapidly. This correlates well with the larger local extremes in strain observed in the strain maps for the plane strain tension loading compared to the plane strain compression. Nevertheless, it is clear that there is a strong correlation between the FEM simulated strain patterns and unbending behaviour seen under plane strain tension and those under transverse plane strain compression.

These findings suggest that transverse compressive loading experimental testing can be used as a surrogate for the tensile loading of the corrugation reinforced composites, while keeping in mind that they tend to be slightly conservative in their predictions of necking strain, local strain patterns and unbending behaviour.

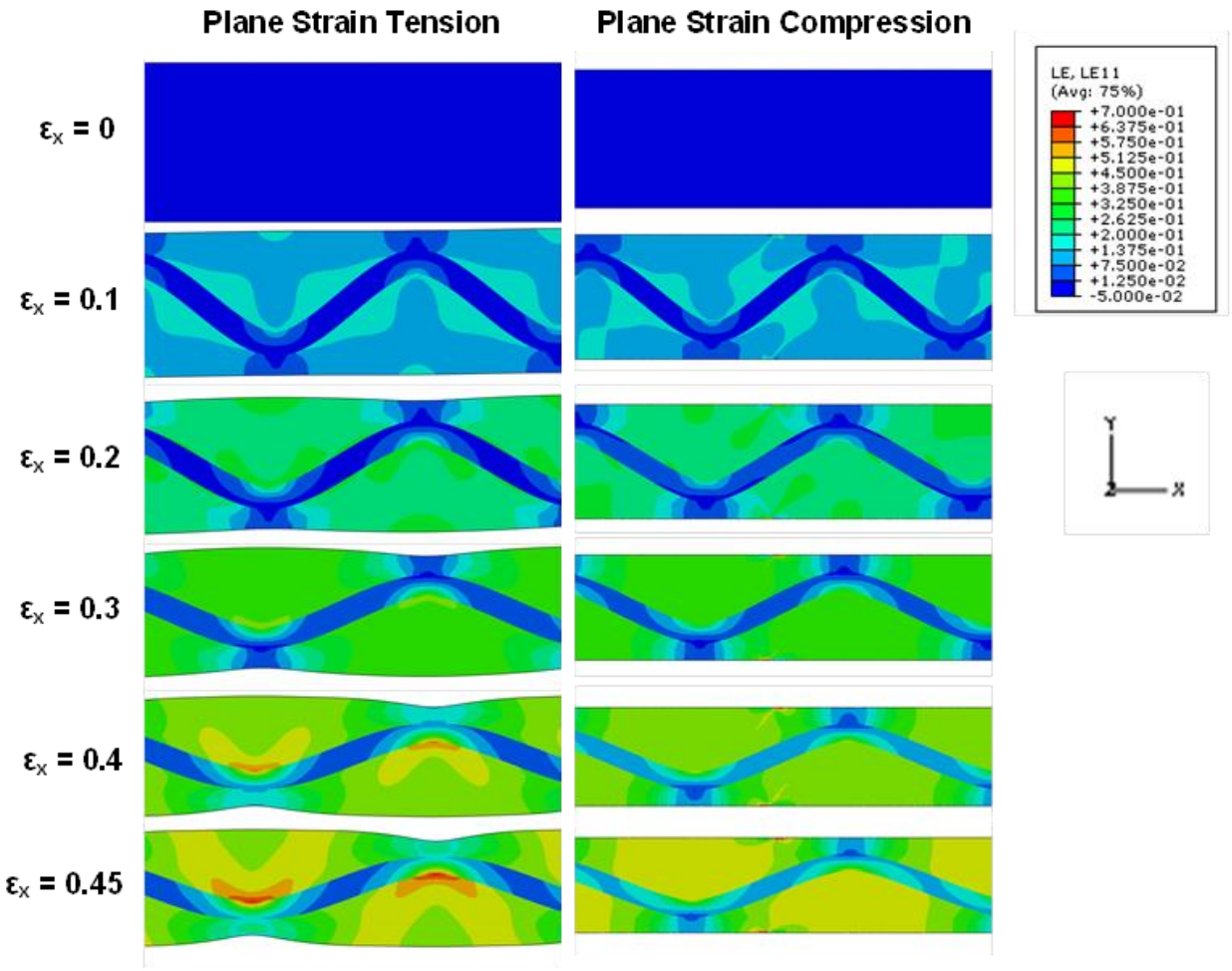


**Figure 5-38: Horizontal (x-direction) strain maps of a corrugation reinforced composite with a copper matrix and 4130 steel reinforcement under both plane strain tension, left and transverse plane strain compression, right, at different levels of overall horizontal strain, $\varepsilon_x$, as labeled on the left.**

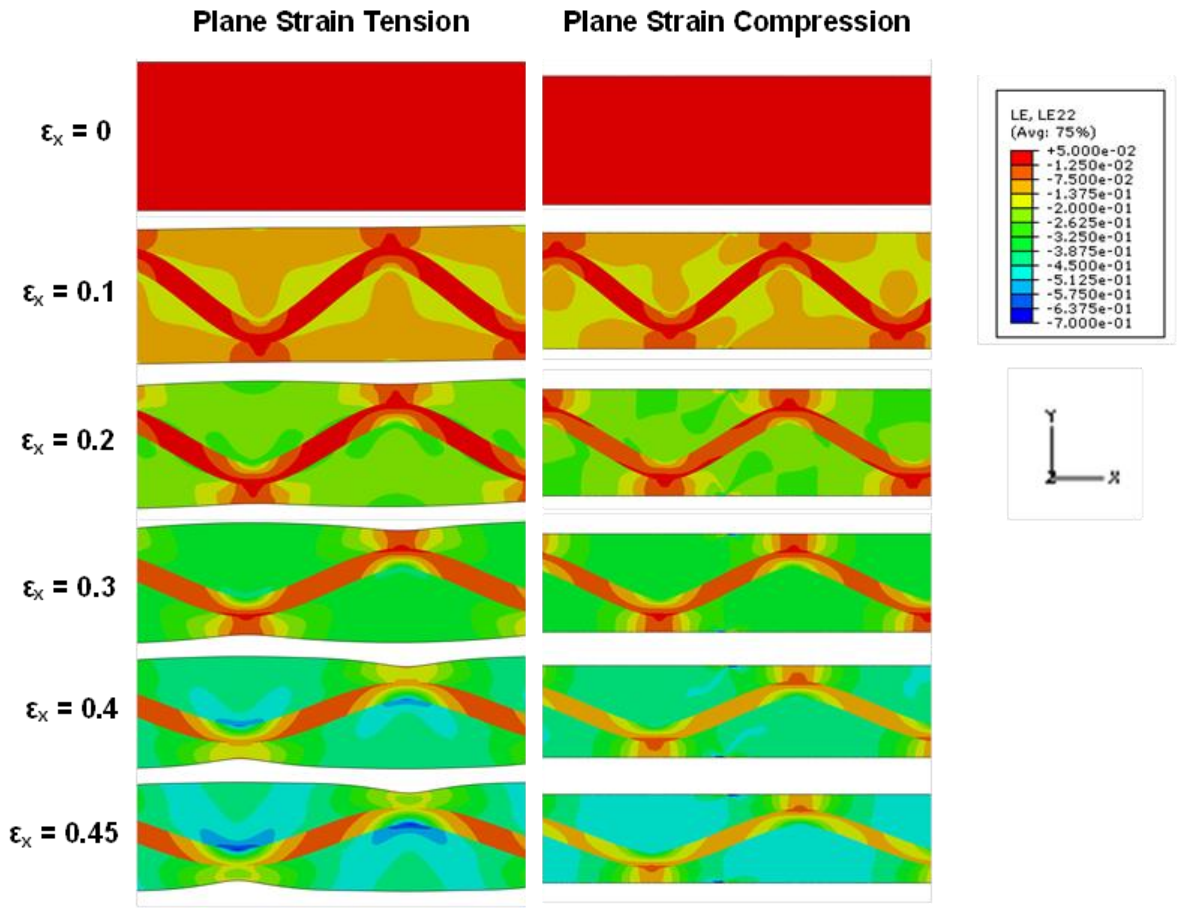


**Figure 5-39: Vertical (y-direction) strain maps of a corrugation reinforced composite with a copper matrix and 4130 steel reinforcement under both plane strain tension, left and transverse plane strain compression, right, at different levels of overall horizontal strain, $\varepsilon_x$, as labeled on the left.**

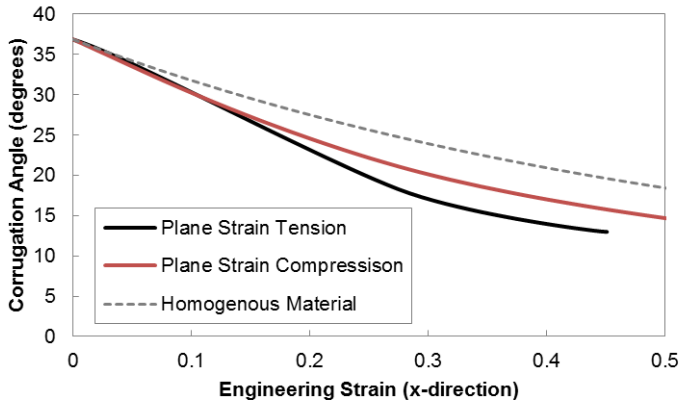


**Figure 5-40: Evolution of the corrugation angle of a corrugation reinforced composite with a copper matrix and 4130 steel reinforcement under both plane strain tension and transverse plane strain compression. Also, included is the equivalent angle evolution for a homogenous material.**

#### 5.2.1.2.2 Transverse Plane Strain Compression

Now that it has been established that there is value to be obtained from transverse plane strain compression tests of these corrugation reinforced composites, the experimental testing of the samples using this loading will be presented. The channel die compression tests were performed using a 100kN tensile testing machine at a deformation rate of 1mm/min. The channel die that was used for these experiments had a channel width of 14mm, a channel height of 25mm, a total length of 80mm, a total width of 80mm and a total height of 50mm. A picture of the channel die can be seen in Figure 5-41 below along with the different stages of preparing the test. The channel was machined from 4340 steel and was subjected to a hardening treatment of austenitizing, quenching and tempering to give it a hardness of around 380 HV. The solder-copper samples that were used for compression were machined from previously made dog-bone samples. The compression samples had dimensions of around 25mm long, 14mm wide and 10mm thick, and were machined to fit perfectly into the channel. In order to obtain strain maps of a part of the sample in an area with no friction against the channel sides and a loading state of plane strain, the samples were cut in half along the length direction to give two 7mm wide samples. A speckle pattern was then spray painted along the inner surface of one of the halves for DIC. After the speckle pattern was applied, it would be photographed by placing the half with the speckle pattern on a pedestal on a predetermined location in front of the DIC camera. After photographing, the halves would then be placed together and inserted into the channel using some light hammering with a soft mallet when necessary. A machined 4340 steel punch would then be placed on top of the sample in the channel and the channel die would be placed on the tensile machine between the compression platens. A small compressive deformation would then be applied using the tensile machine, with the applied force and cross-head displacement being

measured to be used for stress and strain calculations. After the small amount of deformation the force was removed and the sample was taken from the channel, again using hammering when needed, and the process of imaging and deforming was repeated.

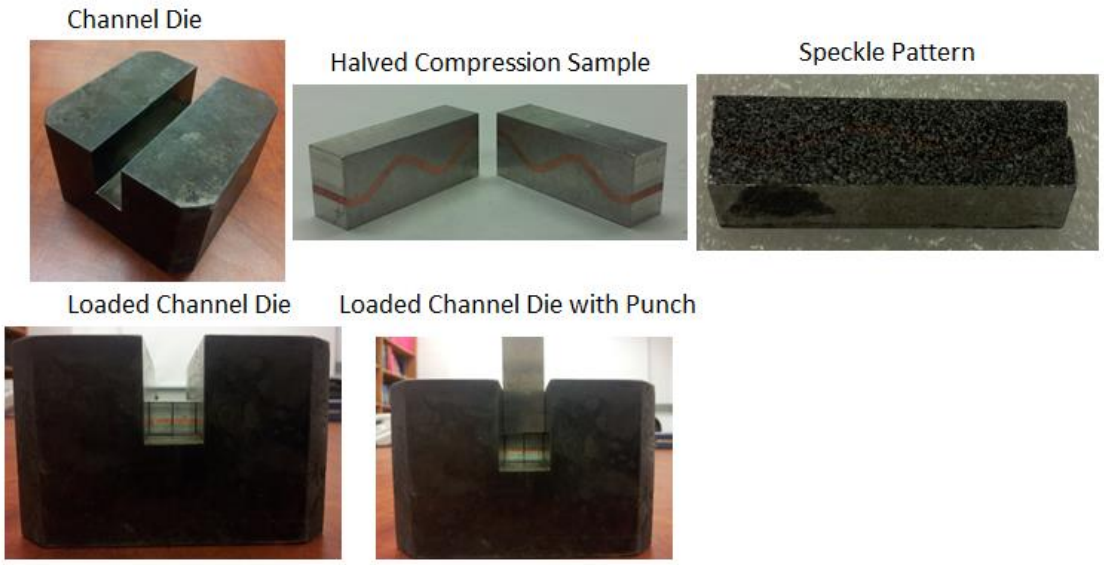


**Figure 5-41: Photographs of channel die and solder-copper corrugated composite with applied speckle pattern used for transverse plane strain compression testing and DIC.**

This process was performed on a corrugation reinforced sample with a solder matrix and copper reinforcement, with a corrugation height of 3.5mm, period of 15mm and thickness of 1.18mm. The transverse deformation of each increment was between 0.25mm and 0.5mm, and a total of four increments were used leading to a total compressive strain of around -0.14. The test was stopped at this point due to the fact that it was becoming increasingly difficult to remove the sample from the channel, and this removal process was beginning to damage the sample. In addition, the speckle pattern had undergone degradation at this point resulting in the increasing loss of data in areas of the strain maps. The difficulty in removing the sample was due to the large forces involved in a channel die process coupled with the constraint of the channel. The degradation of the speckle pattern was likely due to internal friction between the halves in

addition to the increasingly forceful removal process. With this being said, it is still of interest to look at the stress-strain response and strain maps that were acquired during this testing.

A set of strain maps, generated based on the images taken at the end of each increment, can be found in Figure 5-42 below. Note that the colour scale for each strain map is different. Even though it was only possible to obtain strain maps up to a deformation of 14%, these strain maps still show some interesting information. First off, looking at the horizontal strain maps on the left, it is clear that there is minimal stretching occurring in the copper corrugation itself, as evidenced by the blue colour of the corrugation. This agrees well with the strain patterns of the reinforcement shown earlier from FEM simulations, for example in Figure 5-38, in which the reinforcement shows minimal deformation as it unbends. Still looking at the horizontal strain maps on the left, there also emerges the distinctive deformation pattern of higher horizontal strain below peaks and above troughs that is typical of these corrugation reinforced composites, in particular those that are exhibiting unbending behaviour. These regions of high horizontal strain are also regions of high compressive vertical strain as evidenced by their blue colouring on the vertical strain maps on the right side of the figure. As discussed earlier, the unbending of the corrugation leads to high compressive strains in regions below peaks due to a combination of the overall loading geometry and the shape change caused by the unbending corrugation. Due to the constraint caused by the plane strain loading, the high vertical compressive strains in these regions cause large horizontal tensile strains in the same regions in order to conserve volume under plastic deformation. In addition to showing the expected patterns in the reinforcement and in matrix regions under peaks and below troughs, these maps also display regions of low strain, both horizontal-tensile and vertical-compressive, in areas above peaks and below troughs. This also follows the patterns observed in FEM simulations, as shown in Figure 5-38 and Figure 5-39.

Unfortunately, due to chipping and rubbing of the paint as the deformation continued, strain maps at higher amounts of deformation, showing further unbending of the corrugation were not obtainable.

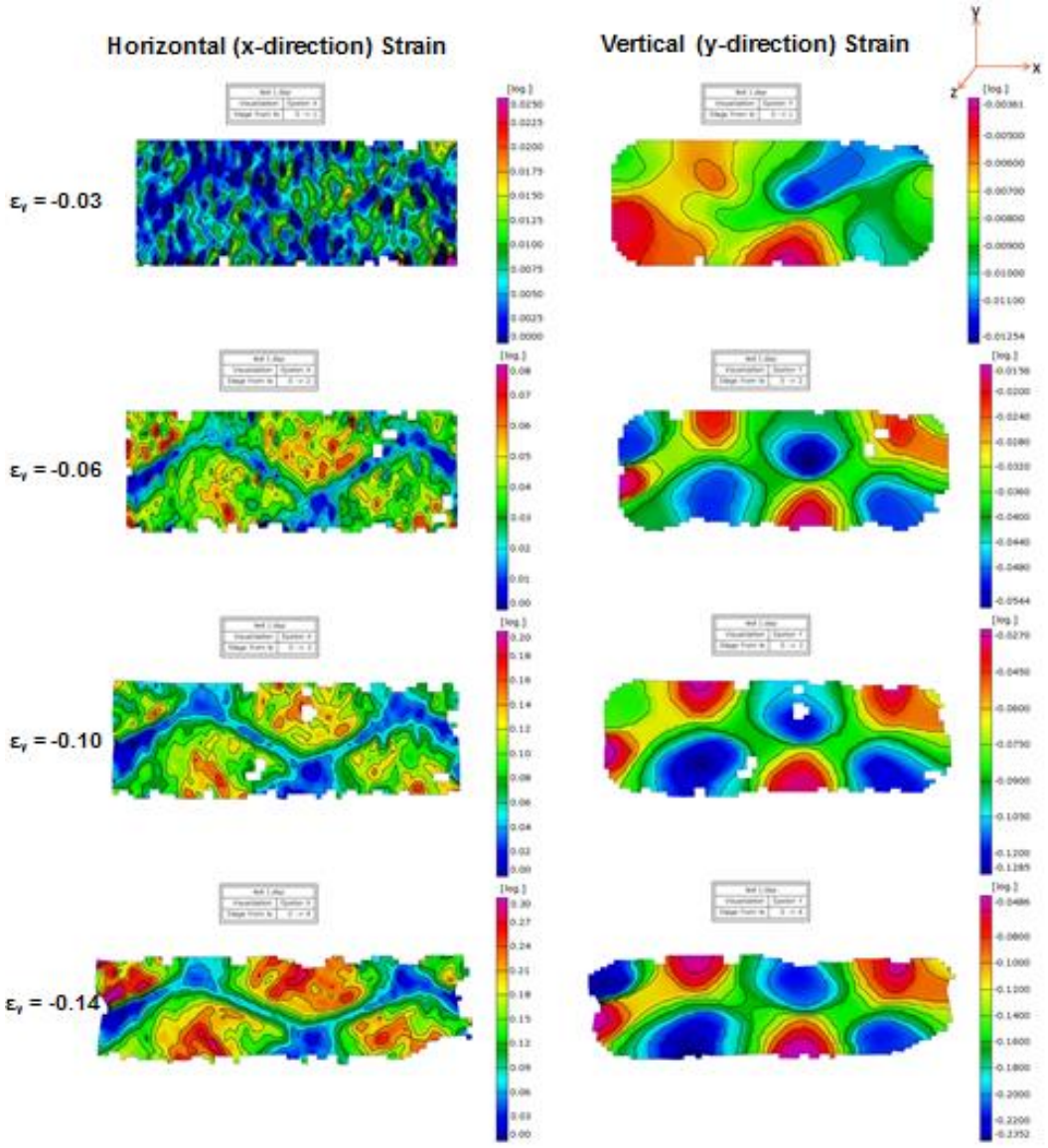


**Figure 5-42: Horizontal (x-direction) strain maps, left, and vertical (y-direction) strain maps, right, of a corrugation reinforced composite with a solder matrix and copper reinforcement under transverse plane strain compression using a channel die, at different levels of overall compression. The corrugation had a height of 3.5mm, period of 15mm, and thickness of 1.18mm.**

In addition to acquiring strain maps, the compressive stress-strain curve was also acquired, as can be seen in Figure 5-43, with the discontinuities in the curve being caused by the necessity to stitch together four stress strain curves, each representing a different interval. The corresponding, indirectly calculated tensile stress strain curve for this sample is seen in Figure 5-44. Also, included in these figures was the result of testing another sample with an identical corrugated geometry that was compressed to a larger amount. Unfortunately, these curves do not provide much information of interest by themselves as there is no curve for a straight reinforcement composite with which to compare. Although, not depicted here, additional corrugation reinforced composites were also tested in this fashion, but suffered from similar issues with regards to pattern degradation before significant deformation could be achieved. In fact, the strain maps of the other samples were much worse due to earlier degradation of the speckle pattern. For the second corrugated sample, whose stress-strain curves were included, some additional analysis was done with regards to corrugation angle evolution. A plot of the evolution of the corrugation angle with overall thickness reduction can be seen in Figure 5-45 along with the expected angle evolution for a homogenous sample. This angle evolution was acquired by looking at a sequence of images of the non-speckled half of the sample and tracking the movement of the peak and trough at each interval. This angle evolution plot suggests that there is significant unbending of the corrugation occurring in these samples, as the corrugation angle is decreasing at a rate larger than that of a homogenous material. This agrees well with the conclusions drawn from the local strain maps, presented earlier.

Despite obtaining some useful information pertaining to early local deformation patterns, after evaluating this experimental technique, the issues with regards to speckle pattern degradation

and the concern that high frictional forces could greatly influence the stress strain response, it was decided to abandon this technique and use another alternative testing arrangement.

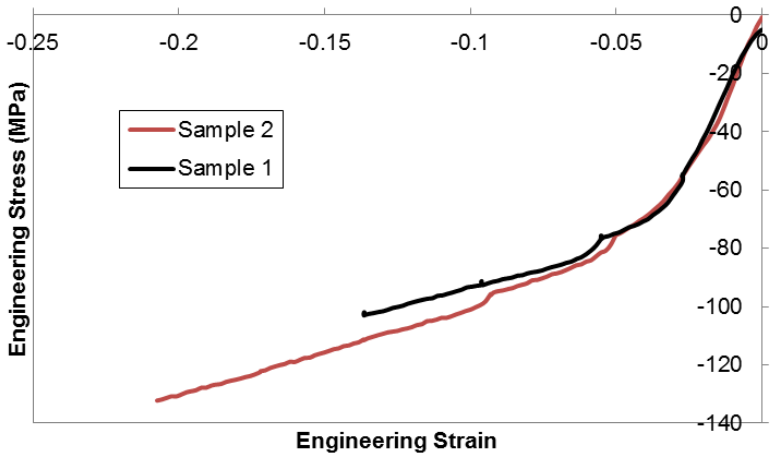


**Figure 5-43: Compressive stress-strain curves from experimental testing of corrugation reinforced composites with a solder matrix and copper reinforcement under transverse plane strain compression using a channel die. The compression test was divided into multiple stages in order to perform DIC. Each curve represents a different sample that was tested.**

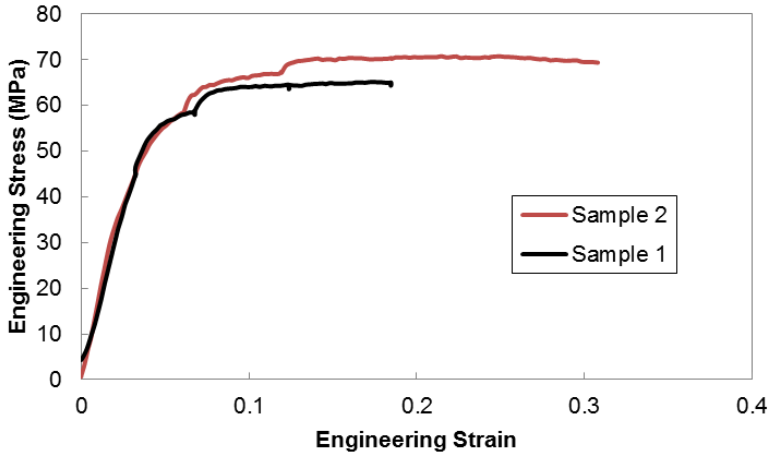


**Figure 5-44: Indirectly calculated tensile stress-strain curves from experimental testing of corrugation reinforced composites with a solder matrix and copper reinforcement under transverse plane strain compression using a channel die. The compression test was divided into multiple stages in order to perform DIC. Each curve represents a different sample that was tested.**

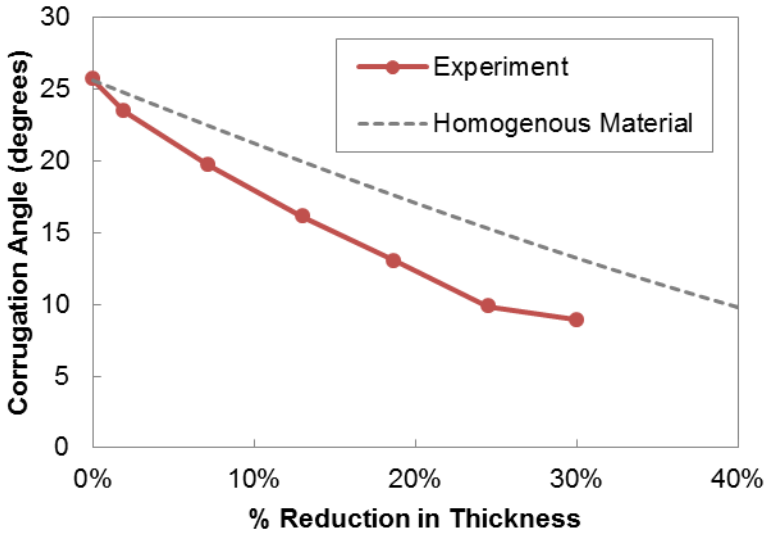


**Figure 5-45: Evolution of the corrugation angle of a corrugation reinforced composite with a solder matrix and copper reinforcement during transverse plane strain compression testing using a channel die. The corrugation had a height of 3.5mm, period of 15mm and thickness of 1.18mm. Also, included is the equivalent angle evolution for a homogenous material.**

#### 5.2.1.2.3 Transverse Uniaxial Compression and Transverse Rolling

The final experimental testing technique that was employed also involved transverse compressive loading. However, in this case instead of performing the compression in a channel die and acquiring stress-strain curves and strain maps from the same sample, the testing was split into two separate testing processes performed on identical samples. One of the samples was subjected to transverse uniaxial compressive loading using a 50kN tensile machine in order to obtain a stress-strain curve and the other sample was spray painted with a speckle pattern and rolled, with images taken of the speckle pattern between passes in order to perform DIC and obtain strain maps. The samples that were used for this testing were machined from the dog-bone tensile samples, and were machined to dimensions of around 15mm (or 30mm) long, 8mm wide and 7.5mm thick. In order to test similar samples using both techniques, a single sample was originally machined around 16mm wide and then cut in half to give two similar 8mm wide samples, one for each technique. The uniaxial compression was performed by first wrapping the

sample in Teflon tape to minimize friction and then placing the sample between the compression platens of the tensile machine. The sample was then compressed in the thickness direction at a deformation rate of 1mm/min or an initial strain rate of around 0.002 /s. The uniaxial compression has advantages over the channel die compression testing including a reduction in the forces required, ability to more easily minimize friction and no damage to the sample due to insertion and removal from the channel. It has the disadvantage of deformation in the width direction that makes it difficult to capture a meaningful strain map on the surface. This is the reason the rolling process was also used. The rolling process began by first spray painting the speckle pattern on the surface and then placing the sample underneath the camera in a predetermined spot and taking a picture. The sample was then passed through a hand rolling mill with the roll gap set to achieve a thickness reduction of around 0.3mm per pass or a compressive strain of around 4%. The speckle pattern was then photographed and the process repeated. The rolling process has some advantages over the channel die process including less damage to the speckle pattern and much easier testing in general. The main disadvantages of this method include conditions that deviate from plane strain near the surface of the sample, where the speckle pattern is applied, and the potential for the sample to bend during rolling. The deviation from plane strain conditions leads to some small deformation in the width direction; however it is small enough that it is still possible to obtain meaningful strain maps.

This testing technique of uniaxial compression combined with rolling and DIC was used on some solder matrix – copper reinforcement composites. Beginning with the uniaxial compression tests, the stress-strain curves for a straight reinforced sample and for a corrugation reinforced sample can be seen in Figure 5-46 below. Both the straight and corrugated samples had a reinforcement thickness of 1.18mm and for the corrugated sample the corrugation height was 3.5mm and the

period was 15mm. Although there does not appear to be much difference between the two curves the curve representing the corrugated sample does exhibit smaller values of compressive stress and has a different curvature than that of the curve representing the straight sample. These differences are items that were noted as being characteristic of an unbending corrugated composite earlier, as illustrated in Figure 5-33 for the copper-steel system modeled using FEM. Performing the calculation to predict the tensile stress-strain behaviour, provides a set of curves, as seen in Figure 5-47, which have been cut off at their values of maximum stress. Again, these curves do not show a large amount of difference from one another; however the corrugated curve shows a slight improvement in "necking" strain over that of the straight curve. Whether this is a result of the reinforcement geometry or just experimental variability is uncertain, as the improvement is rather small. Looking at the work hardening plots of these materials, Figure 5-48, it does appear that the corrugated material exhibited a small boost in work hardening that was absent from the straight curve, that could be attributed to the unbending corrugation.

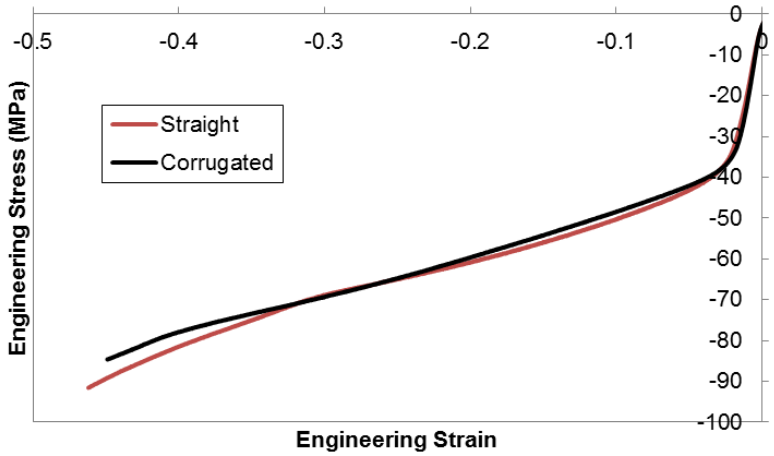


**Figure 5-46: Compressive stress-strain curves from experimental testing of composites with a solder matrix and copper reinforcement under transverse uniaxial compression. One of the samples had a straight reinforcement and the other a corrugated reinforcement.**

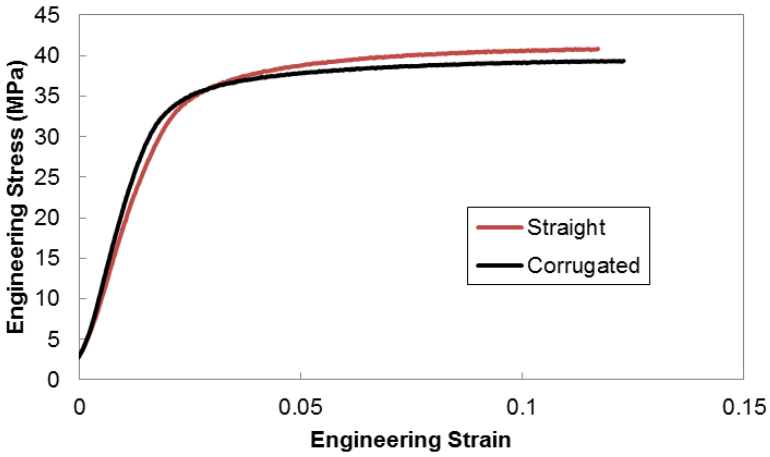


**Figure 5-47: Indirectly calculated tensile stress-strain curves from experimental testing of composites with a solder matrix and copper reinforcement under transverse uniaxial compression. One of the samples had a straight reinforcement and the other a corrugated reinforcement.**

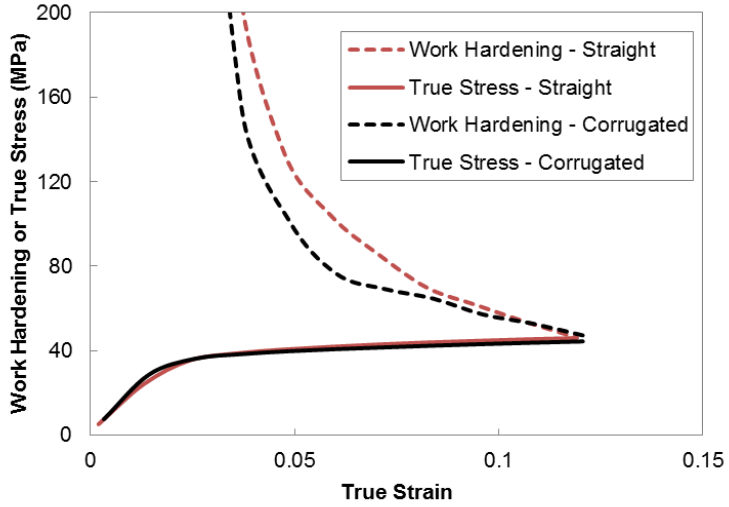


**Figure 5-48: Considere plot based on indirectly calculated tensile stress-strain curves from experimental testing of composites with a solder matrix and copper reinforcement under transverse uniaxial compression. One of the samples had a straight reinforcement and the other a corrugated reinforcement.**

In order to get a better idea as to whether these small signs that are pointing towards an improvement in necking strain as a result of the corrugated reinforcement are legitimate, it is beneficial to perform FEM simulations of this system. A power-law model for the behaviour of copper was already determined as outlined for the second copper model in Table 5-4 and a power-law hardening model for solder was determined as outlined in Table 5-5. Using these

models for the matrix and reinforcement material and creating samples with geometries identical to those for the straight and corrugated samples of interest, 3D simulations were conducted for the transverse uniaxial compression of these composites. The resulting compressive stress-strain curves can be seen in Figure 5-49. At higher values of strain these stress-strain curves appear fairly different than those seen experimentally, with the compressive stress rising rapidly to high values. That being said, at low strains both Figure 5-46 and Figure 5-49 show lower stress values for the corrugated composites compared to their straight counterparts and also both show differences in the curvature and inflection for the corrugated curve compared to the straight curve. This is shown more clearly in Figure 5-50, which plots both the experimental and FEM curves together and focuses on the response at lower values of strain. The rapid increase in compressive stress seen at higher strain values for the FEM simulations is likely due to a combination of the uniaxial loading geometry and the fact that the solder is very soft in comparison to the copper. Due to the softness of the solder it flows a significant amount compared to copper. This additional deformation occurs in both the length and width directions due to the uniaxial compressive loading. As compression progresses this leads to a rapidly enlarging surface area on which the force is being applied. Due to the fact that the stress is being calculated as engineering stress based on the initial cross-sectional area, the true stress is likely much smaller due to the enlarged area. This explains why the compressive stress strain curve increases rapidly for the FEM simulations. It is possible that these large stresses are not seen experimentally due to a build-up of friction limiting the ability of the solder to continue to flow at larger applied forces. It was assumed for the FEM simulations that there was zero friction between the samples and the compression platens. In fact if one compares the surface area of the top of the FEM sample and the experimental sample after 42% of compression, calculating the

areas using ImageJ analysis, the FEM surface area is found to be 20% larger than that observed experimentally. This issue of friction experienced experimentally only seems to be an issue at larger amounts of strain as the stress levels are comparable up to about 25% compression as seen in Figure 5-50.

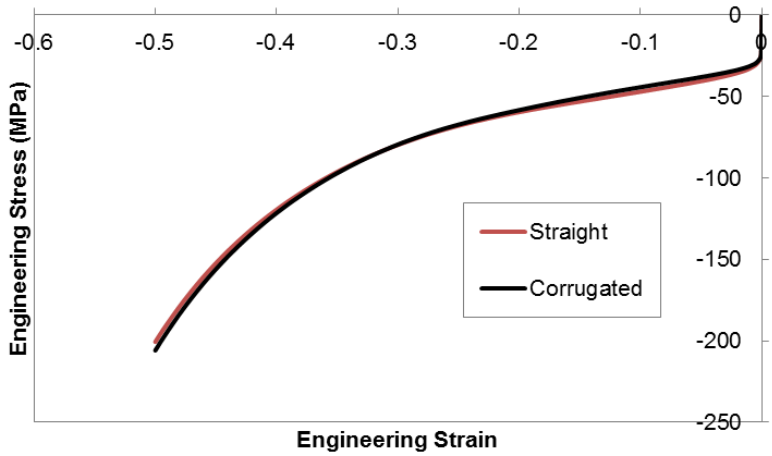


**Figure 5-49: Compressive stress-strain curves from FEM simulations of composites with a solder matrix and copper reinforcement under transverse uniaxial compression. One of the samples had a straight reinforcement and the other a corrugated reinforcement.**

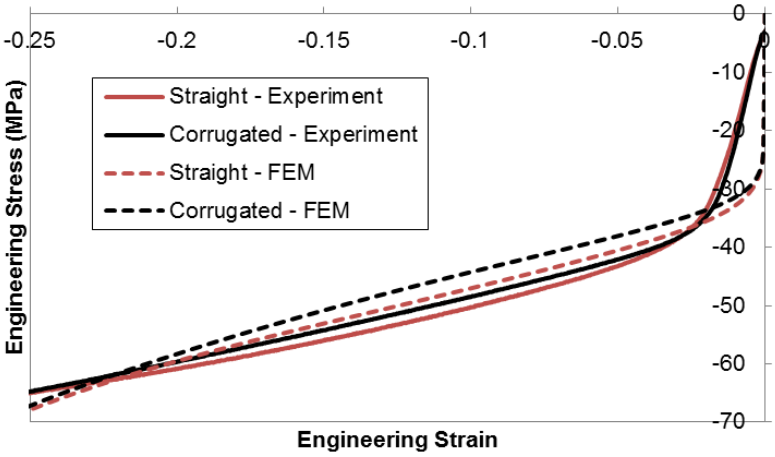


**Figure 5-50: Low strain region of compressive stress-strain curves from FEM simulations and experimental testing of composites with a solder matrix and copper reinforcement under transverse uniaxial compression. For each testing method one of the samples had a straight reinforcement and the other a corrugated reinforcement.**

With regards to estimating the necking strain of these composites, the indirect calculation method for estimating the tensile stress-strain curves was used, with the resulting curves seen in Figure 5-51. This process has been done for both the FEM simulations and experimental testing under transverse uniaxial compression. The curves from the FEM simulations have been cut off not at the peak value of stress, as due to the rapid increase in stress with further compression the peak value is never reached, but rather are cut off at a value dictated by when true stress is first equal to the work hardening rate for the straight case and when the work hardening suddenly increases for the corrugated case. Also included on this plot are the stress strain curves from FEM simulations of these same samples under uniaxial tensile loading. Looking at this plot it is clear that for this system this method used for estimating the tensile behaviour does not capture the absolute values of the stress-strain response of these composites under tension. With that being said, focusing on the FEM results this method still provides a relative estimate of the necking strains when comparing corrugated and straight geometries, predicting a 74% increase (strain increase of 0.11) in necking strain through corrugation, compared to the 57% increase (strain increase of 0.12) observed under actual tensile loading. The improvement in necking strain based on the experimental results is much smaller at only 5% (strain increase of 0.01). This discrepancy could be caused by a number of factors including inaccuracy in estimating the stress-strain relationship for the component materials, error in measuring the corrugation geometry, interfacial weakness altering the transfer of stress from matrix to reinforcement, frictional forces and edge effects. In addition, this method of estimating necking strain is quite rough due to the assumption of isotropic material behaviour and is also highly dependent on the shape of the compressive stress-strain curve, where small variations can lead to larger errors in predicting the necking strain. This assumption of isotropic material behaviour becomes less

appropriate as the differences in flow stress between the matrix and reinforcement become larger. As the difference in flow stresses increase, the amount of deformation observed in the matrix and reinforcement becomes less alike which magnifies the deviation in stress-strain response from that of an isotropic material. Therefore, using this technique for estimating the necking strain becomes less reliable for systems with greater differences in flow stress between the components, such as that seen in the solder-copper system.

In order to better evaluate the use of transverse compression testing as a method for estimating tensile necking strain of these composites, more tests need to be conducted. Based on the findings presented, although the compressive stress-strain curves of the corrugation reinforced samples demonstrate the expected general stress-strain curve shape and stress values relative to that of the straight reinforced samples, as predicted using FEM simulations, the ability to use these curves to estimate necking strain improvement under tensile loading is at this stage inconclusive.

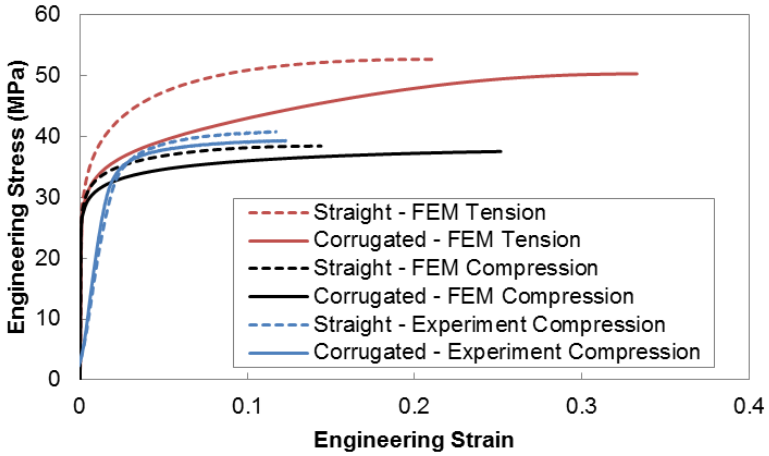


**Figure 5-51: Indirectly calculated tensile stress-strain curves from experimental testing and FEM simulations of composites with a solder matrix and copper reinforcement under transverse uniaxial compression. One of the samples had a straight reinforcement and the other a corrugated. Also, included in this plot for comparison purposes are tensile stress-strain curves from FEM simulations of the same samples under uniaxial tensile loading.**

Shifting the focus to the second half of the testing method, the results of the experiments involving rolling and DIC of this solder-copper system are now presented. As mentioned earlier a photograph of the speckle pattern was taken after each pass through the rolling mill, which was then analyzed in order to generate a collection of strain maps. For these samples, the DIC software package that was used was GOM Correlate. The strain maps for a solder matrix, copper reinforcement sample with a corrugation height of 3.5mm, period of 15mm and reinforcement thickness of 1.18mm, can be seen in Figure 5-52 and Figure 5-53, for longitudinal and transverse strain respectively. Also, included in these figures are the FEM generated strain maps for the equivalent samples under transverse plane strain compression. The colours in the legend are the same for the FEM and the experimental strain maps, and the range is set to accommodate both sets of data. The white spots that begin to emerge on the DIC strain maps represent areas of lost data where the speckle pattern has degraded such that it is no longer possible to calculate the strain in that region. When the accumulation of a number of regions with this loss of data became significant the deformation was stopped.

Comparing the evolution of the strain patterns seen in the experimental maps to those generated from FEM, it appears that the strains in the matrix regions are lower than those predicted by FEM. With that being said, the regions where high strain is expected in order to accommodate an unbending corrugation, that is below peaks and above troughs, show the highest amounts of strain for both the experimental and FEM maps. Similarly, the regions in the matrix where the lowest strains are expected, that is above peaks and below troughs, show the lowest amount of strain. Once again, the experimental testing of these materials yields results that follow the expected trends but with lower absolute values. The potential reasons for this under-prediction of local strain are likely the same as those given earlier for explaining the discrepancies seen in the

stress-strain curves, mainly inaccuracies in representing the materials' stress-strain behaviour in the FEM simulations. Another potential reason that the longitudinal experimental strain map,

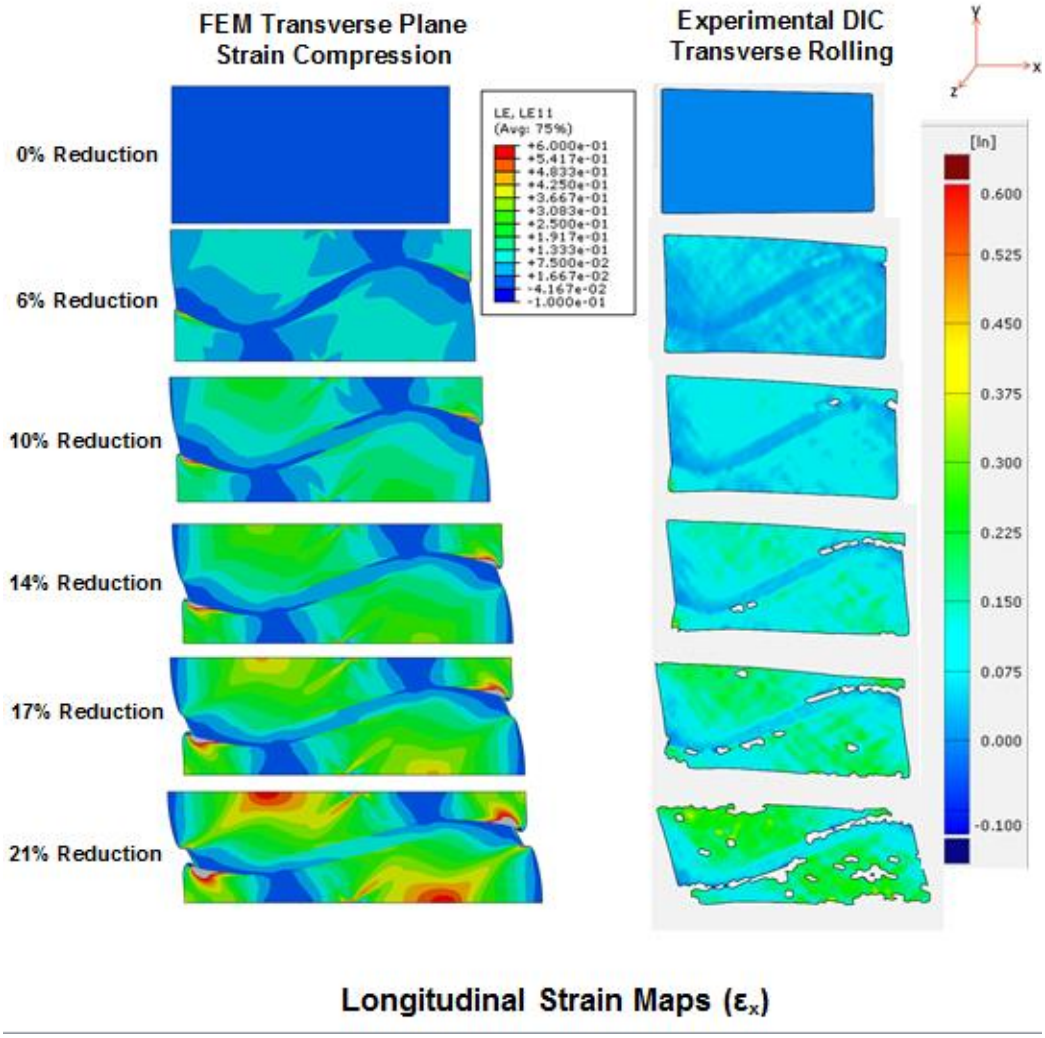


**Figure 5-52: Longitudinal (x-direction) strain maps of a corrugation reinforced composite with a solder matrix and copper reinforcement under transverse plane strain compression loading using FEM (left) and under transverse rolling using experimental DIC (right) at different levels of overall compression.**

Figure 5-52, shows lower local strain values could be the deformation that occurs in the width direction at the surface during rolling that is caused by a local deviation from plane strain conditions. Since the material near the surface is free to deform in this width direction it is possible that due to conservation of volume during plastic deformation, the longitudinal

deformation is consequentially not as large. Shifting the focus to the reinforcement, both the FEM maps and the DIC maps show little deformation occurring in the reinforcement, suggesting that a bending dominated process is occurring. This is a desirable behaviour to see in a material where the ability to unbend dictates the likelihood of improving the necking strain through the use of a corrugated reinforcement. Unfortunately, the resolution of these experimental strain maps is not high enough to see the local variations in strain across the thickness of the

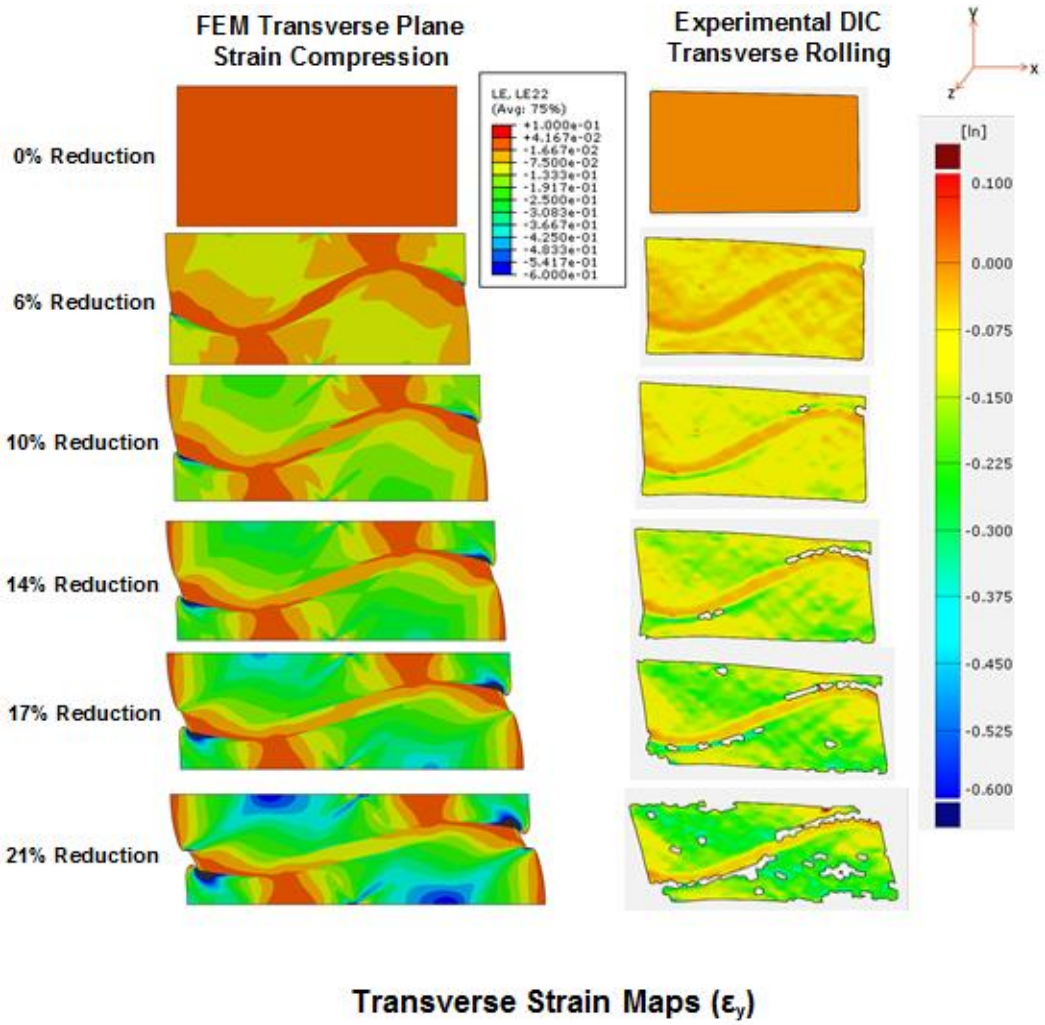


**Figure 5-53: Transverse (y-direction) strain maps of a corrugation reinforced composite with a solder matrix and copper reinforcement under transverse plane strain compression loading using FEM (left) and under transverse rolling using experimental DIC (right) at different levels of overall compression.**

reinforcement at a peak or trough. This data would be valuable in further identifying the nature of the unbending process.

Due to the local surface deviation from plane strain conditions, it is perhaps more appropriate to compare the experimental strain pattern, which is generated for the strains on the outer surface of the rolled sample, to an FEM simulation of the same sample under uniaxial compression. The reason for this is due to the fact that when rolling, the material near the surface is unconstrained and is free to deform in the width direction, much like it would under transverse uniaxial compression. The strain maps comparing the experimental results to this uniaxial compression FEM simulation are shown in Figure 5-54 and Figure 5-55, for longitudinal and transverse strain respectively, again with the same colour legend used for both sets of strain maps in each figure. These maps tend to show a better agreement in terms of absolute strain values between the FEM results and the experimental results, in particular for the longitudinal direction, as shown in Figure 5-54. This gives some credence to the reasoning provided above concerning the differences between the plane strain compression FEM maps and the experimental maps.

The rolling of a sample with a similar corrugation geometry but longer total length, 30mm instead of 15mm, was also performed. The strain patterns for this longer sample better capture the behaviour of an entire period of the corrugation as they do not suffer as much from any edge effects that are present. One of the issues with rolling the shorter samples is that deviations from symmetry can lead to a bending of the samples. This bending is shown in Figure 5-56 for a sample which is asymmetric along the longitudinal midplane. If the sample's length is increased the asymmetry has less of an effect, also shown in Figure 5-56. Also, when the sample is longer, the rolling process, similar to tensile loading, leads to the emergence of a wavy surface due to corrugation unbending. The longitudinal strain maps for this longer sample, with the same

corrugation geometry as the shorter samples presented earlier, can be seen in Figure 5-57. Note that these strain maps only focus on the middle of the sample and ignore the edges. The first four strain maps on the left, and the related colour legend, correspond to an initial speckle pattern. As the rolling progressed the paint began to chip off of this sample and the speckle pattern started to degrade. Therefore, after the fourth map was created, the speckled surface of the sample was sanded using 240 grit silicon carbide grinding paper and the remaining paint was removed. A new speckle pattern was spray painted on and deformation was continued. The latter seven strain

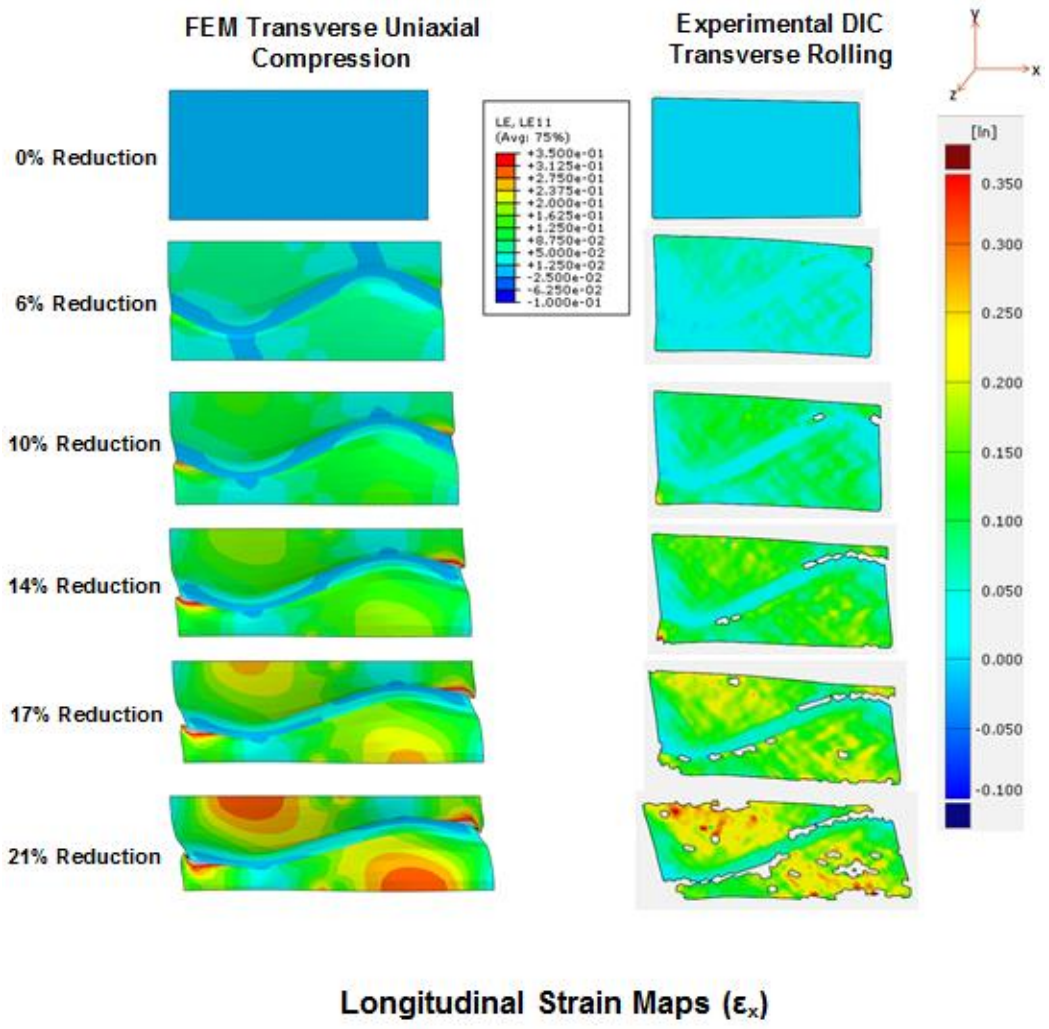


**Figure 5-54: Longitudinal (x-direction) strain maps of a corrugation reinforced composite with a solder matrix and copper reinforcement under transverse uniaxial compression loading using FEM (left) and under transverse rolling using experimental DIC (right) at different levels of overall compression.**

maps on the right, and the related colour legend, found in Figure 5-57, represent the strain patterns for this sample relative to the starting point of 14% reduction in thickness. Therefore, the absolute values of strain in this second set of strain maps are lower than the actual strain present. Unfortunately the software did not have a function to add together the strains of the two sets of data. Regardless, these maps show the patterns expected for a corrugated composite undergoing an unbending process, with high strains below peaks and above troughs, low strains above peaks and below troughs, and minimal stretching deformation in the reinforcement itself.

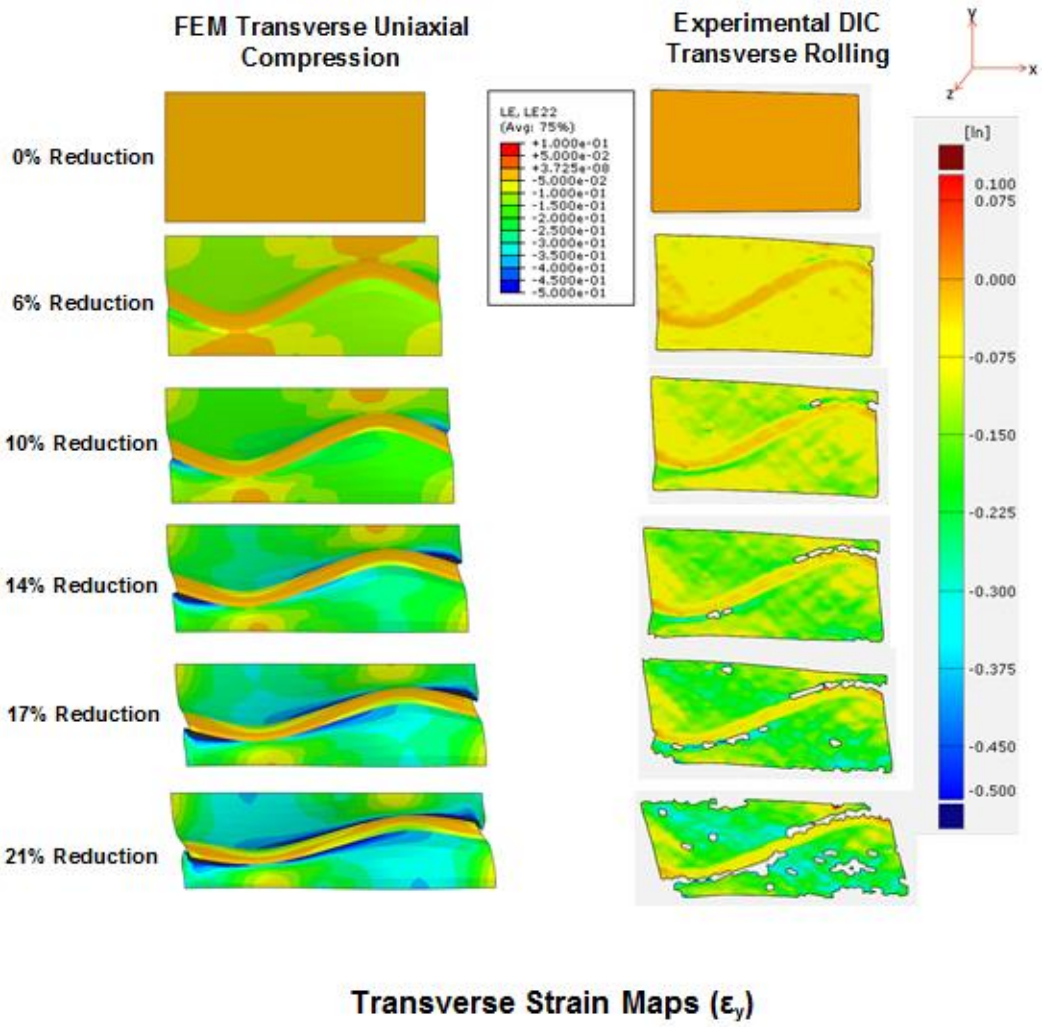


**Figure 5-55: Transverse (y-direction) strain maps of a corrugation reinforced composite with a solder matrix and copper reinforcement under transverse uniaxial compression loading using FEM (left) and under transverse rolling using experimental DIC (right) at different levels of overall compression.**

In addition to the strain maps, it is possible to obtain the evolution of the corrugation angle after each pass through the rolling mill. This can be seen for this longer sample in Figure 5-58. Once again, also included in this figure is the angle evolution for a homogenous sample and that from the FEM simulation under plane strain compression for comparison purposes. The data points for the experimental corrugation angle roughly follow that seen for the FEM corrugation angle, and definitely show an unbending process as the angle is reducing faster than that for a homogenous material. The only concern is that at small levels of strain the experimental angle does not decrease as quickly as that seen in the FEM, which could suggest that the corrugation is resisting unbending initially and is actually stretching. However, as the strain is further increased the angle begins to drop more rapidly, implying an unbending process, and the slow angle evolution at early strains could just be due to experimental measurement error.

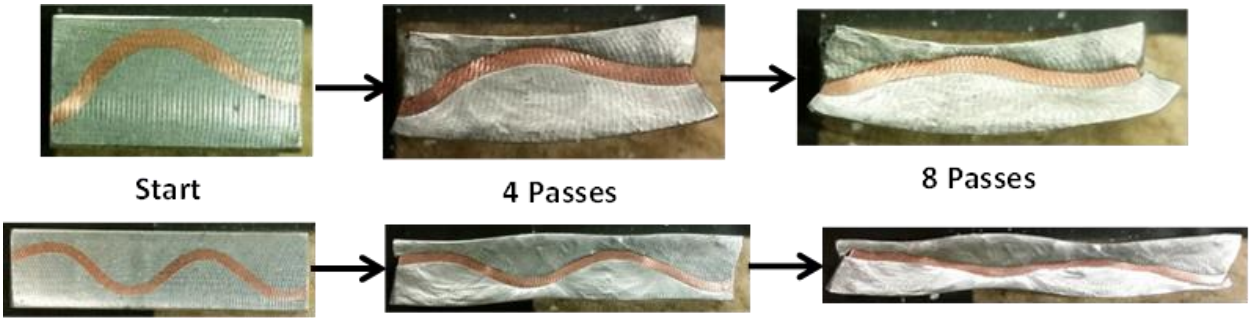


**Figure 5-56: Photographs of a short (15mm) corrugated composite, top, and a long (30mm) corrugated composite, bottom, after different numbers of passes through a hand rolling mill. The composites have a solder matrix and copper reinforcement.**

The work that involves using the uniaxial compression and rolling testing technique for the solder-copper system can be summarized as follows:

- The experimental compressive stress-strain curve of a corrugated composite is shown to have lower stress values and a more significant curvature at low values of strain when

compared to the compressive stress-strain curve of a straight composite. The behaviour is similar to that seen in FEM simulations.

- At higher strain values the stresses observed experimentally are lower than those seen in FEM simulations due to friction limiting the enlargement of the solder surfaces.
- Converting transverse compressive stress strain curves to tensile stress-strain curves does not work well in terms of absolute values for this material system. However, for FEM simulations the relative value of the indirectly calculated necking strains of corrugated

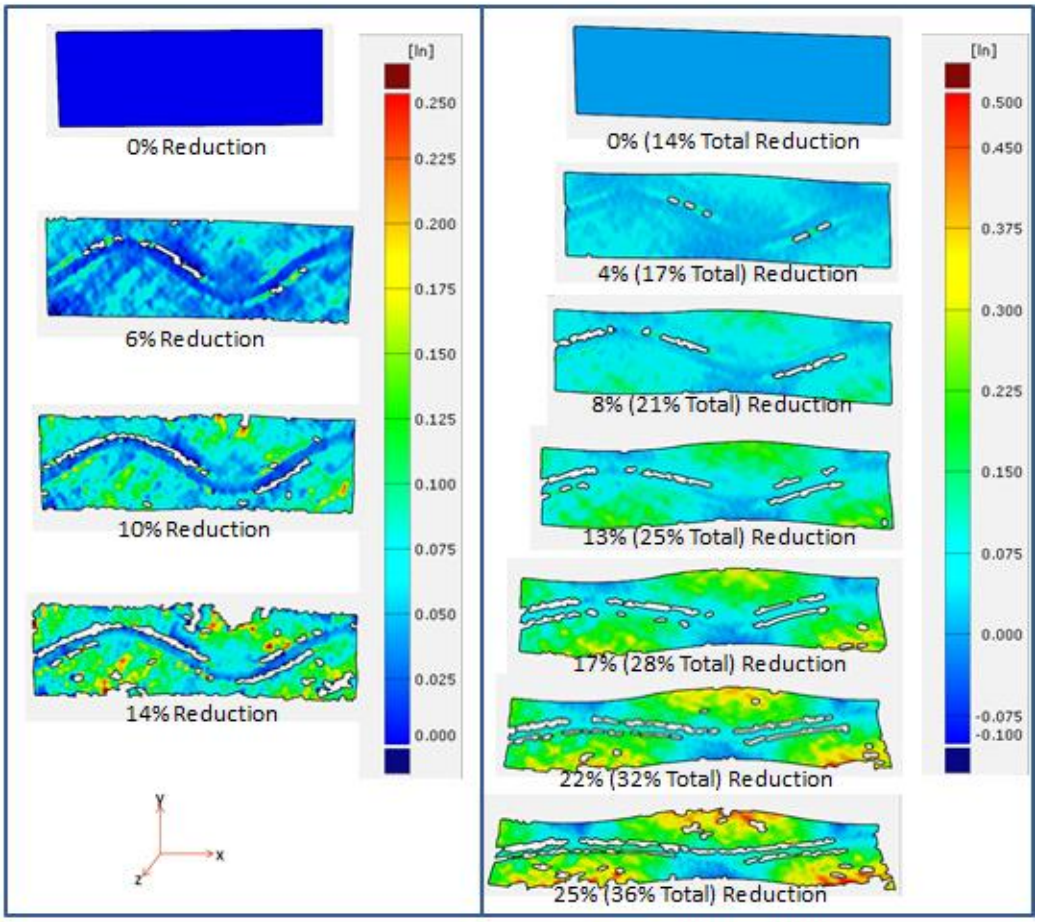


**Figure 5-57: Longitudinal (x-direction) strain maps of a corrugation reinforced composite with a solder matrix and copper reinforcement subjected to transverse rolling deformation, at different levels of overall compression. The sample was 30mm in length. The maps on the left represent the strain for the first applied speckle pattern and the maps on the right represent the second applied speckle pattern, which was applied after rolling to 14% reduction.**

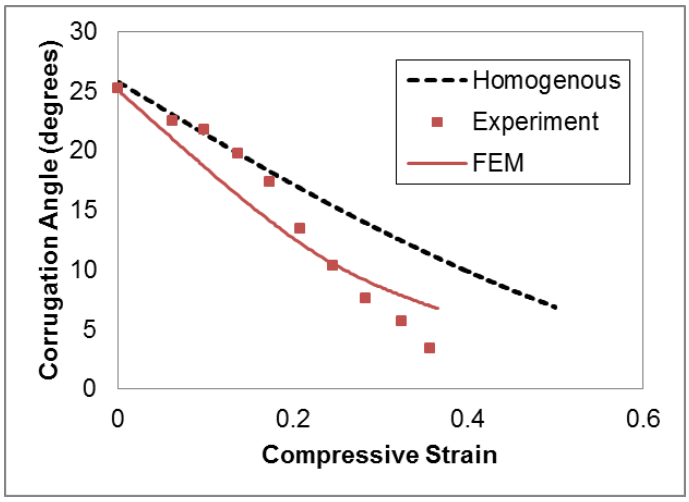


**Figure 5-58: Evolution of the corrugation angle of a corrugation reinforced composite with a solder matrix and copper reinforcement at different levels of overall compression. The FEM curve represents the angle evolution from a simulation of this composite under transverse plane strain compression and the Experiment data points represent the angle evolution from transverse rolling experiments. Also included is the hypothetical angle evolution for a homogenous material.**

composites compared to straight composites is comparable to those seen for the same composites under tensile loading. Experimentally, the predicted improvement in the necking strain through corrugation is much smaller than that seen in the FEM modeling.

- This issue with regards to converting transverse compressive stress-strain data to tensile data is due to the large differences in flow stress between solder and copper. The effectiveness of this technique for predicting necking strain decreases with increasing differences in the flow stress of the component materials, as the deviation from isotropic behaviour becomes magnified.
- Further testing is recommended to evaluate the idea of using transverse uniaxial compression testing to predict tensile behaviour of composites.
- The strain maps generated using DIC for the transversely rolled samples, show good agreement with FEM simulations, particularly when compared to a simulation of a composite loaded under uniaxial compression.

- The strain maps show regions of high strain below peaks and above troughs and regions of low strain above peaks and below troughs, with minimal deformation in the reinforcement itself. These observations are indicators of a composite undergoing an unbending process.
- The use of longer samples reduces sample bending and edge effects and begins to show the distinctive wavy surface with increasing thickness reduction.
- Measurements of the evolving corrugation angle follow that seen in FEM simulations for a sample undergoing corrugation unbending.

Overall, this technique provides good qualitative confirmation of the stress-strain response of these composites and good qualitative confirmation of the local strain patterns during compression. The relatively good agreement between experiment and FEM simulations under compressive loading gives reason to believe that the conclusions made based on FEM simulations under tensile loading in the previous chapter are reasonable to be expected in practice, provided that a strong interface is present. In order to obtain more confidence in the tensile FEM simulations additional experiments need to be performed, ideally spanning a range of material systems. Some effort was made under this research project to test the corrugated geometry for other material systems, but the results were not as convincing as those for the solder-copper system, mainly due to poor adhesion at the interface. Some of this work will now be briefly discussed, including the issues that arose that prevented the testing of these samples from being successful.

### 5.2.2 Other Material Systems

In addition to the solder-copper system, a number of other combinations of materials were used in making corrugated composites. A list of the different material systems is seen in Table 5-7.

The systems that had a tin matrix were created in a manner very similar to that used for the solder matrix composites using the dog-bone casting mould. The main difference being that the temperature of the box furnace was set at 325°C in order to melt the tin, which has a melting point of 232°C. Also, after the IF steel and 304 stainless steel strips were corrugated using the anvil and cylinder technique they were annealed in a tube furnace under an argon gas atmosphere. This annealing was performed at 950°C for 10 minutes for the IF steel and at 900°C for 1 hour for the stainless steel. After annealing, the IF steel and 304 stainless corrugated reinforcements were cleaned using a 10% hydrochloric acid solution and an industrial flux was used to aid in wetting during the pre-coating stage. The plan was to test these samples under plane-strain compression in the channel die. Unfortunately the interface of the samples was poor and they fell apart during the machining process. Additional attempts were made to improve the interface by varying the surface treatment and casting temperatures but the interface remained poor. For this reason the systems with a tin matrix and steel reinforcement were abandoned.

**Table 5-7: Summary of material systems that were used in making corrugation reinforced composites.**

| Matrix | Reinforcement |
|---|---|
| Solder | Copper |
| Tin | Interstitial Free Steel |
| Tin | 304 Stainless Steel |
| Copper | Interstitial Free Steel |
| Copper | 304 Stainless Steel |
| Copper | 4130 Steel |
| Copper | 409 Aluminized Steel |
| Copper | Additive Manufactured GP1 Stainless Steel (17-4) |

The rest of the material systems focused on using a copper matrix with a variety of different steel reinforcements, in order to make compression samples. Due to the fact that the melting point of copper is significantly higher than solder, 1073°C, a different casting process was used. This

casting process was designed such that the researcher would not have to handle the crucible with the molten copper in order to ensure the process was safe.

To begin, the steel reinforcements were corrugated by using strips of steel sheet in the anvil and cylinder apparatus. The casting process was designed to create much shorter samples, with a maximum length of 25mm, and thus shorter strips were used in the corrugating process. This process was used for creating the corrugations made from IF steel, 304 stainless steel, 4130 steel and 409 aluminized steel.

In addition to this manual corrugation process, additional corrugations were made using an additive manufacturing process. By using an additive manufacturing process it is possible to create corrugations with a variety of periods, heights, thicknesses and more complex variations that were not achievable using the anvil and cylinder method. Using the facilities at Mohawk College`s Additive Manufacturing Resource Centre, corrugated samples were printed using the selective laser melting technique on a EOSINT M 270 machine. These samples were made based on CAD drawings prepared with Autodesk Inventor software and were fabricated using stainless steel GP1 powder, which is similar to 17-4 stainless steel. A photo of a set of corrugations that were printed can be seen in Figure 5-59. Before cutting the samples from the base plate they were subjected to a stress-relief treatment to reduce the amount of warping that would occur during cutting. This stress-relief treatment consisted of heating the entire plate in a box furnace at 650°C for 1 hour under an argon atmosphere followed by a slow cool to room temperature. The samples were then cut from the plate and the surfaces were cleaned by dipping them in a concentrated hydrochloric acid solution and placing them in an ultrasonic bath for 2 minutes.

Regardless of whether the corrugations were made using the anvil and cylinder technique or additive manufacturing, the process of casting the copper around the steel corrugation was the same. This casting process was performed using a vertically oriented tube furnace and a set-up involving an arrangement of quartz tubes and graphite crucibles. This setup is illustrated in Figure 5-60 with the different components numbered to aid in the description of the setup.

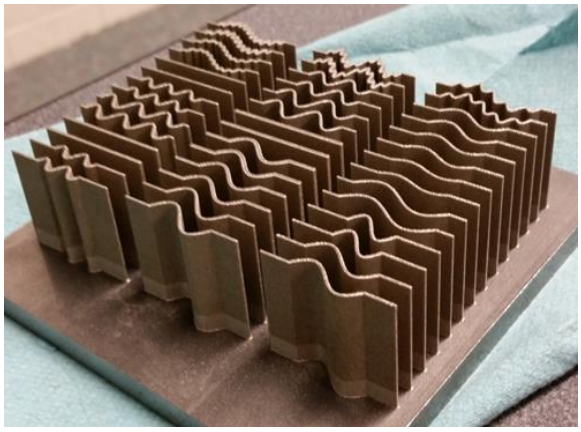

**Figure 5-59: Corrugated GP1 stainless steel samples fabricated using additive manufacturing processes.**

First off, the melting framework is set up. To begin, the tube furnace, number 1, is flipped to a vertical orientation and is placed on a steel table, number 2, with the bottom surface arranged such the bottom opening of the furnace lines up with a slightly smaller hole cut into the table, with a diameter of around 45mm. Next, the bottom quartz tube, number 3, with an outer diameter of 50mm and length of 54cm is placed on the table, around the hole, inside the tube furnace. Placed on top of the bottom tube is the graphite melting crucible, number 4. This melting crucible has an outer diameter of 50mm, inner diameter of 35mm, total height of 9.5cm, cavity height of 8.5cm, and has a tapered hole, with a maximum diameter of 10.5mm drilled through its bottom. Next, a quartz guide tube, number 5, with an outer diameter of 40mm and length of 55cm, is placed on top of the melting crucible. After the top guide tube is in place, a containing quartz tube, number 6, is placed on the table, around the rest of the setup inside the furnace. This

quartz tube has an outer diameter of 57mm that tapers to a diameter of 38mm just at the top. The entire tube has a height of 131cm, and has a small offshoot tube near the top, with diameter of 12mm and 6.5cm length, that is used to introduce argon gas into the system. Finally, a graphite

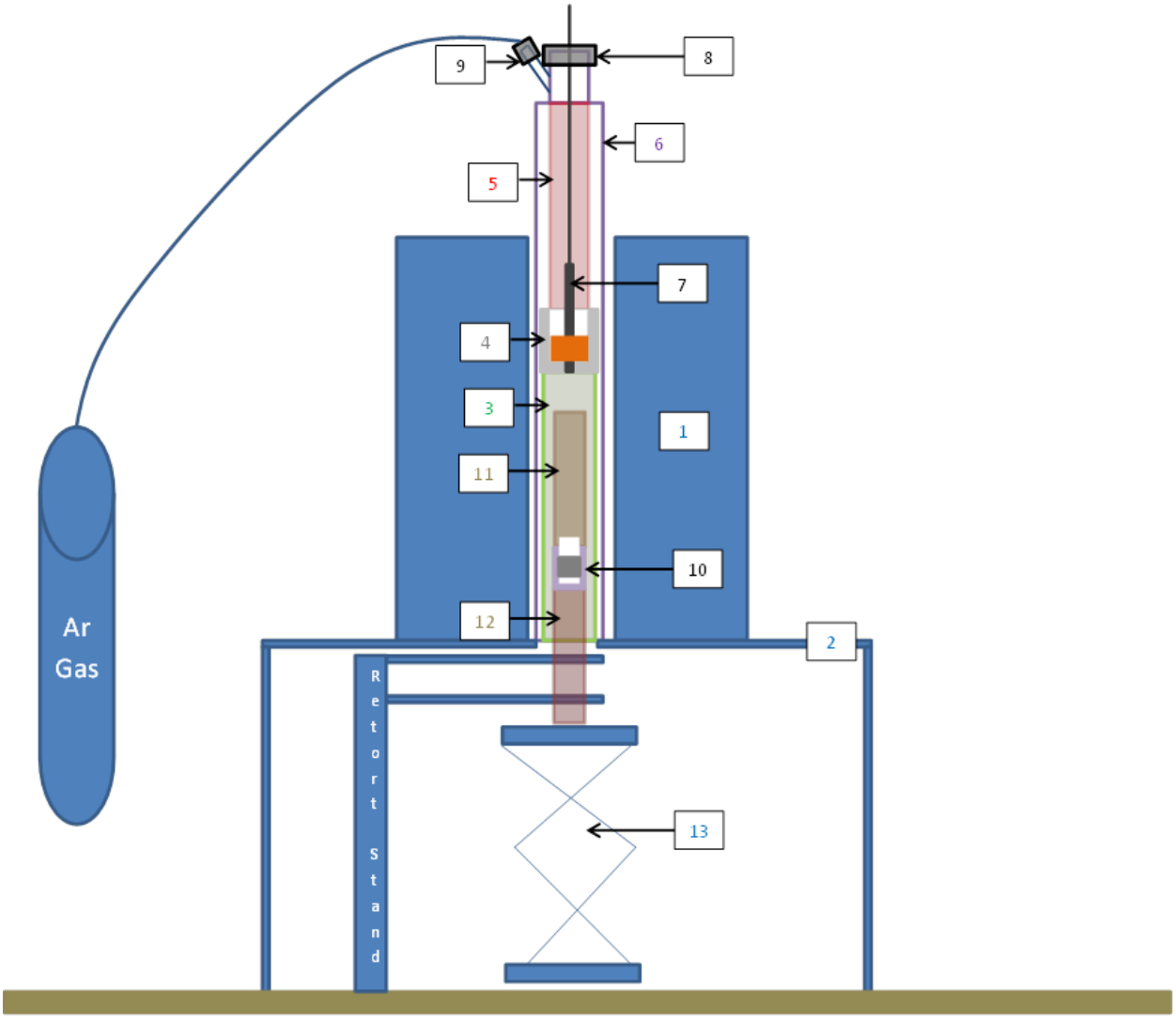


| # | Item | # | Item |
|---|---|---|---|
| 1 | Tube Furnace | 8 | Large Swagelok Fitting |
| 2 | Table (with hole) | 9 | Small Swagelok Fitting |
| 3 | Quartz Support Tube (melting crucible) | 10 | Loaded Graphite Casting Crucible |
| 4 | Graphite Melting Crucible | 11 | Quartz Lower Guide Tube |
| 5 | Quartz Upper Guide Tube | 12 | Quartz Support Tube (casting crucible) |
| 6 | Quartz Containment Tube | 13 | Jack |
| 7 | Graphite Plug and Steel Rod | | |

**Figure 5-60: Labeled diagram of the setup used for casting corrugated samples with a copper matrix.**

rod of diameter 13mm with a tapered end, attached to a steel rod, number 7, is lowered into the setup from the top until the graphite rod plugs the hole in the melting crucible. A Swagelok tube fitting, number 8, is then fitted to the top of the containing quartz tube and also tightened around the steel rod to seal the system from the top. Another Swagelok fitting, number 9, is attached to the offshoot tube and is connected to the argon gas tank. This completes the melting setup. Argon gas is then sent through the system and the tube furnace is set to a temperature of 1125°C and allowed to reach temperature. Once the temperature of the furnace stabilizes the copper is introduced into the system. In order to introduce the copper, the top fitting, number 8, is removed and a quartz tube with a diameter of 25mm and length of 39cm, is placed over the steel rod and lowered into the setup until the bottom of the tube is inside the upper guide tube, number 5. This is done to ensure the copper does not spill and falls entirely into the melting crucible. A funnel is then placed on the top opening of this tube and around 125g of copper shot (99.5%) is poured into the funnel and falls into the melting crucible. It should be noted that the length of the bottom quartz tube, number 3, was selected in order to place the melting crucible at a location in the furnace where its temperature would be between 1125°C and 1150°C. This ensures that the copper will melt relatively quickly and will be sufficiently above the melting temperature such that when cast it will remain liquid while it falls. The funnel and tube are removed, the top fitting is replaced and the copper is left to melt in the furnace for 20 minutes.

After the melting stage is complete the casting apparatus is setup. First the steel corrugation is placed inside a small graphite casting crucible, number 10, as illustrated in the photograph seen in Figure 5-61. This casting crucible has an outer diameter of 35mm, inner diameter of 25mm, height of 3.8cm, and cavity height of around 3.3cm. The top and bottom of the crucible have been machined using a lathe such that there is a small section with a reduced outer diameter at

both ends. These indents are used to hold the crucible in place between quartz tubes. Additionally, grooves were carved into opposite sides of the cavity of the crucible in order to hold the steel strips in place, and the floor of the cavity was machined to give a flat bottom. The loaded casting crucible is then placed underneath a quartz tube, number 11, which is used as the lower guide tube and on top of another quartz tube, number 12 that is used as a support tube. Both of these tubes have an outer diameter of 38mm and a length of 41cm. This stack is then placed on a jack, number 13, located underneath the furnace, which is used to raise the stack into the furnace, through the hole in the table, until the top of the bottom guide tube, number 11, reaches the bottom of the melting crucible, number 4, lined up with the currently plugged hole. This creates a pathway between the melting crucible and the casting crucible for the copper to travel through. Prior to casting, the inner surface of the lower guide tube, number 11, is coated with a boron nitride spray in order to prevent any sticking of the molten copper to the sides of the tube during casting. Once, the stack is in place, the steel rod is pulled up, unplugging the melting crucible, and the copper pours into the casting crucible and solidifies to create the composite. Using the jack, the stack is then lowered out of the furnace and the full casting crucible is placed on a ceramic block to cool. The plug can then be placed back into the hole, and the process is then repeated by loading in more copper, melting it, and casting into another loaded casting crucible. Once a sample has been cooled, the casting crucible is broken open; the sample is removed and then machined into a rectangular sample for compression testing.

The length of the lower guide tube, number 11, was selected to be 41cm based on a couple of trials with different lengths. This length resulted in samples with minimal casting defects, such as voids, coupled with relatively smaller copper grain sizes, of around 200-1000μm. The variation in grain size and porosity with different heights is due to variations in the temperature of the

furnace at different locations. If the guide tube is shorter, the casting crucible is at a higher height in the furnace, which means the temperature of the crucible will be higher and the temperature of the copper will be higher when it reaches the crucible and begins to undergo solidification. These higher temperatures lead to larger grain sizes, up to sizes of 3mm, which are close to the scale of the corrugation height. Grain sizes this large are not desirable as it can lead to inhomogeneity in different regions of the matrix due to variations in grain orientation, making the behaviour of the composite unpredictable. On the other hand, if the temperatures are too low, the porosity increases as the copper solidifies very quickly upon entering the casting crucible. Therefore, there is a trade-off between grain size and porosity that must be balanced in determining the length of the lower guide tube.

**Figure 5-61: Photograph of graphite casting crucibles used to cast copper matrix composites. (Left) A crucible loaded with a corrugated strip and (right) a crucible on its side showing the indents used for balancing the quartz tubes.**

A number of different samples were prepared using this method with varying amounts of success. During the machining of the samples, some of the composites broke apart at the interface due to poor bonding, as shown on the left side of Figure 5-62 for a copper and 4130 steel sample. This happened to some degree for all of the systems with a copper matrix and steel reinforcement. That being said, some samples held together during machining and were tested. Of these successfully machined samples, many of them broke apart during rolling, often after the

first or second pass through the rolling mill, or during compression testing. A sample of copper and the GP1 steel that failed during rolling can be seen on the right side of Figure 5-62. The ability to obtain a strong bond between the copper and the steel was a major issue for these composites and prevented consistent testing from occurring. In particular, the samples that had a stainless steel reinforcement had particularly weak interfaces, likely due to the presence of the passive oxide layer on the steel surface. It was this poor copper-steel interface that motivated the use of aluminized steel as a reinforcement, as it is known that aluminum and copper form a better bond. Unfortunately, these samples also suffered from inconsistent interfacial properties and often fell apart during testing as well. With this in mind, some samples did not fall apart and were successfully tested. A brief discussion of these successful tests will be shown below.

**Figure 5-62: Photographs of samples that failed at the interface prior to successful testing. (Left) Picture of copper-IF steel sample that broke apart at the interface during machining. (Right) Picture of copper-GP1 steel sample, with a before and after shot of samples, that broke apart at the interface during rolling.**

To begin with, samples with IF steel reinforcement were tested using interrupted channel die compression, similar to that done for the solder-copper system. Due to the large improvement in strength of a copper matrix compared to the solder matrix used earlier, very minimal deformation was achieved at relatively large values of applied force. Essentially, the copper was too strong to be tested on samples of this size using a channel die setup. In order to achieve meaningful amounts of strain, large forces would need to be applied, requiring a tensile machine stronger than the 100kN machine that was used. Additionally, there were concerns of safety with regards to applying these forces on the channel die as it was designed. It was also very difficult to

remove the sample from the channel die without damaging it in order to take the photos for the DIC analysis. For these reasons, channel die compression testing of the copper-IF steel system was discontinued and the remainder of the copper matrix samples were prepared for testing using the rolling and uniaxial compression testing techniques.

Unfortunately, successful testing of a set of samples in which a given geometric parameter was varied was not achieved. For example, in a set composites with 5 corrugation heights, only one sample was tested successfully and another with some partial success. This lack of sample consistency did not allow for an evaluation of the effect of geometric parameters. With that being said, successful strain maps were acquired using the rolling and DIC technique for a couple of individual samples across the different material systems. The strain maps for one of these samples, with a corrugated 4130 steel reinforcement will be shown to illustrate the behaviour observed. This sample was machined to a length of 15mm, width of 7mm and height of 8mm and had a corrugated reinforcement with a period of 15mm, height of 5mm and thickness of 0.6mm. The first speckle pattern that was applied flaked off after the first rolling pass which had a compressive strain of 0.025. A new speckle pattern was applied that survived for deformation up to around 15%. A set of horizontal, x-direction, strain maps for this sample is shown in Figure 5-63. Also included in this figure are the strain maps for the same sample simulated using FEM for transverse uniaxial compression loading and transverse plane strain compression loading. Looking at these maps it appears that the experimental results lie somewhere in between that of the FEM uniaxial compression results and FEM plane strain compression results, and in this case are closer to those seen for plane strain compression. For all of the maps, the regions of high and low strain follow those expected for a composite containing an unbending corrugated reinforcement. The maps generated from experimental testing of other samples with a copper

matrix and corrugated steel reinforcement showed similar strain patterns. Similar to the solder-copper system, the experimentally generated strain maps show good agreement with the local strain patterns predicted using FEM.

Unfortunately, at this stage no material system with a copper matrix has yielded successful uniaxial compression testing of both a corrugated and straight sample, and thus no plots of stress-strain curves showing the effect of corrugation for these material systems will be presented. For every material system, either the sample that had a straight reinforcement or the sample with a corrugated reinforcement broke apart during machining or uniaxial compression testing. Therefore, more testing is required for these copper matrix composite systems to compare the stress-strain response seen experimentally to that predicted using FEM simulations.

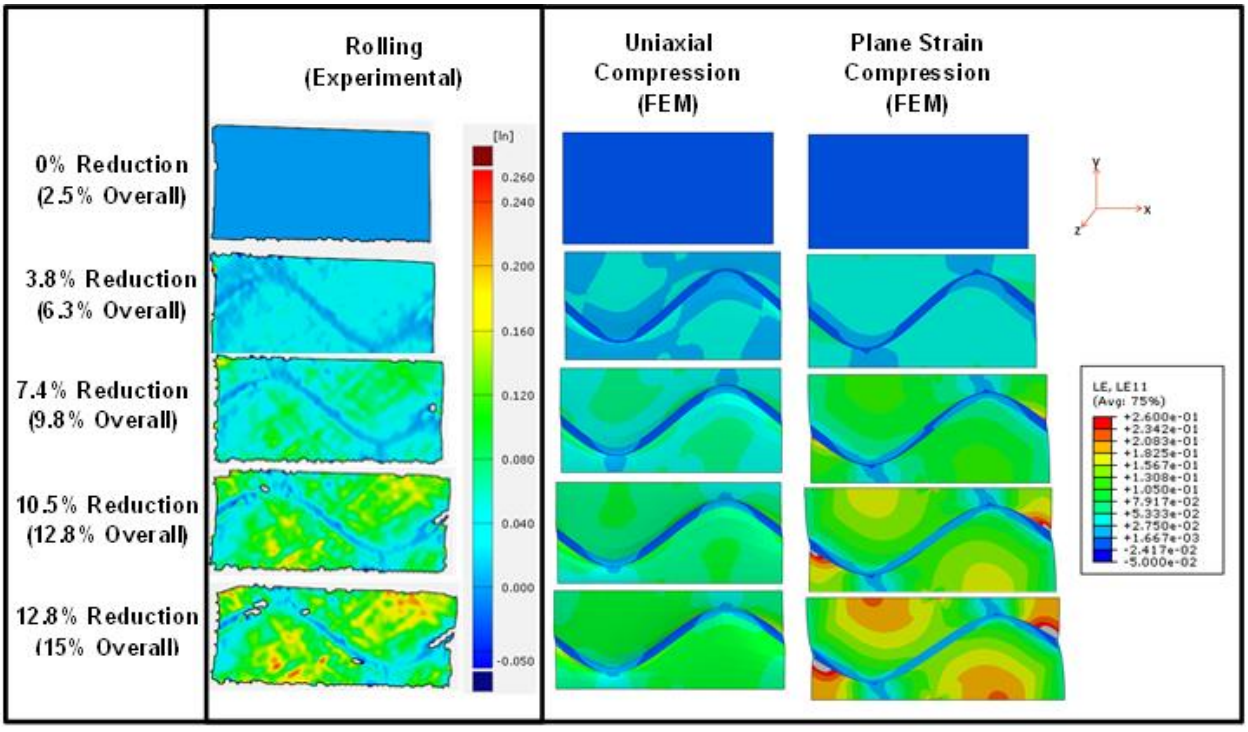


**Figure 5-63: Longitudinal (x-direction) strain maps of a corrugation reinforced composite with a copper matrix and 4130 steel reinforcement under transverse rolling using experimental DIC (left), transverse uniaxial compression loading using FEM (middle), and transverse plane strain compression loading using FEM (right) at different levels of overall compression.**

## 5.3 Summary of Experimental Work

The experimental work that has been performed can be summarized as follows:

- Tensile tests on isolated corrugated strips were performed for copper, IF steel and stainless steel systems. In all cases the stress-strain curves demonstrated the characteristic shape expected for an unbending corrugation, with the increasing work hardening behaviour and showed increases in necking strain as the degree of corrugation was increased, matching the trends shown earlier in the modeling work.
- Comparisons of the experimental stress-strain curves of the isolated corrugated strips to FEM and analytically modelled stress-strain curves show good agreement both in terms of the shapes of the curves and the absolute values. This suggests that confidence can be placed in the conclusions drawn based on FEM simulations of isolated corrugations.
- In addition to performing experiments on isolated corrugations, experimental work was completed that focused on corrugation reinforced composites, focusing on the solder matrix, copper reinforced system. Samples were made using a casting technique and tensile tests were performed on these samples that were spray painted with a speckle pattern to track local strains.
- Imperfections at the interface led to decohesion during loading, and the samples failed prematurely as a result. That being said, increasing work hardening behaviour as a result of reinforcement unbending was observed in the Considere plot of the sample. Additionally, the wavy surface that is caused by an unbending corrugation, which was predicted in FEM simulations, was also observed in the tension tests. Also, the local strain patterns seen in the strain maps qualitatively matched those of the FEM simulations at early stages of deformation.

- To minimize the impact of the interfacial weakness, samples were tested under transverse plane strain compression in a channel die. It was established using FEM that the strain patterns under these conditions would be similar to those seen in tension and that the compressive stress-strain curve can provide some information with regards to expected necking behaviour of a given system under tension. The strain maps generated from the channel die deformation showed excellent qualitative agreement with FEM simulations, however, issues arose with regards to speckle pattern degradation and difficulty removing the samples from the channel, and thus the testing technique was abandoned.
- The final technique used to test these samples involved transverse uniaxial compression tests, to obtain stress-strain data, and rolling and DIC analysis to obtain local strain patterns.
- Both FEM and experimental compressive stress-strain curves showed similar trends relating corrugated and straight samples, however, using the compressive stress-strain curve from the experiments to estimate a tensile necking strain was shown to be relatively ineffective or at least inconclusive in its usefulness.
- The progression of strain maps that were generated from rolling showed good qualitative agreement with FEM simulations under plane strain compression and improved qualitative agreement if compared to FEM simulation under uniaxial compression.
- Finally, in addition to the solder-copper system, numerous tin-steel and copper-steel composites were cast, machined and tested in compression with mixed success due to inconsistent interfacial strength. A strain map for a copper matrix, 4130 steel, corrugated composite was presented with good agreement with FEM simulations.

# 6 Conclusions and Recommendations for Future Work

## 6.1 Conclusions

The work of Bouaziz,[31] Boke,[32] Chou and Takahashi,[44] etc. demonstrate that materials that employ a corrugated architecture have the potential to improve ductility through an unbending process of the corrugation. With this in mind, the goal of this work was to use FEM modeling to gain an understanding of what factors controlled this unbending behaviour and determine under what conditions these materials were capable of achieving the desirable combination of high strength and improved ductility, and were thus capable of traversing desirable areas of material property space. This improved ductility was evaluated by comparing the necking strains of materials with corrugated geometries to those with straight geometries. In order to achieve this goal, parametric studies were performed that investigated the effects of geometric and material parameters on the mechanical response of architectured materials with a corrugated geometry. The FEM modeling work was then compared to experimental tests for validation purposes. This work looked at both isolated corrugations and corrugation reinforced composites.

The work that focused on the isolated corrugations showed a couple main findings. First off, it was found that greater gains in ductility can be achieved by increasing the degree of corrugation, whether that is through increasing the corrugation height, decreasing the period, or increasing the percentage corrugated. This agreed with findings found in literature discussed earlier. Second, in general, changes to material properties have the same effects on strength and ductility regardless of whether the geometry is straight or corrugated. Third, the stress-strain curve of an isolated corrugation has three main regions; an unbending region in which the stress is low but shows increasing work hardening while the corrugation shows bending dominated behaviour, a

transition region wherein work hardening skyrockets and the reinforcement becomes straight, and the stretching region wherein the material behaves like a straight material and shows stretching dominated behaviour. The bending dominated behaviour was confirmed by looking at local stress and strain maps, which showed variations in stress and strain across the thickness of the peaks that matched those expected for an unbending corrugation. Additionally, measurements of the corrugation angle clearly show unbending occurring and plots of the plastic stretching strain in the regions between peaks and troughs showed minimal stretching behaviour while the unbending process was occurring. Finally, it was shown that an analytical model based on modifications to sheet bending calculations, accurately predicts the stress-strain curve of an isolated corrugation. In general, experimental tests performed on isolated corrugations of copper, IF steel and 304 stainless steel showed good agreement with the FEM simulations and the analytical model, and demonstrated the expected trends with regards to changing geometric parameters.

The findings for the isolated corrugations were complemented with the FEM work performed for the corrugation reinforced composites. It was found that under certain conditions, improvements in ductility for these composite materials could be achieved through the use of a corrugated reinforcement geometry. The increasing work hardening behaviour that was found for isolated corrugations was also observed for corrugation reinforced composites, but was muted due to the presence of the matrix and the consequent stress transfer. Depending on the relative properties of the materials, this often led to an earlier initiation of stretch dominated behaviour of the reinforcement. Comparisons between isolated and embedded corrugations of the corrugation angle and stretching strains confirmed the constraint effect of the matrix on unbending

behaviour. These metrics were also used to evaluate how effective a given composite system was in achieving bending dominated behaviour.

Looking at strain maps generated from the FEM simulations, it was evident that a characteristic pattern emerged as a result of the unbending of a corrugated reinforcement. This pattern consists of large deformation in the matrix below peaks and above troughs, and small deformation in the matrix above peaks and below troughs. Using simple thought experiments these strain patterns were explained based on the combined effect of shape changes caused by a moving corrugation and the overall loading of the composite. Additionally, the increasing work hardening behaviour that occurs in these composite materials was explained using simple composite theory with regards to reinforcement alignment and the fact that the geometry evolves with deformation as a result of the unbending corrugation.

It was concluded that in order to show a benefit in ductility through corrugation, the boost in work hardening that comes from the unbending reinforcement must occur at the right time and must be sufficiently large to delay the intersection of the work hardening and stress on a Considere plot. The timing and size of the work hardening boost was found to be dependent on the geometric parameters of the corrugation and when this boost is needed is dependent on the material parameters of the matrix and reinforcement. Therefore, it was found that there is significant interplay between geometry and material with regards to determining whether benefit in ductility through corrugation is possible. In general, it was found that if the matrix yield strength is too low or the matrix hardening rate too high, that the boost in work hardening from an unbending corrugation comes in too early and there is no benefit from corrugation, as straight composites also do not neck until high strains are reached. On the other hand, if the matrix yield strength is too high or the matrix hardening rate too low, the boost in work hardening comes in

too late and the matrix necks early. Therefore, there is a sweet spot for the matrix properties that needs to be met in order for improvement through corrugation to occur. With regards to the reinforcement, the yield strength of the reinforcement needs to be high enough such that the stress transferred from the matrix is insufficient to trigger early stretching of the reinforcement, thus allowing unbending to some degree to provide a boost in work hardening that delays necking.

Provided that the matrix is capable of accommodating an unbending reinforcement, the trends observed with regards to the effect of the degree of corrugation were similar to those seen for isolated corrugations. Increasing the height or decreasing the period of the corrugation led to greater improvements in necking strain, however, the effect of the degree of corrugation was more complicated than in the isolated case due to the introduction of the transition zone.

In order to be able to predict under what conditions improved ductility through corrugation is obtainable, a series of benefit maps and surfaces were generated. These maps and surfaces were shown to be relatively effective tools for predicting the improvement in necking strain of a corrugated composite relative to a straight composite for a system with a given corrugation geometry and component material parameters. These tools were only developed for linear hardening systems at this stage.

Finally, it was demonstrated that corrugation reinforced composites are capable of traversing desirable areas in materials property space defined by high strength and ductility. This was shown using material property charts, for various geometries, volume fractions and arrangements. In particular it was found that improvements in ductility could be achieved by increasing the volume fraction of a corrugated reinforcing phase for which the reinforcing

material itself has lower ductility than that of the matrix. Additionally, it was found that the spacing between corrugated reinforcements can become important due to the fact that decreased spacing can lead to constraint of the matrix, leading to earlier necking.

Experimental fabrication and testing of these corrugation reinforced composites for validation purposes met with a number of difficulties. Much of the experimental work focused on the solder-copper system. Tensile tests performed on cast corrugated composites suffered from interfacial weakness leading to decohesion and early necking. However, it was shown using FEM simulations that it was possible to obtain some valuable information on these composites using transverse compressive loading, which would not suffer as significantly from interfacial defects. This led to the testing of these composites under transverse compressive loading, using channel die compression, uniaxial compression and rolling techniques. Although, these techniques had their own issues, it was possible to obtain some stress-strain curves and strain maps using DIC, for comparison of the modeling work. The experimentally generated strain maps and stress-strain curves showed good qualitative agreement with FEM simulations and on some occasions good quantitative agreement, in particular, with regards to the strain maps generated from rolling experiments. Additional experiments for copper-steel and tin-steel systems also suffered from issues with regards to decohesion at the interface. As will be discussed in the next section, additional experiments will need to be performed to further validate the FEM work; however, these initial experiments show enough agreement to provide moderate confidence that the conclusions drawn based on the modeling efforts are applicable in practice.

Overall, this work demonstrated the effectiveness of using simple parametric studies to gain an understanding of the key factors determining the behaviour of a complicated composite system.

In particular it was effective at determining the interplay that exists in these corrugation reinforced composite materials between geometry and materials, and allowed for the development of effective predictive tools. Finally, this work showed that the use of an architectured materials design approach can lead to achieving a combination of desirable properties that are otherwise unobtainable using standard design practices.

## 6.2 Recommendations for Future Work

Although this research has produced some valuable information with regards to understanding the behaviour and applicability of corrugated materials, it has also illuminated some areas in which there are opportunities for further research, particularly from an experimental standpoint. Some recommendations pertaining to future work in this research area will now be discussed.

First of all, additional experimental work should be performed, potentially still looking at the solder-copper and copper-steel systems, in order to further validate the FEM efforts of this thesis. Additional samples should be made that span a range of values for a given geometric parameter, and these samples should be tested using the uniaxial compression and rolling techniques. The effect of the degree of corrugation can then be evaluated by looking at the compressive and indirectly calculated stress-strain curves, and the corresponding strain maps can be compared to FEM simulations. In order to vary the geometry of the steel corrugations, additive manufacturing using a different alloy powder should be performed, perhaps a low alloy steel or maraging steel. This use of a different steel alloy is recommended to avoid the issues of the oxide layer that is present for the stainless steel alloys. Additionally, once a relatively good interface is established between the steel and the copper, variations on the properties of the steel can be attempted by using heat treatments and/or carburization and decarburization treatments. It would also be of interest to try some other material systems, such as aluminum-steel, copper-tungsten and copper-

nickel and to try and make samples that have multiple corrugated reinforcements, similar to those simulated using FEM in this thesis. Additionally, if a relatively strong interface can be established for one of these systems, it would be of great interest to return to testing these composites under tensile loading, not only to provide valuable information on the effect of geometry on necking strain, but also to evaluate whether the technique for converting compressive stress-strain data to equivalent tensile data is applicable for real samples.

It was mentioned in the previous chapter that the resolution of the DIC technique was insufficient to show variation in strain across the thickness of the reinforcement. A detailed strain map of this region would be a useful piece of information as it would confirm whether local bending of the corrugation peak was occurring. It is possible that this could be achieved using a variation of the DIC technique. Instead of applying a speckle pattern using spray paint, the sample surface could be polished and etched to reveal the microstructure of the reinforcement material. Using a microscope, an image of the microstructure would be captured before and after deformation, and the movement of the microstructural features could be used to estimate local strains present across the thickness of the reinforcement peak.

In addition to generating strain maps using DIC for these composites, another technique that could provide valuable data pertaining to local deformation pattern in these materials is the use of recrystallization heat treatments, similar to the method used in Poole[24]for transverse compression of fiber reinforced composites. This would involve loading a number of identical samples to different levels of overall deformation and performing heat treatments that are capable of causing recrystallization in regions of higher strain. Metallography on the samples would then reveal the emergence of small recrystallized grains in regions where high strain was present, likely in regions below peaks and above troughs.

Another valuable direction for further research of these corrugated materials would be related to developing other fabrication techniques. The efforts of this research project focused on casting techniques, however it would be of interest to have alternative methods for making these materials. Some potential techniques to consider include brazing to form the matrix-reinforcement interface, using a selective laser hardening technique, as performed by Bouaziz,[31] and using diffusion masking and carburization/decarburization as proposed by Chehab et al.[15]

One of the main assumptions that was made for the modeling work in this thesis was a coherent, unbreakable interface. Although this assumption was useful in limiting the variables of the problem to focus on the effects of the geometry and the material components, it is also an unrealistic assumption, as evidenced by the frequent issues with interfacial strength seen experimentally. Therefore, one of the next areas for future work on this topic should be a study on the effect of the strength of the interface using FEM simulations. The effect of this interfacial strength should be tested under different loading conditions, in particular under tensile and transverse compression loading. It would be interesting to see whether the gains in ductility predicted for perfect interfaces are still achievable with interfaces that are more realistic in their definitions. These simulations could then be compared to experimental work, where the strength of the interface is determined using a test similar to a fiber pull-out test or perhaps a bending test.

As part of this research effort, a tool for predicting the benefit through corrugation was developed, in the form of benefit maps and surfaces. In the future it would be of interest to create more of these maps that would be applicable under a larger range of circumstances. This would include creating maps for different volume fractions of reinforcement and generating maps that are more applicable for power-law hardening materials. Ideally, a tool could be developed that took in all of the relevant material and geometric information, and predicted the resultant

necking strain of the composite, similar to how the analytical model developed in this thesis for isolated corrugations is capable of predicting the necking strain and UTS of a given isolated corrugation.

Another potential area for future research involves simulating these corrugation reinforced composites under more complicated loading conditions such as bending or shear. This would provide a more complete picture on the mechanical response of these materials and could be used to generate a forming limit diagram. Additionally, the results could be compared to that observed for isolated corrugations under these different loading geometries, as seen in the literature, to see how the constraint of the matrix impacts the resultant mechanical response.

Similar to the approach used by Shi et al.[52] for strain rate sensitive reinforcing materials; it would be beneficial to look at the effect of strain rate sensitivity of the matrix material on the resultant stress-strain curves. This would be particularly relevant to the solder-copper system as solder shows strong strain-rate sensitivity, especially when tested at room temperature, as discussed in the work of Plumbridge and Gagg.[69] It is likely that consideration of this property could lead to different behaviour for corrugation reinforced composites compared to straight reinforced composites due to the heterogeneous deformation patterns in the matrix. This concern of strain rate sensitivity would also be important for extending the scope of study to include post-necking behaviour and damage evolution, which is a logical next step in expanding the understanding of these corrugated materials.

Broadening the scope of interest, it was proposed in the work of Boke[32] and shown for isolated corrugations in the work of Hu et al.[56], that it would be of interest to extend the corrugated architecture into the width direction. It would interesting to apply this additional dimension of

corrugation and test its effect both using FEM simulations and experimentally. Other variations could include looking at corrugated fibers instead of sheets

Finally, it was mentioned in the literature review chapter that it is not only corrugated structures that show potential for improving necking strain but any curvilinear geometry that undergoes a straightening process during loading. The helical geometry is one that is frequently observed in nature due to its ability to provide ductility and increasing work hardening. With this in mind, it would interesting to explore the behaviour of helical reinforced composites using a similar approach to that used in this thesis for corrugated composites. Additionally, the testing could include in-situ testing with x-ray tomography to capture the evolution of the helical geometry as the sample is loaded. It would interesting to observe what parallels are present between the corrugated and helical architectures, with regards to the relationship between material and geometry.

# 7 References


1. Ashby, M. Designing architectured materials. *Scr. Mater.* **68,** 4–7 (2013).

2. Ashby, M. F. & Bréchet, Y. J. M. Designing hybrid materials. *Acta Mater.* **51,** 5801–5821 (2003).

3. Lu, K., Lu, L. & Suresh, S. Strengthening materials by engineering coherent internal boundaries at the nanoscale. *Science* **324,** 349–52 (2009).

4. Lu, L., Chen, X., Huang, X. & Lu, K. Revealing the maximum strength in nanotwinned copper. *Science* **323,** 607–10 (2009).

5. De Cooman, B. C., Kwon, O. & Chin, K.-G. State-of-the-knowledge on TWIP steel. *Mater. Sci. Technol.* **28,** 513–527 (2012).

6. Jacques, P., Furnémont, Q., Mertens, A. & Delannay, F. On the sources of work hardening in multiphase steels assisted by transformation-induced plasticity. *Philos. Mag. A* **81,** 1789–1812 (2001).

7. Cherkaev, A. & Slepyan, L. Waiting Element Structures and Stability under Extension. *Int. J. Damage Mech.* **4,** 58–82 (1995).

8. Ashby, M. F. Hybrids to fill holes in material property space. *Philos. Mag.* **85,** 3235–3257 (2005).

9. Fleck, N. A., Deshpande, V. S. & Ashby, M. F. Micro-architectured materials: past, present and future. *Proc. R. Soc. A Math. Phys. Eng. Sci.* **466,** 2495–2516 (2010).

10. Ashby, M. F. The properties of foams and lattices. *Philos. Trans. A. Math. Phys. Eng. Sci.* **364,** 15–30 (2006).

11. Bouaziz, O., Bréchet, Y. & Embury, J. D. Heterogeneous and Architectured Materials: A Possible Strategy for Design of Structural Materials. *Adv. Eng. Mater.* **10,** 24–36 (2008).

12. Brechet, Y. & Embury, J. D. Architectured materials: Expanding materials space. *Scr. Mater.* (2012). doi:10.1016/j.scriptamat.2012.07.038

13. Dyskin, A. V., Estrin, Y., Pasternak, E., Khor, H. C. & Kanel-Belov, A. J. Fracture Resistant Structures Based on Topological Interlocking with Non-planar Contacts. *Adv. Eng. Mater.* **5,** 116–119 (2003).

14. Bouwhuis, B. A. *et al.* Deformation twinning as a strengthening mechanism in microtruss cellular materials. *Scr. Mater.* **63,** 609–612 (2010).

15. Chehab, B., Zurob, H., Embury, D., Bouaziz, O. & Brechet, Y. Compositionally Graded Steels: A Strategy for Materials Development. *Adv. Eng. Mater.* **11,** 992–999 (2009).

16. Abu Samk, K., Yu, B. & Hibbard, G. D. Architectural design in stretch-formed microtruss composites. *Compos. Part A* **43,** 955–961 (2012).

17. Cicoria, R., Chehab, B. & Zurob, H. Diffusion as a method for producing architectured materials. *Scr. Mater.* **68,** 17–21 (2013).

18. Srinivasan, A. V., Haritos, G. K. & Hedberg, F. L. Biomimetics: Advancing man-made materials through guidance from nature. *Appl. Mech. Rev.* **44,** 463–482 (1991).

19. Dunlop, J. W. C. & Brechet, Y. J. M. Architectured Structural Materials: A Parallel Between Nature and Engineering. in *2009 MRS Spring Meet.* 1–11 (2009).

20. Kelly, A. & W.R., T. Tensile Properties of Fibre-Reinforced Metals: Copper/Tungsten and Copper/Molybdenum. *J. Mech. Phys. Solids* **13,** 329–350 (1965).

21. Brown, L. M. & Clarke, D. R. The work hardening of fibrous composites with particular reference to the copper-tungsten system. *Acta Metall.* **25,** 563–570 (1977).

22. Mortensen, A., Pedersen, O. B. & Lilholt, H. On the Work Hardening of Fiber Reinforced Copper. *Scr. Mater.* **38,** 1109–1115 (1998).

23. Ozturk, T., Poole, W. J. & Embury, J. D. The deformation of Cu-W laminates. *Mater. Sci. Eng.* **148,** 175–178 (1991).

24. Poole, W. J. The deformation of copper-tungsten composites. (1993).

25. Cox, H. L. The elasticity and strength of paper and other fibrous materials. *Br. J. Appl. Phys.* **3,** 72–78 (1952).

26. Eshelby, J. D. The determination of the elastic field of an ellipsoidal inclusion, and related problems. *Proc. R. Soc. Lond. A. Math. Phys. Sci.* **241,** 376–396 (1957).

27. Semiatin, S. L. & Piehler, H. R. Deformation of Sandwich Sheet Materials in Uniaxial Tension. *Metall. Trans. A* **10,** 85–96 (1979).

28. Semiatin, S. L. & Piehler, H. R. Formability of Sandwich Sheet Materials in Plane Strain Compression and Rolling. *Metall. Trans. A* **10,** 97–107 (1979).

29. Dayyani, I., Ziaei-Rad, S. & Salehi, H. Numerical and Experimental Investigations on Mechanical Behavior of Composite Corrugated Core. *Appl. Compos. Mater.* **19,** 705–721 (2012).

30. Thill, C. *et al.* Investigation of trapezoidal corrugated aramid/epoxy laminates under large tensile displacements transverse to the corrugation direction. *Compos. Part A Appl. Sci. Manuf.* **41,** 168–176 (2010).

31. Bouaziz, O. Geometrically induced strain hardening. *Scr. Mater.* **68,** 28–30 (2013).

32. Boke. Numerical Simulation of Mechanical Behavior of Reinforced Sheet Metals. (2012).

33. Dayyani, I., Shaw, a. D., Saavedra Flores, E. I. & Friswell, M. I. The Mechanics of Composite Corrugated Structures: A Review with Applications in Morphing Aircraft. *Compos. Struct.* **133,** 358–380 (2015).

34. Ge, R., Wang, B., Mou, C. & Zhou, Y. Deformation characteristics of corrugated composites for morphing wings. *Front. Mech. Eng. China* **5,** 73–78 (2010).

35. Park, K.-J., Jung, K. & Kim, Y.-W. Evaluation of homogenized effective properties for corrugated composite panels. *Compos. Struct.* **140,** 644–654 (2016).

36. Luo, S., Suhling, J. C., Considine, J. M. & Laufenberg, T. . The bending stiffnesses of corrugated board. *Mech. Cellul. Mater.* **145,** 15–26 (1992).

37. Gilchrist, A. ., Suhling, J. C. & Urbanik, T. J. Nonlinear Finite Element Modeling of Corrugated Board. *Mech. Cellul. Mater.* **231,** 101–106 (1999).

38. Zangani, D., Robinson, M. & Gibson, A. G. Progressive Failure of Composite Hollow Sections with Foam-Filled Corrugated Sandwich Walls. *Appl. Compos. Mater.* **14,** 325–342 (2007).

39. Hanagud, S., Craig, J. I., Sriram, P. & Zhou, W. Energy Absorption Behaviour of Graphite Epoxy Composite Sine Webs. *J. Compos. Mater.* **23,** 448–459 (1989).

40. Bogetti, T. A., Gillespie, J. W. J. & Lamontia, M. A. Influence of Ply Waviness on the Stiffness and Strength Reduction on Composite Laminates. *J. Thermoplast. Compos. Mater.* **5,** 344–369 (1992).

41. McIntyre, J. S., Rasmussen, M. L., Bert, C. W. & Kline, R. A. Resonance in fiber-reinforced composite materials with sinusoidal stiffness properties. *Wave Motion* **30,** 97–123 (1999).

42. Williams, R. R., Howard, W. E. & Martin, S. M. Composite sandwich structures with rapid prototyped cores. *Rapid Prototyp. J.* **17,** 92–97 (2011).

43. Chiskis, A. & Parnes, R. Nonlinear Effects in the Extension of an Elastic Space Containing a Wavy Layer Inclusion. *J. Mech. Phys. Solids* **46,** 1213–1251 (1998).

44. Chou, T.-W. & Takahashi, K. Non-linear elastic behaviour of flexible fibre composites. *Composites* **18,** 25–34 (1987).

45. Abdelrahman, W. G. & Nayfeh, A. H. Micromechanical modeling of stress distribution in undulated composites under axial loading. *Mech. Mater.* **30,** 83–90 (1998).

46. Katz, A., Trinh, C., Wright, J., Tu, W. & Pindera, M.-J. Plastic strain localization in periodic materials with wavy brick-and-mortar architectures and its effect on the homogenized response. *Compos. Part B Eng.* **68,** 270–280 (2015).

47. Khatam, H. & Pindera, M.-J. Thermo-elastic moduli of periodic multilayers with wavy architectures. *Compos. Part B Eng.* **40,** 50–64 (2009).

48. Khatam, H. & Pindera, M. Parametric finite-volume micromechanics of periodic materials with elastoplastic phases. *Int. J. Plast.* **25,** 1386–1411 (2009).

49. Khatam, H. & Pindera, M.-J. Plasticity-triggered architectural effects in periodic multilayers with wavy microstructures. *Int. J. Plast.* **26,** 273–287 (2010).

50. Cavalcante, M. A. A., Khatam, H. & Pindera, M.-J. Homogenization of elastic–plastic periodic materials by FVDAM and FEM approaches – An assessment. *Compos. Part B Eng.* **42,** 1713–1730 (2011).

51. Khatam, H. & Pindera, M.-J. Microstructural scale effects in the nonlinear elastic response of bio-inspired wavy multilayers undergoing finite deformation. *Compos. Part B Eng.* **43,** 869–884 (2012).

52. Shi, Y., Zhao, P. Z., Wu, P. D., Lloyd, D. . & Embury, J. . Effect of Rate Sensitivity on Structural Sandwich Plates with Sinusoidal Corrugated Cores. *Adv. Eng. Mater.* **18,** 1250–1258 (2016).

53. Besse, C. C. & Mohr, D. Optimization of the Effective Shear Properties of a Bidirectionally Corrugated Sandwich Core Structure. *J. Appl. Mech.* **80,** 1–10 (2013).

54. Besse, C. C. & Mohr, D. Plasticity of formable all-metal sandwich sheets: Virtual experiments and constitutive modeling. *Int. J. Solids Struct.* **49,** 2863–2880 (2012).

55. Seong, D. Y., Jung, C. G., Yang, D. Y., Moon, K. J. & Ahn, D. G. Quasi-isotropic bending responses of metallic sandwich plates with bi-directionally corrugated cores. *Mater. Des.* **31,** 2804–2812 (2010).

56. Hu, Y., Li, W., An, X. & Fan, H. Fabrication and mechanical behaviors of corrugated lattice truss composite sandwich panels. *Compos. Sci. Technol.* **125,** 114–122 (2016).

57. Kagawa, Y., Okuhara, H., Nakata, E. & Yoshida, S. Tensile Properties of Helical Fiber Reinforced Composite Metals.pdf. *J. Japanese Inst. Met.* **46,** 313–322 (1982).

58. Kagawa, Y., Nakata, E. & Yoshida, S. Fracture Behavior and Toughness of Helical Fiber Reinforced Composite Metals. in *Prog. Sci. Eng. Compos.* 1457–1464 (1982).

59. Baley, C. Analysis of the flax fibres tensile behaviour and analysis of the tensile stiffness increase. *Compos. Part A Appl. Sci. Manuf.* **33,** 939–948 (2002).

60. Reiterer, A., Lichtenegger, H., Tschegg, S. & Fratzl, P. Experimental evidence for a mechanical function of the cellulose microfibril angle in wood cell walls. *Philos. Mag. A* **79,** 2173–2184 (1999).

61. Matin Ghahfarokhi, Z. & Golestanian, H. Effects of nanotube helical angle on mechanical properties of carbon nanotube reinforced polymer composites. *Comput. Mater. Sci.* **50,** 3171–3177 (2011).

62. Slepyan, L. I., Krylov, V. I. & Parnes, R. Helical inclusion in an elastic matrix. *J. Mech. Phys. Solids* **48,** 827–865 (2000).

63. Huang, W. & You, Z. Analysis of Mechanical Properties of Pipes with Helical Reinforcement under Axial Tension. *Adv. Mater. Res.* **189-193,** 1822–1826 (2011).

64. Labossiere, P. Mechanical Properties and Performance of Materials. 1–29 (2007). at <http://courses.washington.edu/me354a/>

65. *Atlas of Stress Strain Curves*. 95 (ASM International, 2002).

66. Hosford, William, F. & Caddell, Robert, M. *Metal Forming: Mechanics and Metallurgy*. 196 (Cambridge University Press, 2007).

67. Fraser, M., Zurob, H., Wu, P. & Bouaziz, O. Analytical Model of the Unbending Behavior of Corrugated Reinforcements. *Adv. Eng. Mater.* **16,** 872–877 (2014).

68. Bouaziz, O., Allain, S., Barcelo, D. & Niang, R. Strengthening by plastic corrugated reinforcements: an efficient way for strain-hardening improvement by architecture. in *2009 MRS Spring Meet.* 1–6 (2009). doi:10.1557/PROC-1188-LL05-01

69. Plumbridge, W. J. & Gagg, C. R. Effects of strain rate and temperature on the stress-strain response of solder alloys. *J. Mater. Sci. Mater. Electron.* **10,** 461–468 (1999).